Preparations for Measurement of Electroweak Boson Production Cross-Sections using the Electron Decay Modes, with the Compact Muon Solenoid Detector

David Robert Wardrope

Department of Physics,
Imperial College London

CERN-THESIS-2010-012
29/10/2009

A thesis submitted to Imperial College London
for the degree of Doctor of Philosophy
and the Diploma of Imperial College.

Abstract

The Compact Muon Solenoid was designed to make discoveries at the TeV scale : to elucidate the nature of electroweak symmetry breaking and to search for physics beyond the Standard Model. For any such discovery to be credible, it must first be demonstrated that the CMS detector is understood. One mechanism to make this demonstration is to measure "standard candle" processes, such as W and Z production. This thesis describes preparations undertaken to make these measurements using the electron decay modes, with $\int Ldt = 10\,\mathrm{pb}^{-1}$ of collision data.

The energy resolution of the electromagnetic calorimeter was measured in test beam data. An improved method of deriving the optimised weights necessary for amplitude reconstruction is described.

The measurement of electron charge using tracks is impaired by the electron showering in the tracker material. A novel charge measurement technique that is complementary to the existing method was assessed.

Missing transverse energy is a powerful discriminating variable for the selection of $\mathrm{W}^{\pm} \rightarrow \mathrm{e}^{\pm}\,\nu_{\mathrm{e}}$ events, however it is difficult to simulate accurately due to its global nature. The Ersatz Missing Energy method was developed to provide reliable and accurate descriptions of missing energy from data using readily reconstructible $\gamma^{*}/\mathrm{Z} \rightarrow \mathrm{e}^{+}\mathrm{e}^{-}$ events. The method is described and evaluated.

Finally, the measurement strategy for W and Z boson production cross-sections in early data is outlined and analysed using simulated data. Significant results can be obtained with only $\int Ldt = 10\,\mathrm{pb}^{-1}$.

Declaration

This dissertation is the result of my own work, except where explicit reference is made to the work of others, and has not been submitted for another qualification to this or any other university. This dissertation does not exceed the word limit specified in the College Regulations.

The copyright of this thesis rests with the author and no quotation from it or information derived from it may be published without the prior written consent of the author.

David Wardrope

Acknowledgements

There are many people to whom I owe my thanks for their help over the past four years, at Imperial College, CERN and elsewhere.

Chief among them is Chris Seez, my supervisor, who has provided me with excellent guidance throughout the course of my work. He was never too busy to deal with my questions and always knew the answers.

I'm very grateful to Georgios Daskalakis for his help getting me started when I moved out to CERN and his leadership of the electroweak electrons group. *Ευχαριστὼ πολὺ* for the invitation to visit Athens!

Merci beaucoup to Alex Zabi for all his help on the test beam analysis and CSA08.

I would like to thank Jon Hays, Alex Tapper, Geoff Hall and the rest of the Imperial College CMS group for their advice and support.

Thanks to Robin Nandi for taking over the Ersatz work so I could write up.

Thanks to Claire Timlin, Dave Evans, Nikos Rompotis and the rest of the LTA students for making Geneva a fun place to be. Thanks to Chris Eames, David Lee, Kostas Petridis, Mark Pesaresi, Mark Tibbetts, Joe Walding, Andy Rose, Theo Christoudias and Hakan Yilmaz for making my PhD experience so enjoyable.

The largest debts of gratitude I owe are to Erica Brereton and my family. Erica for being so wonderful, sticking by me during my time in Geneva and proof reading this entire thesis. My family, for nurturing my interest in science from an early age and for their constant love, support and encouragement throughout my life.

Thank you all.

Contents

List of Figures **13**

List of Tables **21**

1 Electroweak Theory **23**

1.1 The Standard Model 23

1.2 U(1) Invariance 24

1.3 SU(2) Invariance 27

1.4 The Glashow-Salam-Weinberg Model 28

1.5 Spontaneous Symmetry Breaking and the Higgs Mechanism 31

1.5.1 Fermion Masses 36

1.6 Electrons and the Electroweak Interaction 36

1.7 W and Z Cross-Section Measurements at the LHC 37

2 The Compact Muon Solenoid **41**

2.1 LHC 41

2.2 CMS Detector 45

2.2.1 Solenoid 47

2.2.2 Tracking System 48

2.2.3 Electromagnetic Calorimeter 51

2.2.4 Hadronic Calorimeter 56

2.2.5 Muon System 58

2.2.6 Trigger and Data Acquisition System 59

3 Amplitude Reconstruction in the Electromagnetic Calorimeter **63**

3.1 Experimental Set-up 63

3.1.1 Electron Beam 63

3.1.2 H4 Experimental Area 64

3.2 ECAL Front End Electronics 65

3.3 Amplitude Reconstruction 66
3.4 Weight Determination 66
3.4.1 Weights for the Asynchronous Running 67
3.5 Determination of Signal Representations 68
3.5.1 Improved Method 70
3.6 Performance of Improved Weights 72
3.7 Energy Resolution as a Function of Energy 76
3.8 Synchronous Running 77
3.9 Conclusions 80

4 Electron Reconstruction and Identification 81
4.1 Electron Reconstruction 81
4.1.1 Energy Measurement 84
4.1.2 Track Finding 87
4.1.3 Supercluster-Track Combination 90
4.2 Electron Charge Determination 90
4.3 Electron Identification 95
4.4 Electron Isolation 96
4.5 Electron Trigger 99

5 Phenomenology of W and Z Production 101
5.1 Parton Distribution Functions 101
5.2 Production of Massive Vector Bosons 103
5.3 $q\bar{q} \rightarrow \mathrm{W} \rightarrow \mathrm{e}\nu_{\mathrm{e}}$ 109
5.4 $q\bar{q} \rightarrow \mathrm{Z} \rightarrow \mathrm{e}^{+}\mathrm{e}^{-}$ 111
5.5 Current Accuracy of Predictions 112

6 Missing Transverse Energy 115
6.1 Introduction 115
6.2 Data Analysed 117
6.3 Properties of W and Z decay at LHC 119
6.4 Rescaling of Lepton Momenta 120
6.5 The Ersatz Missing Energy Calculation 123
6.6 Reconstruction Level 126
6.6.1 Event and Object Selection 127
6.6.2 Calorimetric Missing Transverse Energy 129
6.6.3 Electron Energy Removal 132

6.6.4 Calculation of Ersatz Missing Transverse Energy 133
6.6.5 Correction for Electron and Ersatz Neutrino Selection Inefficiency 133
6.6.6 Correction for Ersatz Neutrino Acceptance 134
6.7 Results 137

7 Measurement of the W and Z Cross-Sections 145
7.1 Introduction 145
7.2 Cross-section Measurement 146
7.3 Data Analysed 146
7.4 Event Selection 146
7.4.1 Trigger 146
7.4.2 Electron Selection 148
7.4.3 Selection of $W^\pm \rightarrow e^\pm \nu_e$ Events 148
7.4.4 Selection of $\gamma^*/Z \rightarrow e^+e^-$ Events 150
7.5 Tag and Probe Efficiency Measurements 152
7.5.1 Tag and Probe Selection 153
7.5.2 Factorisation of Efficiency 153
7.5.3 Kinematically Dependent Efficiencies 154
7.5.4 Event Efficiencies 155
7.5.5 Tag and Probe Efficiency Results 156
7.6 Signal Yield and Background Estimation 157
7.6.1 Signal Yield Estimation for $Z \rightarrow e^+ e^-$ 157
7.6.2 Background Subtraction and Signal Yield for $W^\pm \rightarrow e^\pm \nu_e$ 157
7.6.3 Uncertainties in $W^\pm \rightarrow e^\pm \nu_e$ Signal Yield Estimation 161
7.6.4 Signal Yield Estimate for $W^\pm \rightarrow e^\pm \nu_e$ 163
7.7 Integrated Luminosity Measurement 163
7.8 Acceptance Calculation 164
7.9 Results 165
7.10 Conclusions 166

8 Summary and Conclusions 169
8.1 Summary 169
8.2 Epilogue 171

Bibliography 175

List of Figures

1.1 eeγ vertex in QED 26

1.2 Cross-sections for e$^-$ and e$^+$ charged current DIS vs. longitudinal polarisation of e$^\mp$ beam 29

1.3 Symmetry breaking classical potential 32

1.4 Feynman diagrams showing the interactions between electrons and the gauge bosons 38

1.5 Comparison of experimental results and Standard Model predictions . . . 39

2.1 LHC accelerator chain 42

2.2 LHC schematic 43

2.3 LHC bunch structure 45

2.4 Compact Muon Solenoid perspective cutaway 46

2.5 Cross-section of silicon strip tracker sensor 48

2.6 Tracker geometry schematic 50

2.7 p_T resolution of the inner tracking system 51

2.8 Transverse impact parameter resolution of the inner tracking system . . . 51

2.9 ECAL geometry schematic 52

2.10 Bremsstrahlung energy loss mechanism of electrons 53

2.11 Electron-positron pair creation from photon in nuclear magnetic field . . 53

2.12 Illustration of the development of an electromagnetic shower 54

2.13 Longitudinal energy deposition profile for electrons in $PbWO_4$ 54

2.14 Energy deposition against lateral distance for 50 GeV electrons, at different depths in $PbWO_4$ 54

2.15 ECAL 3×3 energy resolution 56

2.16 Illustration of the development of an hadronic shower. 57

2.17 HCAL geometry schematic 58

2.18 Muon geometry schematic 59

2.19 Illustration of Level 1 Trigger eγ algorithm 60

2.20 Event display showing a cosmic muon passing through CMS 62

3.1 Configuration to provide an electron beam to H4. 64

3.2 ECAL Very Front End Schematic 66

3.3 Example of ECAL Signal Pulse 67

3.4 Ecal Signal Samples vs Time 69

3.5 Ecal Signal Samples vs Time for Central Electrons 70

3.6 Illustration of Correction Calculation for Phase-Dependent Bias 72

3.7 Residual Between Reference Weight Derived Signal Representation and Analytic Function 73

3.8 Signal representation for crystal 248, supermodule 16 73

3.9 Signal representation derived from 30 000 events and from 2 000. 74

3.10 Difference between profiles derived from 30 000 and 2 000 electrons 74

3.11 Amplitude reconstructed in the 3×3 array around 25 different crystals for 120 GeV electrons using standard weights. 75

3.12 Amplitude reconstructed in the 3×3 array around 25 different crystals for 120 GeV electrons using optimised weights. 76

3.13 Amplitude in the 3×3 array around 25 different crystals for 120 GeV electrons, reconstructed by optimized weights derived using only 2000 events per crystal. The resolution is similar (within errors) to that obtained with 30 000 event weights. 77

3.14 Energy resolution, $\sigma(E)$, as a function of energy, measured with optimized weights. 78

3.15 The phase between time of trigger and system clock for asynchronous running, as measured by the TDC. 78

3.16 The phase between time of trigger and system clock for 25 ns running, as measured by the TDC. 78

3.17 Amplitude in the 3×3 array around 25 different crystals for 90 GeV electrons in the 25 ns test beam running. Standard weights are used for reconstruction. 79

3.18 Amplitude in the 3×3 array around crystal 172. 79

4.1 Resolutions of barrel electron energy measurement by tracker, ECAL and the combination of the two, versus electron energy. 82

4.2 Resolutions of endcap electron energy measurement by tracker, ECAL and the combination of the two, versus electron energy. 82

4.3 Tracker material budget 83

4.4 Fraction of initial electron energy lost through bremsstrahlung for 10, 30 and 50 GeV electrons. 83

4.5 Average electron energy deposition in ECAL barrel 84

4.6 Illustration of hybrid ECAL clustering algorithm. 85

4.7 Illustration of ECAL multi5×5 clustering algorithm 86

4.8 Illustration of supercluster driven seeding of electron track finding. 89

4.9 Number of hits found per track for KF, GSF and HLT tracks. 90

4.10 Illustration of electron charge mis-identification by the GSF tracking algorithm. 91

4.11 Illustration of $\Delta\phi$ between the pixel direction and the supercluster. . . . 92

4.12 $\Delta\phi$ of electrons and positrons with $p_T = 35\,\mathrm{GeV}$. 93

4.13 Mis-identification fraction for the various charge determination methods, vs $|\eta|$ 93

4.14 $\sigma_{\eta\eta}$ of electrons in EB, for four different levels of calibration and alignment knowledge. 96

4.15 H/E of electrons in EB, for four different levels of calibration and alignment knowledge. 96

4.16 $\Delta\eta_{\mathrm{in}}$ of electrons in EB, for four different levels of calibration and alignment knowledge. 96

4.17 $\Delta\phi_{\mathrm{in}}$ of electrons in EB, for four different levels of calibration and alignment knowledge. 96

4.18 Illustration of track isolation algorithm. 97

4.19 Illustration of track isolation algorithm. 98

5.1 Deep inelastic scattering. 102

5.2 LHC Parton Kinematics 104

5.3 Parton Distribution Functions for $Q^2 = m_{\mathrm{Z}}^2$ 105

5.4 Flavour of W parent quarks in pp collisions. 106

5.5 W boson rapidity at LHC. 107

5.6 Transverse momentum of the W boson : comparison of SHERPA MC simulation to D0 data. 108

5.7 Transverse momentum of the Z boson : comparison of SHERPA MC simulation to CDF data. 108

5.8 $q\bar{q} \rightarrow \mathrm{W}^+ \rightarrow \mathrm{e}^+\nu_{\mathrm{e}}$ 109

5.9 $\mathrm{W} \rightarrow \mathrm{e}\nu_{\mathrm{e}}$ in W rest frame, showing momenta, decay angles and helicity. . 110

5.10 $q\bar{q} \rightarrow \mathrm{Z} \rightarrow \mathrm{e}^+\mathrm{e}^-$ 111

5.11 Z boson rapidity distributions calculated at LO, NLO and NNLO in QCD, for $\sqrt{s} = 14\,\mathrm{TeV}$ 113

5.12 W boson rapidity distributions calculated at LO, NLO and NNLO in QCD, for $\sqrt{s} = 14\,\mathrm{TeV}$ 113

6.1 Transverse momentum of the W and Z bosons. 120

6.2 Transverse momentum of electrons in $\mathrm{W}^{\pm} \rightarrow \mathrm{e}^{\pm}\,\nu_{\mathrm{e}}$ and $\mathrm{Z} \rightarrow \mathrm{e}^{+}\,\mathrm{e}^{-}$ 121

6.3 Transverse momentum of neutrinos in $\mathrm{W}^{\pm} \rightarrow \mathrm{e}^{\pm}\,\nu_{\mathrm{e}}$ and ersatz neutrinos in $\mathrm{Z} \rightarrow \mathrm{e}^{+}\,\mathrm{e}^{-}$ 121

6.4 Transverse momentum of electrons in $\mathrm{W}^{\pm} \rightarrow \mathrm{e}^{\pm}\,\nu_{\mathrm{e}}$ and the rescaled transverse momentum of electrons in $\gamma^{*}/\mathrm{Z} \rightarrow \mathrm{e}^{+}\mathrm{e}^{-}$. 122

6.5 Transverse momentum of neutrinos in $\mathrm{W}^{\pm} \rightarrow \mathrm{e}^{\pm}\,\nu_{\mathrm{e}}$ and the rescaled transverse momentum of ersatz neutrinos in $\gamma^{*}/\mathrm{Z} \rightarrow \mathrm{e}^{+}\mathrm{e}^{-}$. 122

6.6 Invariant mass of the W and the rescaled electrons in $\gamma^{*}/\mathrm{Z} \rightarrow \mathrm{e}^{+}\mathrm{e}^{-}$. . . . 123

6.7 Transverse momentum of electrons in $\mathrm{W}^{\pm} \rightarrow \mathrm{e}^{\pm}\,\nu_{\mathrm{e}}$ and the rescaled transverse momentum of electrons in $\gamma^{*}/\mathrm{Z} \rightarrow \mathrm{e}^{+}\mathrm{e}^{-}$ after mass reweighting. . . 124

6.8 Transverse momentum of neutrinos in $\mathrm{W}^{\pm} \rightarrow \mathrm{e}^{\pm}\,\nu_{\mathrm{e}}$ and the rescaled transverse momentum of ersatz neutrinos in $\gamma^{*}/\mathrm{Z} \rightarrow \mathrm{e}^{+}\mathrm{e}^{-}$ after mass reweighting.124

6.9 True simulated missing transverse energy in $\mathrm{W}^{\pm} \rightarrow \mathrm{e}^{\pm}\,\nu_{\mathrm{e}}$ and $\mathrm{Z} \rightarrow \mathrm{e}^{+}\,\mathrm{e}^{-}$ events. 125

6.10 Ersatz missing transverse energy in $\mathrm{Z} \rightarrow \mathrm{e}^{+}\,\mathrm{e}^{-}$ and true missing transverse energy in $\mathrm{W}^{\pm} \rightarrow \mathrm{e}^{\pm}\,\nu_{\mathrm{e}}$. 125

6.11 Ersatz $\not{E}_T$ and true $\not{E}_T$ in $\mathrm{W}^{\pm} \rightarrow \mathrm{e}^{\pm}\,\nu_{\mathrm{e}}$, after electron p_T and invariant mass selection. All available events used. 126

6.12 Ersatz $\not{E}_T$ and true $\not{E}_T$ in $\mathrm{W}^{\pm} \rightarrow \mathrm{e}^{\pm}\,\nu_{\mathrm{e}}$, after electron p_T and invariant mass selection. Number of $\mathrm{Z} \rightarrow \mathrm{e}^{+}\,\mathrm{e}^{-}$ corresponds to $\int L dt = 10\,\mathrm{pb}^{-1}$ . . . 126

6.13 Ersatz $\not{E}_T$ showing background contamination without ersatz neutrino selection : EB. 129

6.14 Ersatz $\not{E}_T$ showing background contamination after ersatz neutrino selection : EB. 129

6.15 Ersatz $\not{E}_T$ showing background contamination without ersatz neutrino selection : EE. 130

6.16 Ersatz $\not{E}_T$ showing background contamination without ersatz neutrino selection : EB. 130

6.17 Missing transverse energy reconstructed in the calorimeter for $\mathrm{W}^{\pm} \rightarrow \mathrm{e}^{\pm}\,\nu_{\mathrm{e}}$ and $\gamma^{*}/\mathrm{Z} \rightarrow \mathrm{e}^{+}\mathrm{e}^{-}$ events. 131

6.18 Noise in 3×3 trigger towers around the actual neutrino. 132

6.19 Event weights applied for electron $\epsilon(p_T, \eta) \neq \epsilon(p'_T, \eta')$ 135

6.20 Efficiency of ersatz neutrino selection versus $|\eta|$. 136

6.21 Ersatz reconstructed missing transverse energy, compared with $\not{E}_T$ in $\mathrm{W}^{\pm} \rightarrow \mathrm{e}^{\pm}\,\nu_{\mathrm{e}}$ events with the neutrino within the detector acceptance. . . 136

6.22 Ersatz reconstructed missing transverse energy without neutrino acceptance correction. 137

6.23 Multiplicative factors used to correct for limited ersatz neutrino acceptance.137

6.24 Ersatz reconstructed missing energy, with all corrections applied. 138

6.25 Ersatz reconstructed missing energy, with all corrections applied. Normalisation is to the number of $\mathrm{W}^{\pm} \rightarrow \mathrm{e}^{\pm}\,\nu_{\mathrm{e}}$ events expected for $\int Ldt = 10\,\mathrm{pb}^{-1}$. Statistical accuracy corresponds to $\int Ldt = 10\,\mathrm{pb}^{-1}$ 139

6.26 Bias in $\not{E}_T$ selection efficiency measured by Ersatz Missing Energy method.140

6.27 $\not{E}_T$ selection efficiency measured by Ersatz Missing Energy method, compared with the actual efficiencies. 142

7.1 $\not{E}_T$ distribution of events after $\mathrm{W}^{\pm} \rightarrow \mathrm{e}^{\pm}\,\nu_{\mathrm{e}}$ selection, showing signal and background. 149

7.2 m_{ee} distribution of events after $\gamma^{*}/\mathrm{Z} \rightarrow \mathrm{e}^{+}\mathrm{e}^{-}$ selection, showing signal and background. 151

7.3 Efficiency vs E_T of electron reconstruction; selection as a $\mathrm{W}^{\pm} \rightarrow \mathrm{e}^{\pm}\, \nu_{\mathrm{e}}$ electron; and acceptance by the HLT, for a probe supercluster. 155

7.4 Efficiency vs η of electron reconstruction; selection as a $\mathrm{W}^{\pm} \rightarrow \mathrm{e}^{\pm}\, \nu_{\mathrm{e}}$ electron; and acceptance by the HLT, for a probe supercluster. 155

7.5 Efficiency vs E_T of electron reconstruction; selection as a $\gamma^*/\mathrm{Z} \rightarrow \mathrm{e}^+\mathrm{e}^-$ electron; and acceptance by the HLT, for a probe supercluster. 156

7.6 Efficiency vs η of electron reconstruction; selection as a $\gamma^*/\mathrm{Z} \rightarrow \mathrm{e}^+\mathrm{e}^-$ electron; and acceptance by the HLT, for a probe supercluster. 156

7.7 $\not{E}_T$ distribution of signal and background events after the full $\mathrm{W}^{\pm} \rightarrow \mathrm{e}^{\pm}\, \nu_{\mathrm{e}}$ selection, apart from the track isolation criterion which is inverted. . . . 158

7.8 Division of the data into four discrete regions for signal yield estimation. 159

7.9 Comparison of the $\not{E}_T$ distribution of the hadronic background in region BA to that in region CD. 160

7.10 $\mathrm{W}^{\pm} \rightarrow \mathrm{e}^{\pm}\, \nu_{\mathrm{e}}$ signal yield uncertainty versus F_z bias. 162

List of Tables

1.1 Summary of fundamental fermions in the Standard Model 24

1.2 Summary of fundamental bosons in the Standard Model 25

2.1 LHC beam parameters for the peak design luminosity. 44

3.1 Comparison of 25 ns bunch structure results to results from standard test beam bunch structure, obtained using optimised weights. 80

4.1 Mis-identification rates for different methods of electron charge determination. 94

4.2 Electron pixel-seed search window parameters, for offline and HLT reconstruction. 99

5.1 Predictions for W^+, W^- and Z total cross-sections at the LHC, calculated at LO and NNLO in perturbative QCD. Uncertainties are one sigma PDF uncertainties 113

6.1 Datasets used in the analysis of the Ersatz Missing Energy method. . . . 117

6.2 Ersatz neutrino selection efficiencies : EB 128

6.3 Ersatz neutrino selection efficiencies : EE 128

6.4 Effect of not performing Ersatz $\not\!\!E_T$ Corrections. 141

7.1 Datasets analysed in $W^\pm \rightarrow e^\pm \nu_e$ and $\gamma^*/Z \rightarrow e^+e^-$ cross-section measurement analysis. 147

7.2 Electron selection criteria used for the $W^\pm \rightarrow e^\pm \nu_e$ cross-section analysis. 149

7.3 $W^{\pm} \rightarrow e^{\pm}\,\nu_e$ event selection efficiencies for signal and QCD backgrounds. 150

7.4 $W^{\pm} \rightarrow e^{\pm}\,\nu_e$ event selection efficiencies for electroweak backgrounds. . . . 150

7.5 Electron selection criteria for the $\gamma^*/Z \rightarrow e^+e^-$ cross-section analysis. . . 151

7.6 $\gamma^*/Z \rightarrow e^+e^-$ event selection efficiencies for signal and QCD backgrounds. 152

7.7 $\gamma^*/Z \rightarrow e^+e^-$ event selection efficiencies for signal and electroweak backgrounds. 152

7.8 Tag and Probe efficiency results for $W^{\pm} \rightarrow e^{\pm}\,\nu_e$ and $\gamma^*/Z \rightarrow e^+e^-$. . . . 157

7.9 Theoretical uncertainties in the calculated acceptances. 165

7.10 $W^{\pm} \rightarrow e^{\pm}\,\nu_e$ cross-section results. 165

7.11 $\gamma^*/Z \rightarrow e^+e^-$ cross-section results. 166

7.12 Systematic uncertainties in $W^{\pm} \rightarrow e^{\pm}\,\nu_e$ cross-section measurement . . . 166

7.13 Systematic uncertainties in $\gamma^*/Z \rightarrow e^+e^-$ cross-section measurement . . . 167

1 Electroweak Theory

"Behind the complicated details of the world stand the simplicities."
— Graham Greene

The electroweak vector bosons mediate the unified electromagnetic and weak forces. They are the photon, $\mathrm{W}^{\pm}$ and Z. The current work details preparations that have been made for the measurement of the W and Z production cross-sections at the Large Hadron Collider. These massive bosons were first discovered in 1983 at the CERN SPS collider [1, 2, 3, 4].

This Chapter gives an overview of the theoretical underpinnings of the electroweak bosons within the Standard Model. It shows how the vector bosons arise from imposing local gauge invariance on the Lagrangian; how the electroweak symmetry is broken; how the W and Z bosons become massive; and finally how the photon, W and Z interact with electrons. The phenomenology of W and Z production at the LHC is discussed in Chapter 5.

The content of this chapter draws from [5, 6, 7, 8].

1.1 The Standard Model

The Standard Model is a combination of quantum field theories that describe the observed fundamental particles and their interactions. These fundamental particles are summarised in Tables 1.1 and 1.2.

The interactions of the fundamental particles can be incorporated into the quantum field theories describing their dynamics by invoking the gauge principle - demanding

	Quarks				Leptons			
	$Q = +\frac{2}{3}$		$Q = -\frac{1}{3}$		Q = -1		Q = 0	
1st Generation	up	(u)	down	(d)	electron	(e)	electron neutrino	(ν_{e})
2nd Generation	charm	(c)	strange	(s)	muon	(μ)	muon neutrino	(ν_{μ})
3rd Generation	top	(t)	bottom	(b)	tau	(τ)	tau neutrino	(ν_{τ})

Table 1.1: The fermions – spin-$\frac{1}{2}$ particles obeying Fermi-Dirac statistics. Quarks carry colour charge and so interact with gluons. Leptons do not. Q is the electric charge. The corresponding antiparticles have charges with opposite sign to those listed. The generations are ordered by mass, e.g. the mass of the electron, $m_{\mathrm{e}} = 511\,\mathrm{keV}$; the muon, $m_{\mu} = 106\,\mathrm{MeV}$; the tau, $m_{\tau} = 1.78\,\mathrm{GeV}$.

that gauge symmetries, or invariances, are present in the theory. This leads directly to the inclusion of gauge bosons that mediate the interactions within the theory.

The Standard Model Lagrangian is invariant under transformations that are known in group theoretic terms as $\mathrm{SU}(3)_C \times \mathrm{SU}(2)_L \times \mathrm{U}(1)_Y$. The associated gauge bosons are the spin-1 bosons listed in Table 1.2. The $\mathrm{SU}(3)_C$ symmetry term results in quantum chromodynamics (QCD) [9] – a theory which describes the interactions of particles which carry colour charge, i.e. the quarks and gluons. A meaningful discussion of QCD is not within the scope of this thesis, as the focus is on the electroweak sector of the Standard Model, derived from the $\mathrm{SU}(2)_L \times \mathrm{U}(1)_Y$ symmetries. As will be shown, these symmetries result in the electroweak gauge bosons : the massive W and Z; and the massless photon.

In more concrete terms, the electroweak Lagrangian is invariant under transformations belonging to both the SU(2) and U(1) groups. These transformations are unitary (hence U) and in the case of SU(2) have determinant +1 (special). Furthermore, these transformations are 'local' – they are spacetime dependent.

1.2 U(1) Invariance

Consider the Dirac Lagrangian density [12] :

$$\mathcal{L} = \bar{\psi}\left(i\gamma^{\mu}\partial_{\mu} + m\right)\psi \tag{1.1}$$

Spin	Boson		Mass (GeV)
0	Higgs	(H)	> 114.4 (95% C.L.)
1	photon	(γ)	0
	W	(W)	80.403 ± 0.029
	Z	(Z)	91.1876 ± 0.0021
	gluon	(g)	0

Table 1.2: The bosons – integer spin particles obeying Bose-Einstein statistics. The bosons with spin-1 are the gauge bosons, which mediate the interactions : photon, W and Z are the electroweak gauge bosons; gluons are the QCD gauge bosons. The Higgs boson, responsible for generating the fundamental particle masses, has not been observed but searches have excluded the existence of the Higgs with $m_{\mathrm{H}} <$ 114.4 GeV [10] and 160 GeV $< m_{\mathrm{H}} <$ 170 GeV [11].

where $\psi = \psi(x)$ is a Dirac spinor representing a fermion and $\bar{\psi} = \psi^{\dagger}\gamma^{0}$. γ^{μ} are the standard gamma matrices.

U(1) transformations have one generator, $\alpha(x)$, leading to finite, unitary, and local transformations of the form $U(\alpha) = e^{-iq\alpha(x)}$:

$$\psi \rightarrow \psi' = e^{-iq\alpha(x)}\psi \tag{1.2}$$

Where q is a (dimensionless) constant.

$m\bar{\psi}'\psi' = m\bar{\psi}e^{+i\alpha(x)}e^{-i\alpha(x)}\psi = m\bar{\psi}\psi$, so the second term in (1.1) is clearly invariant under this transformation. However, as $\alpha(x)$ is spacetime dependent, $\partial_{\mu}\alpha(x) \neq 0$ and therefore :

$$\partial_{\mu}\psi \rightarrow \partial_{\mu}\psi' = e^{-iq\alpha(x)}\partial_{\mu}\psi - iq\big(\partial_{\mu}\alpha(x)\big)e^{-iq\alpha(x)}\psi \tag{1.3}$$

The second term shows that the Lagrangian density of (1.1) is not locally invariant under (1.2) due to the second term in (1.3). However, it can be made invariant if a gauge field, $B_{\mu} = B_{\mu}(x)$, is included in the theory. This field must transform as :

$$B_{\mu} \rightarrow B'_{\mu} = B_{\mu} + \partial_{\mu}\alpha(x) \tag{1.4}$$

B_μ is used to modify the derivative ∂_μ into the covariant derivative :

$$\mathrm{D}_\mu = \partial_\mu + iqB_\mu \tag{1.5}$$

which has the desired behaviour that :

$$\mathrm{D}_\mu\psi \rightarrow \mathrm{D}_\mu\psi' = e^{-iq\alpha(x)}\mathrm{D}_\mu\psi \tag{1.6}$$

thus leading to the following Lagrangian, which is invariant under the U(1) transformation :

$$\mathcal{L} = \bar{\psi}\left(\gamma^\mu \mathrm{D}_\mu + m\right)\psi + \frac{1}{4}F^{\mu\nu}F_{\mu\nu} \tag{1.7}$$

$F^{\mu\nu} = \partial^\mu B^\nu - \partial^\nu B^\mu$ is the energy-momentum tensor for the field, B^μ. It is locally gauge invariant.

Remarkably, the imposition of local gauge invariance onto the Dirac equation Lagrangian (1.1) has resulted in (1.7) – the Quantum Electrodynamic Dynamics (QED) Lagrangian. The gauge field, B_μ, may be identified as the photon, with the correct couplings of form $q\bar{\psi}\gamma^\mu\psi B_\mu$ resulting from the use of the covariant derivative, D_μ.The resulting Feynman diagram for the vertex is shown in Figure 1.1. The move from a description of the dynamics of free particles to a theory which incorporates the interactions of such particles through intermediate vector bosons has resulted from demanding that certain symmetries are respected.

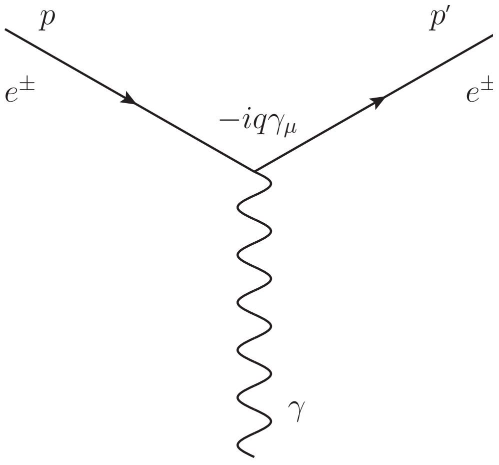

Figure 1.1: The eeγ vertex of Quantum Electrodynamics, arising as a consequence of local gauge invariance.

The application of Noether's Theorem[13] gives the symmetry current as $N^{\mu}_{\psi} = \bar{\psi}\gamma^{\mu}\psi$. q is identifed as the electric charge and the electromagnetic current is therefore $j^{\mu} = q\bar{\psi}\gamma^{\mu}\psi$.

An important aspect of the QED Lagrangian is that it does not permit a photon mass term, which would take the form $m^2_{\gamma}B_{\mu}B^{\mu}$. Such a term would violate local gauge invariance.

In the Standard Model, the $\mathrm{U}(1)_Y$ symmetry is associated – not with the electric charge q – but with weak hypercharge, Y, (hence $\mathrm{U}(1)_Y$). However, the $\mathrm{SU}(2)_L \times \mathrm{U}(1)_Y$ is spontaneously broken, leaving a $\mathrm{U}(1)_{EM}$ with electric charge as its generator, as observed in nature. This will be discussed more in Section 1.5

1.3 SU(2) Invariance

Imposing local gauge invariance under SU(2) transformations follows a similar logic to the U(1) case. However, there are additional features which result from the richer group structure. The principal difference is that SU(2) has $2^2 - 1 = 3$ generators, T_i, of transformations rather than the one $\alpha(x)$ of U(1). T_i obey the group algebra :

$$[T_i, T_j] = i\epsilon_{ijk}T_k \tag{1.8}$$

The special unitary local transformations generated by these T_i take the form :

$$\mathrm{U}(\theta) = e^{-ig_W \mathbf{T}.\boldsymbol{\theta}(x)} \tag{1.9}$$

where g_W is the coupling strength, $\mathbf{T} = (T_1, T_2, T_3)$ and $\theta(x) = (\theta_1, \theta_2, \theta_3)$ carries the spacetime dependence of the transformation. T_i are each associated with a gauge field, W^i_{μ} $(i \in \{1, 2, 3\})$ which transform under SU(2) as :

$$\boldsymbol{T}.\boldsymbol{W}'_{\mu} = \mathrm{U}(\theta)\boldsymbol{T}.\boldsymbol{W}_{\mu}\mathrm{U}^{-1}(\theta) + \frac{i}{g}\left(\partial_{\mu}\mathrm{U}(\theta)\right)\mathrm{U}^{-1}(\theta) \tag{1.10}$$

In an analogous manner to the U(1) example above, SU(2) local gauge invariance is maintained by use of the covariant derivative :

$$\mathrm{D}_\mu = \partial_\mu + ig\mathbf{T}.\mathbf{W}_\mu \tag{1.11}$$

which again has the desired transformation properties :

$$\mathrm{D}_\mu \psi^{(t)} \rightarrow \mathrm{D}_\mu \psi^{(t)\prime} = \mathrm{U}\,(\theta)\mathrm{D}_\mu \psi^{(t)} \tag{1.12}$$

where $\psi^{(t)}$ is an SU(2) multiplet (analogous to the U(1) singlet ψ in the previous section). This covariant derivative gives rise to the interactions between the SU(2) gauge fields and the particles represented by $\psi^{(t)}$. The coupling g_W is the same for all SU(2) multiplets (a consequence of the non-Abelian nature of SU(2)). This is in contrast to the U(1) case, where q could take on different values, e.g. -1 for the electron, but $-1/3$ for the down quark.

The field strength tensor for the gauge fields is defined as follows :

$$\boldsymbol{F}^{\mu\nu} = \partial^\mu \boldsymbol{W}^\nu - \partial^\nu \boldsymbol{W}^\mu - g\boldsymbol{W}^\mu \times \boldsymbol{W}^\nu \tag{1.13}$$

The non-Abelian nature of SU(2) (c.f. (1.8)) reveals itself in the $g\boldsymbol{W}^\mu \times \boldsymbol{W}^\nu$ term. The presence of g, the gauge coupling constant, implies that the gauge fields carry SU(2) charge. There are interactions between the gauge fields directly.

The final form for the SU(2) invariant Dirac Lagrangian is then :

$$\mathcal{L} = \bar{\psi}^{(t)}\left(\gamma^\mu \mathrm{D}_\mu + m\right)\psi^{(t)} + \frac{1}{4}\boldsymbol{F}^{\mu\nu}\boldsymbol{F}_{\mu\nu} \tag{1.14}$$

As in the U(1) case, inserting mass terms for the gauge fields into the Lagrangian would violate gauge invariance. While in the case of QED and the photon this is desirable as the photon is massless, the weak gauge bosons are massive. In the Glashow-Salam-Weinberg model, this problem is tackled by the Higgs mechanism.

1.4 The Glashow-Salam-Weinberg Model

Glashow [14], Salam [15] and Weinberg [16] state that the symmetry group of the electroweak theory is $\mathrm{SU}(2)_L \times \mathrm{U}(1)_Y$. The SU(2) symmetry is that of weak isospin, denoted

t. The subscript L denotes that the weak gauge fields only couple to left-handed fermions – those with negative helicity. This is observed in experiment, as illustrated in Figure 1.2.

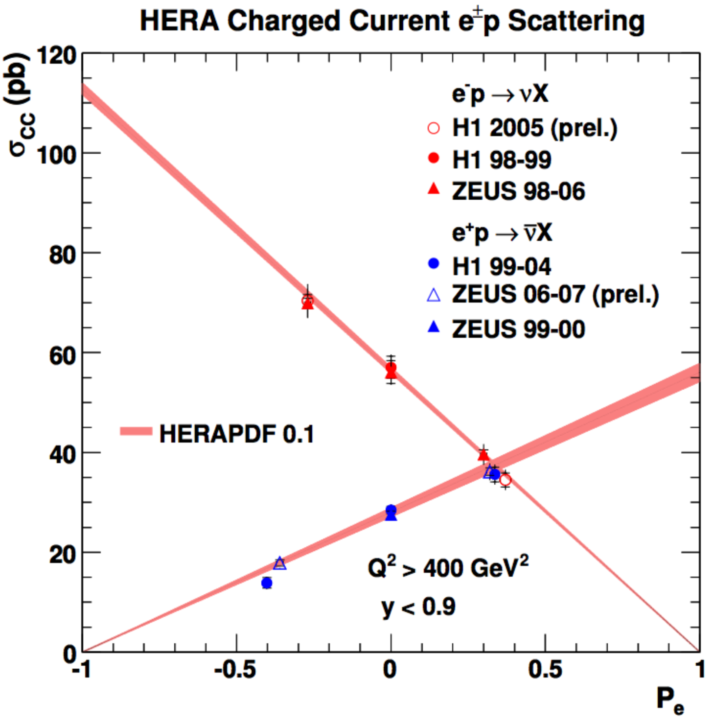

Figure 1.2: Cross-sections for e^- and e^+ charged current DIS vs. longitudinal polarisation of $e^{\mp}$ beam measured at HERA [17]. The cross-section falls to zero for right-handed electrons and left-handed positrons as a result of the $SU(2)_L$ nature of the weak interactions.

The Dirac spinors ψ can be considered as superpositions of left- and right-handed fermions and can be projected onto left ψ_L and right ψ_R components by the projection operators :

$$\psi_L = \hat{P}_L\psi = \frac{(1-\gamma_5)}{2}\psi \qquad \psi_R = \hat{P}_R\psi = \frac{(1+\gamma_5)}{2}\psi \tag{1.15}$$

The Dirac spinors representing the left-handed fermion fields are combined in SU(2) doublets and assigned the following isospin quantum numbers :

$$\begin{array}{l} t_3 = +\frac{1}{2} \\ t_3 = -\frac{1}{2} \end{array} \quad \begin{pmatrix} \nu_e \\ e^- \end{pmatrix}_L \quad \begin{pmatrix} \nu_\mu \\ \mu^- \end{pmatrix}_L \quad \begin{pmatrix} \nu_\tau \\ \tau^- \end{pmatrix}_L \quad \begin{pmatrix} u \\ d' \end{pmatrix}_L \quad \begin{pmatrix} c \\ s' \end{pmatrix}_L \quad \begin{pmatrix} t \\ b' \end{pmatrix}_L \tag{1.16}$$

Several aspects of the weak interaction are encapsulated in these assignments. The electric charge of the doublet members differs by 1, so the gauge field responsible for transitions between them must have charge ± 1. Moreover, for leptons these transitions are strictly bound to remain within generations (as listed in Table 1.1). This is a statement that the lepton numbers are conserved. In the case of the quarks[1] however, the states within these weak isospin multiplets are not the QCD eigenvectors, but rather are combinations of them. These combinations are given by the Cabibo-Kobayashi-Maskawa matrix [18], [19]:

$$\begin{pmatrix} \mathrm{d}' \\ \mathrm{s}' \\ \mathrm{b}' \end{pmatrix} = \begin{pmatrix} V_{ud} & V_{us} & V_{ub} \\ V_{cd} & V_{cs} & V_{cb} \\ V_{td} & V_{ts} & V_{tb} \end{pmatrix} \begin{pmatrix} \mathrm{d} \\ \mathrm{s} \\ \mathrm{b} \end{pmatrix} \tag{1.17}$$

The resulting cross-generational couplings in the quark sector permit the weak decay of hadrons such as the $\mathrm{K}^{\pm}$, which would otherwise be stable within the Standard Model. These couplings are also the source of **CP** (combined charge-parity symmetry) violation in the Standard Model.

The right handed fermion fields are SU(2) singlets ($t = 0$, $t_3 = 0$) :

$$\mathrm{e}^-{}_R \qquad \mu^-{}_R \qquad \tau^-{}_R \qquad \mathrm{u}_R \qquad \mathrm{d}'_R \qquad \mathrm{c}_R \qquad \mathrm{s}'_R \qquad \mathrm{t}_R \qquad \mathrm{b}'_R \tag{1.18}$$

Within the GSW framework neutrinos are considered massless[2] and so only have one definite helicity - found experimentally to be left-handed [20].

The separation of the left- and right-handed fermions into separate $\mathrm{SU}(2)_L$ multiplets means that the incorporation of a mass term as in (1.1) would break the symmetry, since $m\bar{\psi}\psi$ couples the left- and right-handed components of the spinors :

$$m\bar{\psi}\psi = m\left(\bar{\psi}_L\psi_R + \bar{\psi}_R\psi_L\right) \tag{1.19}$$

If only the left-handed components are subject to the $\mathrm{SU}(2)_L$ transformations (1.9), then clearly these mass terms are not gauge invariant. The masses of the fermions will be shown to arise through couplings to the Higgs sector in Section 1.5.

---

[1] All three quark colours are included in the multiplets.

[2] Although neutrino oscillation experiments have shown that at least two of the neutrinos have mass.

The weak hypercharge, Y_W, is the generator of the U(1) symmetry and is calculated as :

$$Y_W = 2\left(Q - t_3\right) \tag{1.20}$$

Gauging the combined $\mathrm{SU}(2)_L \times \mathrm{U}(1)_Y$ group gives 4 gauge bosons – the number that are observed in nature (in addition to the gluons). The Lagrangian for these gauge bosons is :

$$\mathcal{L}_G = -\frac{1}{4}\boldsymbol{F}^{\mu\nu}\boldsymbol{F}_{\mu\nu} - \frac{1}{4}B^{\mu\nu}B_{\mu\nu} \tag{1.21}$$

where $\boldsymbol{F}^{\mu\nu}$ is the energy-momentum tensor for the SU(2) gauge bosons and $B^{\mu\nu}$ that for the U(1) gauge boson.

These four bosons are however all massless and do not yet correspond to the physical states. This problem is rectified by recognising that the $\mathrm{SU}(2)_L \times \mathrm{U}(1)_Y$ symmetry is in fact broken and by introducing the scalar Higgs field.

1.5 Spontaneous Symmetry Breaking and the Higgs Mechanism

A SU(2) doublet containing a charged and a neutral scalar field is introduced, with $Y_W = \frac{1}{2}$:

$$\phi = \begin{pmatrix} \phi^+ \\ \phi^0 \end{pmatrix} \tag{1.22}$$

This scalar field couples to the gauge bosons through the covariant derivatives (1.5) and (1.11), giving a Lagrangian invariant under $\mathrm{SU}(2)_L \times \mathrm{U}(1)_Y$:

$$\mathcal{L}_\phi = \left(\partial^\mu\phi^\dagger - ig_W\boldsymbol{W}^\mu.\boldsymbol{T}\phi^\dagger - ig'_W Y_W B^\mu\phi^\dagger\right)\left(\partial_\mu\phi - ig_W\boldsymbol{W}_\mu.\boldsymbol{T}\phi - ig'_W Y_W B_\mu\phi\right) - V\left(\phi^\dagger\phi\right) \tag{1.23}$$

where the classical potential term $V\left(\phi^\dagger\phi\right)$ is chosen to have the form :

$$V\left(\phi^\dagger\phi\right) = \frac{\lambda}{4}\left(\phi^\dagger\phi\right)^2 - \mu^2\phi^\dagger\phi \tag{1.24}$$

Note the negative mass term $-\mu^2\phi^\dagger\phi$. If $\lambda > 0$ and $\mu^2 > 0$, this potential will not be the typical 'well' with a unique minimum at $\phi = 0$, but rather will have an unstable maximum there. The minima satisfy the condition $|\phi\phi^\dagger| = \sqrt{\frac{2\mu^2}{\lambda}} \equiv \frac{v^2}{2}$. These can be considered as an annulus of degenerate classical potential ground states in the $\mathrm{SU}(2)_L \times \mathrm{U}(1)_Y$ space as illustrated in Figure 1.3. In field theoretic terms the classical potential minimum can be interpreted as a set of degenerate vacua, $|0\rangle$, such that :

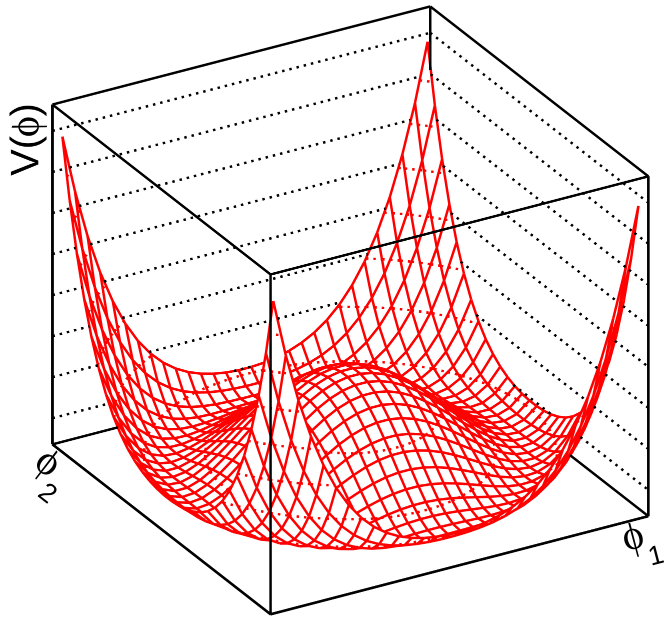

Figure 1.3: For an SU(2) doublet of scalars, ϕ, the classical potential $V\left(\phi^\dagger\phi\right) = \frac{\lambda}{4}\left(\phi^\dagger\phi\right)^2 - \mu^2\phi^\dagger\phi$ is represented here in two dimensions. $\phi = (0,0)$ is an unstable maximum and there is a continuum of degenerate ground states which satisfy $\phi^\dagger\phi = \frac{2\mu^2}{\lambda}$.

$$\langle 0|\phi\phi^\dagger|0\rangle = \frac{v^2}{2} \tag{1.25}$$

As already stated, (1.23) with (1.24) is invariant under $\mathrm{SU}(2)_L \times \mathrm{U}(1)_Y$ and thus this *set* of vacua is too. However, any particular vacuum in which the system will actually lie is not – the symmetry is 'spontaneously broken' – as an $\mathrm{SU}(2)_L \times \mathrm{U}(1)_Y$ transformation would move the system from one vacuum to another. In some sense, nature has to 'choose' a particular direction in the $\mathrm{SU}(2)_L \times \mathrm{U}(1)_Y$ space for the ground state from the symmetric ring of degenerate minima and in doing so breaks the symmetry.

Since all the vacua are equivalent, there is freedom to choose one which is convenient to work with :

$$\langle 0|\phi|0\rangle = \begin{pmatrix} 0 \\ \frac{v}{\sqrt{2}} \end{pmatrix} \tag{1.26}$$

While none of the original transformations leave (1.26) unchanged, transformations which use the combination $Y_W + t_3$ as a generator does. There is thus one 'unbroken symmetry' of the system remaining. From (1.20), this generator can be identified as electric charge.

Goldstone's Theorem [21] states that for each continuous global symmetry which is spontaneously broken, a massless scalar boson results. Indeed, these bosons can be shown to arise in the local case by examining excitations about (1.26) :

$$\phi = e^{-i\boldsymbol{\xi}(\mathbf{x}).\mathbf{T}/2v} \begin{pmatrix} 0 \\ \frac{1}{\sqrt{2}}\big(v + H(x)\big) \end{pmatrix} \tag{1.27}$$

in (1.23) :

$$\mathcal{L} = \frac{1}{2}\partial_\mu H \partial^\mu H + \mu^2 H^2 + \frac{1}{8}\partial_\mu \xi \partial^\mu \xi - \frac{\mu^4}{\lambda} + \text{interactions} \tag{1.28}$$

There are four scalar particles : the three massless Goldstone bosons ξ_i and the physical Higgs boson, H, which has mass $m_H = \sqrt{2}\mu$.

No massless scalar particle has been observed. The Higgs mechanism [22] removes these unphysical Goldstone bosons from locally invariant gauge theories by fixing the gauge appropriately :

$$\begin{aligned}\phi \to \phi' &= U(\xi)\phi \\ &= e^{+i\boldsymbol{\xi}(\mathbf{x}).\mathbf{T}/2v}\phi \\ &= \begin{pmatrix} 0 \\ \frac{1}{\sqrt{2}}\big(v + H(x)\big) \end{pmatrix}\end{aligned} \tag{1.29}$$

As a result of fixing to this unitary gauge, there will be no Goldstone bosons. However, there were *ab initio* three degrees of freedom associated with them which cannot simply disappear.

Of course, the gauge is not fixed by (1.29) in isolation – the gauge bosons must also transform as in (1.10) :

$$\boldsymbol{T}.\boldsymbol{W}'_\mu = U(\xi)\boldsymbol{T}.\boldsymbol{W}_\mu U(\xi)^{-1} + \frac{i}{g}\left(\partial_\mu U(\xi)\right)U(\xi)^{-1} \tag{1.30}$$

The Goldstone bosons have been 'absorbed' into the gauge bosons. The addition of this extra degree of freedom to the gauge bosons will become clear upon expanding (1.23) with (1.29). As a first step towards this, examine the covariant derivative D_μ:

$$\mathrm{D}_\mu\phi = \left(\partial_\mu - \frac{ig_W}{2}\boldsymbol{W}_\mu.\boldsymbol{T} - \frac{ig'_W Y_W}{2}B_\mu\right)\phi \tag{1.31}$$

$$= \partial_\mu\phi + \frac{i}{2}\begin{pmatrix} g'_W Y_W B_\mu + g_W {W^3}_\mu & g_W\left(W^1_\mu - iW^2_\mu\right) \\ g_W\left(W^1_\mu + iW^2_\mu\right) & g'_W Y_W B_\mu - g_W W^3_\mu \end{pmatrix}\phi \tag{1.32}$$

The terms $W^1_\mu \pm iW^2_\mu = \sqrt{2}W^\pm_\mu$ are readily identified with the physical $\mathrm{W}^\pm$ bosons. The weak mixing angle, θ_W, is defined through the relationship :

$$\tan\theta_W = \frac{g'_W}{g_W} \tag{1.33}$$

and is used to define new fields :

$$A_\mu = \sin\theta_W W^3_\mu + \cos\theta_W B_\mu \tag{1.34}$$

$$Z_\mu = \cos\theta_W W^3_\mu - \sin\theta_W B_\mu \tag{1.35}$$

to be identified with the photon and Z respectively. These physical fields are linear superpositions of the SU(2) and U(1) gauge fields.

The assignments (1.34) and (1.35) are verified in two ways. The first is to show the form of the coupling. Retaining only the W^3_μ and B_μ components of (1.31) :

$$\begin{aligned} \mathrm{D}_\mu\phi &= \left(\partial_\mu + \frac{i}{2} g_W t_3 W_3 + \frac{i}{2} g'_W Y_W B_\mu\right)\phi \\ &= \left(\partial_\mu + \frac{i}{2} g_W \sin\theta_W \left(Y_W + t_3\right) A_\mu + \frac{i g_W}{2\cos\theta_W}\left(t_3 - \sin^2\theta_W \left(Y + t_3\right)\right) Z_\mu\right)\phi \quad (1.36) \end{aligned}$$

The field A_μ has a coupling strength proportional to electric charge $(Y_W + t_3)$ – like the photon. This sets the further relationship :

$$e = g_W \sin\theta_W \quad (1.37)$$

The second verification comes from expanding the Lagrangian (1.23) using the ϕ definition of (1.29) and the new physical vector bosons :

$$\begin{aligned} \mathcal{L}_\phi =& \frac{1}{2}\partial^\mu H \partial_\mu H + \frac{1}{2} m_H^2 H^2 + \frac{\mu^4}{\lambda} - \frac{\lambda v}{4} H^3 + \frac{\lambda}{16} H^4 \quad (1.38) \\ &+ \frac{1}{4}\left(g_W^2 v^2 W^{\mu -} W^+_\mu + 2 g_W^2 v H W^{\mu -} W^+_\mu + 2 g_W^2 H^2 W^{\mu -} W^+_\mu\right) \\ &+ \frac{1}{8}\left(\frac{g_W^2 v^2}{\cos^2\theta_W} Z^\mu Z_\mu + \frac{2 g_W^2 v}{\cos^2\theta_W} H Z^\mu Z_\mu + \frac{2 g_W^2}{\cos^2\theta_W} H^2 Z^\mu Z_\mu\right) \end{aligned}$$

There is no mass term for A_μ, clearly identifying it as the massless photon. In contrast, the W and Z bosons have gained masses through the terms $\frac{1}{4} v^2 g_W^2 W^{\mu -} W^+_\mu$ and $\frac{v^2 g_W^2}{8\cos^2\theta_W} Z^\mu Z_\mu$:

$$m_W = \frac{g_W v}{2} \quad (1.39)$$

$$m_Z = \frac{g_W v}{2\cos\theta_W} = \frac{m_W}{\cos\theta_W} \quad (1.40)$$

Massive bosons have an additional degree of freedom compared with massless bosons - longitudinal polarisation. The degree of freedom associated with the scalar Goldstone bosons that were gauged into the gauge bosons has manifest as this longitudinal polarisation, resulting in massive W and Z bosons. The remaining terms of (1.38) are the three- and four-point couplings of the Higgs and the massive vector bosons.

1.5.1 Fermion Masses

As previously stated, in the Standard Model the fermions must also gain their masses via the Higgs sector. The couplings take the form of SU(2) gauge invariant Yukawa couplings :

$$\mathcal{L}_{\text{Yukawa}} = -g_f \left(\bar{\psi}_L \phi f_R + \bar{f}_R \phi^\dagger \psi_L\right) \tag{1.41}$$

where g_f is the Yukawa coupling strength, specific to each fermion. ψ is the SU(2) multiplet for the fermions; ϕ is the SU(2) doublet of (1.22); and f_R is the corresponding right-handed fermion singlet. SU(2) invariance of this Lagrangian is maintained because the scalar product of the two SU(2) multiplets is formed in each term.

Considering perturbations about the vacuum as in (1.26) and using the electron as our archetype :

$$\begin{aligned} -\frac{g_f}{\sqrt{2}}\begin{pmatrix}\bar{\nu}_L & \bar{e}_L\end{pmatrix}\begin{pmatrix}0 \\ v+H\end{pmatrix} e_R - \frac{g_f}{\sqrt{2}}\bar{e}_R\begin{pmatrix}0 & v+H\end{pmatrix}\begin{pmatrix}\nu_L \\ e_L\end{pmatrix} & \qquad (1.42) \\ = -\frac{g_f v}{\sqrt{2}}\bar{e}e - \frac{g_f}{\sqrt{2}}\bar{e}eH & \qquad (1.43) \end{aligned}$$

The electron has obtained a mass :

$$m_e = \frac{g_f v}{\sqrt{2}} \tag{1.44}$$

and couples to the scalar Higgs boson through the second term. Since the neutrino does not have a right-handed component, it does not couple to the Higgs boson and has remained massless.

1.6 Electrons and the Electroweak Interaction

The kinetic terms of the GSW Lagrangian density for the fermions is :

$$\mathcal{L}_{KTfermions} = i\bar{\psi}_L\gamma^\mu \mathrm{D}_\mu \psi_L + i\bar{\psi}_R\gamma^\mu \mathrm{D}_\mu \psi_R \tag{1.45}$$

where ψ_L is to be considered as the sum of the doublets in (1.16) and ψ_R the sum of the singlets (1.18). D_μ is the appropriate covariant derivative – (1.31) for the left-handed doublets and $\mathrm{D}_\mu = \partial_\mu - ig'_W Y_W B_\mu$ for the right-handed singlets.

Inserting the electron doublets and singlets into (1.45) leads to couplings to the photon, $\mathrm{W}^\pm$ and Z. These are illustrated in Figure 1.4. Beginning with the $\mathrm{W}^\pm$:

$$\begin{aligned} & -\frac{g_W}{2\sqrt{2}}\gamma^\mu \begin{pmatrix} \bar{\nu}_L & \bar{e}_L \end{pmatrix} \begin{pmatrix} 0 & W^+ \\ W^- & 0 \end{pmatrix} \begin{pmatrix} \nu_L \\ e_L \end{pmatrix} \\ = & -\frac{g_W}{2\sqrt{2}}\bar{\nu}\gamma^\mu\left(1-\gamma^5\right)eW^- - \frac{g_W}{2\sqrt{2}}\bar{e}\gamma^\mu\left(1-\gamma^5\right)\nu W^+ \end{aligned} \tag{1.46}$$

We see that the $\mathrm{W}^\pm$ couple only to left-handed leptons, as observed in nature (Figure 1.2).

The neutral bosons couple to both the left- and right-handed electrons :

$$\begin{aligned} & \frac{1}{2}\nu_L\gamma^\mu\nu_L\left(g'_W Y_W B_\mu + g_W {W^3}_\mu\right) + \frac{1}{2}e_L\gamma^\mu e_L\left(g'_W Y_W B_\mu - g_W {W^3}_\mu\right) + \frac{1}{2}g'_W Y_W \bar{e}_R\gamma^\mu e_R B_\mu \\ = & \frac{g_W}{4\cos\theta_W}\nu\gamma^\mu\left(1-\gamma^5\right)Z_\mu + \frac{g_W}{4\cos\theta_W}\bar{e}\left(\gamma^\mu\left(1-\gamma^5\right) - 4\sin^2\theta_W\gamma^\mu\right)eZ_\mu + g_W\sin\theta_W\bar{e}\gamma^\mu eA\mu \end{aligned} \tag{1.47}$$

1.7 W and Z Cross-Section Measurements at the LHC

The LHC will provide access to an energy regime that has never before been reached in the laboratory and so the physics programme of CMS is broad. The principal focus is on the discovery of the Higgs boson, but there is a wide range of extended, alternative or exotic possibilities beyond the Standard Model that CMS may search for at the LHC. Nature may exhibit larger symmetries, for example Supersymmetry; or it may feature large extra dimensions; or perhaps something completely unexpected.

While performing measurements of the electroweak bosons within such an experimental programme is of course intrinsically interesting, the electroweak sector has been subjected to many stringent tests by many different experiments (e.g. [23]). It will be years before the LHC experiments can accumulate enough data to rival the statistical precision of these measurements. However, because the electroweak sector is so

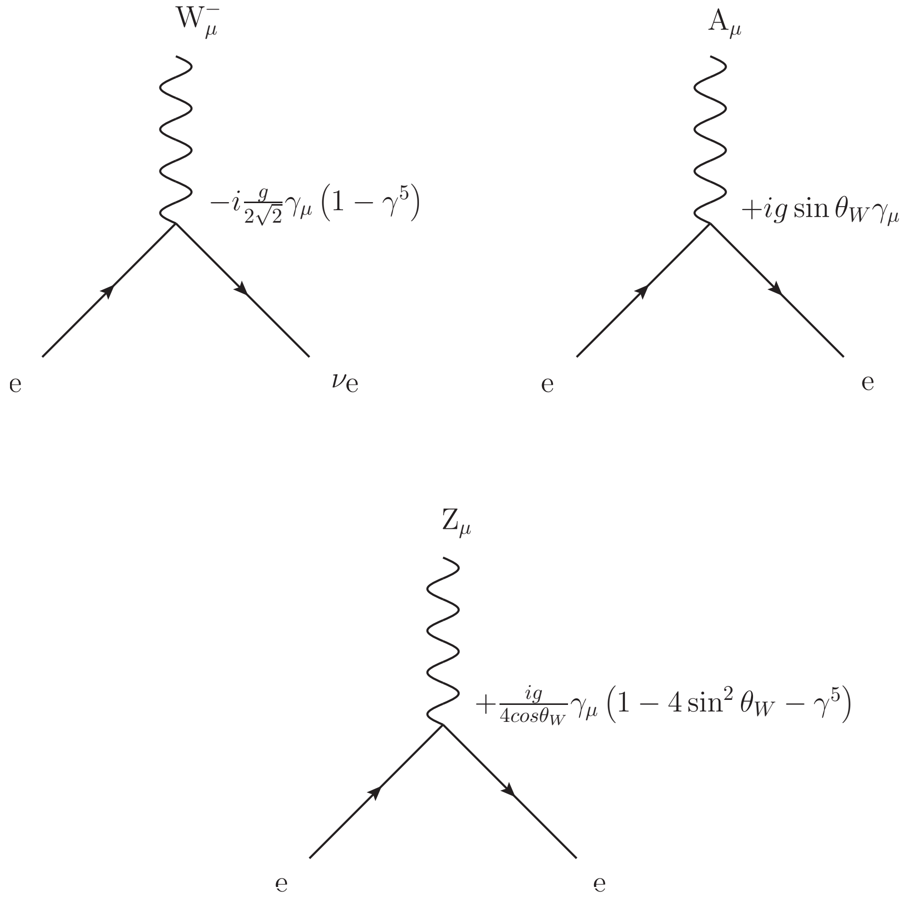
W^-_μ
$-i\frac{g}{2\sqrt{2}}\gamma_\mu\left(1-\gamma^5\right)$
e
ν_e
A_μ
$+ig\sin\theta_W\gamma_\mu$
e
e
Z_μ
$+\frac{ig}{4cos\theta_W}\gamma_\mu\left(1-4\sin^2\theta_W-\gamma^5\right)$
e
e

Figure 1.4: Feynman diagrams showing the interactions between electrons and the gauge bosons.

well understood (Figure 1.5), it will provide ‘Standard Candles’ for the experimental programme that will be vital for credible discoveries to be made.

For instance, measurements of the electroweak bosons will be used to calibrate and measure the alignment of the CMS detectors *in situ* [25]; to set the Jet Energy Scale [26]; and to tune energy corrections for electron reconstruction [27]. As will be discussed in the current work, they provide an ideal testbench for monitoring and optimising the triggering, reconstruction and selection of leptons.

The understanding of the leptons gained in this way will be directly transferable to many of the most promising discovery channels. W and Z bosons decay into high transverse momentum, isolated leptons which are conspicuous in hadron collisions and as such are readily triggered and selected. Many potential discovery channels share this distinctive signature. Furthermore, electroweak vector bosons may be one of the

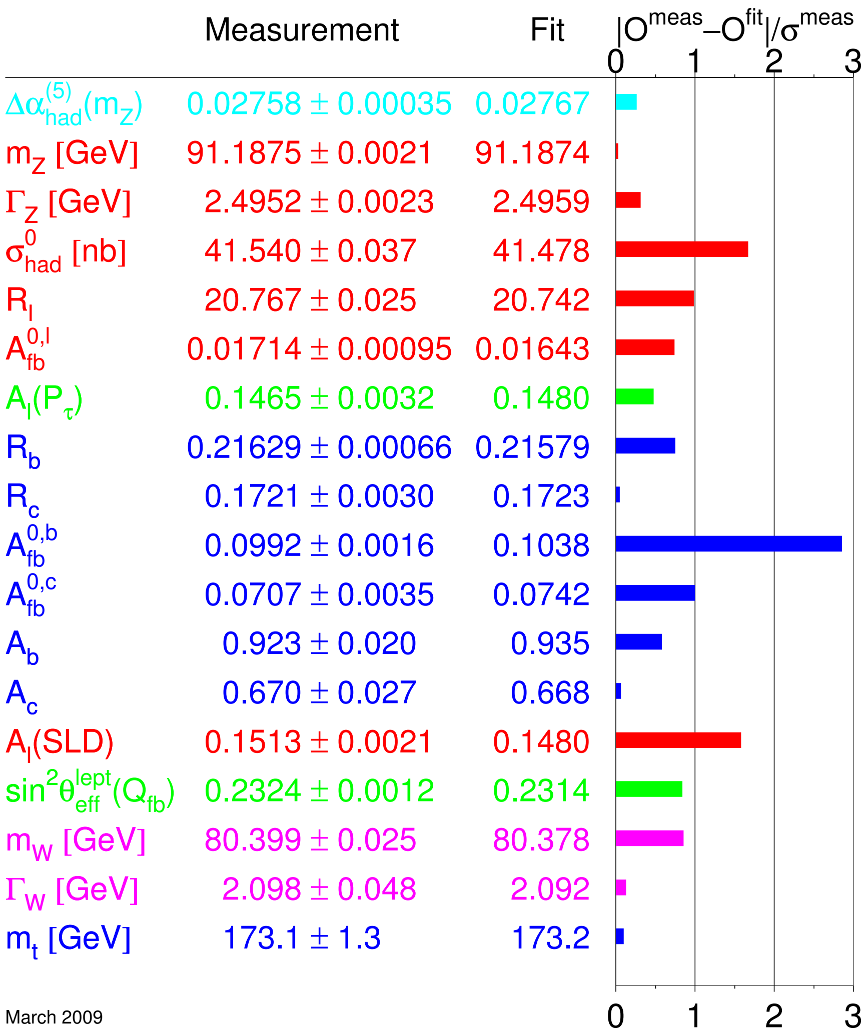

	Measurement	Fit
$\Delta\alpha_{had}^{(5)}(m_Z)$	0.02758 ± 0.00035	0.02767
m_Z [GeV]	91.1875 ± 0.0021	91.1874
Γ_Z [GeV]	2.4952 ± 0.0023	2.4959
σ_{had}^0 [nb]	41.540 ± 0.037	41.478
R_l	20.767 ± 0.025	20.742
$A_{fb}^{0,l}$	0.01714 ± 0.00095	0.01643
$A_l(P_\tau)$	0.1465 ± 0.0032	0.1480
R_b	0.21629 ± 0.00066	0.21579
R_c	0.1721 ± 0.0030	0.1723
$A_{fb}^{0,b}$	0.0992 ± 0.0016	0.1038
$A_{fb}^{0,c}$	0.0707 ± 0.0035	0.0742
A_b	0.923 ± 0.020	0.935
A_c	0.670 ± 0.027	0.668
A_l(SLD)	0.1513 ± 0.0021	0.1480
$\sin^2\theta_{eff}^{lept}(Q_{fb})$	0.2324 ± 0.0012	0.2314
m_W [GeV]	80.399 ± 0.025	80.378
Γ_W [GeV]	2.098 ± 0.048	2.092
m_t [GeV]	173.1 ± 1.3	173.2

Figure 1.5: Comparison of experimental results and Standard Model predictions. The fourth column shows the pulls, i.e. the difference between experimental and theoretical results, in units of experimental measurement error. The experimental data is taken from the LEP, Tevatron and SLC experiments. The SM prediction is a result of a fit to the electroweak precision data from these experiments. [24]

principal backgrounds for such channels and so characterising their reconstruction in CMS is vital.

The relatively large production cross-sections of W and Z bosons and their characteristic decays permit measurements to be made early in LHC running. The topic of this thesis is on preparations made and strategies developed for a measurement of the W and Z production cross-sections with only $\int Ldt = 10\,\mathrm{pb}^{-1}$.

2 The Compact Muon Solenoid

The Compact Muon Solenoid (CMS) [28] is a general purpose detector at the Large Hadron Collider (LHC) at CERN. This chapter describes the LHC and how the challenges of the high instantaneous luminosity and high rate are met by CMS. The description of CMS focusses on the subdetectors used for electron reconstruction : the inner tracker and the electromagnetic calorimeter.

2.1 LHC

The Large Hadron Collider [29] is a 26.7 km circumference, proton-proton collider situated near Geneva, Switzerland. It consists of two accelerating rings which have separate magnetic fields and vacuum pipes, but share a cryogenic structure.The LHC has a nominal centre-of-mass energy $\sqrt{s} = 14\,\mathrm{TeV}$ and a design luminosity of $L = 10^{34}\,\mathrm{cm}^{-2}\mathrm{s}^{-1}$ at two of its Interaction Points (IP). The high energy and high luminosity are motivated by the search for the mechanism of electroweak symmetry breaking and phenomena beyond the Standard Model. Both of these require the study of rare particle interactions with constituent centre-of-mass collision energies, $\sqrt{\hat{s}}$, of $\sim O(1\,\mathrm{TeV})$.

The maximum energy of LHC collisions is dictated by the radius, R, of the existing LEP tunnel which houses the collider and the integrated magnetic field around the ring. The integrated field is given by the magnetic field generated by the dipoles and the effective 'bending radius' of the magnets. The LHC uses superconducting NbTi magnets, cooled to 2K, which generate a nominal field of 8.33 T with $R_{bending} = 2803.95\,\mathrm{m}$. These parameters then allow a proton momentum of $7\,\mathrm{TeV}c^{-1}$:

$$p = eBR_{bending} = 3 \times 10^{8} \times 8.33 \times 2803.95\,\mathrm{eV} = 7.00\,\mathrm{TeV}c^{-1} \tag{2.1}$$

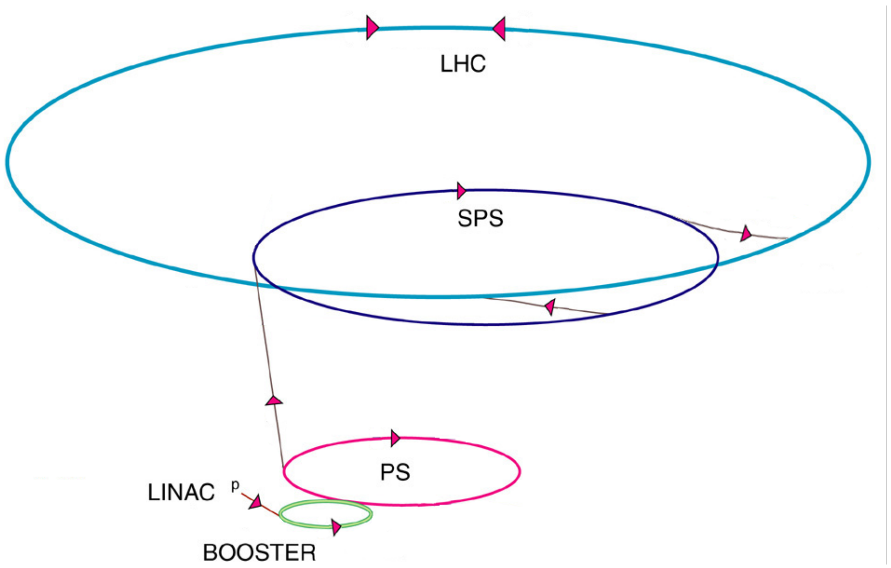

Figure 2.1: The Large Hadron Collider and its preceding accelerators. Protons are initially accelerated in Linac 2 and the Proton Synchotron Booster before being injected into the Proton Synchotron (PS). The PS accelerates the protons to an energy of 25 GeV and subsequently injects these into the Super Proton Synchotron (SPS) which accelerates them to 450 GeV. The protons are then injected into the LHC at Points 2 and 8 (Figure 2.2) to form the two counter-rotating beams. These are then accelerated to full energy before collisions are established by crossing the beams.

The rate of events expected, R_{event}, is the product of the luminosity and the cross-section for that event :

$$R_{event} = L\sigma_{event} \tag{2.2}$$

Study of rare processes therefore requires a high luminosity. For example, a promising discovery channel for a low mass Higgs boson is $\mathrm{H} \rightarrow \gamma\ \gamma$, yet for $m_H = 115\,\mathrm{GeV}$, the predicted $\sigma\,(\mathrm{pp} \rightarrow \mathrm{H}) \cdot BR\,(\mathrm{H} \rightarrow \gamma\gamma) \sim 100\,\mathrm{fb}$ leads to a rate of only 10^{-3} Hz at $L = 10^{34}\,\mathrm{cm}^{-2}\mathrm{s}^{-1}$. (For comparison, the total inelastic proton-proton cross-section is $\sim 60\,\mathrm{mb}$ giving a rate of 600 MHz.)

The protons of the LHC beams are bunched, with a separation of 25 ns between the bunches. The luminosity is related (2.3) to the number of protons per bunch, n_b; the number of bunches in each beam, N_b and the revolution frequency of these bunches, f_{rev}. γ_r is the Lorentz factor; ϵ_n, the normalised transverse emittance; β^*, the betatron function at the interaction point and F, the geometric luminosity reduction factor arising from the crossing angle at the interaction points.

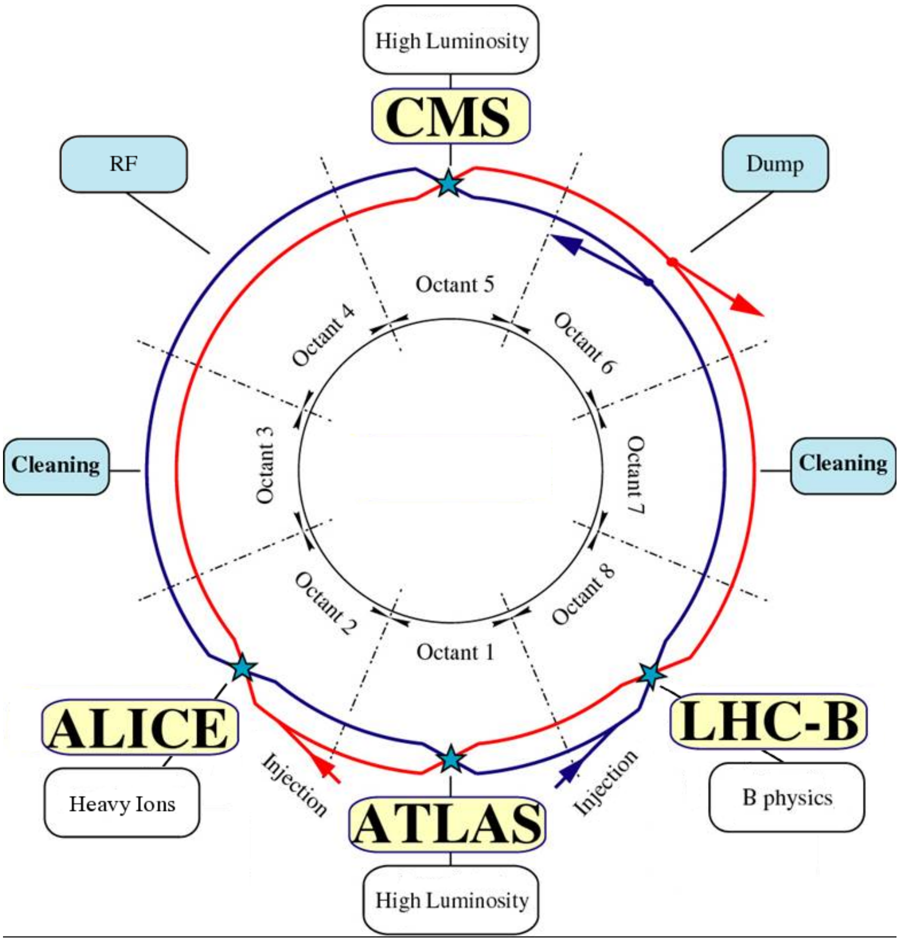
High Luminosity
CMS
RF
Dump
Octant 5
Octant 4
Octant 6
Octant 3
Octant 7
Cleaning
Cleaning
Octant 2
Octant 8
Octant 1
ALICE
LHC-B
Heavy Ions
Injection
Injection
B physics
ATLAS
High Luminosity

Figure 2.2: A schematic of the Large Hadron Collider showing the positions of the main experiments. The beam switches magnet bores at these four points, allowing collisions to take place. The two general purpose detectors, CMS and ATLAS [30], are located diametrically opposite each other at the high luminosity interaction points. The other two interaction points, for LHCb [31] and ALICE [32], are shared with the injection systems for the two beams.

$$L = \frac{N_b^2 n_b f_{rev} \gamma_r}{4\pi \epsilon_n \beta^*} F \tag{2.3}$$

The machine parameters needed to obtain the design luminosity are shown in Table 2.1.

Number of protons per bunch N_b	1.15×10^{11}
Number of bunches n_b	2808
Revolution frequency f_{rev}	11.245 kHz
Lorentz Factor γ_r	7461
Transverse normalised emittance ϵ_n	3.75 µm rad
Betatron function β^*	0.55 m
Geometric luminosity reduction factor F	0.836

Table 2.1: LHC beam parameters for the peak design luminosity.

There is a pattern of proton bunches - "filled" bunches - and intervals with no proton bunches - referred to as "empty" or "missing" bunches. These empty bunches are due to the system of injecting bunches into the LHC from the preceding accelerators and to ensure the safe ejection of the beam at the end of a run. The pattern is illustrated in Figure 2.3. In total, there are 3564 bunches, both filled and empty, in an LHC fill.

The collision of two proton bunches with nominal parameters causes approximately 20 inelastic events, as can be seen using equations 2.2 and 2.3 :

$$\begin{aligned} R &= L\sigma \\ N &= \frac{L}{n_b f_{rev}} \sigma \\ &= \frac{1 \times 10^{34}}{2808 \times 11245} 6 \times 10^{-26} \\ &= 19 \end{aligned} \tag{2.4}$$

Most of these will be minimum bias, "pile-up" events, acting only to obscure interesting interactions which have a much lower cross-section.

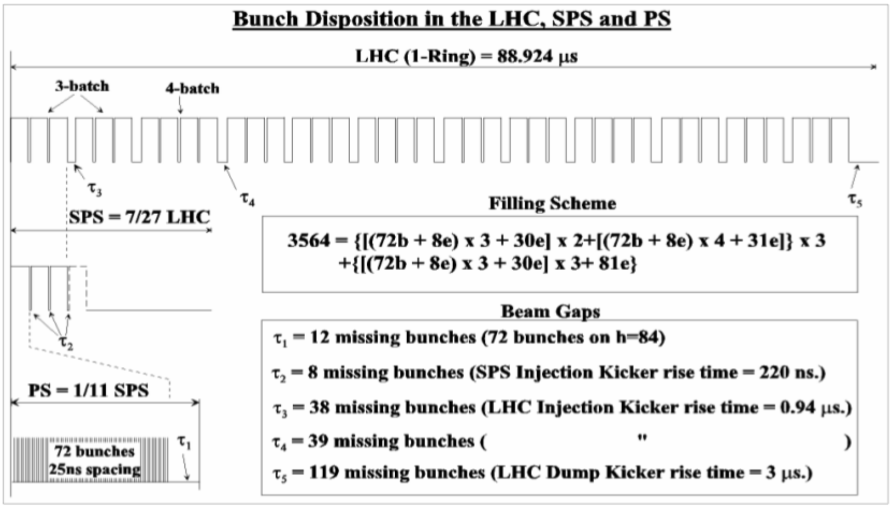
Bunch Disposition in the LHC, SPS and PS
LHC (1-Ring) = 88.924 μs
3-batch
4-batch
τ3
τ4
τ5
SPS = 7/27 LHC
Filling Scheme
3564 = {[(72b + 8e) x 3 + 30e] x 2+[(72b + 8e) x 4 + 31e]} x 3
+{[(72b + 8e) x 3 + 30e] x 3+ 81e}
Beam Gaps
τ2
τ1 = 12 missing bunches (72 bunches on h=84)
τ2 = 8 missing bunches (SPS Injection Kicker rise time = 220 ns.)
τ3 = 38 missing bunches (LHC Injection Kicker rise time = 0.94 μs.)
τ4 = 39 missing bunches (")
τ5 = 119 missing bunches (LHC Dump Kicker rise time = 3 μs.)
PS = 1/11 SPS
72 bunches
25ns spacing
τ1

Figure 2.3: The Proton Synchotron produces six batches of 72 bunches of 25 GeV protons, with 25 ns bunch spacing. Three or four of these batches are injected into the Super Proton Synchotron and accelerated to 450 GeV, before injection into an LHC beam. This procedure is repeated twelve times, leaving 119 missing bunches at the end of the bunch train to ensure safe ejection.

2.2 CMS Detector

The high centre-of-mass energy of the LHC collisions mean that particles with mass $O\,(100\,\mathrm{GeV})$, such as W and Z bosons, will be produced over a wide rapidity range. The CMS detector has therefore been constructed to have good rapidity coverage to detect their decay products. The measurement of all the products of the collisions further demands complete azimuthal angle coverage and a hermetic detector.

To ensure a good track momentum resolution for charged, high p_T particles a high-field, large bore, solenoid magnet is employed, with an operating field strength of 3.8 T. The solenoid bore is great enough for the calorimeters to be within it.

The p-p luminosity of $L = 10^{34}\,\mathrm{cm}^{-2}\mathrm{s}^{-1}$ imposes a number of demands on CMS. The inner and forward subdetectors (including associated front-end electronics and services) must be radiation hard in order to cope with the extremely high particle flux, which would otherwise cause radiation damage and unacceptably degrade their performance.

All of the detectors must have a fast response, in order to cope with the 40 MHz bunch crossing frequency. This is critical in subdetectors which participate in the Level-1 trigger system. The data acquisition system must meet the challenges imposed by the 40 MHz bunch crossing frequency.

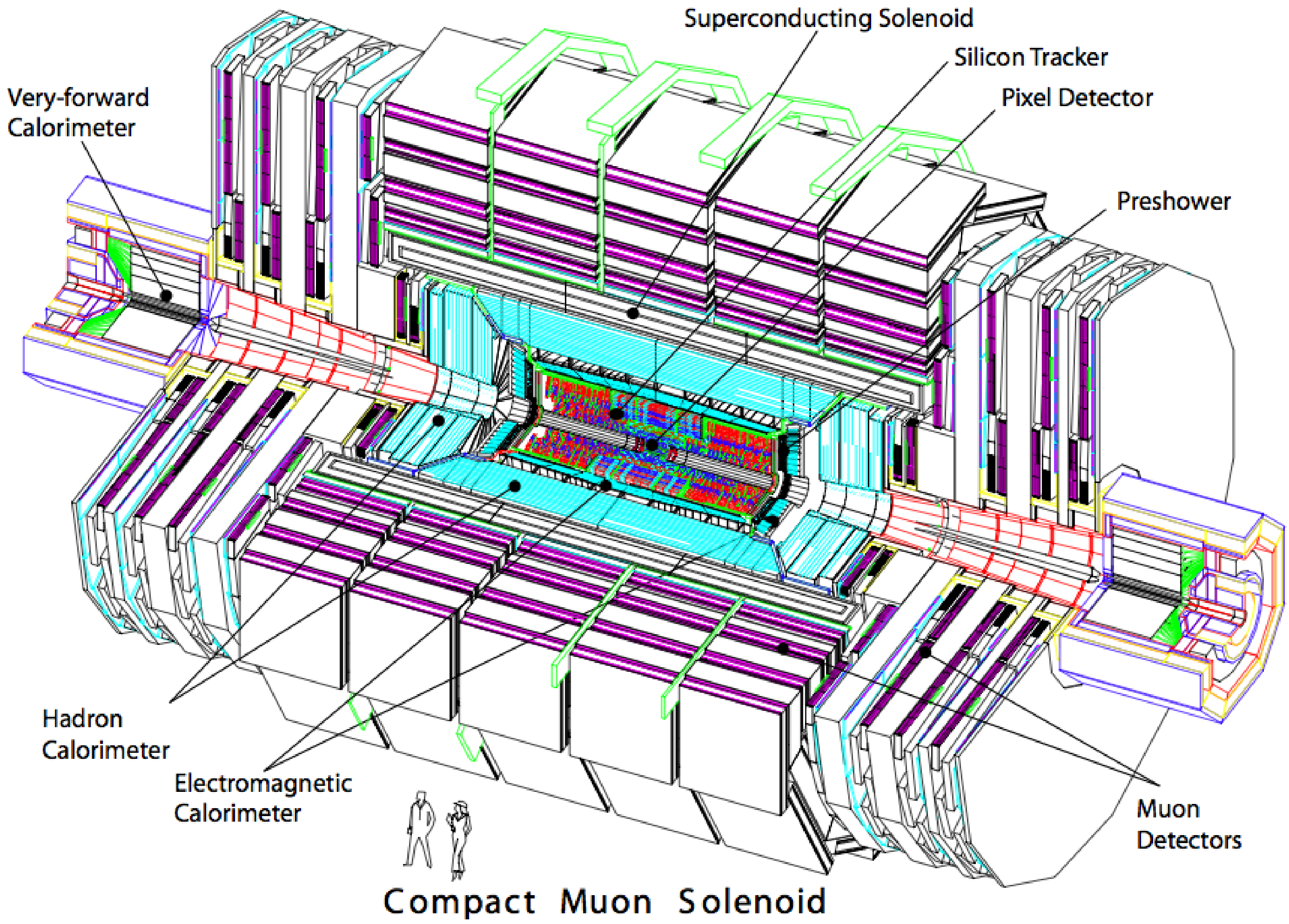
Superconducting Solenoid
Silicon Tracker
Pixel Detector
Very-forward Calorimeter
Preshower
Hadron Calorimeter
Electromagnetic Calorimeter
Muon Detectors
Compact Muon Solenoid

Figure 2.4: The Compact Muon Solenoid.

The subdetectors must have sufficient granularity to reconstruct and measure properties of the interaction of interest in the presence of twenty pile-up events per bunch crossing. A large number of well-synchronised detector channels are necessary to avoid confusion both with these interactions in the same bunch crossing and others in the preceding and subsequent crossings. These channels must be properly calibrated and their alignment measured to achieve the full potential performance of CMS.

CMS uses a right-handed Cartesian coordinate system with its origin at the nominal interaction point at the centre of the detector. The x-axis is defined with $x > 0$ toward the centre of the LHC from the origin. The y-axis points vertically upwards from the origin. r is the radial distance in the $x - y$ plane while ϕ is the azimuthal angle from the x-axis in this plane : $-\pi \leq \phi < \pi$. θ is the polar angle from the z-axis : $0 \leq \theta \leq \pi$. Pseudorapidity is defined as $\eta = -\ln \tan \frac{\theta}{2}$. A distinction is to be drawn between particle η, ϕ and θ which express the direction of the particle and detector η, ϕ and θ which describe the position of a point with respect to the nominal interaction vertex.

Natural units are employed throughout the current work.

2.2.1 Solenoid

The CMS solenoid is a superconducting magnet constructed from a four-layer winding of aluminium-stabilised NbTi Rutherford cable, with an iron return yoke instrumented with muon detection stations. It has a magnetic length of 12.5 m and a cold bore diameter of 6.3 m. The large bore permits a large inner tracking volume with a lever arm of ~ 1.2 m for good momentum resolution, while allowing the calorimeters to be within the magnet, minimising dead material before them and hence improving their resolution. The length : radius ratio provides an extremely uniform magnetic field, even in the forward regions of the detector.

Within the magnet bore, the magnetic field is 3.8 T in the positive z direction and in the return yoke $\sim$ 2 T, enabling the unambiguous determination of muon charges up to $p_T \sim 1$ TeV. The magnet has operated stably at 4 T, but 3.8 T has been chosen as the operating field in order to preserve the magnet in excellent condition over the lifetime of the CMS experiment (expected to be significantly more than a decade).

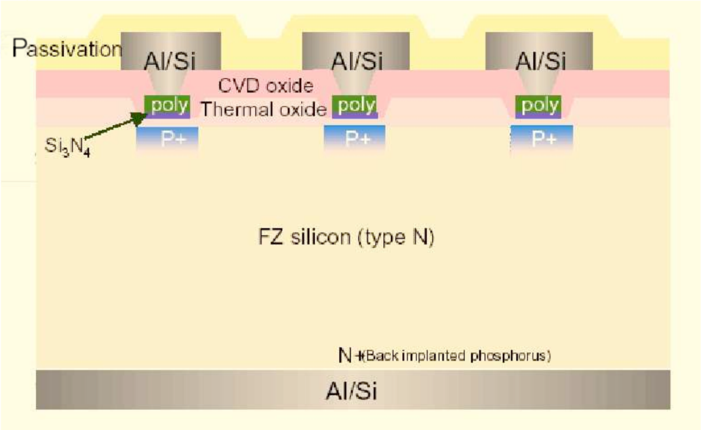

Figure 2.5: A cross-section of a Silicon Strip Tracker sensor. The junction side is at the top of the schematic, ohmic at the bottom. The p+ implantations define the strip geometry.

2.2.2 Tracking System

The CMS inner tracking system will accurately measure the trajectory of charged particles from the interaction point. The solenoidal magnetic field, with strength B (in Tesla), causes these particles of charge ze to follow a helical trajectory with a radial curvature, R (in metres), and pitch angle, λ, which is related to the momentum of the particle by (2.5).

$$pcos\lambda = 0.3zeBR \tag{2.5}$$

$$p_T = 0.3zeBR \tag{2.6}$$

Precise knowledge of the origin of the trajectories gives information about the vertex of the events being studied. Particles with large impact parameters, i.e. those originating from a displaced secondary vertex, include decay products of long-lived particles such as B hadrons.

The CMS tracking system is based entirely on silicon semiconductor sensor technology. These sensors are p-n junction diodes operated with a reverse bias voltage applied, which creates a depletion layer free of mobile charge carriers. This is the active region of the sensor. Charged particles traversing this region lose energy by ionisation, creating mobile charge carriers that are swept to the electrodes by the electric field of the reverse bias. The resulting signals are then processed by low noise, fast, radiation hard electronics.

The use of silicon semiconductors as detectors is motivated by several factors. It allows areas to be covered with a high density of sensors. Due to the density of silicon and its low ionisation energy, active layers need only be O(100 µm) thick : resulting in short charge collection times, reductions in the necessary bias voltages and improved position measurement resolutions. The CMS silicon sensors have been shown to be radiation hard, capable of operating in the extreme radiation environment of the LHC . The innermost pixel layers are expected to remain operational for over 2 years at $L = 10^{34}\,\mathrm{cm}^{-2}\mathrm{s}^{-1}$, while the silicon strip tracker has an expected lifetime of 10 years.

Silicon sensors provide the technology for fast, radiation hard, high granularity and high resolution tracking necessary for the LHC environment, where each bunch crossing occurs at 25 ns intervals and generates ∼1000 charged particles to track. However, there are practical limitations to the detector granularity that can be achieved, as each channel requires power. Densely packed sensors imply a high power density, which in turn requires cooling, particularly as the tracker must be maintained at a temperature $\leq -10°\mathrm{C}$ in order to limit radiation damage. The necessary cabling and piping introduces material into the inner detector and adversely affects the physics performance of the tracker - firstly by impinging on the volume it is possible to instrument and secondly by increasing the probability of bremsstrahlung, photon conversions, multiple scattering and nuclear interactions.

As a result of these considerations, the size of the sensors varies as a function of (principally radial) distance from the interaction point. The geometry of the CMS tracker is shown in Figure 2.6. Closest to the interaction point is the pixel detector, which provides good impact parameter point resolution and disentangles the combinatoric problem of track-finding using sensitive regions of size 100 µm in $R-\phi$ and 150 µm in z. This pixel size results in a position resolution of ∼10 µm in $R-\phi$ and 15–20 µm in z and maintains an extremely low occupancy of 10^{-4}, even at $L = 10^{34}\,\mathrm{cm}^{-2}\mathrm{s}^{-1}$. The pixel detector thus provides excellent knowledge of the inner states of tracks. 66 million pixels are distributed over three barrel pixel layers and two forward disks in each z direction, giving a total sensitive area of approximately $1\,\mathrm{m}^2$.

At radii greater than 20 cm, the charged particle flux is reduced sufficiently to allow the use of silicon strip detectors while maintaining low occupancy. Measuring particle tracks using the Silicon Strip Tracker (SST) gives a lever arm of r = 120 cm for precise

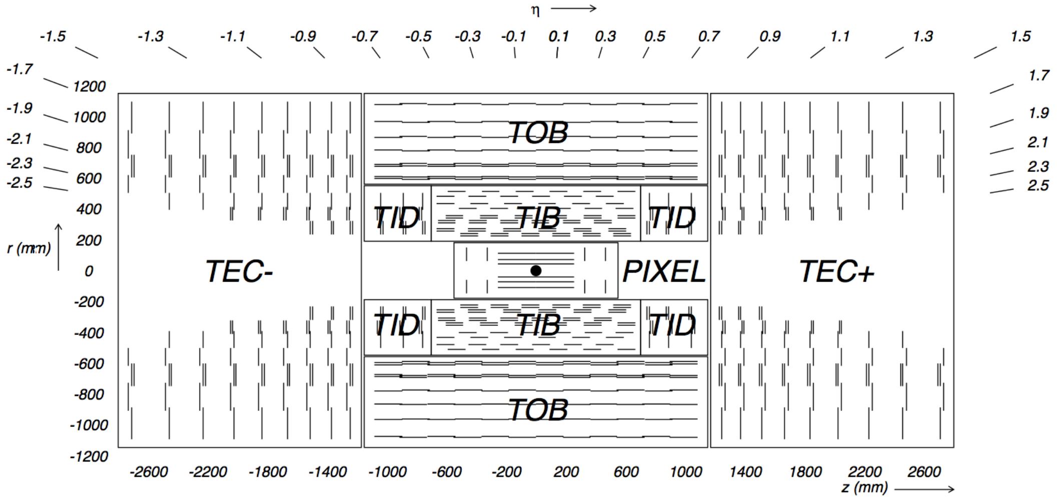
η
-1.5
-1.3
-1.1
-0.9
-0.7
-0.5
-0.3
-0.1
0.1
0.3
0.5
0.7
0.9
1.1
1.3
1.5
-1.7
-1.9
-2.1
-2.3
-2.5
1.7
1.9
2.1
2.3
2.5
r (mm)
1200
1000
800
600
400
200
0
-200
-400
-600
-800
-1000
-1200
TOB
TID
TIB
TID
TEC-
PIXEL
TEC+
TID
TIB
TID
TOB
-2600
-2200
-1800
-1400
-1000
-600
-200
200
600
1000
1400
1800
2200
2600
z (mm)

Figure 2.6: The geometry of the inner tracking system, shown in the $R - z$ plane. Lines represent detector modules, with double lines showing the position of the stereo tracking modules.

momentum measurement. The four layers comprising the Tracker Inner Barrel (TIB) and the six Inner Disks (TID) are located between $20\,\text{cm} < r < 55\,\text{cm}$, with strip dimensions $O(100\,\mu\text{m}) \times 10\,\text{cm}$, leading to an occupancy of 2–3%. The Tracker Outer Barrel (TOB) surrounds the TIB and TID, with six layers extending to a radius of 120 cm. The Tracker Endcaps (TEC) consist of 9 disks on each side, extending from $124\,\text{cm} < |z| < 282\,\text{cm}$ and providing coverage up to $\eta \leq 2.5$. As the charged particle flux is further reduced in these regions, strips of length 25cm are employed, giving an expected occupancy of approximately 1% at $L = 10^{34}\,\text{cm}^{-2}\text{s}^{-1}$.

In both TIB and TOB the strips are oriented along the beam axis, while in the TID and TEC they point radially. The first two layers in the TIB and TOB, along with the inner two rings of the TID and TEC (and TEC ring 5) have two detector modules mounted back-to-back, with a 100 mrad stereo angle between them. These stereo detectors provide a measurement of the complementary coordinate for their detector (z in the TIB and TOB; r in TID and TEC).

An example of the expected performance of the inner tracking system is shown in Figures 2.7 and 2.8. This performance will only be obtained if the actual position and orientation of the tracker sensors are well measured. This alignment is carried out using the Laser Alignment System that monitors positions of tracker substructures to $O(100\,\mu\text{m})$ and using track-based alignment algorithms [33][34] on cosmic ray, beam halo and collision events that will align individual sensor modules. The track-based algorithms will align the inner tracker to a precision such that there will be no effect on performance significant compared to its intrinsic resolution.

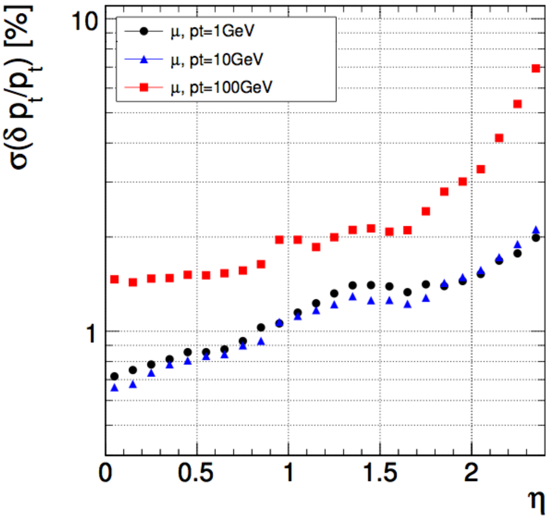

Figure 2.7: Transverse momentum resolution of inner tracking system for muons of $p_T = 1$, 10 and 100 GeV.

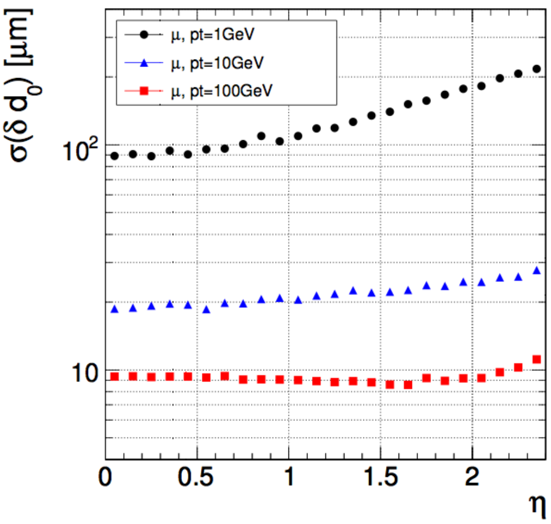

Figure 2.8: Transverse impact parameter resolution of inner tracking system for muons of $p_T = 1$, 10 and 100 GeV.

2.2.3 Electromagnetic Calorimeter

The electromagnetic calorimeter absorbs and measures the energy of electrons and photons. It is a homogeneous calorimeter comprising 75 848 lead tungstate ($PbWO_4$) crystals equipped with fast, radiation hard readout electronics. The ECAL is divided into a central barrel (EB) and two endcap (EE) subdetectors (Figure 2.9). A preshower detector is located in front of each endcap.

The ECAL barrel is constructed in two cylindrical halves (EB+ and EB-), joining at $z = 0$. Each comprises 18 supermodules which contain 1700 crystals arranged in an $\eta - \phi$ geometry : 20 crystals in ϕ by 85 in η. The supermodules each cover 20° in ϕ and extends from $0 \leq |\eta| \leq 1.479$. Each is split into 4 modules : module 1 is 20 crystals in ϕ by 25 in η, covering $|\eta| < 0.435$; the other modules are 20 crystals in ϕ by 20 in η. The nominal distance between supermodules is 6 mm ; between modules is 0.5 mm and 0.35 mm between crystals within modules. The crystal axes are 'quasi-projective' : they are aligned to point 3° from the nominal interaction point in both θ and ϕ to minimise the number of particle trajectories aligned with the gaps between crystals.

The ECAL endcaps are each made of two 'dees', which hold 3 662 crystals arranged in an $x - y$ geometry. The crystals are grouped into 5×5 supercrystals. The crystal axes in the EE are aligned to point 1300 mm beyond the nominal interaction point, again minimising the effects of intercrystal gaps.

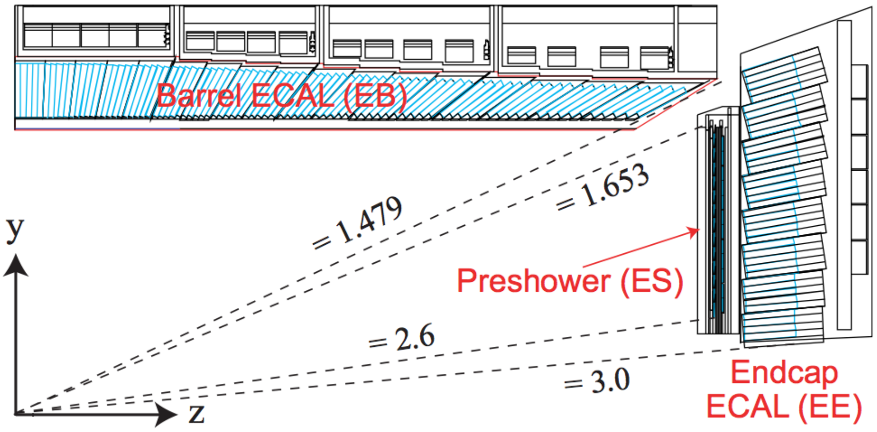

Figure 2.9: The geometry of one quarter of the electromagnetic calorimeter, shown in the $R - z$ plane. The ECAL barrel begins at $R = 1290$mm and the endcaps at $|z| = 3150$mm with the magnet on.

Electrons and photons propogating in the $PbWO_4$ predominantly lose their energy through radiative processes. In the high electric field of atomic nuclei electrons emit bremsstrahlung photons (Figure 2.10), while photons are converted into electron-positron pairs (Figure 2.11). In the case of electrons, the energy $E(x)$ which remains after traversing a distance x is given by :

$$E(x) = E_0 e^{-\frac{x}{X_0}} \tag{2.7}$$

where E_0 is the initial energy and the constant X_0 is known as the radiation length. For $PbWO_4$, $X_0 = 8.9$mm. Pair production by photons has a probability of $e^{-\frac{7}{9}}$ in 1 X_0.

If the energy of the incoming electron or photon is sufficiently high then the process of bremsstrahlung or pair production begins an electromagnetic shower, or cascade, in which the secondary particles subsequently radiate energy leading to the generation of more particles with lower energy. This process (illustrated in Figure 2.12) continues until the energy of the shower particles falls below some critical value, E_C. Below this critical energy, no more particles are generated, as the dominant energy loss mechanisms are

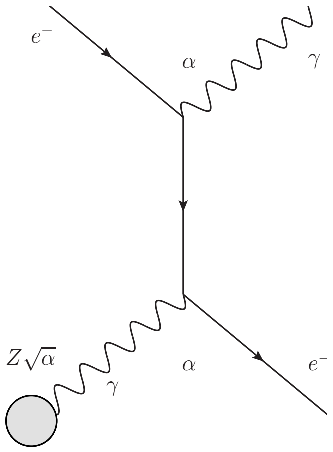

Figure 2.10: Feynman diagram of the bremsstrahlung energy loss mechanism of electrons.

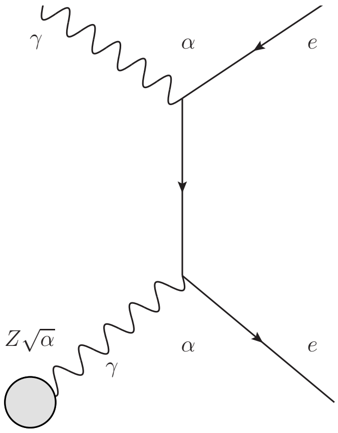

Figure 2.11: Feynman diagram of electron-positron pair creation from photon in nuclear magnetic field.

Compton scattering and the photoelectric effect for photons and ionisation for electrons. From 2.7, this shower maximum occurs at a depth of :

$$\frac{x}{X_0} = ln\left(\frac{E_0}{E_C}\right) \tag{2.8}$$

Figure 2.13 shows the longitudinal profile of energy deposition : one can see that due to the short radiation length of $PbWO_4$ $\sim 100\%$ of the incident electron energy is contained within crystals of 230 mm length ($25.8\,X_0$).

The lateral development of the shower is due to multiple scattering of electrons off the shower axis. The average lateral deflection of an electron with critical energy is the Moliére radius, R_M, which for lead tungstate is 22 mm. A typical shower consists of a narrow cone of cascade particles (90 % of the shower energy is contained within $1R_M$) surrounded by a wider halo of low energy electrons and photons. This can be seen in Figure 2.14. The ECAL crystals are approximately $1\,R_M \times 1R_M$ in cross-section, leading to a highly granular calorimeter suitable for the high occupancy LHC environment. At $R = 1290$ mm, this corresponds to 0.0174×0.0174 in $\eta - \phi$, providing excellent precision on measurements of the position of electromagnetic showers.

In $PbWO_4$ the energy lost by ionisation is deposited into the crystal lattice. This energy is transferred to luminescent centres, at Pb sites and defects related to oxygen

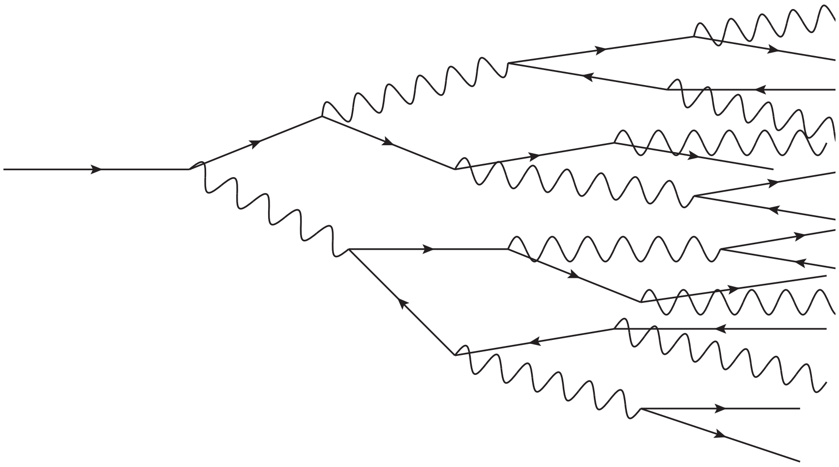

Figure 2.12: Illustration of the development of an electromagnetic shower.

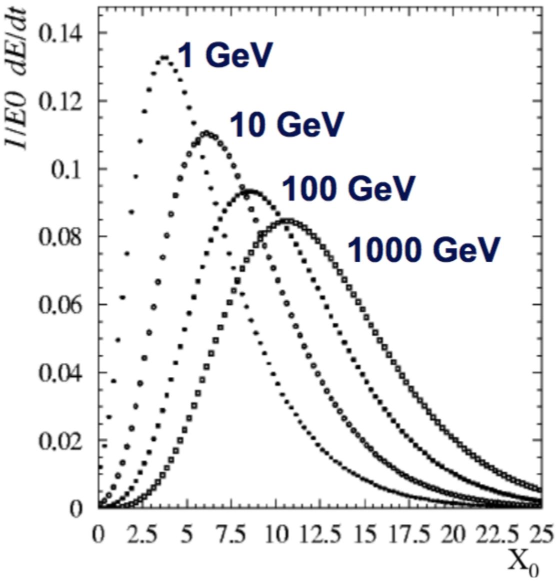

Figure 2.13: Energy deposition against longitudinal distance for 1, 10, 100 and 1000 GeV electrons in $PbWO_4$.

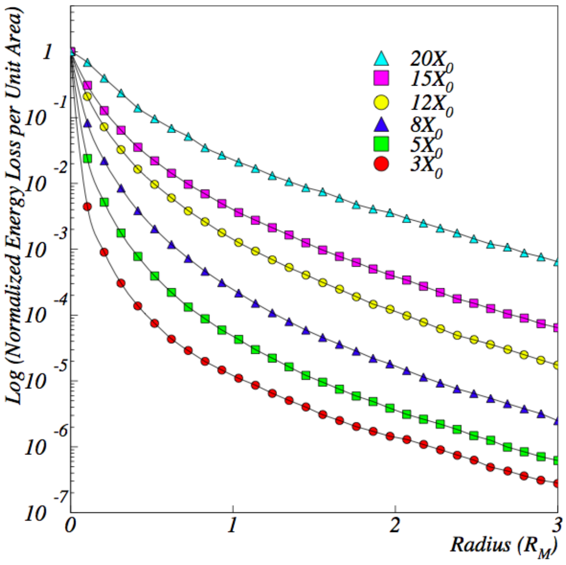

Figure 2.14: Energy deposition against lateral distance for 50 GeV electrons, at different depths in $PbWO_4$.

vacancies, where the energy is emitted as scintillation photons. These scintillation photons are detected by avalanche photodiodes (APDs) in EB and vacuum phototriodes in EE. The light yield is low, with only 4.5 photoelectrons/MeV being produced in the photodetectors. However the scintillation decays of the two modes are fast – with lifetimes of approximately 30 ns and 10 ns – leading to $\sim 80\%$ of the light being emitted within 25 ns.

Due to the fluctuating nature of the electromagnetic showers, the measurement of energy in calorimeters is stochastic. As lead tungstate is a fully active calorimeter medium, i.e. a combined absorber and scintillator, it makes almost full use of the shower particles leading to excellent energy resolution despite the low light yield. The energy resolution – shown in Figure 2.15 – can be parameterised as :

$$\left(\frac{\sigma}{E}\right)^2 = \left(\frac{S}{\sqrt{E}}\right)^2 + \left(\frac{N}{E}\right)^2 + C^2 \tag{2.9}$$

where S is the stochastic term resulting from photostatistics and the incomplete lateral containment of the crystals (typically 5×5) used to obtain the energy measurement. N is the noise term, which incorporates electronic noise and any pile-up energy. C is a constant term which accounts for inter-crystal intercalibration errors, non-uniformities in the detector (such as in light collection) and radiation damage. Radiation damage does not impair the lead tungstate scintillation mechanism, but rather causes colour absorption bands which reduces the transparency of the crystals. This will be monitored and corrected for using a laser system.

A pre-installation intercalibration of the barrel crystals has been performed using cosmic rays, with a calibration precision of approximately 1.5% and 9 supermodules have been calibrated during the 2006 testbeam to 0.3% [35]. The endcap crystals are expected to have an intercalibration precision of $\sim 10\%$, obtained from crystal light yield and VPT response measurements. The ultimate intercalibration precision will be reached using *in situ* measurements of collision data. In the very early running, intercalibration will by performed by reconstructing the invariant mass of π^0 and η in $\pi^0 \rightarrow \gamma\,\gamma$ and $\eta \rightarrow \gamma\,\gamma$ decays. As the tracker alignment becomes better measured, the ratio of energy measured in the ECAL to track momentum in $\mathrm{W}^{\pm} \rightarrow \mathrm{e}^{\pm}\,\nu_{\mathrm{e}}$ events will be used. $\mathrm{Z} \rightarrow \mathrm{e}^{+}\,\mathrm{e}^{-}$ events will be used to set the absolute energy scale.

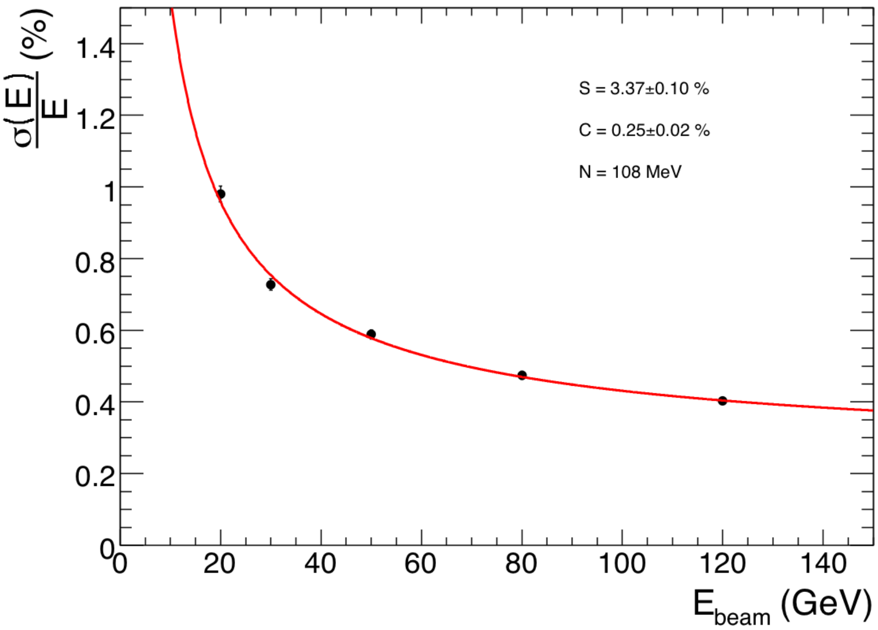

Figure 2.15: Resolution vs Energy of the CMS ECAL measured in beam tests. Energy reconstruction was performed using 25 3×3 arrays, as described in Chapter 3.

The ECAL Preshower

The preshower detector (ES) is a sampling calorimeter, consisting of two layers of lead absorber each followed by a layer of silicon strip sensors. The first absorber layer is $2X_0$ thick and is followed by strips oriented along y. The second absorber layer is $1X_0$ thick and is followed by strips oriented along x. The strips have a pitch of 1.9 mm.

The preshower provides excellent granularity in the region $1.653 \leq |\eta| \leq 2.6$, providing for precise position and shower shape measurements that assist in the rejection of π^0s which are a background for photons.

The presence of the ES in front of the EE impairs the energy resolution. This can be approximated as an additional $5\%/\sqrt{E}$ sampling contribution convoluted into the stochastic term in the resolution.

2.2.4 Hadronic Calorimeter

The hadronic calorimeter measures the energy of hadrons. The hadronic shower, illustrated in Figure 2.16 is similar to the electromagnetic, but is governed by the strong force. Energy is lost by the incident hadron in inelastic collisions with the atomic nuclei of the calorimeter. A significant fraction of this energy goes into creating π^0 and η mesons which decay into photons, giving an electromagnetic component of the shower. This is complemented by photons from highly excited nuclei. The hadronic component results from both the creation of charged hadrons and the breakup of nuclei. The response to these two components is different : the CMS HCAL is "non-compensating".

Hadronic showers penetrate more deeply than electromagnetic cascades and are more extensive laterally, although they are also characterised by a 'core' of high energy particles surrounded by a cone with a softer energy spectrum. Interaction length, λ, is the hadronic shower analogue to radiation length.

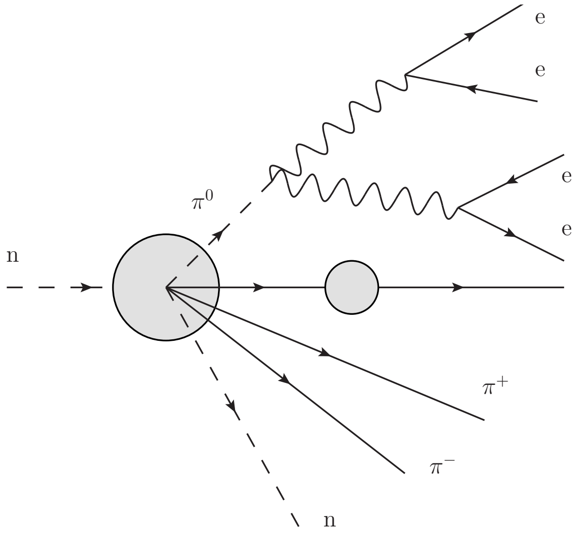

Figure 2.16: Illustration of the development of a hadronic shower, showing the electromagnetic component descending from a π^0; and the hadronic component consisting of charged hadrons and nuclear spallation products.

Only the energy from the ionisation caused by charged particles is detectable. The 'invisible' energy is that of recoiling nuclei and neutrons which gradually thermalise. Hadronic cascades typically have many fewer secondary particles than electromagnetic, leading to larger statistical fluctuations. Furthermore, the CMS HCAL is a sampling calorimeter. These factors lead to a much larger stochastic term in the energy resolution of the HCAL than in the resolution of the ECAL.

The CMS HCAL (Figure 2.17) uses brass absorber-plastic scintillator layers. The scintillators are connected by wavelength shifting fibres to hybrid photodiodes for readout. In the barrel, HB, the calorimeter is segmented into 0.087×0.087 $\eta-\phi$ 'towers'. HB is supplemented by HO outside the solenoid, which increases the depth of the calorimeter

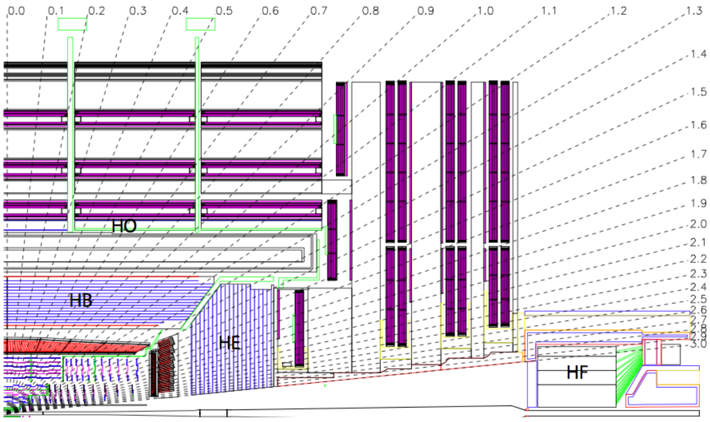

Figure 2.17: The geometry of one quarter of the hadronic calorimeter, shown in the $R - z$ plane. The hadronic barrel (HB), outer (HO), endcap (HE) and forward (HF) subdetectors are shown.

system to 10λ. The endcaps, HE, are segmented with the same dimensions for $|\eta| < 1.6$, with towers 0.17×0.17 for $|\eta| > 1.6$. The endcap calorimeters are also 10λ deep.

Forward Calorimeter

The forward calorimeters (HF) of CMS extends calorimetric coverage to $|\eta| = 5$. In order to cope with the extreme radiation in these regions, they are constructed from cylinders of steel absorber and quartz fibres which are oriented along z. Čerenkov light is generated in these fibres by particles with phase velocity greater than the speed of light in quartz. These signals are guided by the fibres to photomultipliers.

The fibres are bundled to provide granularity of 0.175×0.175 in $\eta - \phi$. One half of the fibres run the whole length of the absorber : the others begin 22 cm into the absorber. These two sets are read out separately and due to the differing penetrative power of electromagnetic and hadronic particles, provide separation between the two.

2.2.5 Muon System

Muons carry no colour charge and have a very high critical energy ($\sim$350 GeV in iron). Thus, energy loss by relativistic muons is dominated by ionisation up to this energy. This energy loss is approximately the minimum possible, hence muons are highly penetrating 'minimum ionising particles'. The CMS muon system is therefore the outermost detector system. It consists of four layers of detectors (Figure 2.18). In the barrel, drift

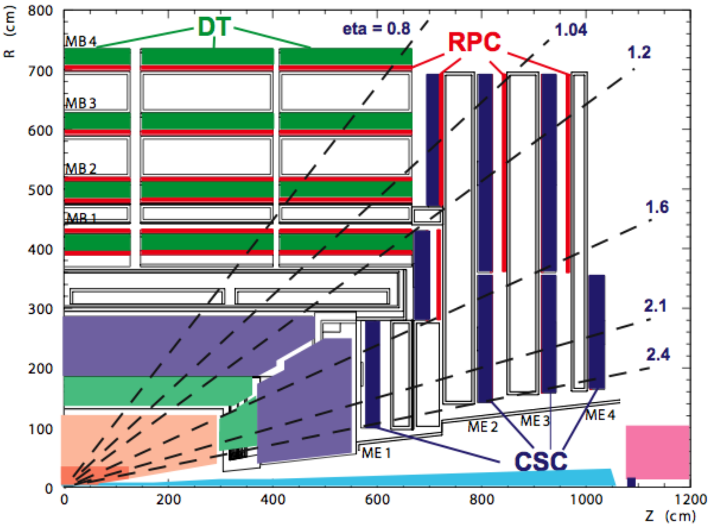

Figure 2.18: The geometry of the muon system, shown in the $R-z$ plane.

chambers are used for their excellent spatial resolution; while in the endcaps, where the expected occupancy is higher, cathode strip chambers are employed. Both of these are supplemented with resistive plate chamber detectors (up to $|\eta| < 1.6$) which provide excellent time resolution, reducing combinatoric backgrounds and aiding triggering.

2.2.6 Trigger and Data Acquisition System

In high luminosity running, CMS will generate $\sim 1\,\mathrm{MB}$ of zero-suppressed data per bunch crossing [28]. Combined with the 40 MHz bunch crossing rate, this leads to a data rate of $O\,(40\,\mathrm{TB\,s^{-1}})$. There is insufficient bandwidth to transfer this data off-detector and insufficient storage to retain it. The data acquisition system can sustain an input rate of $\sim 100\,\mathrm{GB\,s^{-1}}$ and the sustainable rate to storage for subsequent processing and analysis is $O\,(100\,\mathrm{MB\,s^{-1}})$. These two rates lead to a two stage data reduction system, comprising the Level-1 and High Level Trigger systems.

Level-1 Trigger System

The Level-1 Trigger uses low resolution detector data and simple algorithms running on custom hardware to achieve the required data reduction factor of ~ 500. The full detector data are stored in pipeline buffers on the detector front-end while the Level-1 decision is being made. These buffers are 128 bunch-crossing deep, giving $3.2\,\mu\mathrm{s}$ for the data to be transmitted, algorithms to be run and decision to be distributed to the detector front-end electronics. In the event of a decision to accept, the buffered data are pushed into the data acquisition system.

Due to the architecture of the inner tracker and preshower detectors, their information cannot be used within the 3.2 µs available for Level-1 decision making. Therefore electrons and photons share a Level-1 Trigger algorithm, illustrated in Figure 2.19. The algorithm operates on trigger towers, 5×5 arrays of crystals which follow the HCAL tower granularity. The E_T of the electromagnetic candidate is calculated as the E_T of the highest energy tower and the E_T of the adjacent tower with maximum energy. The electromagnetic nature of the object is insisted upon by requiring a narrow electromagnetic-like shower shape (the fine-grain veto) and limited hadronic energy behind the ECAL trigger towers. Isolation criteria can also be applied, with fine-grain veto and hadronic activity criteria applied to the neighbouring towers and a further demand of at least one "quiet corner". A quiet corner is an L-shaped group of five neighbouring towers (shown as grey lines in Figure 2.19) which have an energy sum less than some threshold.

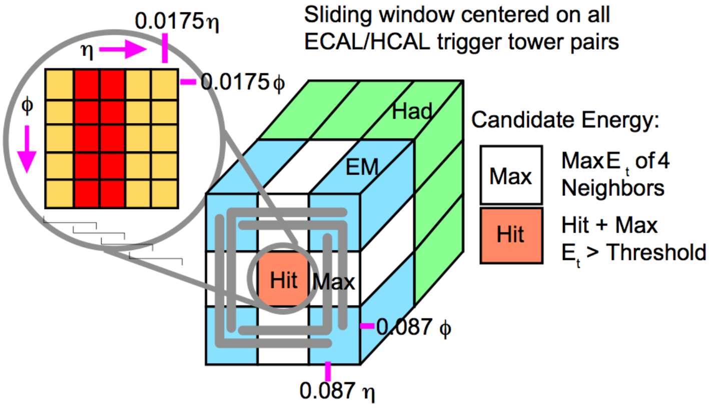

Figure 2.19: Illustration of Level 1 Trigger eγ algorithm.

Final Level-1 decisions are made using the four best isolated and four best non-isolated electromagnetic candidates.

High Level Trigger and Data Acquisition System

After a Level-1 accept, the event is 'built' - the data from the buffers are acquired and combined into a coherent record of the bunch crossing. The High-Level Trigger runs on commodity PCs, using the full resolution data (including data from the tracker) and sophisticated algorithms which are similar to those used for offline event reconstruction. The electron reconstruction algorithm will be discussed in Chapter 4.

CMS Performance in Extended Operation

The CMS detector was operational during the LHC beam commissioning in September 2008, although the inner tracking system and solenoid were unpowered. Events featuring beam halo muons were recorded, as were those with sprays of $\mathcal{O}(10^5)$ muons caused by proton bunches striking closed collimators 150 m upstream of CMS. These events were used to commission the beam monitoring apparatus and synchronise detector channels in the ECAL, HCAL and muon systems

The LHC beam activity was followed by a month of cosmic ray data-taking using the entire detector [36]. CMS operated well over this extended period – recording 2.7×10^6 cosmic muon events – with a data-taking efficiency of 70%. These events were used for CMS alignment, calibration and performance studies. All detector subsystems were found to meet their design specification.

The inner tracking system had 98% of both pixel and silicon strip tracker channels active. Repairs were undertaken following the exercise to increase the number of active channels. The alignment of the tracker modules was measured using muon tracks to a precision of 3-4 µm in the barrel and 3-14 µm in the endcaps (for the smallest pitch coordinate). The absolute energy loss in the silicon strip sensors was calibrated. Measurements were made of the Lorentz angles; hit and track reconstruction efficiencies; and the track parameter resolutions.

The ECAL operated well, with the stability of temperature and high voltage within the design parameters, and with 98.3% of EB channels and 99.7% of EE channels active. The majority of inactive barrel channels have been restored to operation. A higher level of noise than that measured during construction was observed in nine supermodules, however the 3+5 amplitude reconstruction method (Chapter 3) effectively suppresses this additional noise contribution. The precalibration constants were verified and in the case of the EE were updated for the 3.8T magnetic field. The sequence of laser, pedestal and test-pulse events that will be carried out in the LHC abort gap was tested.

The HB, HE and HF calorimeters operated well with 99.3% of channels functional, however the outer hadronic calorimeter suffered hybrid photodiode (HPD) failures with only 87% of channels functional by the end of the exercise. The HPD operating voltage has been reduced and the malfunctioning HPDs replaced. The intercalibration of the HCAL channels was improved and updated for magnetic field effects.

The muon subsystems which participated had 97.7% of chambers active (the end-cap resistive plate chambers were not commissioned until the end of the exercise). Track-based methods were used to measure the alignment of the drift-tube chambers to $\mathcal{O}(300\,\mu\text{m})$ and the cathode strip chambers to $\mathcal{O}(200\,\mu\text{m})$.

The muon reconstruction was studied. Using both inner tracker and muon chambers, the p_T resolution was measured to be less than 1% for $p_T \sim 10\,\text{GeV}$, rising to 8% for $p_T \sim 0.5\,\text{TeV}$ muons. Figure 2.20 shows a cosmic muon reconstructed in all the CMS subdetectors.

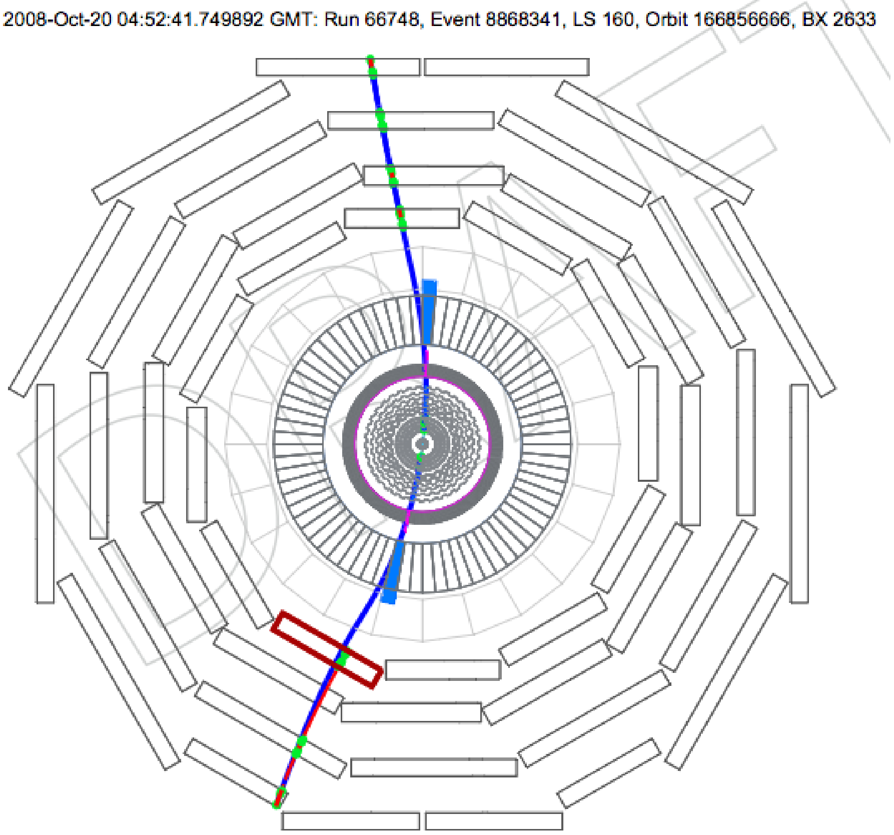
2008-Oct-20 04:52:41.749892 GMT: Run 66748, Event 8868341, LS 160, Orbit 166856666, BX 2633

Figure 2.20: Event display showing a cosmic muon passing through CMS. The reconstructed trajectory is shown in blue. The muon chamber and inner tracking hits are shown in green. The HCAL and ECAL energy deposits are shown in blue and magenta respectively.

3 Amplitude Reconstruction in the Electromagnetic Calorimeter

The CMS electromagnetic calorimeter has been tested extensively during its construction, installation and commissioning. In 2006, nine supermodules equipped with final systems were studied and the 15300 constituent crystals were intercalibrated to an accuracy of $\sim 0.3\,\%$ at the H4 beamline at CERN. The supermodules were exposed to over two billion electrons, ranging in energy from 15 GeV to 250 GeV, providing a rich data set for analysis.

In this chapter a study of amplitude (energy) reconstruction with the ECAL is presented, using the results to perform an analysis of its basic performance.

3.1 Experimental Set-up

3.1.1 Electron Beam

The H4 extraction line from the Super Proton Synchrotron is situated in the North Area of CERN. It provides very high purity electron beams with a momentum range from 10 GeV to 300 GeV. An example beam configuration is shown in Figure 3.1. Protons (typically 10^{12} per bunch) are steered from the SPS onto the beryllium target T2, which creates a spray of hadrons. The neutral pions among these hadrons subsequently decay into photons. A fraction of these photons will then create an electron-positron pair in a lead converter immediately before the experimental area. Beams of either electrons or positrons can then be selected. The beam is steered and particle momentum selected using the main dipole magnets and focussed using quadropoles. The intensity, size and momentum of the electron beam at H4 is fine-tuned using collimators. Centring of the beam is monitored by scintillator fingers and controlled using trim dipole magnets.

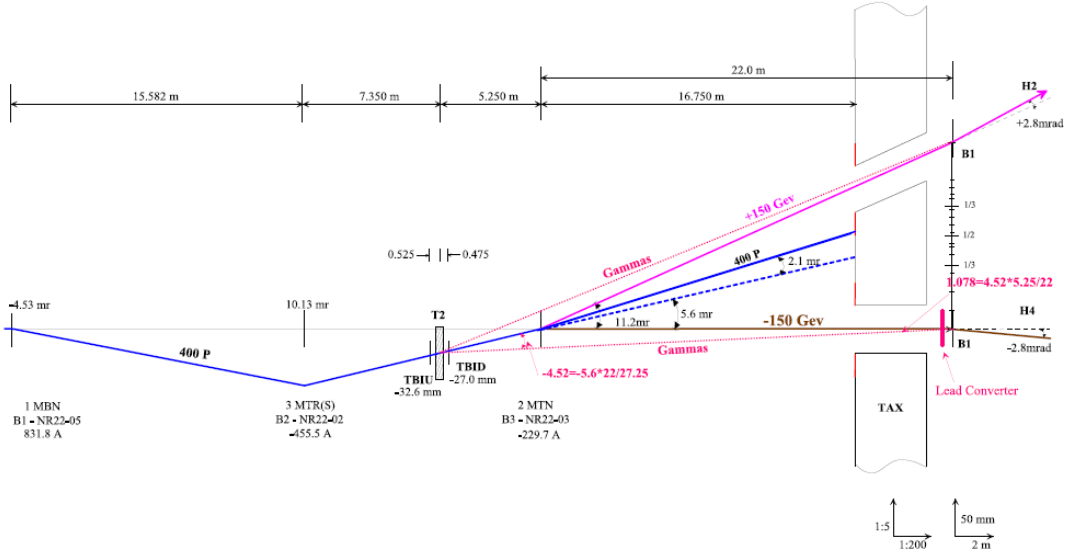
15.582 m
7.350 m
5.250 m
22.0 m
16.750 m
H2
+2.8mrad
B1
+150 Gev
Gammas
400 P
2.1 mr
1/3
1/2
1/3
1.078=4.52*5.25/22
0.525
0.475
-4.53 mr
10.13 mr
T2
5.6 mr
11.2mr
-150 Gev
H4
400 P
TBID
-27.0 mm
TBIU
-32.6 mm
Gammas
B1
-2.8mrad
-4.52=-5.6*22/27.25
Lead Converter
1 MBN
B1 - NR22-05
831.8 A
3 MTR(S)
B2 - NR22-02
-455.5 A
2 MTN
B3 - NR22-03
-229.7 A
TAX
1:5
1:200
50 mm
2 m

Figure 3.1: Beam set-up to provide an equitable distribution of beam between the H2 and H4 experimental areas, with protons from the SPS being steered onto the beryllium target T2 via bending magnets B1 and B2. Electrons produced in the lead converter are then selected and steered to the H4 experimental area.

The ECAL electronics are designed for LHC operation, operating with a 25 ns clock period, matching the 40 MHz bunch crossing frequency of the LHC. Except in special operating periods, the H4 beam has no time structure and thus the readout trigger is asynchronous with the ECAL electronics. This places special requirements upon the amplitude reconstruction, as described in Section 3.4.1.

3.1.2 H4 Experimental Area

In the H4 experimental area, the supermodules were mounted on a computer controlled table that could rotate the supermodule in both η and ϕ with great precision, allowing every part of it to be exposed to the beam. The table was positioned such that incident particles would impinge on the ECAL with an offset of $\sim 3°$ relative to the crystal axis, reproducing the quasi-pointing geometry of the completed CMS detector with respect to the nominal interaction vertex.

Differences between the test beam set-up and the *in situ* CMS environment are that at H4 there is no magnetic field and very little material in front of the supermodule while in CMS there is the 3.8 T solenoidal field and up to 1.7 X_0 of material. The effects of this on electron reconstruction are discussed in Chapter 4. The test-beam allowed the measurement of the intrinsic ECAL resolution, independent of these effects.

Data taking was triggered using plastic scintillator tiles, with a 20 mm × 20 mm area – slightly smaller than the crystal front face cross sectional area. The phase between triggers given by these tiles and the electronics clock was measured using a time to digital converter (TDC).

Four layers of scintillating fibre hodoscopes were used to measure the transverse position of electrons incident on the front face of the crystals. An impact point resolution of 250 μm was obtained in both x and y [37](corresponding to η and ϕ respectively.)

3.2 ECAL Front End Electronics

An ECAL supermodule consists of 1700 $PbWO_4$ crystals, grouped into 68 trigger towers. These trigger towers each define a discrete readout unit, with 25 crystals connected to five very front end (VFE) cards. These cards (illustrated in Figure 3.2) are in turn connected to a motherboard, with further connections to a front end (FE) card and to off-detector electronics.

The scintillation light produced in the lead tungstate crystals is detected by the avalanche photodiodes (APD). The signals produced by the APDs are shaped and amplified in parallel with multiple gains (nominally 1, 6 and 12) by the Multiple Gain Pre-Amplifier (MGPA), before subsequent digitization by a multiple channel ADC. The unsaturated channel which used the largest gain is then read out, along with 2 bits denoting the gain used. Multiple gains are necessary in order to preserve the excellent ECAL precision over a dynamic range larger than that provided by the 12 bit ADCs used. Saturation occurs at an amplitude equivalent to an energy of 1.7 TeV in the EB and 3 TeV in the EE.

The ADC output is then passed to the front end card, where trigger primitives are generated and the data are buffered until a Level-1 accept is received. If a Level-1 accept is received, the data are transmitted off-detector via optical fibre.

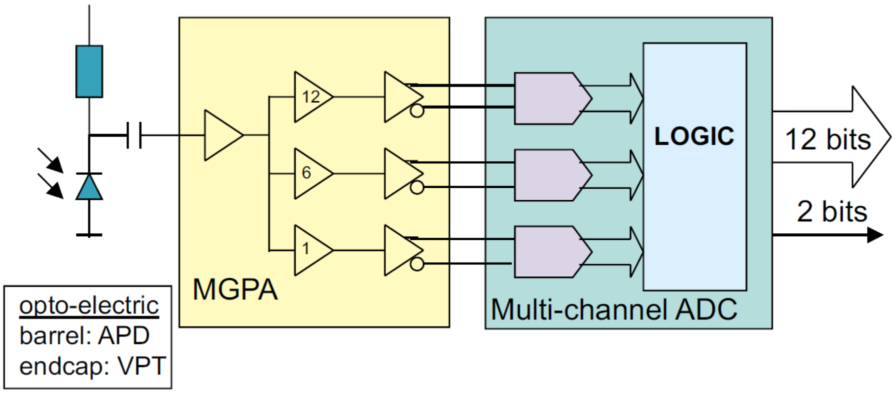

Figure 3.2: Schematic of one channel of the CMS ECAL Very Front End. Every signal is processed in parallel through the three channels shown, before the logic unit decides to read out the most precise and accurate channel (the non-saturated channel with highest gain).

3.3 Amplitude Reconstruction

Signals are sampled by the ADC every 25 ns and in standard operation the data transmitted for an event are a series of 10 (more generally $4n + 2$) samples. The signal amplitude is reconstructed using a linear combination of these samples : $\hat{A} = \sum_i w_i S_i$, where S_i is the sample value in ADC counts and w_i is a weight. This is a digital filtering technique that aims to minimise the noise in the reconstructed amplitude. The weights are determined using a signal representation, as described in Section 3.4. Weights for samples on the rising edge of the signal pulse (peaking time is 50 ns) are set to zero, leaving 3 presamples before the pulse to sample the pedestal and 5 samples during the pulse - this scheme is referred to as “pedestal subtracting” or “$3+5$” weights. The timing of channels was adjusted so the signal peaked between sample 5 and 6 to minimise any possible signal contamination of the third pedestal measuring presample.

3.4 Weight Determination

A more complete description of the procedure of weight determination can be found in [38]. In summary, the objective of the weights methods is to obtain a precise measurement of the signal amplitude that minimises the noise contribution and hence accurately measures the energy deposited in the ECAL. Optimised weights can be extracted by minimizing with respect to the weights the expression :

$$\chi^2 = \sum_{i,j} (S_i - G_i)\mathbf{C}_{ij}(S_j - G_j) \tag{3.1}$$

where G_i comes from a representation of the signal that must be determined, as described in Section 3.5. $\mathbf{C}_{ij}$ represents the correlation of noise between sample i and j and is determined using data with no signal.

An example of a signal pulse is shown in Figure 3.3. Sets of weights can be derived to measure not only the amplitude, A, but also the time of the peak, T_{max} and the pedestal, P. The T_{max} is of particular interest as it allows the timing of each channel in the ECAL to be measured and adjusted.

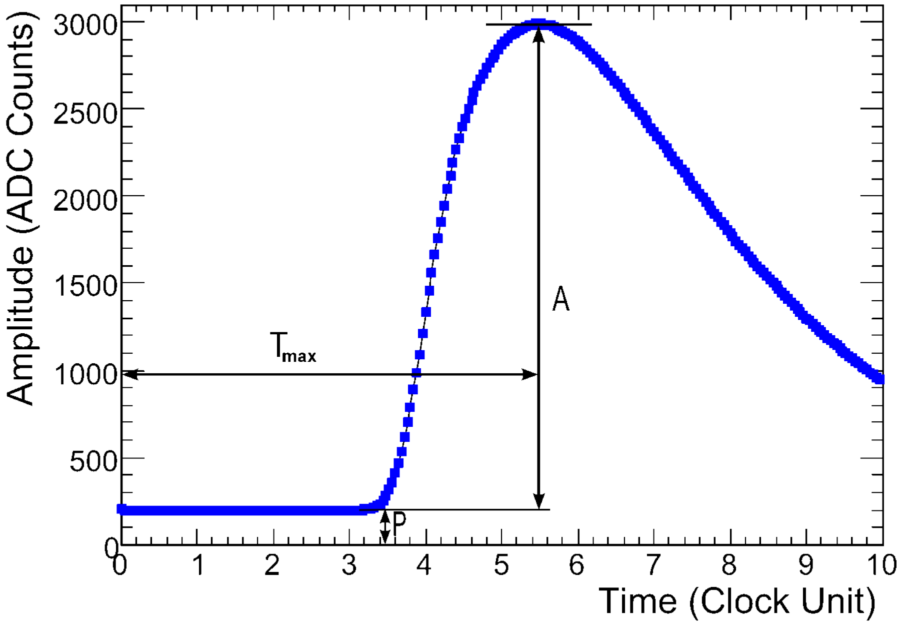

Figure 3.3: An example of the signal pulse, showing the amplitude, A; the time of the maximum signal, T_{max}; and the pedestal, P. A clock unit is 25 ns. The blue squares correspond to 250 signal samples : a series of 10 samples for each of the 25 TDC offsets.

3.4.1 Weights for the Asynchronous Running

The ADC sampling frequency is 40 MHz, matching the LHC bunch crossing frequency. As a result, the signal pulses of particles coming from LHC bunch crossings will always be sampled at the same points on the pulse. It has previously been shown [38] that for CMS running only one series of weights is needed for an accurate reconstruction of energy over the whole ECAL (after setting channel timings and accounting for particle time-of-flight), as bias in amplitude caused by the (very small) residual fixed timing differences between channels will be accounted for by the intercalibration. The effect of timing fluctuations between events – principally due to longitudinal vertex variation – is negligible.

In test beam running, the incident particles do not shower in the ECAL at a fixed phase to the clock. Thus the signal sampling, which is performed every 25 ns, will not sample the same points on the pulse. This would result in variations in the amplitude reconstructed for particles of the same energy, unless the signal is described more fully using phase-dependent weights.

The events are divided into 25 bins of 1 ns according to their phase difference and a set of weights for each of these is determined. A TDC measures the offset between the time of triggering (corresponding to the signal pulse) and the system clock (and hence the sampling). Using this information, the signal amplitude is calculated using the correct set of weights.

Small differences between the signal pulses of each channel cause a smaller, residual, phase dependent bias that results in a degradation of energy resolution. This bias is removed by using sets of unique, “optimised” weights, determined for each crystal individually. These optimised weights ensure that amplitude is consistently reconstructed, irrespective of the phase of the incident electron signal.

Such ‘optimised’ weights are not necessary for CMS running because the synchronous nature of the sampling means any channel-to-channel signal shape discrepancy will be manifest only as a fixed bias which will be removed as part of the intercalibration.

These optimised weights effectively enable measurements of the ECAL performance made with the asynchronous test beam to be related to the performance in LHC running conditions.

3.5 Determination of Signal Representations

Accurate signal representations are needed to derive optimised weights that can properly reconstruct energies in the asynchronous test beam running. Figure 3.4 shows samples in ADC counts against time for approximately 30 000 120 GeV electrons.

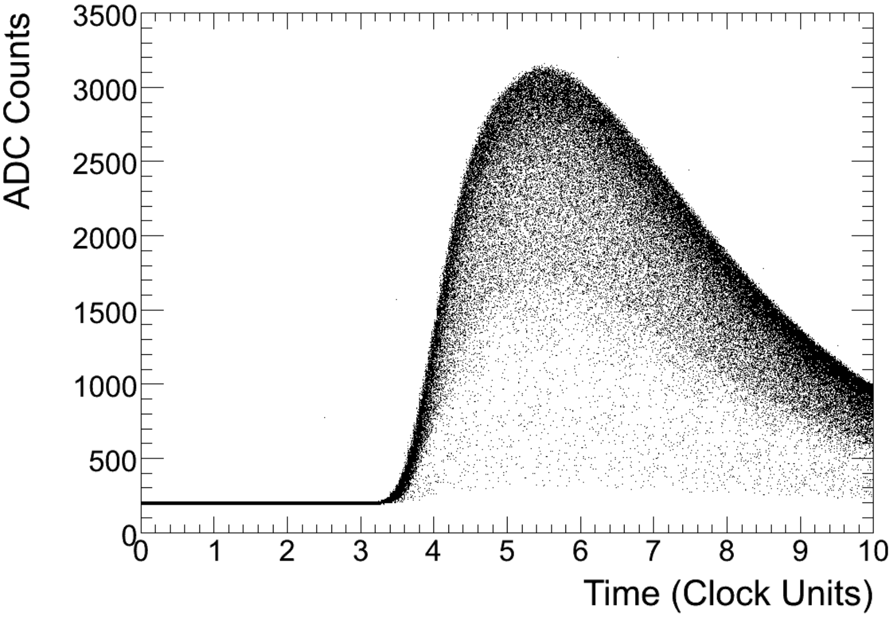

Figure 3.4: Scatter plot showing the signal samples vs time for approximately 30 000 events, for 120 GeV electrons.

The impact position of an electron affects the amplitude of the signal due to the variation of the containment of energy. More energy will be deposited in the crystal for electrons that impact centrally. All aspects of the pulse representation, such as its width, should remain unchanged as these are manifestations of crystal and electronic parameters.

In order to best determine the signal representation, it is necessary to factor out these amplitude variations. A simple scheme is to use tight hodoscope cuts to limit the signals considered to those within a narrow amplitude range. However, doing this severely reduces the number of events that can be used – limiting the accuracy of the profile determination. For crystals that had only limited exposure to beam, for example those for which only intercalibration runs were taken, any further loss of shape information severely impacts the determination of the representation. This means only a very limited number of crystals (those with high statistics runs available) can have optimised weights built. The effect of such a hodoscope cut is shown in Figure 3.5.

Even after the hodoscope restriction is applied, a significant number of events outside of the narrow amplitude range is observed. When averaging over the samples within 1ns bins corresponding to the intervals used for weight determination, any samples from these events will draw the average of the bin away from its true value – the profile will

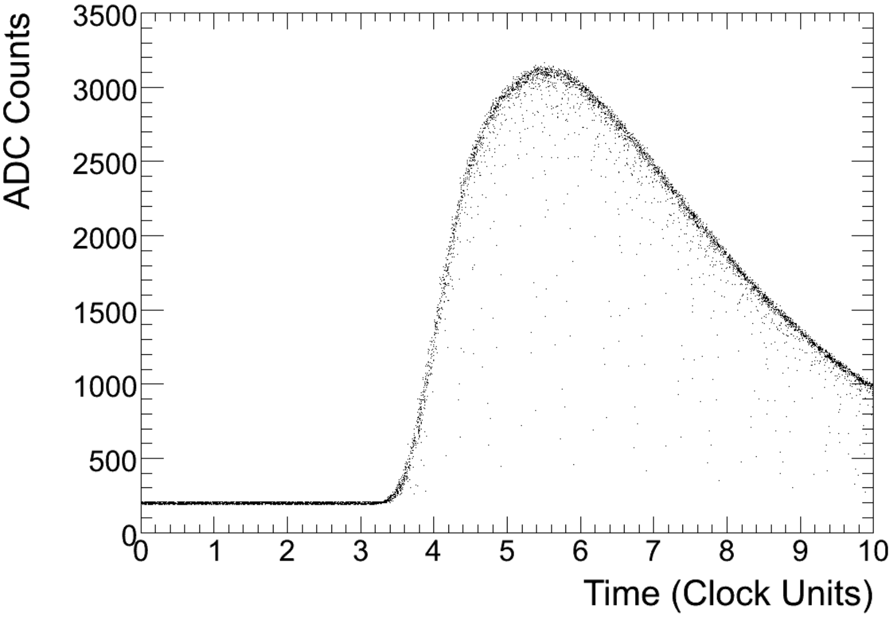

Figure 3.5: Scatter plot showing the signal samples vs time for 120 GeV electrons that satisfy a 4 mm × 4 mm hodoscope condition, from the same event set as Figure 3.4. In many time bins, there are a significant number of samples far removed from the narrow range expected for central impact electrons.

not have the smoothness exhibited by the signal and is therefore a poor description of it.

Schemes that iteratively scale outlying samples remaining after hodoscope cuts to place the signal amplitude within a certain range of the mean – even those that have some shape smoothing algorithm applied – give signal descriptions of inadequate quality unless a very large number of events is used ($>$ 100 000, as in [39]).

3.5.1 Improved Method

What is needed to avoid the problems mentioned in the previous section is a method of constructing a precise representation of the signal pulse for any channel using runs containing only a few thousand events. Each point on the required digital representation of the signal pulse corresponds to one of the 25 bins in phase (repeated cyclically). The events contributing to each of the 25 bins are different. For the shape to be correctly represented each bin must correspond to the same total signal amplitude. The simplest way to achieve this is to normalize all samplings in each event by the signal amplitude before recording them (i.e. multiply each sampling (after pedestal subtraction) by $1/\hat{A}$, where $\hat{A}$ is an estimate of the signal amplitude). The estimate of the amplitude is made with 25 sets of reference weights calculated for a crystal in SM10, which was equipped with near-final electronics and studied in the 2004 ECAL test beam campaign. The rescaled samplings are recorded in 1 ns phase bins before being averaged to provide a representation of the signal pulse.

The representation of the signal resulting from the previous procedure is not completely smooth. This can be shown by fitting the profile with an analytic function describing the pulse shape. To study the details of this effect, the fit was repeated for each clock cycle, forcing the best possible fit over the 25 phase bins of this cycle (this was realised by increasing the errors for the bins outside the cycle under study - the errors were multiplied by a large number). This process is illustrated in Figure 3.6 for the 7th clock cycle. Figure 3.7 shows the residuals for four cycles near the peak : the residuals clearly repeat in a cyclical manner every 25 ns. These cyclical residuals are ascribed to the use of 25 sets of reference weights derived from a particular shape, slightly different to that of the channel being evaluated.

To remove these biases, a correction factor was determined corresponding to the inverse of the 25 residuals coming from the 7th clock cycle, where the function is almost straight. This correction is then applied to the phase bins in every other sampling and the resulting curve (shown in Figure 3.8) is used as the pulse representation to calculate the weights (which will be called in the following the “optimised weights”) for the channel under study.

Limited Statistics Case

A major aim of the 2006 Test Beam was the precalibration of the supermodules used. To achieve this, every crystal was exposed to 2000 electron events. The performance of the improved method for determining a signal representation using these data sets was assessed by comparing a profile created from an intercalibration run with another with 30 000 events for the same crystal. Figure 3.9 has both profiles overlaid and the similarity is striking, with only the rising edge showing slight differences. The difference between the two profiles is plotted in Figure 3.10. Samples taken from the rising edge are not used to reconstruct amplitudes, with the corresponding weights being set to zero. The rising edge is particularly susceptible to timing jitter, as the derivative of the pulse here is extremely large.

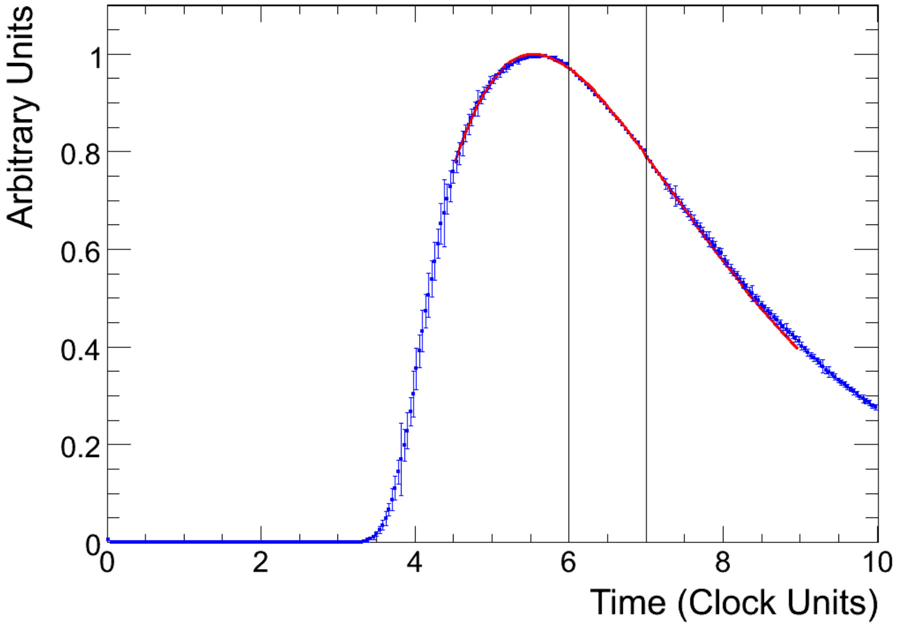

Figure 3.6: The blue points are the average values of the signal pulse in each bin after rescaling with amplitudes calculated from reference weights. The two vertical lines show the range that is used to determine the bias correction. The error bars show the errors used for the fit. Inside the range used to determine the bias correction they are simply the statistical error, outside the range they have been artificially increased. The red line is the analytic function.

The close match between the performance of the method in both the intercalibration and high statistics cases clearly demonstrates that weights can be determined for every crystal in the test beam supermodules. Moreover, the reproducibility of the results using two different data sets illustrates the robustness of the method. The performance of the weights produced using both data sets are examined in Section 3.6.

3.6 Performance of Improved Weights

In order to assess the performance of these new weights, the energy resolution in arrays of crystals in supermodule 16 has been measured. Optimised weights were determined using high statistics data (30 000 events per crystal) for 49 crystals around trigger tower (TT) 10[1]. Using these weights, amplitudes were reconstructed for each centrally incident electron (incident in 4mm × 4 mm region around the point of maximum shower contain-

---

[1] This particular trigger tower and supermodule are chosen simply because of the availability of this high statistics data

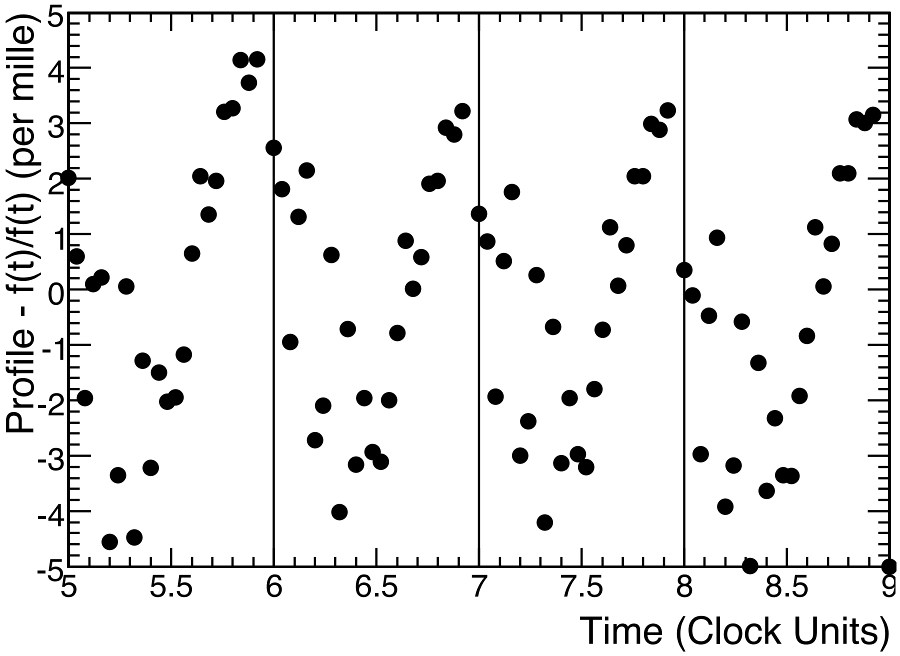

Figure 3.7: For each clock cycle (delineated by vertical lines) an analytic function was fitted to the signal representation obtained using the reference weights. The points show the residuals between these fits and the signal representation.

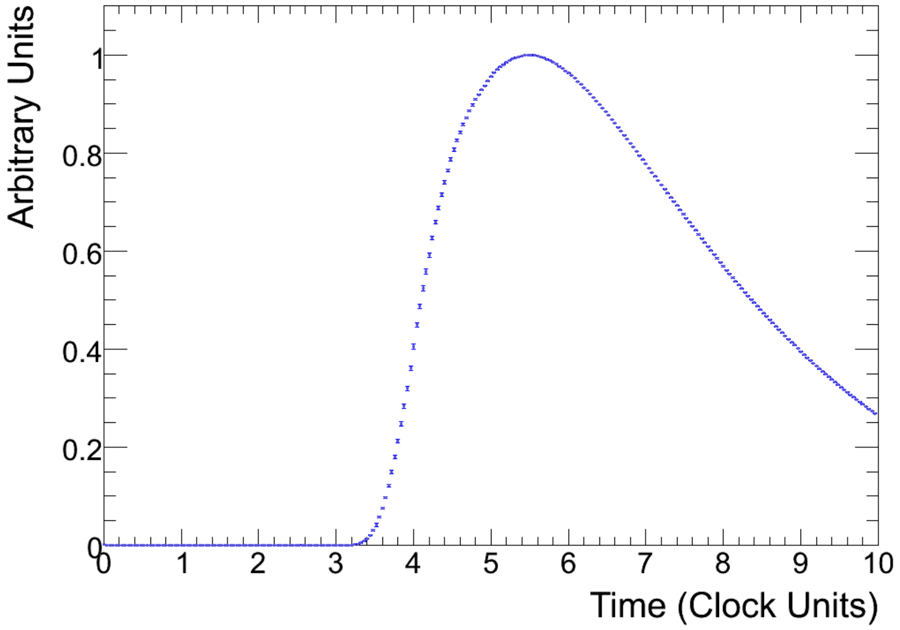

Figure 3.8: A fully processed profile created with 30 000 events for crystal 248 of supermodule 16.

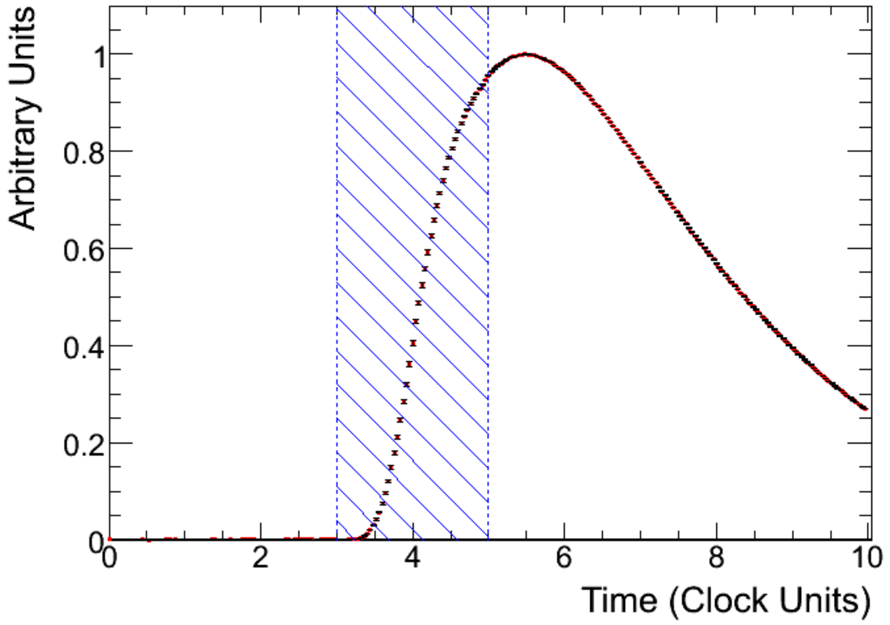

Figure 3.9: For the same crystal, the green profile is generated from a high statistics run of 30 000 events, the red profile from an intercalibration run of 2 000 events. The two profiles are on top of each other and cannot be distinguished. The amplitude sum does not include samples from the rising edge, indicated by the shaded area.

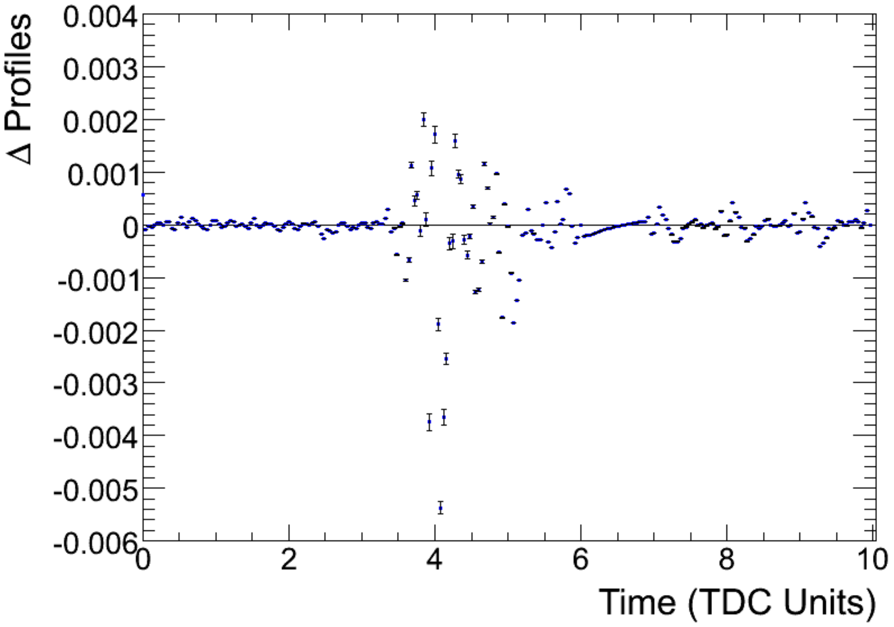

Figure 3.10: High statistics profile - intercalibration profile. The area of largest difference corresponds to the rising edge.

ment) and summed in 3 × 3 arrays (using the intercalibration constants). This was done for each of the 25 crystals of TT10 and the amplitudes for these 25 3 × 3 arrays were then combined into a single distribution. The amplitudes were then rescaled to place the peak of this distribution at the beam energy. A Crystal Ball fit [40] was then performed. The Crystal Ball function is a combination of a Gaussian peak with a polynomial tail. The result is shown in Figure 3.12. It can be contrasted with the result in Figure 3.11, which was obtained with the same data, but reconstructed using the standard weights.

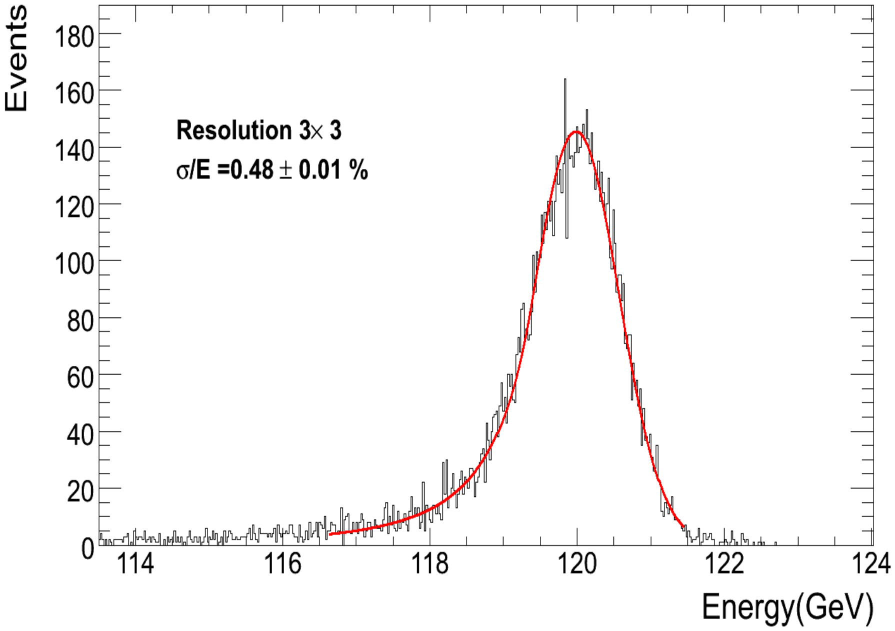

Figure 3.11: Amplitude in the 3 × 3 array around 25 different crystals for 120 GeV electrons using standard weights for reconstruction. Resolution is measured using a Crystal Ball fit.

The performance of the improved weights derived using the method of this thesis is clearly demonstrated by these figures. There is a substantial improvement in energy resolution between the two results, and the value of $0.40 \pm 0.01\%$ is compatible with the 2004 result of $0.39 \pm 0.01\%$. It must be remarked that the 2004 result was obtained for a single array of 3 × 3 crystals, whereas the resolution presented here also has intercalibration accuracy uncertainties convoluted. The 2004 results were obtained using weights derived with 200 000 events.

The weights derived from only 2000 events perform extremely similarly to the weights derived from 30 000 events, as shown in Figures 3.12 and 3.13. As the event samples are independent, this is evidence that the method for deriving the weights is robust and its results are reproducible. The good performance of the method using only a small number

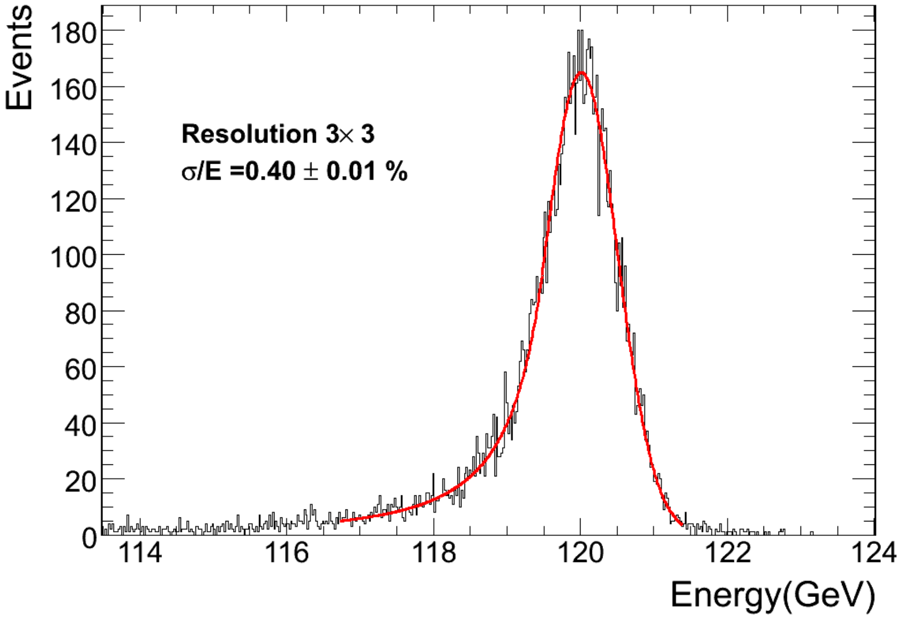

Figure 3.12: Amplitude in the 3×3 array around 25 different crystals for 120 GeV electrons reconstructed by optimized weights determined using 30 000 events. The resolution of $0.40 \pm 0.01\%$ is a marked improvement on that obtained with the standard weights.

of events affords the opportunity to optimise weights for every crystal precalibrated in the 2006 Test Beam Campaign.

3.7 Energy Resolution as a Function of Energy

Resolutions were determined for the same crystal arrays at various beam energies ranging from 20 GeV to 120 GeV. This enabled the resolution of the ECAL to be measured and parameterized. This parameterization is :

$$\left(\frac{\sigma}{E}\right)^2 = \left(\frac{S}{\sqrt{E}}\right)^2 + \left(\frac{N}{E}\right)^2 + C^2 \tag{3.2}$$

where S is the stochastic term, N the noise and C the constant term. The measurements and fitted function are shown in Figure 3.14.

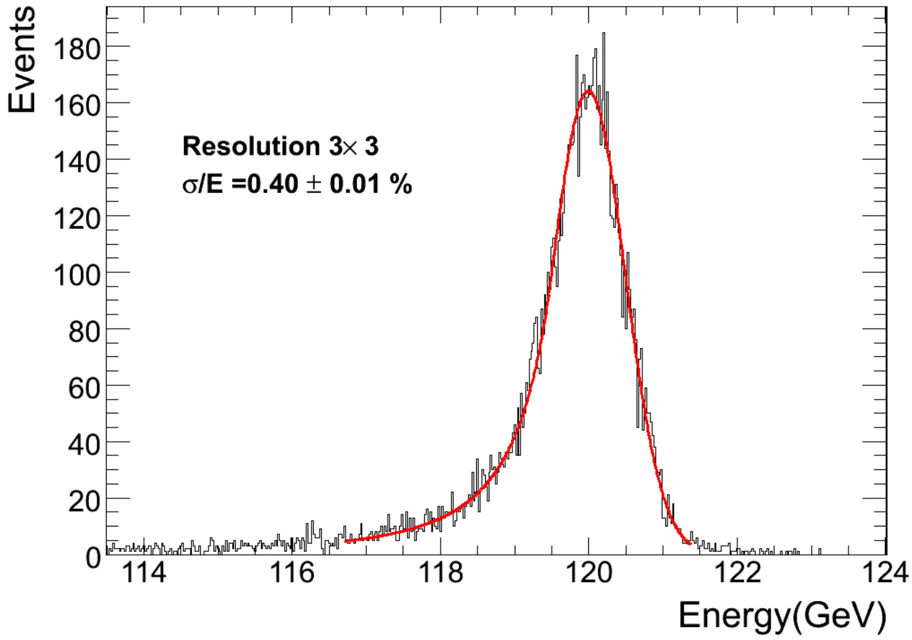

Figure 3.13: Amplitude in the 3 × 3 array around 25 different crystals for 120 GeV electrons, reconstructed by optimized weights derived using only 2000 events per crystal. The resolution is similar (within errors) to that obtained with 30 000 event weights.

This measured resolution agrees with the results of [39], which measured the energy resolution in a single array of 3 × 3 crystals. The measured resolution satisfies the requirements set for the calorimeter.

3.8 Synchronous Running

As described in Section 3.4.1, the impact of particles with the ECAL will be at fixed phase relative to the electronics clock during LHC operation. In the ECAL 2006 Test Beam Campaign, there was a period when the SPS provided bunches of protons separated by 25 ns, the nominal value of LHC pp running. This mode of operation provides an opportunity to assess the capabilities of both the ECAL at LHC and the optimized weights reproduction of this performance. As the test beam collides protons with a fixed target rather than colliding two bunches of protons, the phase variation of the 25 ns test beam running will be larger than that of the LHC. The phase between the particles and the TDC was measured for both synchronous and asynchronous running and is shown in Figures 3.15 and 3.16.

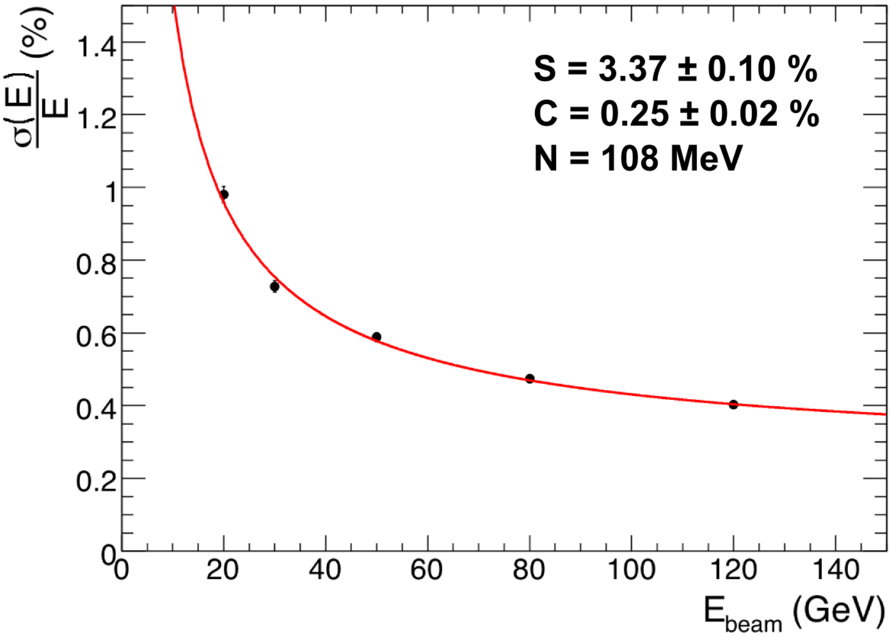

Figure 3.14: Energy resolution, $\sigma(E)$, as a function of energy, measured with optimized weights.

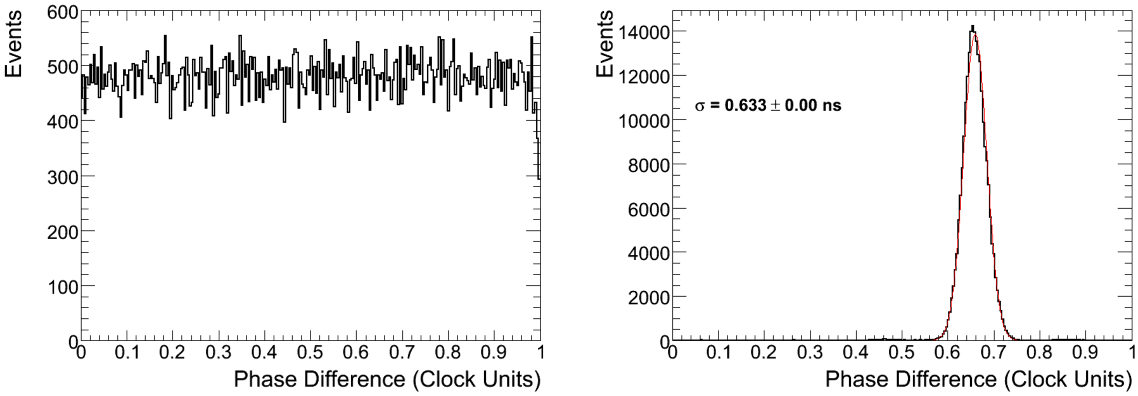

Figure 3.15: The phase between time of trigger and system clock for asynchronous running, as measured by the TDC.

Figure 3.16: The phase between time of trigger and system clock for 25 ns running, as measured by the TDC.

Figure 3.16 shows that the 25 ns run is much closer to being synchronous than the general test beam case. The finite TDC resolution limits the measurement, but only three (1 ns) phase bins are populated, with residual variation in phase difference of $\sigma = 0.633\,\mathrm{ns}$. The expected variation in CMS is $\sim 0.2\,\mathrm{ns}$.

As stated in Section 3.4.1, amplitude in CMS will be reconstructed using a single set of 3+5 weights, possible due to the small variation in phase difference between signals in the ECAL and sampling. The performance of such a scheme in the 25 ns running can be evaluated and compared to the performance measured with the optimised weights in asynchronous running. Sufficient rates of electrons with energies of 120 GeV were difficult to obtain in 25 ns running, so the following results are for 90 GeV.

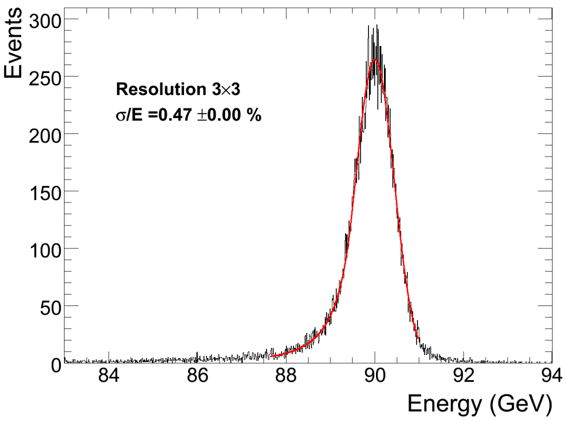

Figure 3.17: Amplitude in the 3×3 array around 25 different crystals for 90 GeV electrons in the 25 ns test beam running. Standard weights are used for reconstruction.

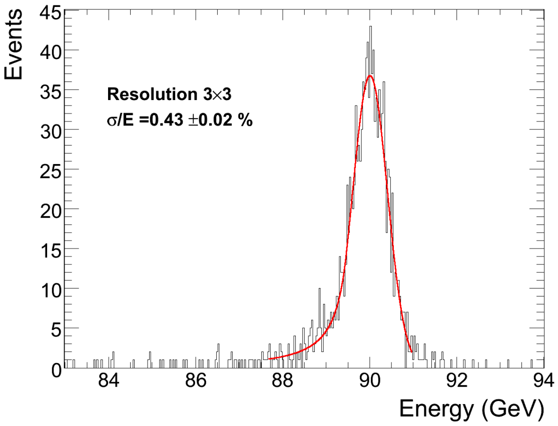

Figure 3.18: Amplitude in the 3×3 array around crystal 172.

Using the energy resolution function shown in Figure 3.14, the resolution for 90 GeV electrons is calculated as $0.43\% \pm 0.00\%$. The result in Figure 3.17 of 0.47% is thus worse than expected. The discrepancy probably comes mainly from the fact that the CMS-like conditions are not exactly reproduced, as noted above, since 3 TDC bins are populated and only 1 set of weights is used.

Another possible contribution is from intercalibration errors in the combined resolution result. The supermodule and channels used for the synchronous running test might be intercalibrated less well than those used for the optimized weights test. To investigate this, the energy resolution in individual 3x3 arrays was examined. The results of this test, described below, were inconclusive.

The mean resolution obtained was 0.44%, with a standard deviation of 0.03%. An example of a distribution in a single 3×3 array is shown in Figure 3.18. For comparison, the energy resolution obtained for the individual 3 × 3 arrays using the 120 GeV data used in Section 6 is 0.38%. This can be compared to the combined result of 0.40% using optimized weights, and 0.48% using standard weights. The results are tabulated in Table 3.1

Table 3.1: Comparison of 25 ns bunch structure results to results from standard test beam bunch structure, obtained using optimised weights.

90 GeV	
Synchonous (single set of weights)	0.47%
Asynchronous with optimised weights (estimated from Fig. 3.14)	0.43%
Synchronous, individual channel average	0.44%
120 GeV	
Asynchronous with optimized weights	0.40%
Asynchronous with optimized weights, individual channel average	0.38%
Asynchronous, standard weights	0.48%

3.9 Conclusions

As the arrival of particles at the H4 test beam was not synchronised with the ECAL clock, it was necessary to determine phase-dependent, channel specific weights for amplitude reconstruction in order to measure the intrinsic performance of the CMS ECAL. A new method of determining signal representations for channels with only a limited exposure to beam was developed and used to calculate optimised weights.

These optimised weights were used in several studies of the ECAL test beam data. In this analysis, optimised weights were used to reconstruct signals in order to assess the energy resolution of the CMS ECAL, with particular emphasis on combining results from many crystals.

The energy resolution was measured to be $0.40 \pm 0.01\%$ at 120 GeV over 25 crystals and for the parameterisation of resolution as a function of energy, the stochastic term was measured to be $3.37 \pm 0.10\% \sqrt{E(GeV)}$; the noise, 108 MeV; and the constant, 0.3%. This resolution, measured using a large number of crystals, meets the design goals set for the calorimeter.

4 Electron Reconstruction and Identification

"The electron is not as simple as it looks."
— Sir William Lawrence Bragg

The reconstruction and identification of electrons with the CMS detector is described and a novel method of charge measurement – complementary to the existing track-based measurement – is evaluated.

4.1 Electron Reconstruction

Electrons are reconstructed in the CMS detector using a combination of data from the inner tracking system and from the electromagnetic calorimeter. The inner tracker measures the trajectory (including the vertex position) of electrons in the magnetic field, allowing their charge and momentum to be determined. The electromagnetic calorimeter measures the electron energy and position in the ECAL.

The energy and momentum measurements are complementary – the fractional error of the track-based momentum measurement is proportional to p, while the calorimetric energy fractional error is proportional to $1/\sqrt{E}$. Thus the best estimate of the electron's energy is obtained from the combination of the tracker and calorimetric measurements. This is shown in Figures 4.1 and 4.2.

It is clear that using inner tracking information for electron reconstruction is beneficial. However, the presence of the tracker material between the vertex and the ECAL poses a particular challenge. The depth of material is shown as a function of η in Figure 4.3. As previously discussed (Chapter 2.2.3), electrons predominantly lose energy

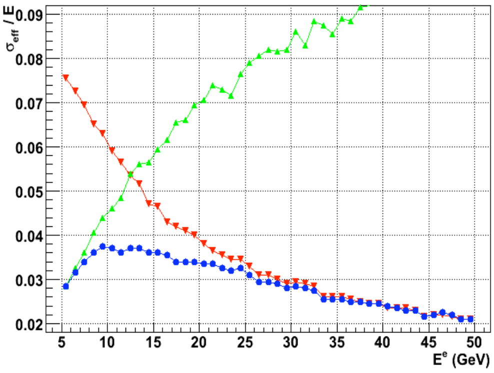

Figure 4.1: Resolutions of barrel electron energy measurement by tracker, ECAL and the combination of the two, versus electron energy.

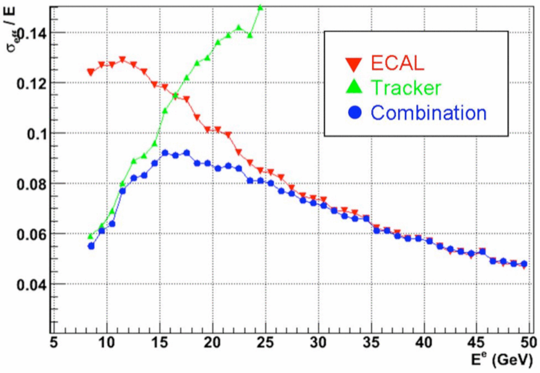

Figure 4.2: Resolutions of endcap electron energy measurement by tracker, ECAL and the combination of the two, versus electron energy.

through the radiative process of bremsstrahlung emission, with the energy remaining after 1 X_0 given by (2.7). The energy loss is substantial when integrated over the depth of the tracker, as shown in Figure 4.4.

The emitted bremsstrahlung photons do not bend in the magnetic field while the electron does : resulting in the energy of the electron being spread in the azimuthal (ϕ) direction. In order for the ECAL to measure the initial energy of the electron, special 'clustering' reconstruction algorithms must be used that incorporate this spread of energy.

The radiative processes also necessitate the use of dedicated electron track reconstruction algorithms. Electrons will lose a significant fraction of their energy in the tracker material and so the parameters of the trajectory will change as the electron traverses the tracker. Special energy-loss modelling is therefore required in the reconstruction algorithms. Furthermore, the radiated photons have a significant probability of pair-converting into electrons which will create their own 'hits' in the tracker, hindering track-finding and so impairing the momentum and charge measurement. Optimisation of the tracking algorithms minimises this problem and a dedicated method for determining electron charge has been developed.

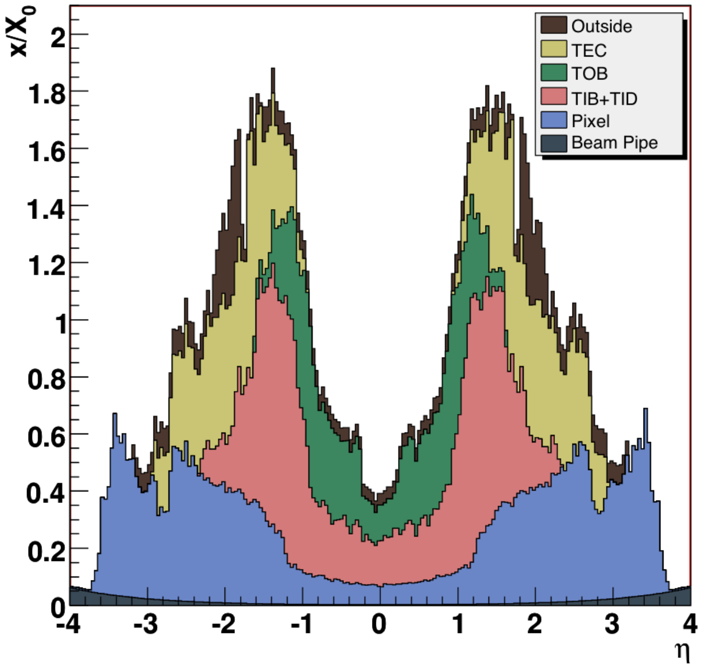

Figure 4.3: Tracker material budget in units of radiation length, showing the contribution of different detector components in front of the ECAL. The peak material depth is at the tracker barrel - endcap transition.

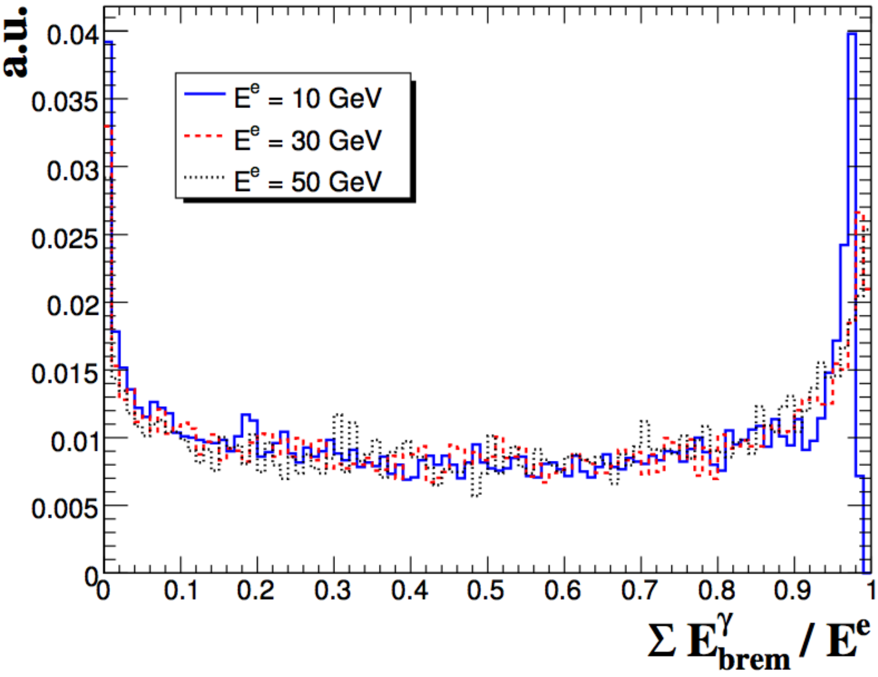

Figure 4.4: Fraction of initial electron energy lost through bremsstrahlung for 10, 30 and 50 GeV electrons [41].

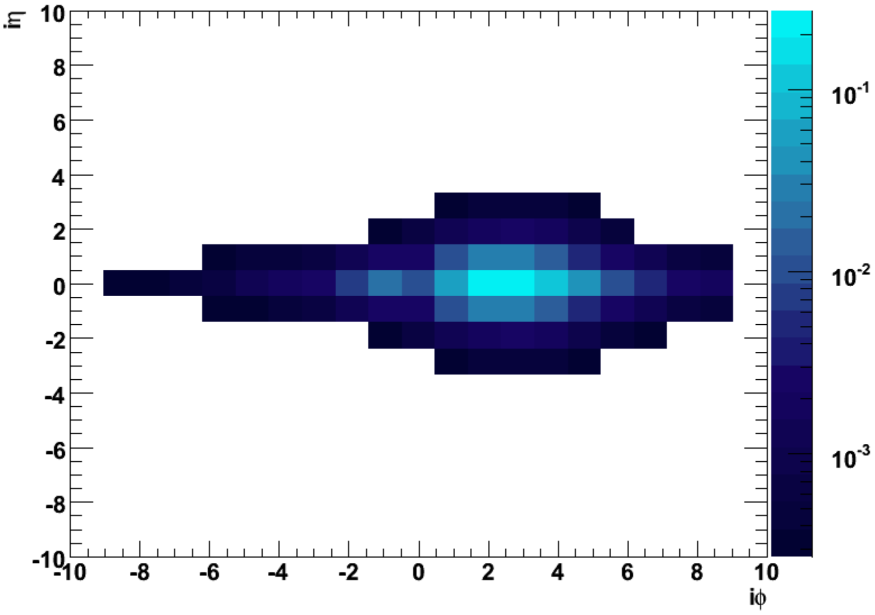

Figure 4.5: Map of average electron energy deposition in the ECAL barrel, from CMSSW simulation. The coordinates iη and iϕ are the integer number of crystals along the η and ϕ axes. The lighter tones represent higher energy deposits, which are shown as fractions of the reconstructed supercluster energy.

4.1.1 Energy Measurement

Electromagnetic showers are narrow – in the test beam, 25 crystals arranged in a 5×5 window contained 97% of the energy of electrons which struck the centre of the middle crystal. The energy of the incident electrons could therefore be reconstructed by summing the energies measured in these 25 crystals. In CMS running, such simple reconstruction will only be used for photons that remain unconverted in the tracker material[1].

To reconstruct the energy of an electron at the vertex, all the energy that was radiated must be dynamically 'clustered' : the crystals that have had energy deposited by an individual electromagnetic particle must be grouped. Two independent clustering algorithms are necessary due to the differing geometries of the ECAL barrel and endcap, though both define 'superclusters' that reflect the narrow spread of energy in pseudorapidity and the wide spread in azimuthal angle (Figure 4.5). The extent of the spread in the η direction is essentially constant, while the ϕ extent varies.

---

[1] Electrons which have not lost significant energy through bremsstrahlung could also be reconstructed using a 5×5 array

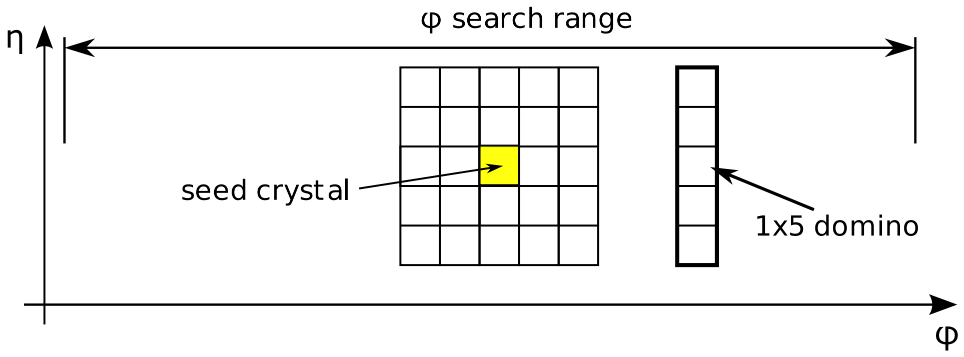

Figure 4.6: Illustration of the Hybrid algorithm, which clusters the energy of the electrons, which is well-contained in η, but spread in ϕ.

The Hybrid algorithm is used to measure energy in the barrel [42]. It had been noted that dynamic clustering algorithms degraded energy resolution compared to fixed arrays such as 5×5 clusters [42]. The Hybrid algorithm benefits from the $\eta - \phi$ geometry of the barrel by building clusters with fixed η width strips of five crystals, with only the ϕ extent of the cluster determined dynamically. The algorithm – illustrated in Figure 4.6 – operates as follows :

1. The barrel crystals are sorted in a list by descending order of E_T.
2. If the highest energy crystal in the list has $E_T > E_T^{seed}$ this crystal 'seeds' a new cluster. Otherwise the clustering algorithm ends.
3. A five crystal strip running in the η direction (a "domino") and centred on the seed crystal is constructed. If this domino has energy $E_{domino} > E_{thresh}$, it is added to the cluster.
4. For each crystal at the same η as the seed crystal and at ϕ within some predefined range, repeat 3.
5. After this process, group the dominoes into local maxima, or 'basic clusters'. Those basic clusters with $E < E_{clus}$ are not included in the supercluster.
6. The crystals incorporated into the supercluster are removed from the ordered list of 1.
7. The process repeats from 2 until all crystals with energy deposits have been considered.

The multi5×5 algorithm [43] is used in the endcap, where the crystals are not arranged in an $\eta - \phi$ geometry and thus the hybrid algorithm may not be applied.

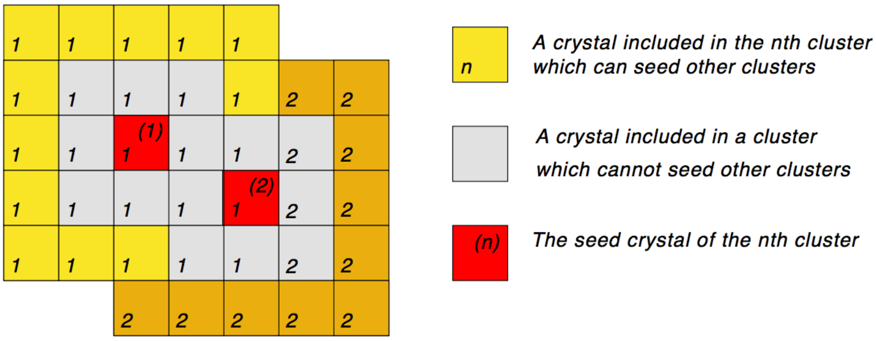
1 1 1 1 1
1 1 1 1 1 2 2
1 1 (1) 1 1 1 2 2
1 1 1 1 (2) 1 2 2
1 1 1 1 1 2 2
2 2 2 2 2
n
A crystal included in the nth cluster which can seed other clusters
A crystal included in a cluster which cannot seed other clusters
(n)
The seed crystal of the nth cluster

Figure 4.7: An illustrative example of the multi5 × 5 algorithm, showing the result of step 3.

Multi5 × 5 builds superclusters from multiple fixed 5 × 5 arrays rather than using fully dynamic clustering.

1. The endcap crystals are sorted in a list by descending order of E_T.
2. If the highest energy crystal has $E_T > E_T^{seed}$, this crystal 'seeds' a new cluster. Otherwise the clustering algorithm ends.
3. The energy of this seed crystal is compared to the four adjacent crystals. If the seed is highest, it is a local maximum and a 5 × 5 array is constructed from the unclustered crystals about the seed.
4. The outer 16 crystals of the 5 × 5 are each considered to seed another 5 × 5 array, repeating 3. Thus, overlapping 5 × 5 arrays may be formed, although each crystal is considered part of only one cluster. (As illustrated in Figure 4.7.)
5. The crystals incorporated into the basic cluster are removed from the list of 1.
6. This process continues until all energy deposits have been clustered.
7. The resulting list of basic clusters is sorted by E_T. Additional clusters are sought in an $\eta - \phi$ window around the highest remaining E_T cluster. All clusters found within the window are then grouped into a supercluster and removed from the list of clusters.
8. The superclustering continues until all clusters are considered.

The ECAL endcap is augmented by the preshower detector, which absorbs some of the energy of the incoming electrons before they interact with the crystals. To include this energy, interpolations between the primary vertex and the ECAL superclusters are made. Any energy deposits found within a window around the intersection of these interpolations and the preshower are included in the corresponding supercluster energy.

The energy of the electron can be estimated by summing the energy deposits in the clustered crystals. However, this 'raw' supercluster energy must be corrected for a number of effects in order to achieve an accurate measurement. These corrections, F are applied as multiplicative factors :

$$E = F \sum_i G c_i A_i \tag{4.1}$$

where E is the corrected energy and $\sum_i G c_i A_i$ is the raw energy of the cluster.

Corrections should be made for the following effects :

- The stepped front face of the ECAL barrel leads to lateral shower leakage. This is η dependent for the step depth increases with η : exposing more of the sides of the crystals and allowing more lateral leakage.
- Bremsstrahlung radiation leads to the energy of the electron being smeared and spread between several showers. The ECAL will have a different response to these showers, dependent on the fraction of the energy lost.

Further corrections for the following effects have been studied, but are not yet used :

- The impact position of electrons with respect to the cluster boundary causes a 'local containment variation' – this is the variation in the fraction of the energy of an electromagnetic shower contained by the cluster.
- Electrons impinging near the inter-module and inter-supermodule gaps see an effective reduction in the depth of the calorimeter, leading to leakage from the rear of the crystals and an impaired energy measurement.
- Non-multiplicative corrections are made to the cluster energy sum to account for dead channels – those which have no response to particles – and saturated channels – those where the apparent energy deposited in the crystal exceeds the dynamic range of the channel. These use measurements from the surrounding crystals and the well-known properties of showers to replace the incorrect measurement.

4.1.2 Track Finding

Electron track finding is seeded using the supercluster position measurement, which uses the distribution of energy within the showers to determine the position of shower maximum. The position of each cluster is calculated as :

$$x = \frac{\sum_i x_i W_i}{\sum_i W_i} \tag{4.2}$$

where x_i is the position of crystal i. Due to the quasi-pointing of the crystal axis towards the nominal interaction vertex, x_i depends on the depth of the shower. W_i is the weight given to crystal i :

$$W_i = W_0 + \log\left(\frac{E_i}{\sum_j E_j}\right) \tag{4.3}$$

W_0 controls the minimum energy fraction that crystals must have in order to contribute to the position measurement.

The supercluster position is the energy-weighted mean of the positions of its constituent clusters. These clusters should measure all the energy radiated by the electron and so this position corresponds to that of a non-radiating electron.

The supercluster energy and position can therefore be used to propagate a helix backwards to the vertex in order to search for tracks. This is done for both charge hypotheses. Reconstructed tracker hits ("hits") are deposits of ionisation energy from charged particles that are detected and read out for use in track finding. Hits compatible with each supercluster-derived helix are sought in the pixel detector and inner layers of the silicon strip tracker, as illustrated in Figure 4.8.

The first and second pixel layers are searched for a compatible hit in a wide window about the interpolated helix. If a compatible hit is found, this is used along with the supercluster position and the beamspot to form an improved pair of trajectories for the two charge hypotheses. This trajectory is propagated through the following pixel layers in turn, where a much narrower window is used to search for a second compatible hit. If a second hit is not found in the pixel endcap disks, the first layer of the tracker inner disk is searched in order to maintain tracking efficiency at high η.

If a second compatible hit is found, the trajectory is once again refined and used to seed the full tracking process. Using the supercluster to seed electron track finding greatly reduces the combinatoric complexity of the problem, leading to much faster electron reconstruction.

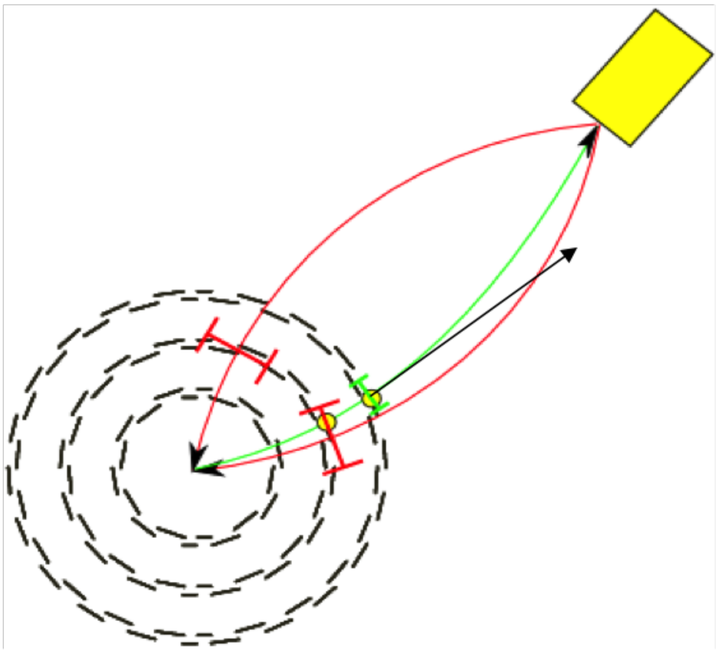

Figure 4.8: Illustration of supercluster driven seeding of electron track finding. [44]

Offline electron reconstruction uses the Gaussian Sum Filter tracking algorithm [45], which is a modification of the standard Kalman Filter (KF) [46] algorithm used for tracking in CMS. The principal difference is that to accommodate the non-Gaussian scattering of the electrons when extrapolating through the tracker layers, the measurement uncertainties and estimated parameters are modelled using a sum of several Gaussians. Using multiple component Gaussians allows a more accurate representation of both the core and tail of the relevant distributions than the single Gaussians used in the Kalman filter. In particular, use is made of an approximation of the Bethe-Heitler model of electron bremsstrahlung energy loss [47], built using a sum of Gaussians.

Figure 4.9 shows that the GSF tracking algorithm with Bethe-Heitler energy loss finds more hits along tracks than the standard CMS KF. Moreover, the peak at 13 hits per track implies that most electron trajectories are followed from the inner to the outer layers of the tracker. This allows a good estimation of the trajectory of the electron at the ECAL surface, in addition to at the vertex. Using this information, comparisons can be made between tracker and calorimeter data to classify and identify electrons. It is also possible to estimate the fraction of the electron's energy lost to bremsstrahlung in the material of the tracker :

$$f_{brem} = \frac{p_{in} - p_{out}}{p_{in}} \tag{4.4}$$

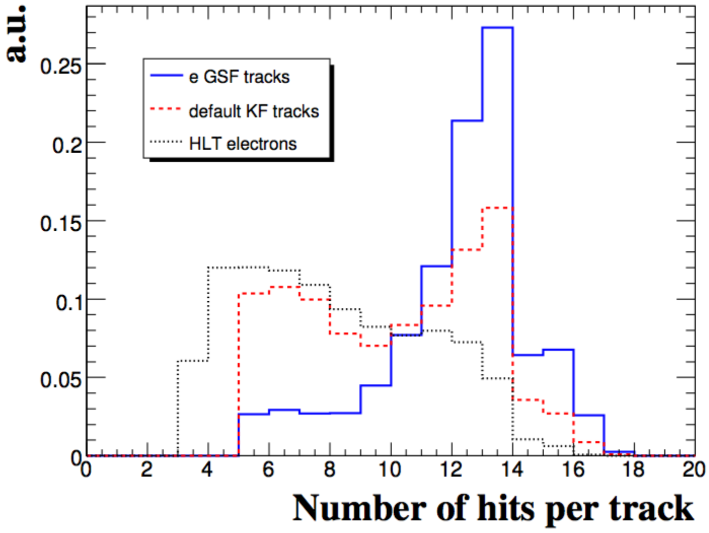

Figure 4.9: Number of hits found per track for Kalman Filter, Gaussian Sum Filter and HLT-Kalman Filter tracks.[41]

where p_{in} is the momentum estimate at the vertex and p_{out} the estimate at the last hit.

4.1.3 Supercluster-Track Combination

The reconstructed electron object used in this thesis is the combination of the supercluster and the supercluster-seeded track. Track seeding is only done if the supercluster $E_T > 4\,\mathrm{GeV}$ and the ratio of hadronic to electromagnetic energy, $H/E < 0.1$. The supercluster-track combination is promoted to a reconstructed electron object if they satisfy loose geometrical matching criteria : $\Delta\eta_{\mathrm{in}} < 0.02$ and $\Delta\phi_{\mathrm{in}} < 0.1$. These criteria are explained in Section 4.3.

The electron energy can be estimated by the combination of the ECAL and tracker measurements, weighted by their respective errors.

4.2 Electron Charge Determination

The electromagnetic charge of particles is determined by measuring the curvature in ϕ induced by the magnetic field. Measurement of this curvature for electrons is impaired by the emission of bremsstrahlung photons that can convert into an electron-positron pair, creating additional hits in the tracker. These additional hits may cause problems

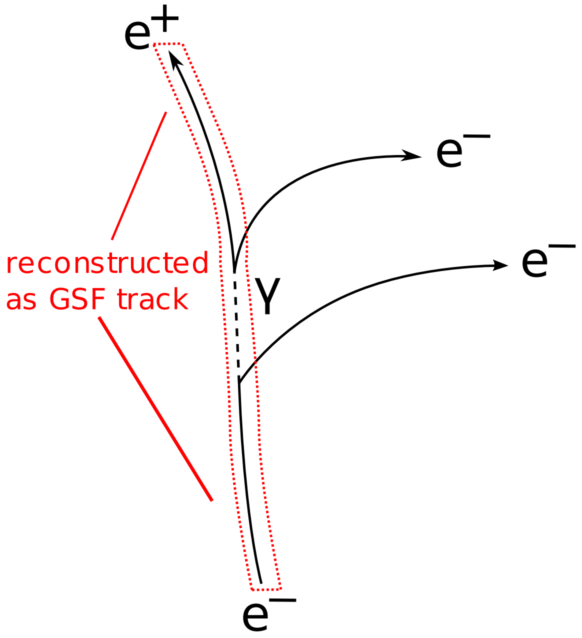

Figure 4.10: Illustration of electron charge mis-identification by the GSF tracking algorithm.

in the pattern recognition : they can be incorporated into the track, causing problems in the fitting; or the track finding can begin following one of the conversion legs rather than continuing to track the original electron. This is illustrated in Figure 4.10.

An alternative method of charge determination is examined here, which is unaffected by the tracker problems and is thus complementary to the GSF track charge measurement. In this method, the direction of curvature of the electron's trajectory is determined by comparing the ϕ position of the electron's supercluster with the ϕ direction of its pixel hits from the vertex (Figure 4.11). As most material lies after the pixel detector, the electrons have only a very low probability of emitting significant radiation before or during this first ϕ measurement. The position measured by the supercluster is the point at which a non-radiating electron would impinge on the ECAL. The difference between the pixel ϕ and the supercluster ϕ is denoted as $\Delta\phi$. If $\Delta\phi > 0$, the particle is identified as a positron; if $\Delta\phi < 0$, an electron. The expected $\Delta\phi$ difference can be calculated using (2.5) :

$$\Delta\phi = q \sin^{-1}\left(\frac{0.15 B R_E}{p_T}\right) \tag{4.5}$$

where q is the charge of the particle; B, the magnetic field strength (in T); and R_E, the radial distance of the supercluster from the vertex (in m).

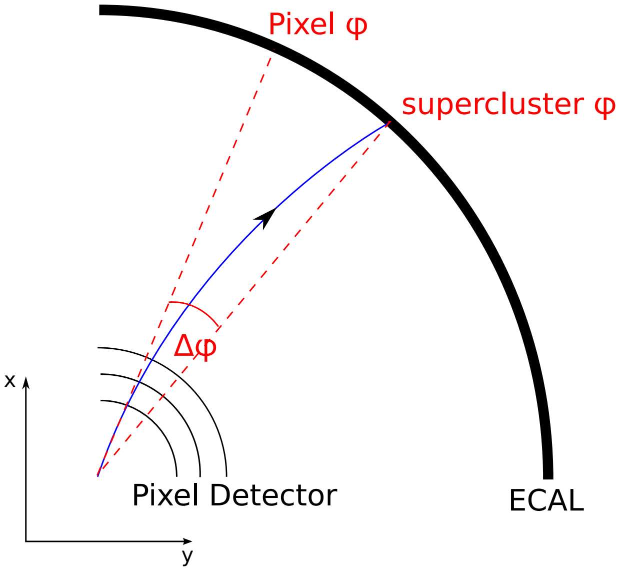

Figure 4.11: Illustration of $\Delta\phi$ between the pixel direction and the supercluster

The distribution of $\Delta\phi$ is shown in Figure 4.12 for both electrons and positrons with $p_T = 35\,\mathrm{GeV}$. The form of the distribution is described by (4.5). The peaks at $\Delta\phi = \pm 0.022$ are electrons and positrons that impact the ECAL barrel, which is at a fixed radius of $R_E = 1.36\,\mathrm{m}$. The bulges evident at lower $|\Delta\phi|$ are electrons and positrons that impinge on the ECAL endcaps. The radial position of these superclusters is not fixed, ranging within $55\,\mathrm{cm} < R_E < 140\mathrm{cm}$ and so the $\Delta\phi$ varies too.

The small proportion of positrons with $\Delta\phi < 0$ and electrons with $\Delta\phi > 0$ are those that would have their charge mis-identified by this method. Approximately 50% of errors are caused by poor supercluster ϕ measurement and 50% by the pixel ϕ measurement. It can be seen in Figure 4.13 that the $\Delta\phi$(pixel, SC) charge mis-identification fraction has a sharp peak at $|\eta| \approx 1.479$. This is likely due to the EB-EE transition causing an incorrect supercluster position determination. There is also a large increase as $|\eta| \rightarrow 2.5$, probably caused by the worsening supercluster ϕ resolution and the use of TID seeds. The increase visible from $|\eta| > 1.2$ is probably a result of the increased pixel material budget in this region, visible in Figure 4.3.

The rate of mis-identification is shown in Table 4.1, along with those of the GSF track charge determination. No demands are made of the electrons beyond those of reconstruction. Applying an electron selection would reduce the charge mis-identification

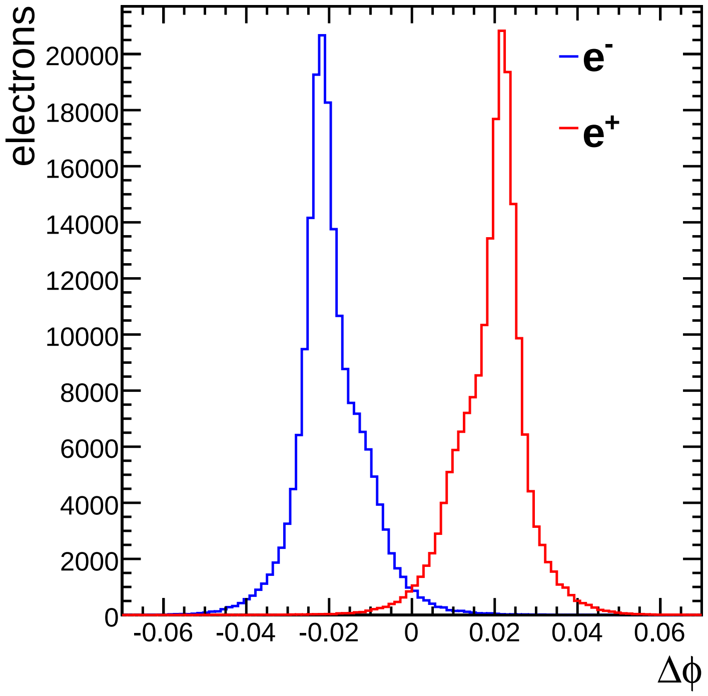

Figure 4.12: $\Delta\phi$ of electrons and positrons with $p_T = 35\,\mathrm{GeV}$.

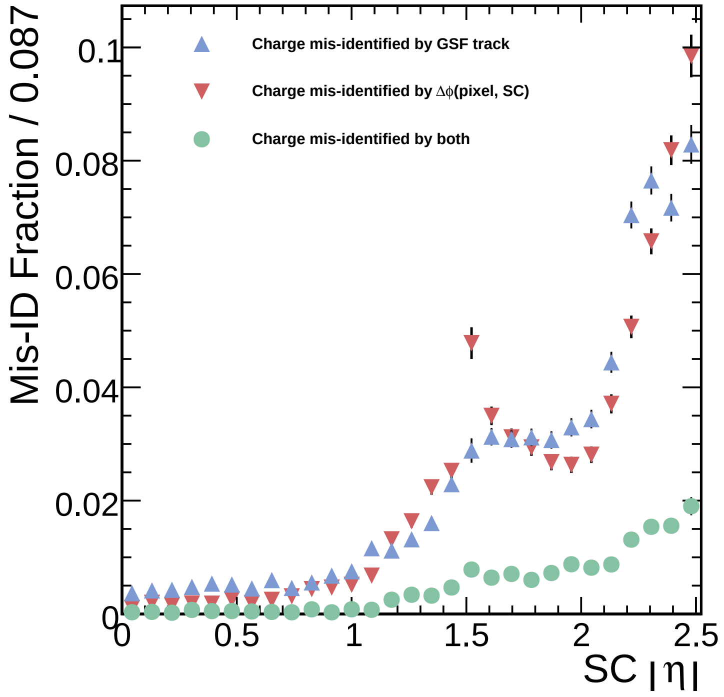

Figure 4.13: Mis-identification fraction for the various charge determination methods, vs $|\eta|$. For $E_T = 35\,\mathrm{GeV}$ electrons.

fractions, but even electrons that meet tight identification criteria have significant fractions. These fractions are those found in CMSSW 2.1.12. The fractions will vary between software versions if the tracker material description used in the simulation or the reconstruction algorithms are changed. The small fraction of electrons that have their charge mis-identified by both the $\Delta\phi$(pixel, SC) and GSF track, relative to the individual mis-identification rates, demonstrate that the two methods are complementary. There is potential to reduce the charge mis-identification for electrons by a factor of four if a suitable method to combine the two measurement techniques were found.

	Charge Mis-Identification Fraction (%)	
Charge Determination Method	$p_T = 10\,\mathrm{GeV}$	$p_T = 35\,\mathrm{GeV}$
$\Delta\phi$(pixel, SC)	0.598 ± 0.057	2.14 ± 0.02
GSF Track	0.872 ± 0.069	2.30 ± 0.02
$\Delta\phi$(pixel, SC) AND GSF track	0.241 ± 0.036	0.46 ± 0.01
$\Delta\phi$(pixel, SC) OR GSF track	0.987 ± 0.074	3.52 ± 0.03

Table 4.1: Mis-identification rates for different methods of electron charge determination.

A method of matching the GSF track of the electron to the corresponding Kalman Filter track on the basis of shared hits has been implemented in CMSSW 3. The efficiency of matching is 97.3%. The KF tracking algorithm models only ionisation (Bethe-Bloch) energy loss and has tighter search windows and χ^2 criteria. As a result, in the event of significant radiation – radiation likely to cause charge determination problems – the track finding terminates. Although the charge measurement accuracy will be reduced by the shorter track, it is not likely to suffer the problem of the GSF track charge determination and therefore provides a third complementary measurement. It has been shown [48] that this additional electron charge measurement can be used to reduce the mis-identication fraction by a similar amount to the $\Delta\phi$(pixel, SC) method.

This third complementary technique had recently been combined [49] with the GSF and $\Delta\phi$(pixel, SC) charge measurements to form a voting logic system, in which the majority charge result is used. This simple and robust method reduces the charge mis-identification rate by a factor of ~ 2 for electrons, with no loss of efficiency.

4.3 Electron Identification

The identifying trait of an electron – the combination of both track and electromagnetic shower – in the CMS detector is distinctive and it is unlikely for another particle to emulate this signature. However, QCD di-jet events have a cross-section which is orders of magnitude larger than $\mathrm{W}^{\pm} \rightarrow \mathrm{e}^{\pm}\,\nu_{\mathrm{e}}$ and $\mathrm{Z} \rightarrow \mathrm{e}^{+}\,\mathrm{e}^{-}$ events and the sheer number of potential fake electrons can lead to a significant fake rate. This potential is compounded by the bremsstrahlung from real electrons making them appear more jet-like.

The fake rate can however be substantially reduced by demanding additional criteria of the track, electromagnetic shower and the matching between the two. Several powerful variables have been identified and used in the analyses that follow in Chapters 6 and 7. These variables have been studied in simulated data and found to perform well where the simulated detector has been misaligned and miscalibrated to approximately the level expected in the early data-taking period [50]. This is illustrated in Figures 4.14 – 4.17.

The $\sigma_{\eta\eta}$ variable is a measure of the η width of the electromagnetic shower within a 5×5 array of crystals. Due to the compact nature of electromagnetic showers, $\sigma_{\eta\eta}$ is smaller for electrons and photons than for hadronic particles. It is defined as :

$$\sigma_{\eta\eta}^{2} = \frac{\sum_{i}^{5\times 5} w_i (\eta_i - \bar{\eta}_{5\times 5})^2}{\sum_{i}^{5\times 5} w_i} \tag{4.6}$$

$\bar{\eta}_{5\times 5}$ is the energy weighted mean of the crystals' η positions, which are denoted η_i. The energy weight, w_i, is defined in (4.3). The $\sigma_{i\eta i\eta}$ variable is a variation of $\sigma_{\eta\eta}$ that uses the relative $i\eta$ coordinate, defined in terms of number of crystals, rather than the absolute η coordinate. This makes $\sigma_{i\eta i\eta}$ insensitive to the gaps between ECAL modules which enlarge the $\sigma_{\eta\eta}$ due to the increased displacement between the crystals of the 5×5.

Low hadronic energy behind the supercluster is demanded because electromagnetic showers are well-contained longitudinally. The criteria is expressed as the ratio of hadronic energy to the supercluster energy because some energy from electrons may leak into the HCAL through cracks in the ECAL. The hadronic energy is the sum of the HCAL tower energies within $\Delta R < 0.1$ of the supercluster position.

Genuine electrons should demonstrate a good geometric matching between the supercluster position and the point at which the electron trajectory (determined at the vertex) is extrapolated to impinge on the ECAL. $\Delta\eta_{\mathrm{in}}$ and $\Delta\phi_{\mathrm{in}}$ are the differences between these points in the η and ϕ directions respectively.

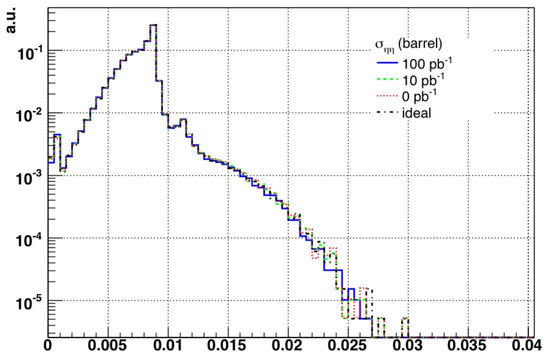

Figure 4.14: $\sigma_{\eta\eta}$ of electrons in EB, for four different levels of calibration and alignment knowledge [50].

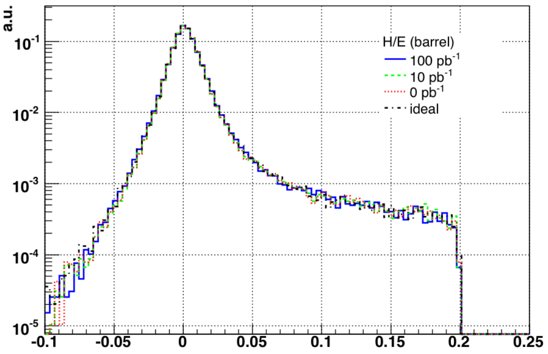

Figure 4.15: $\frac{H}{E}$ of electrons[2] in EB, for four different levels of calibration and alignment knowledge [50].

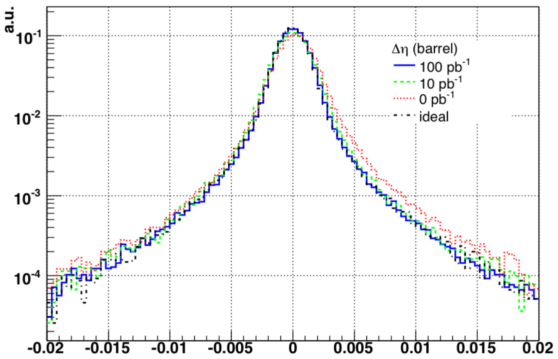

Figure 4.16: $\Delta\eta_{\text{in}}$ of electrons in EB, for four different levels of calibration and alignment knowledge [50].

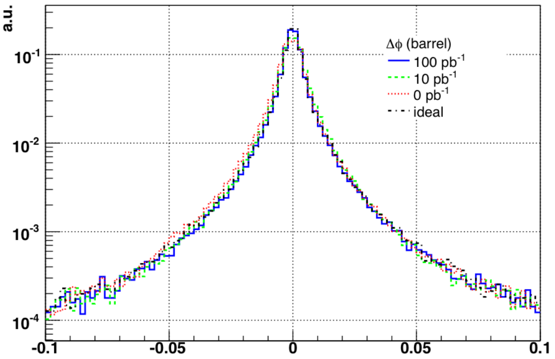

Figure 4.17: $\Delta\phi_{\text{in}}$ of electrons in EB, for four different levels of calibration and alignment knowledge[50].

4.4 Electron Isolation

Electrons arising from the decay of electroweak bosons are isolated : there are few, if any, particles emitted in a similar direction. Hadronic jets, in contrast, are composites of numerous final state hadrons and thus are inherently non-isolated. Hadronic jet backgrounds can therefore be reduced by imposing isolation demands in the tracker, ECAL and HCAL. To first order, the efficiency and rejection power of these isolation cuts should be independent of any electron identification selection made.

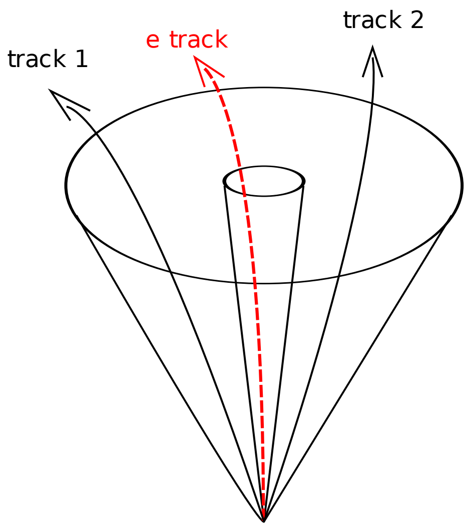

Figure 4.18: Illustration of track isolation algorithm. The p_T of the electron track is excluded by the inner cone veto. The isolation sum is therefore $p_T^{\text{track 1}} + p_T^{\text{track 2}}$, assuming they are both greater than 1 GeV.

The efficacy of isolation may be impaired by additional pile-up interactions in the bunch crossing. The isolation thresholds used in this work were all optimised using events simulated by CMSSW without pile-up and so may suffer reduced efficiency in real data-taking. Previous results [51] however, have demonstrated that isolation is an effective selection tool even at instantaneous luminosities much greater than those anticipated for the early data-taking period.

Isolation in the tracker involves summing the p_T of all tracks with $p_T > 1\,\text{GeV}$ within an annular region $0.015 < \Delta R < 0.3$. It should be checked that the origin of the tracks is compatible with the electron's, however in the results shown this was not done. The tracks used are the general collection of Kalman Filter tracks, seeded by pixel hits, that are found in the event. This collection will likely include a track for the electron : the inner cone is used to prevent this electron track entering the isolation cone and 'self-vetoing' itself. Figure 4.18 is an illustration of the track isolation calculation.

The calculation of isolation in the ECAL is complicated by the spread of the electron's energy in ϕ. The inclusion of electron energy in the isolation sum is avoided by defining the "Jurassic" region. The E_T of crystals within a cone of $\Delta R < 0.4$ are included only if they are outside this region, which is defined as the union of a narrow cone around the supercluster position with a strip extended in ϕ. This veto region is the red shaded

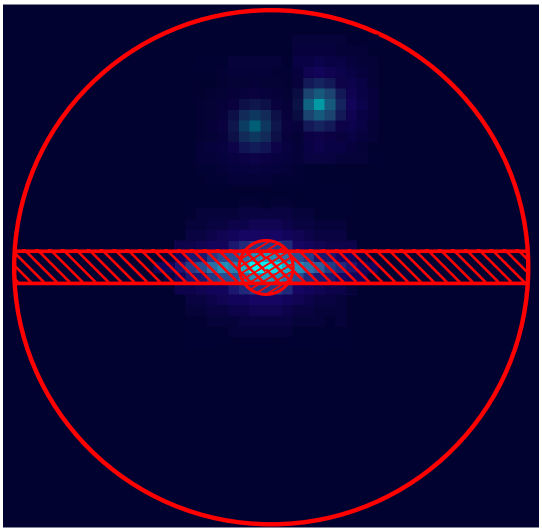

Figure 4.19: Illustration of the ECAL isolation algorithm. The Jurassic veto region is the red shaded area which excludes the electron energy from the ECAL isolation sum. Only energy outside this region and within $\Delta R < 0.4$ enters the sum (e.g. the two deposits shown in the upper half of the cone).

area in Figure 4.19. In the barrel, the inner cone has a radius $\Delta R = 0.045$ and the strip has an η width $\Delta\eta = 0.04$ and extends over the full diameter of the outer cone. In the endcap, the strip dimensions are the same, but the inner veto cone has a larger radius, $\Delta R = 0.07$. To be included in the isolation sum, rechits must have $E > 80\,\mathrm{MeV}$ in the barrel and $E > 300\,\mathrm{MeV}$ in the endcap.

HCAL isolation in the CMS software version used in this work is defined simply as the sum of all HCAL tower energies within a cone of $\Delta R < 0.4$ around the supercluster position. No veto cone is defined, as little of the electron's energy is expected to be deposited in the HCAL. This definition leaves the HCAL isolation correlated with the H/E identification criteria. An improved definition of both cuts, used in later versions of the software, disentangles them.

Although there is some redundancy in performing isolation calculations in each of the three subdetectors, each isolation does provide complementary selection power. The track isolation rejects jets with charged particle components, even if the energy of those components is too low for the HCAL to measure reliably; ECAL isolation rejects jets with neutral components like π^0 mesons, which decay electromagnetically; and the HCAL isolation rejects neutral hadrons, which do not interact with the ECAL.

4.5 Electron Trigger

The reconstruction of electrons for the High Level Trigger (HLT) is performed using similar algorithms to the offline reconstruction, with some modifications to decrease the processing time needed. Including Level-1, the trigger process or "path" is separated into four steps, each more complex and computationally intensive than the last. The trigger path is terminated if no promising candidates for the next step are found. This is necessary if the average HLT time per event is to be kept below 40 ms.

The High Level Trigger electron paths all begin only if the required Level-1 electromagnetic trigger accepts the event. The first step, Level-2, constructs superclusters using the full resolution calorimeter data in the regions of interest defined by the Level-1 trigger, rather than searching the whole ECAL for superclusters to evaluate. If these superclusters match the Level-1 candidate in η and ϕ, an E_T requirement (higher than the Level-1) is placed on the supercluster.

After Level-2 has been satisfied, Level-2.5 introduces track information from the pixel detector and searches for pixel hits compatible with the supercluster, as described in Section 4.1.2. To increase rejection power and so reduce the background acceptance rate, the HLT pixel hit search window parameters used are quite restrictive. Looser parameters are used in the offline reconstruction in order to maintain high efficiency when reconstructing electrons not involved in the trigger decision. The window parameters are summarised in Table 4.2

Pixel Hit Search Parameters	First Pixel Hit Window		Second Pixel Hit Window	
	$\Delta\phi$ (mrad)	Δz(cm)	$\Delta\phi$ (mrad)	Δz (cm)
Offline	$[-125, +75]$	± 15	± 2	± 0.07
HLT Ideal	$[-25, +15]$	± 15	± 1	± 0.05
HLT Start-up	$[-35, +25]$	± 15	± 5	± 0.05
HLT Large	$[-45, +30]$	± 15	± 10	± 0.2

Table 4.2: Electron pixel-seed search window parameters, for offline and HLT reconstruction.

If matching pixel-seeds are found, these are used in Level-3 to seed track-finding as described earlier. The Gaussian Sum Filter tracking algorithm is too computationally intensive for use in the HLT, so the the faster Kalman Filter tracking algorithm is used in order to meet the timing requirements. A stringent χ^2 demand is made when performing the trajectory building, so the tracks are effectively terminated when a significant radiation of energy takes place. This shorter track is then an accurate measure of the electron trajectory properties at the vertex.

If a suitable track is found, the electron tracks are loosely geometrically matched to the seed supercluster. If this match is successful, an HLT accept is given by this path and the event will be recorded. It is possible to impose additional criteria on the electron, for example the isolations and identification properties that have been discussed. However, in the early data-taking period in which a $\int Ldt = 10\,\mathrm{pb}^{-1}$ cross-section measurement will be made, the event rate is sufficiently low that these are unnecessary.

The conceptual design of the HLT can clearly be seen in this progression of stages - efficiency in terms of processing and data access is achieved by incrementally increasing the amount of information used, while expeditiously rejecting poor candidates.

5 Phenomenology of W and Z Production

This chapter builds on the discussion of W and Z bosons within the Standard Model from Chapter 1 to discuss the phenomenology of W and Z boson production at the LHC, focussing on those areas most relevent to the analysis presented in subsequent chapters.

5.1 Parton Distribution Functions

The Large Hadron Collider will principally collide protons, the most common kind of hadron. Hadrons are $\mathrm{SU}(3)_C$ singlet bound-states of quarks and gluons, which are collectively known as partons. Although bound by the strong force of QCD, partons are asymptotically free [52], [9] and so for sufficiently energetic interactions, hadronic scattering can be treated as the incoherent sum of partonic scattering :

$$\sigma = \int dx_1 dx_2 f_1^{(P_1)}(x_1, Q^2) f_2^{(P_2)}(x_2, Q^2) \hat{\sigma}(\hat{s}) \tag{5.1}$$

where x_1 and x_2 are fractions of the proton momenta which are carried by the interacting partons, P_1 and P_2 respectively. Knowledge of the composition of the proton in terms of these partons is encoded as parton distribution functions (PDFs), $f_i^{(P_j)}(x, Q^2)$. Q is the characteristic momentum scale of the hard scattering : for example in the Drell-Yan process, $Q = m_{l^+l^-}$.

$$\hat{s} = x_1 x_2 s \tag{5.2}$$

is the centre-of-mass energy of the colliding partons and $\hat{\sigma}(\hat{s})$ is the parton-level cross-section. The expression (5.1) holds because of the property of factorisation, which

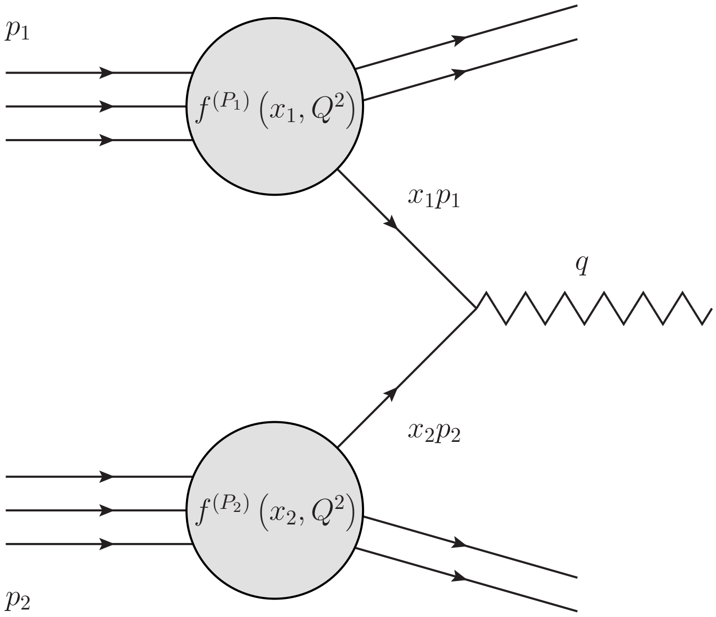

Figure 5.1: Deep inelastic scattering between two protons can be considered as scattering between the constituent partons.

enables the separation of the high-energy, short-range parton scattering that can be calculated with perturbative QCD from the long-range, low-energy, non-perturbative physics that describes the hadrons themselves. This low-energy part is subsumed into the PDFs.

The parton distribution functions $f_i^{(P_j)}(x,Q^2)$ express the number density of partons of type i within the hadron, which have a fraction of the momentum of the hadron between x and $x+dx$. The 'naïve' parton content of the proton is uud. These quarks are known as valence quarks. However, QCD predicts that these quarks can radiate gluons and these in turn can split into quark-antiquark pairs. Quarks (and antiquarks) produced in this manner are known as sea quarks. These excitations of $q\bar{q}$ depend on Q^2, for there is a higher possibility of radiation with higher Q^2.

With random fluctuations of the sea, the number of partons of type i in the hadron, n_i is not constant :

$$\int_0^1 f_i(x)dx = n_i \tag{5.3}$$

However, for the proton the difference between the number of u and $\overline{\mathrm{u}}$ must be :

$$\int_0^1 dx\,\big[\mathrm{u}\big(x,Q^2\big)-\overline{\mathrm{u}}\big(x,Q^2\big)\big]=2 \tag{5.4}$$

in order for the hadron to be considered a proton. Likewise for d and $\overline{\mathrm{d}}$:

$$\int_0^1 dx\,\big[\mathrm{d}\big(x,Q^2\big)-\overline{\mathrm{d}}\big(x,Q^2\big)\big]=1 \tag{5.5}$$

The parton distribution functions are not calculable with perturbative QCD or any other current technique. However, they are universal so can be obtained from global fits to data from many experiments. Such fits are provided by several groups, such as MRSW [53] or CTEQ [54]. The evolution of the PDFs with the scale Q^2 can be described by perturbative QCD through the DGLAP equations [55]. This enables PDFs measured at the lower energies currently available to be extrapolated to the LHC kinematic region. The kinematic regions of the HERA collider and the LHC are shown in Figure 5.2.

The parton distribution functions from the MSTW2008 set are shown in Figure 5.3, for a $Q^2 = m_Z^2$. Several important attributes of the PDFs for this Q^2 may be noted. The excess of the valence quarks u and d over the sea quarks $\overline{\mathrm{u}}$ and $\overline{\mathrm{d}}$ is particularly evident for $0.01 \le x \le 1$. The gluon is dominant over a large range of x. The sea is not flavour symmetric - for example the strange quark PDF is smaller than the up and down anti-quark PDFs.

5.2 Production of Massive Vector Bosons

The inclusive production and decay of the massive vector bosons is similar to the Drell-Yan mechanism. The formula for the total cross-section is (5.1), with the partonic level cross-section $\hat{\sigma}$ calculable from the fermion-boson couplings that were derived in Chapter 1 : (1.46) and (1.47).

The partons involved in W production are predominantly $\mathrm{u}\overline{\mathrm{d}}$ and $\mathrm{d}\overline{\mathrm{u}}$ over the range of potential LHC energies (Figure 5.4) – however $\mathrm{s}\overline{\mathrm{c}}$ contributes 21% of total W cross-section at $\sqrt{s} = 10\,\mathrm{TeV}$ and $\mathrm{c}\overline{\mathrm{s}}$ contributes 15%. This shows the increased importance of the sea in the LHC kinematic region, compared to the Tevatron, where the charm-strange contribution is only 5%.

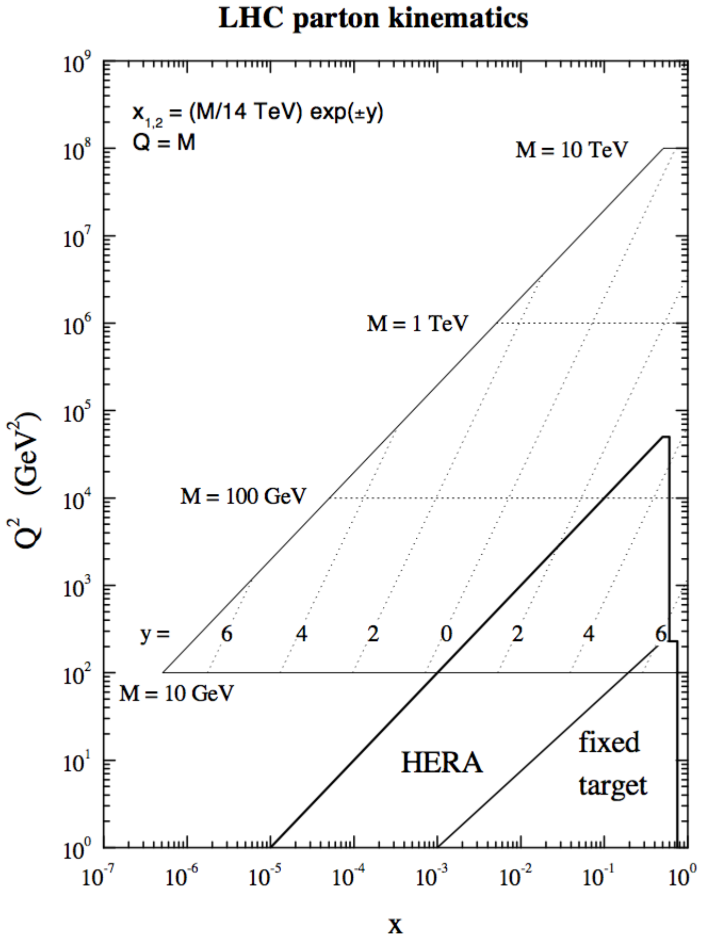

Figure 5.2: The range of x and Q^2 probed in the production of an object of mass M and rapidity y at the LHC, $\sqrt{s} = 14\,\text{TeV}$.

The leading order matrix element for W boson production is :

$$\mathcal{M} = \frac{-ig_W}{2\sqrt{2}} V_{qq'} \bar{u}_a(p_1, s)\gamma_\mu\big(1-\gamma^5\big)v_b(p_2, r)\epsilon_\alpha \tag{5.6}$$

where $V_{qq'}$ is the CKM coefficient for each quark pair. (5.6) leads to the differential cross-section with respect to rapidity :

$$\frac{d\sigma(\text{pp} \to \text{W}^+)}{dy} = \frac{\pi g_W^2}{24 m_W^2} \sum_{q,\bar{q}'} |V_{qq'}|^2 x_1 q\big(x_1, m_W^2\big) x_2 \bar{q}\big(x_2, m_W^2\big) \tag{5.7}$$

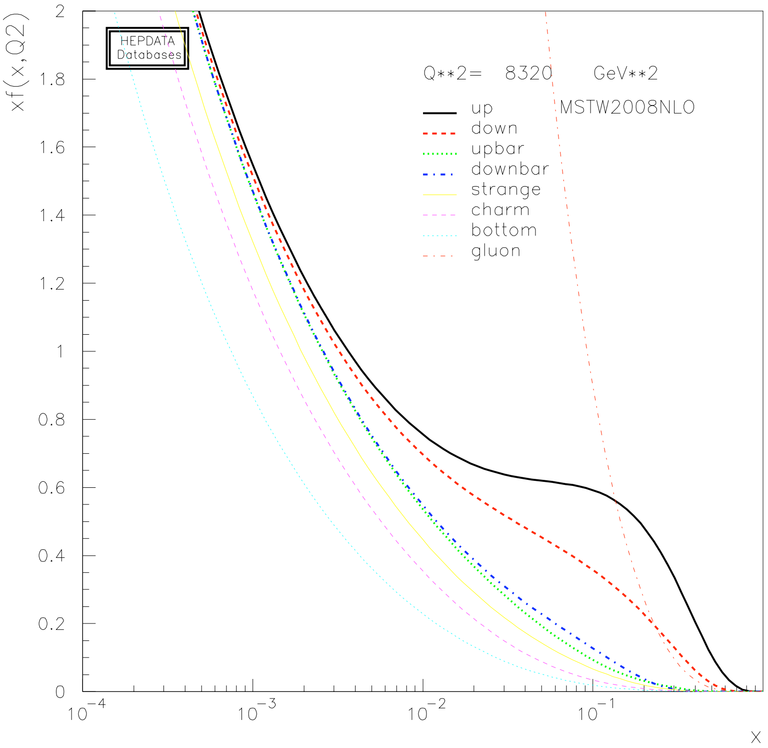

Figure 5.3: Parton distribution functions from the MSTW2008NLO set [53], for $Q^2 = m_Z^2$.

A factor of 1/3 is included to account for the quark colours. The fractional momenta carried by the partons are given by the relationship :

$$x_{1,2} = \frac{M}{\sqrt{s}} e^{\pm y} \tag{5.8}$$

Clearly the rapidity distribution of the W boson is determined predominantly by the scattered parton momenta. The distributions calculated with the MRST99 PDF sets are shown in Figure 5.5. The 'bump' of the W^+ distribution at $|y| \sim 3$ can be understood by considering Figure 5.2. For centrally produced W bosons, the momenta carried by the scattered partons must be approximately equal and opposite – in contrast, for $|y| \sim 3$, W bosons must have been produced by the scattering of one parton with momentum fraction $x \sim 10^{-4}$ and another with $x \sim 0.1$. For $Q^2 = m_W^2$, there is a peak in the u quark distribution at $x \sim 0.1$ because it is a valence quark. This makes production of a W^+ more likely at this rapidity. The W^- distribution is similar, although the feature at $|y| \sim 3$ is smaller because of (5.5).

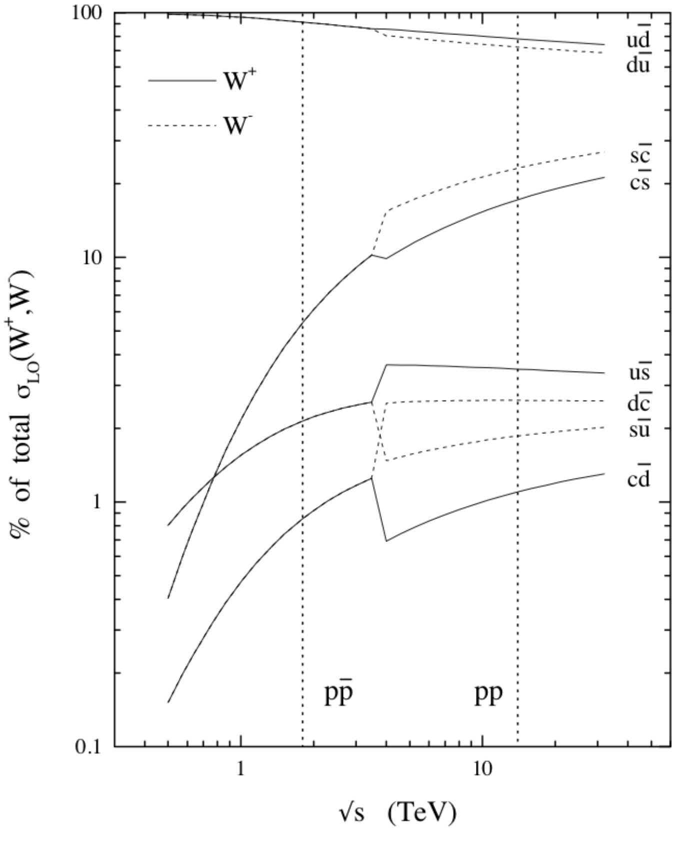

Figure 5.4: Decomposition of the W$^+$ (solid line) and W$^-$ (dashed line) total cross sections in p̄p and pp collisions by parent quark flavours. Due to the symmetry of p̄p collisions, the W$^+$ and W$^-$ have the same flavour parents, while differences are present for pp. The differing contributions of each flavour result from the differing CKM coefficients for each quark pairing and the composition of the proton. [56]

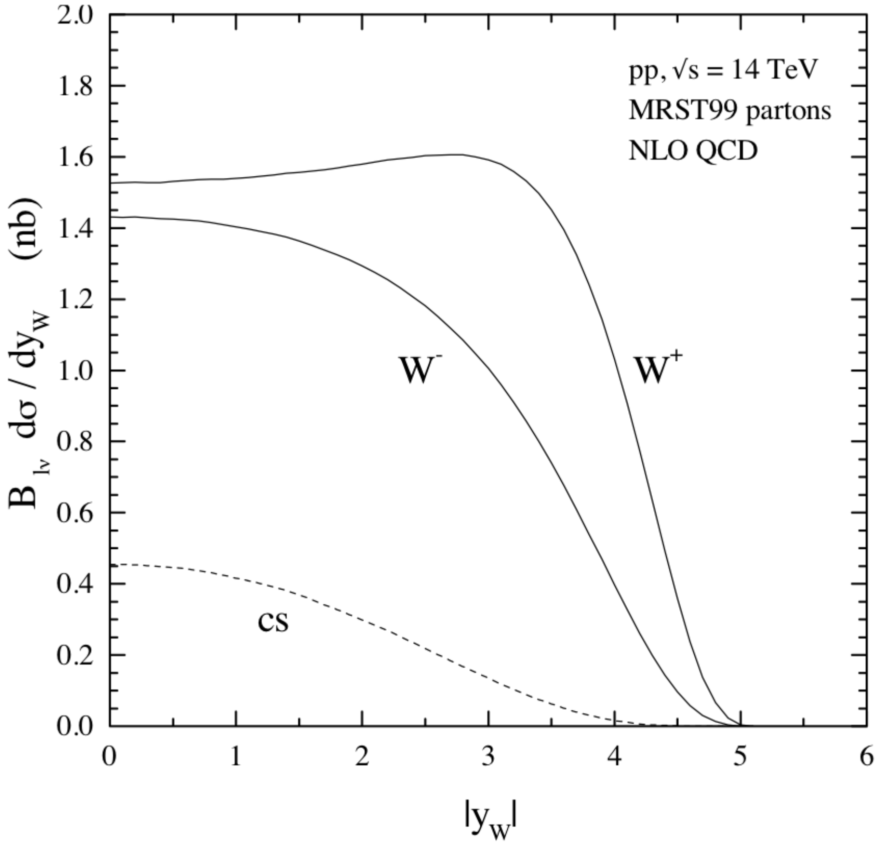

Figure 5.5: Rapidity of W^+ and W^- calculated using MRST99 PDFs, at $\sqrt{s} = 14\,\text{TeV}$. The rapidity of those $W^\pm$ produced by charm-strange interaction is shown as a dashed line. [56]

For Z bosons, PDFs play the same role defining the rapidity distribution, which is shown in Figure 5.11. The effect of the u valence quarks is less pronounced than for W^+, though their effect is evident in the wider rapidity 'plateau' of Z production compared to the W^- distribution.

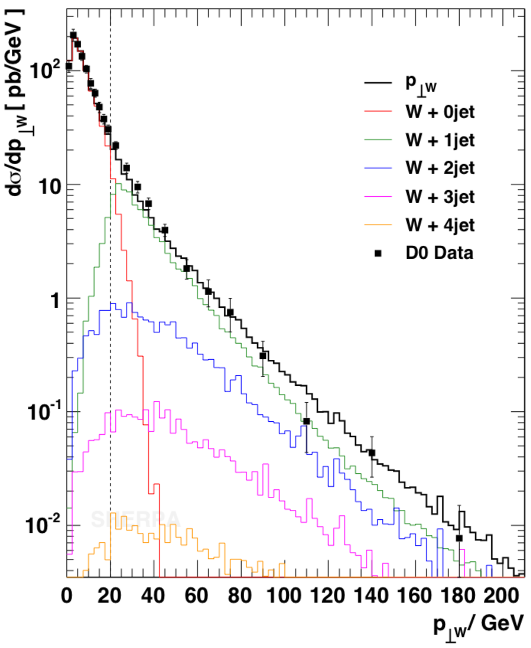

Figure 5.6: Transverse momentum of the W boson : comparison of SHERPA MC simulation (black line, indicated $p_{\perp W}$) to Run I D0 data (points). The distributions of $p_{\perp W}$ for the different jet multiplicity components are shown as coloured lines. [57]

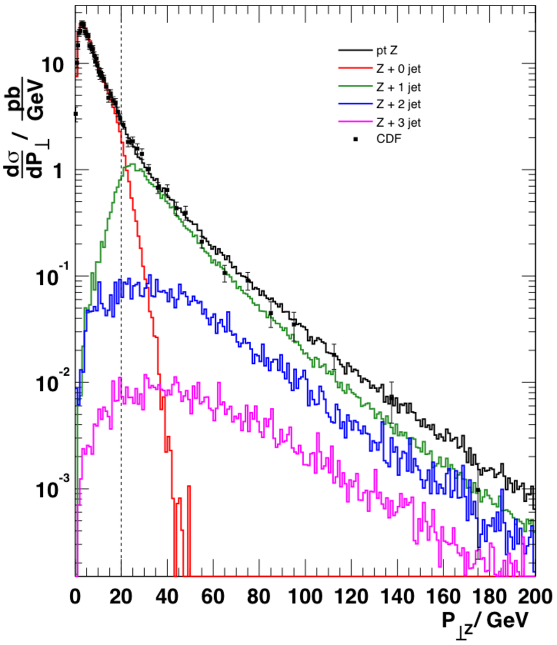

Figure 5.7: Transverse momentum of the Z boson : comparison of SHERPA (black line, indicated $p_{\perp Z}$) to Run I CDF data (points). The jets are defined by a k_T algorithm. The 'merging cut' is shown by the dashed vertical line. [57]

The transverse momentum distributions of W and Z bosons as produced at the Tevatron are shown in Figures 5.6 and 5.7 and compared with the predictions of the SHERPA generator. In leading order Drell-Yan production the massive vector bosons are produced with zero transverse momentum ($p_T \ll m_W$) because the partons involved in the interaction are assumed to be collinear with the colliding protons. However, the partons will have 'intrinsic' transverse momentum within the proton of $O(1\,\mathrm{GeV})$ and so the massive vector bosons will have non-zero transverse momentum. This can be seen in the figures in the W + 0 jet and Z + 0 jet distributions. The other source of transverse

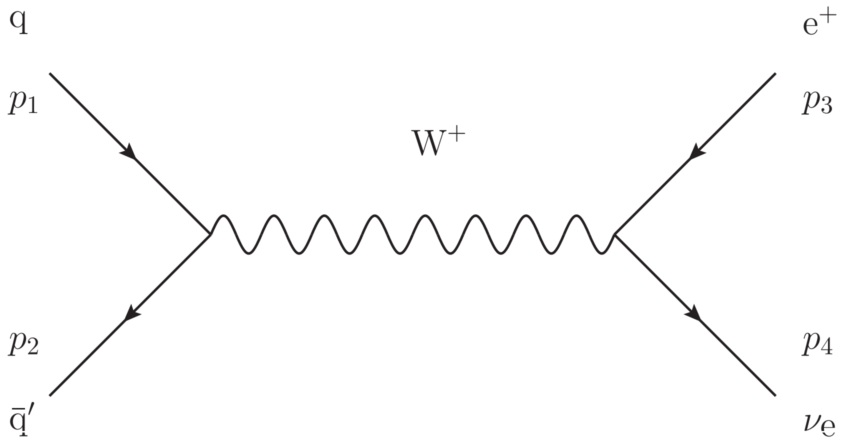

Figure 5.8: Leading order Feynman diagram for $q\bar{q} \rightarrow \mathrm{W}^+ \rightarrow \mathrm{e}^+\nu_\mathrm{e}$

momentum – responsible for the 'power-law' tail in the p_T spectrum – is emission of additional partons[1], for example $q\bar{q} \rightarrow$ Wg and qg $\rightarrow$ Zq. This is shown in the W and Z + n jets distributions ($n > 0$). Both sources are necessary to explain the p_T spectra of the boson.

5.3 $\mathbf{q\bar{q} \rightarrow W \rightarrow e\nu_e}$

The leading order Feynman diagram is shown in Figure 5.8.

For $q\bar{q} \rightarrow \mathrm{W}^+ \rightarrow \mathrm{e}^+\nu_\mathrm{e}$, the leading order matrix element arising from (1.46) and a propagator term for the massive W is :

$$\mathcal{M} = \frac{ig_W^2 V_{qq'}}{8} u_\sigma(p_1, r')\gamma^\mu\big(1+\gamma^5\big)\bar{v}_\rho(p_2, r)\frac{g_{\mu\nu} + \frac{k_\mu k_\nu}{m_W^2}}{k^2 + m_W^2}\bar{u}_\lambda(p_3, s)\gamma^\nu\big(1+\gamma^5\big)v_\alpha(p_4, s') \tag{5.9}$$

The squared matrix element, with initial spin states averaged and final spin states summed over is :

$$|\bar{\mathcal{M}}|^2 = g_W^4 |V_{qq'}|^2 \frac{\left(p_3.p_1\right)^2}{\left(\left(p_1+p_2\right)^2 - m_W^2\right)^2 - \Gamma_W^2 m_W^2} \tag{5.10}$$

---

[1] The SHERPA merging cut defines a region of jet production (i.e. 'hard' emission of partons) governed by matrix element calculation and a region of jet evolution (i.e. 'soft' emission) driven by parton showers).

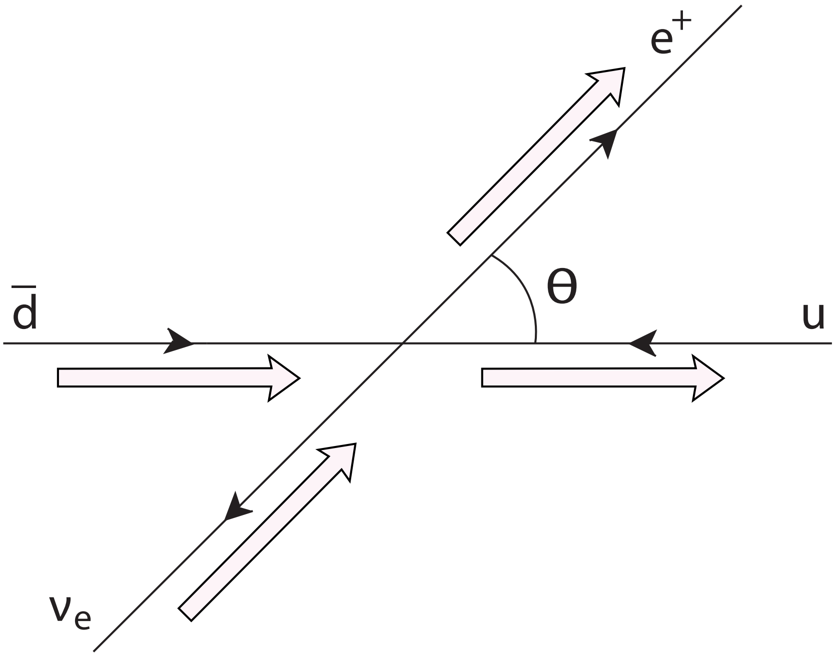

Figure 5.9: W → eν_e in W rest frame, showing momenta as line arrows and helicities as block arrows.

The additional term $\Gamma_w^2 m_W^2$ relates to the finite width of the physical W boson and avoids the pole at $(p_1 + p_2)^2 = m_W^2$. Integrating over phase-space and taking u$\overline{\mathrm{d}}$ → $\mathrm{W}^+ \rightarrow \mathrm{e}^+\nu_e$ as a concrete example leads to the differential cross-section :

$$\frac{d\hat{\sigma}}{d\cos\hat{\theta}} = \frac{g_W^4 |V_{ud}|^2}{8\pi} \frac{\hat{s}(1+\cos\theta)^2}{(\hat{s}-m_W^2)^2 - \Gamma_W^2 m_W^2} \tag{5.11}$$

where θ is the angle between the incoming down anti-quark and the positron in the W rest frame, as illustrated in Figure 5.9. The positron is not emitted isotropically in this frame, but rather the cross-section is largest when $\theta = 0$, i.e. when the positron is emitted in the direction of the incoming $\overline{\mathrm{d}}$. This is due to helicity effects arising from the SU(2) symmetry of the electroweak sector. In the massless approximation (valid as $m_q, m_e \ll m_W$), the incoming u is left-handed and the $\overline{\mathrm{d}}$ right-handed. The emitted positron must be right-handed and neutrino left-handed and so in order to conserve helicity, the momentum of the positron is preferentially along the $\overline{\mathrm{d}}$ direction. This helicity effect reduces the excess of positrons that would be expected at high rapidity as a result of the momentum distribution of u quarks.

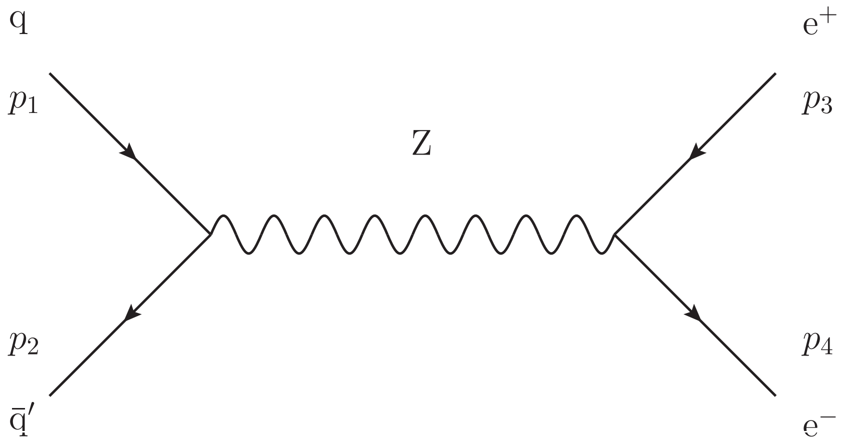

Figure 5.10: Leading order Feynman diagram for $q\bar{q} \to \mathrm{Z} \to \mathrm{e^+e^-}$.

The transverse momentum of electrons in the W rest frame is dictated by the angular distribution (5.11), where :

$$\cos\hat{\theta} = \left(1 - \frac{4p_T^2}{m_W^2}\right)^{\frac{1}{2}} \tag{5.12}$$

leading to the differential cross-section :

$$\frac{1}{\hat{\sigma}}\frac{d\hat{\sigma}}{dp_T^2} = \frac{8C}{m_W^2}\left(1 - \frac{2p_T^2}{m_W^2}\right)\left(1 - \frac{4p_T^2}{m_W^2}\right)^{-\frac{1}{2}} \tag{5.13}$$

where C is a constant. There is a singularity in (5.13) at $p_T = m_W/2$, giving rise to the characteristic 'Jacobian peak'. This unphysical singularity is not observed because of the finite width of the bosons. The peak is further smeared by the boson's transverse momentum.

5.4 $\mathrm{q\bar{q}} \longrightarrow \mathrm{Z} \longrightarrow \mathrm{e^+e^-}$

The leading order matrix element for $q\bar{q} \to \mathrm{Z} \to \mathrm{e^+e^-}$ is :

$$\mathcal{M} = \frac{ig_W^2}{8} u_\sigma(p_1, r')\gamma^\mu\big(g_V^q + g_A^q\gamma^5\big)\bar{v}_\rho(p_2, r)\frac{g_{\mu\nu} + \frac{k_\mu k_\nu}{m_Z^2}}{k^2 + m_Z^2}\bar{u}_\lambda(p_3, s)\gamma^\nu\big(g_V^e + g_A^e\gamma^5\big)v_\alpha(p_4, s') \tag{5.14}$$

where g_V^f and g_A^f are the vector and axial coupling terms respectively : $g_V^f = \frac{1}{2}t_3 - \sin^2\theta_W Q$ and $g_A^f = -\frac{1}{2}t_3$. (The coupling term derived in (1.47) can be expressed in terms of these coupling terms.)

The angular distribution is then :

$$\frac{d\hat{\sigma}}{d\cos\hat{\theta}} \sim \left[(g_V^q)^2 + (g_A^q)^2\right]\left[(g_V^e)^2 + (g_A^e)^2\right]\left(1+\cos^2\hat{\theta}\right) + 8g_V^q g_A^q g_V^e g_A^e \cos\hat{\theta} \qquad (5.15)$$

This angular dependence is quite different to the W decay because the Z decay has both V ± A components.

The transverse momenta of the electrons have a similar form to those from Z decay, although they peak at $p_T = m_Z/2$.

5.5 Current Accuracy of Predictions

Current calculations of the W and Z production cross-sections and the decay to electrons are available to NNLO in QCD and NLO in EWK. The boson rapidity predictions for the LHC are shown in Figures 5.11 and 5.12. The uncertainties on these NNLO predictions due to the missing higher order corrections are $\leq 1\%$. The principal source of uncertainties limiting the accuracy of the theoretical cross-section prediction are those associated with the parton distribution functions. The recent combination of results from the HERA experiments has greatly improved knowledge of the PDFs for W and Z production; in particular, uncertainties in the low x sea have been reduced. The PDF uncertainty from experimental sources is estimated to be 1% [59]. Furthermore, PDF sets like MSTW08 are now available with full NNLO evolution, improving the accuracy of the description for the LHC. The PDF uncertainties including these higher order corrections, model uncertainties and the experimental error are estimated to be $\sim 2\%$. Other uncertainties are difficult to quantify at NNLO, and "at LHC may be 1%-2% in each case" [53].

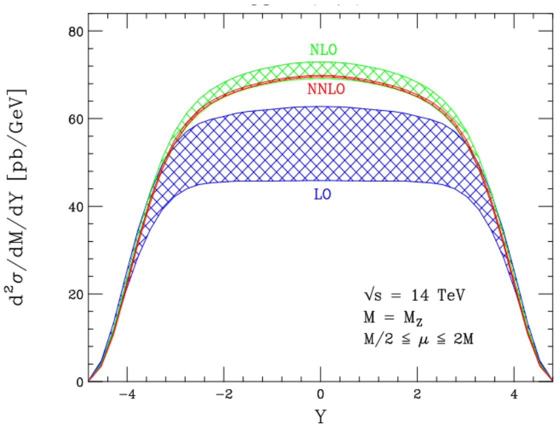

Figure 5.11: Z boson rapidity distributions calculated at LO, NLO and NNLO in QCD. Results are for $\sqrt{s} = 14\,\text{TeV}$, using the MRST99 PDFs. The bands depict the effect of varying the renormalisation and factorisation scales within $m_Z/2 \leq \mu \leq 2m_Z$. [58]

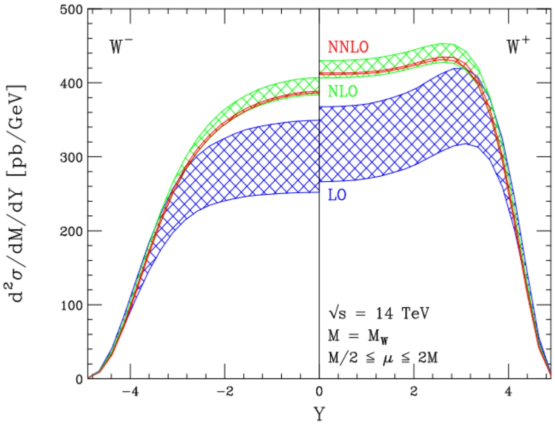

Figure 5.12: W boson rapidity distributions calculated at LO, NLO and NNLO in QCD, using the MRST99 PDFs. The distributions are y symmetric, so only half are shown for both W$^+$ and W$^-$. [58]

$\sqrt{s} = 10\,\text{TeV}$	$B_{l\nu}.\sigma_{\text{W}^+}$ (nb)	$B_{l\nu}.\sigma_{\text{W}^-}$ (nb)	$B_{l^+l^-}.\sigma_{\text{Z}}$ (nb)
MSTW08 LO	$7.35^{+0.08}_{-0.12}$ $\left(^{+1.1\%}_{-1.6\%}\right)$	$5.22^{+0.06}_{-0.09}$ $\left(^{+1.1\%}_{-1.7\%}\right)$	$1.163^{+0.011}_{-0.017}$ $\left(^{+1.0\%}_{-1.5\%}\right)$
MSTW08 NNLO	$8.88^{+0.15}_{-0.15}$ $\left(^{+1.7\%}_{-1.6\%}\right)$	$6.47^{+0.11}_{-0.11}$ $\left(^{+1.7\%}_{-1.6\%}\right)$	$1.429^{+0.024}_{-0.022}$ $\left(^{+1.7\%}_{-1.6\%}\right)$

$\sqrt{s} = 14\,\text{TeV}$	$B_{l\nu}.\sigma_{\text{W}^+}$ (nb)	$B_{l\nu}.\sigma_{\text{W}^-}$ (nb)	$B_{l^+l^-}.\sigma_{\text{Z}}$ (nb)
MSTW08 LO	$10.69^{+0.14}_{-0.19}$ $\left(^{+1.3\%}_{-1.8\%}\right)$	$7.83^{+0.10}_{-0.14}$ $\left(^{+1.2\%}_{-1.8\%}\right)$	$1.736^{+0.019}_{-0.028}$ $\left(^{+1.1\%}_{-1.6\%}\right)$
MSTW08 NNLO	$12.39^{+0.22}_{-0.21}$ $\left(^{+1.8\%}_{-1.7\%}\right)$	$9.33^{+0.16}_{-0.16}$ $\left(^{+1.7\%}_{-1.7\%}\right)$	$2.051^{+0.035}_{-0.033}$ $\left(^{+1.7\%}_{-1.6\%}\right)$

Table 5.1: Predictions for W$^+$, W$^-$ and Z total cross-sections at the LHC, calculated at LO and NNLO in perturbative QCD. Uncertainties are one sigma PDF uncertainties. Adapted from [53].

6 Missing Transverse Energy

"Eliminate all other factors, and the one which remains must be the truth"
— Sir Arthur Conan Doyle

This chapter describes the Ersatz Missing Energy method, a technique developed to model the properties of reconstructed missing energy in $\mathrm{W}^{\pm} \rightarrow \mathrm{e}^{\pm}\,\nu_{\mathrm{e}}$ events, using $\mathrm{Z} \rightarrow \mathrm{e}^{+}\,\mathrm{e}^{-}$ events as an analogue. This technique is intended for use in the $\mathrm{W}^{\pm} \rightarrow \mathrm{e}^{\pm}\,\nu_{\mathrm{e}}$ cross-section measurements in early data and was employed in Chapter 7.

Initially, the method is explained and demonstrated at generator level before Section begins the description of the technique's use on CMS data and it's evaluation using simulated 'pseudo-data'.

6.1 Introduction

In hadron collisions, it is possible to infer the presence of a non-interacting particle, such as a neutrino, by projecting all the energy of the event onto the transverse plane and summing vectorially. The transverse momentum of the particle is estimated by the missing transverse energy :

$$\not{E}_T = -\sum_{k=1}^{E\,deposits} (E_k \cos\phi_k \hat{\mathbf{i}} + E_k \sin\phi_k \hat{\mathbf{j}}) \sin\theta_k = \not{E}_x \hat{\mathbf{i}} + \not{E}_y \hat{\mathbf{j}}. \qquad (6.1)$$

The accuracy and precision of this measurement are limited by the acceptance of the CMS detector; by the energy measurement resolution for all of the deposits, by pile-up, and by instrumental problems such as noisy, dead or hot channels. Many of these limitations are expected to be particularly acute in early data, when there will be a limited knowledge of the calorimeter calibration and instrumental problems will perhaps be more frequent.

Despite these limitations, $\not{E}_T$ is a powerful discriminating variable that will be used in the selection of $\mathrm{W}^{\pm} \rightarrow \mathrm{e}^{\pm}\, \nu_{\mathrm{e}}$ events for an early cross-section measurement [60]. A set of tight identification criteria will be demanded of the reconstructed electrons and then the distribution of $\not{E}_T$ (or a related variable, m_T) will be used to further discriminate between signal and background. A precise separation of signal and background can be made if accurate descriptions of the $\not{E}_T$ distributions of signal and background are available.

QCD di-jet background is inherently difficult to simulate and this is compounded by the large cross-sections of these events and the high rejection factors needed to perform an analysis. This motivates a method to obtain a QCD di-jet background description from collision data by inverting one (or more) of the electron selection criteria. This has the effect of rejecting the $\mathrm{W}^{\pm} \rightarrow \mathrm{e}^{\pm}\, \nu_{\mathrm{e}}$ signal and other sources of high P_T, isolated electrons. An appropriate variable to invert maintains a high signal efficiency and minimises kinematic bias. High efficiency for signal is desirable in order that as much signal as possible is rejected when the inverse criterion is applied. Those background events rejected by the selection criteria must not be significantly different kinematically from those passing it, in order to retain an accurate description of the $\not{E}_T$ shape.

Estimating the $\not{E}_T$ properties of $\mathrm{W}^{\pm} \rightarrow \mathrm{e}^{\pm}\, \nu_{\mathrm{e}}$ events is more difficult. Although it is possible to generate the hard interaction in the events more accurately, the simulation of missing energy is limited by the global nature of $\not{E}_T$ measurement. There are many sources of inaccuracy, from the modelling of the underlying event to the simulation of the detector and its imperfections. Obtaining a unbiased $\not{E}_T$ description from data is difficult because of the high level of background contamination in $\mathrm{W}^{\pm} \rightarrow \mathrm{e}^{\pm}\, \nu_{\mathrm{e}}$ samples.

One solution – proposed and examined here – is the ‘Ersatz’ Missing Energy method which uses kinematically similar, readily identifiable $\mathrm{Z} \rightarrow \mathrm{e}^{+}\,\mathrm{e}^{-}$ events to provide the necessary $\mathrm{W}^{\pm} \rightarrow \mathrm{e}^{\pm}\, \nu_{\mathrm{e}}$ $\not{E}_T$ “template”. By selecting $\mathrm{Z} \rightarrow \mathrm{e}^{+}\,\mathrm{e}^{-}$ events and removing the energy of one electron from the E_T sum, an ersatz (artificial) $\not{E}_T$ is created. If these measurements are made using data from the same data sample as the $\mathrm{W}^{\pm} \rightarrow \mathrm{e}^{\pm}\, \nu_{\mathrm{e}}$ cross-section measurement they should account for most detector effects which may influence the $\not{E}_T$ of $\mathrm{W}^{\pm} \rightarrow \mathrm{e}^{\pm}\, \nu_{\mathrm{e}}$ events. The lower rate of $\mathrm{Z} \rightarrow \mathrm{e}^{+}\,\mathrm{e}^{-}$ events limits the statistical

Process	σ (pb)	ϵ	Equivalent $\int Ldt$ (pb^{-1})
$\mathrm{W}^{\pm} \rightarrow \mathrm{e}^{\pm}\,\nu_{\mathrm{e}}$	11850	0.738	126
$\gamma^{*}/\mathrm{Z} \rightarrow \mathrm{e}^{+}\mathrm{e}^{-}$ ($m_{ee} > 40\,\mathrm{GeV}$)	1232	0.701	952
Wenu†	11850	0.738	127
Light flavour di-jets :			
$20\,\mathrm{GeV} < \hat{p}_T < 30\,\mathrm{GeV}$	4×10^{8}	8×10^{-3}	6.36
$30\,\mathrm{GeV} < \hat{p}_T < 80\,\mathrm{GeV}$	1×10^{8}	4.7×10^{-2}	4.96
$80\,\mathrm{GeV} < \hat{p}_T < 170\,\mathrm{GeV}$	1.9×10^{6}	0.15	19.2
Heavy flavour di-jets :			
$20\,\mathrm{GeV} < \hat{p}_T < 30\,\mathrm{GeV}$	4×10^{8}	4.8×10^{-4}	10.4
$30\,\mathrm{GeV} < \hat{p}_T < 80\,\mathrm{GeV}$	1×10^{8}	2.4×10^{-3}	8.40
$80\,\mathrm{GeV} < \hat{p}_T < 170\,\mathrm{GeV}$	1.9×10^{6}	1.2×10^{-2}	47.2

Table 6.1: Datasets used in the analysis of the Ersatz Missing Energy method. ϵ is the efficiency of the generator level filtering (e.g. to account for geometrical acceptance) and is included in the equivalent $\int Ldt$. All samples were generated using PYTHIA 6.416 at $\sqrt{s} = 10\,\mathrm{TeV}$.
†This $\mathrm{W}^{\pm} \rightarrow \mathrm{e}^{\pm}\,\nu_{\mathrm{e}}$ sample also considered as background for ersatz $\not{E}_T$ calculation.

precision of the template for analyses of very low integated luminosities or extremely inefficient electron selections : results in Section 6.7 indicate that the ersatz method is suitable for use in the planned '10 pb^{-1}' cross-section measurements.

6.2 Data Analysed

This analysis was performed in version 2.2.10 of the CMS software, CMSSW, on the Summer 08 datasets listed in Table 6.1. These samples were all generated in PYTHIA 6.416 [61] with $\sqrt{s} = 10\,\mathrm{TeV}$; matter interactions of the final state particles was carried out using GEANT4 [62]; detector and HLT simulation was performed in CMSSW 2.1.9; and final reconstruction was performed in CMSSW 2.2.1. No miscalibration or misalignment was applied to these samples, although the beamspot position was set to (300 µm 0, 0) to reflect possible early beam conditions.

The QCD background samples had been filtered such that the events had a higher probability of passing the isolated single electron trigger, with the effect of significantly increasing the equivalent integrated luminosity of the samples. This ‘preselection’ was based on properties of the final state particles as generated by PYTHIA : avoiding the computationally intensive matter interaction and detector simulation steps.

The heavy flavour di-jets sample comprises those events which contain a generator level electron – with $E_T > 10\,\mathrm{GeV}$ and $|\eta| < 2.5$ – that originated from the decay of a b or c hadron.

The light flavour di-jet sample does not overlap the heavy flavour sample : any events satisfying the heavy flavour filter conditions are rejected. The EM content of the sample is enriched by selecting two event types :

1. Events that have isolated electrons, charged pions and kaons with $E_T > 20\,\mathrm{GeV}$ and $|\eta| < 2.5$. There are two isolation criteria, both using a cone radius of $\Delta R < 0.1$:

   - charged particles within the cone must have $\sum E_T < 4\,\mathrm{GeV}$
   - charged and neutral particles (excluding photons) within the cone $\sum E_T < 7\,\mathrm{GeV}$.

2. Events with suitable clusters of stable particles (with $E_T > 1\,\mathrm{GeV}$) around seed electrons or photons. The seed must have $E_T > 5\,\mathrm{GeV}$ within $|\eta| < 2.5$. The dimensions of the clusters are limited :

   - in EB, to a strip of 0.4 width in ϕ and 0.06 height in η
   - in EE, to a circle of 15 cm radius in the $x - y$ plane.

   In order to pass the filter, the cluster contents must satisfy :

   - $\sum E_T > 20\,\mathrm{GeV}$
   - $\sum E_T$ of hadronic particles is 50% or less of the total $\sum E_T$ of the cluster.

   The following isolation criteria are also demanded, using a cone radius of $\Delta R < 0.2$, must be met :

   - charged particles must have $\sum E_T < 5\,\mathrm{GeV}$
   - charged and neutral particles (excluding photons) must have $\sum E_T < 10\,\mathrm{GeV}$.

Several other background samples, such as Z $\rightarrow \tau\tau$, were analysed but found to be negligible.

6.3 Properties of W and Z decay at LHC

As discussed in Chapter 5, W and Z bosons are both produced via the Drell-Yan mechanism at the LHC and they decay in a similar manner. However, there are several key differences that must be considered before a useful ersatz missing energy can be created.

In order to make the necessary comparisons, inconsistencies in the generator-level filtering of the $W^{\pm} \rightarrow e^{\pm} \nu_e$ and $Z \rightarrow e^+ e^-$ data samples (Table 6.1) must be accounted for. These samples were filtered to retain only events with one or two electrons (respectively) within $|\eta| < 2.7$, but the filtering was done differently for the two samples. For $Z \rightarrow e^+ e^-$, the electrons used to filter had HEPEVT status code 1 [63], which corresponds to the final state electrons; for $W^{\pm} \rightarrow e^{\pm} \nu_e$, the filter considered electrons with HEPEVT status code 3, corresponding to electrons from the hard process. To remove this discrepancy, the events were further filtered – $Z \rightarrow e^+ e^-$ based on the properties of status 3 electrons and $W^{\pm} \rightarrow e^{\pm} \nu_e$ on status 1 – so that the remaining events in each sample satisfied both conditions.

No generator-level filter was applied to the $W^{\pm} \rightarrow e^{\pm} \nu_e$ events based on the properties of the neutrino, for neutrinos are not detected and so detector acceptance considerations do not apply. Ersatz neutrinos are formed from electrons, which are only reconstructed within the detector acceptance. To create an accurate ersatz missing energy distribution from reconstructed data, it is necessary to make a correction to account for $W^{\pm} \rightarrow e^{\pm} \nu_e$ events where the neutrinos are outside the detector acceptance. This correction is based on Monte Carlo simulation.

Generator level comparisons were carried out to assess whether $Z \rightarrow e^+ e^-$ events are a good analogue for $W^{\pm} \rightarrow e^{\pm} \nu_e$ events where the neutrino is within the detector acceptance. The following comparisons are therefore made to $W^{\pm} \rightarrow e^{\pm} \nu_e$ events which have a neutrino with $|\eta| < 2.5$.

Electrons are required to lie within the region $|\eta| < 2.5$. In $Z \rightarrow e^+ e^-$ events, one electron was selected at random to be the ersatz neutrino. The energy of this electron will be removed from the missing transverse energy calculation in order to simulate the neutrino in $W^{\pm} \rightarrow e^{\pm} \nu_e$ decay.

The lepton p_T in the boson rest frame is given to leading order by (5.13). In the lab frame, the principal influences on the p_T are : the mass of the parent boson; the angular distribution of the decay; the momentum of the parent boson.

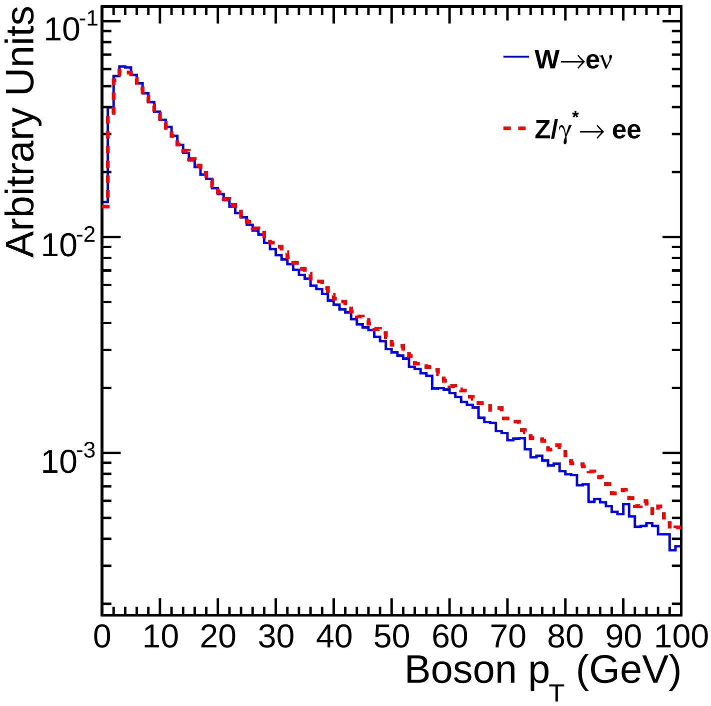

Figure 6.1: Transverse momentum of the W and Z bosons.

The transverse momentum of the W and Z bosons are shown in Figure 6.1. The distributions are very similar, although the Z p_T has a slightly more pronounced tail that probably results from the slightly higher Q^2 probed.

The transverse momenta of the leptons in $\gamma^*/\mathrm{Z} \to \mathrm{e}^+\mathrm{e}^-$ and $\mathrm{W}^\pm \to \mathrm{e}^\pm\, \nu_\mathrm{e}$ is shown in Figures 6.2 and 6.3. They peak at $p_T \sim m_Z/2$ and $p_T \sim m_W/2$ respectively. In the Ersatz Missing Energy method, a rescaling of the lepton momenta in $\mathrm{Z} \to \mathrm{e}^+\,\mathrm{e}^-$ events is performed, based on the boson mass.

6.4 Rescaling of Lepton Momenta

The first step is to calculate the four-vector of the Z, k^μ, from the properties of its electron daughters (p_1^μ and p_2^μ).

$$k^\mu = p_1^\mu + p_2^\mu \tag{6.2}$$

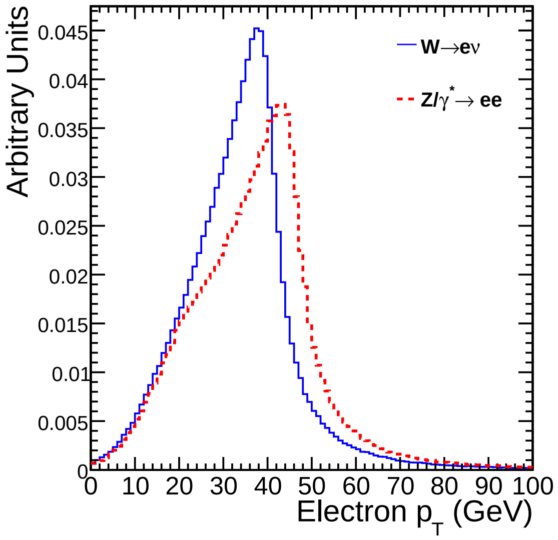

Figure 6.2: Transverse momentum of electrons in $W^{\pm} \rightarrow e^{\pm} \nu_e$ and $Z \rightarrow e^+ e^-$.

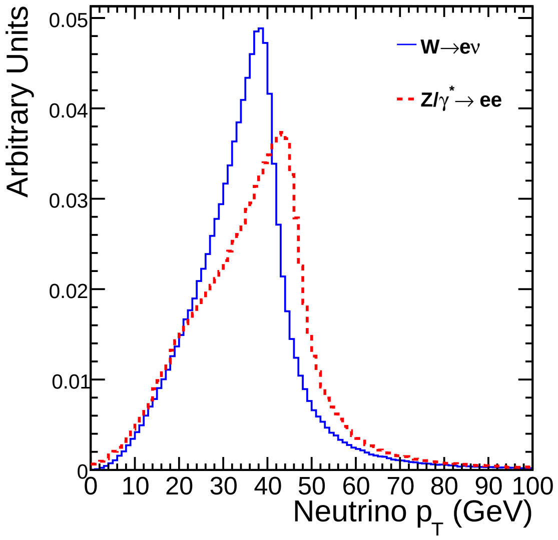

Figure 6.3: Transverse momentum of neutrinos in $W^{\pm} \rightarrow e^{\pm} \nu_e$ and ersatz neutrinos in $Z \rightarrow e^+ e^-$.

These daughters are then boosted (${\Lambda^{\nu}}_{\mu}$) to the rest frame of the Z boson, where their four-vectors are multiplied by a scaling factor to account for the differing boson masses.

$$p'^{\nu}_{1r.f.} = \frac{m_W}{m_Z} {\Lambda^{\nu}}_{\mu} p^{\mu}_1 \tag{6.3}$$

Finally, k_W, is calculated to represent the W boson four-momentum. This uses the three-momentum of the Z boson, but scales its mass by m_W/m_Z. Another boost is then applied to the leptons based on this four-momentum, leaving the transformed electron p_T as in Figures 6.4 and 6.5.

$$k_W = \left(\left(\frac{m_W^2}{m_Z^2} k^{\mu} k_{\mu} + k^i k_i \right)^{\frac{1}{2}}, \quad k_x, \quad k_y, \quad k_z \right) \tag{6.4}$$

$$p'^{\kappa}_1 = \frac{m_W}{m_Z} {\Lambda^{\kappa}}_{\nu} {\Lambda^{\nu}}_{\mu} p^{\mu}_1 \tag{6.5}$$

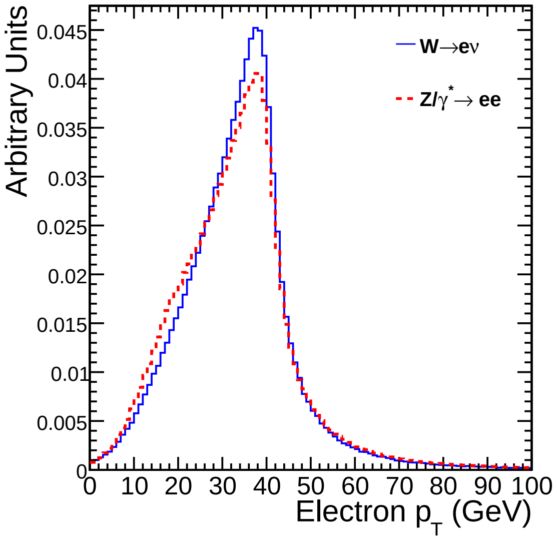

Figure 6.4: Transverse momentum of electrons in $\mathrm{W}^{\pm} \to \mathrm{e}^{\pm}\,\nu_{\mathrm{e}}$ and $\gamma^*/\mathrm{Z} \to \mathrm{e}^+\mathrm{e}^-$. The p_T of electrons from Z has been rescaled to correspond to a boson mass of m_W.

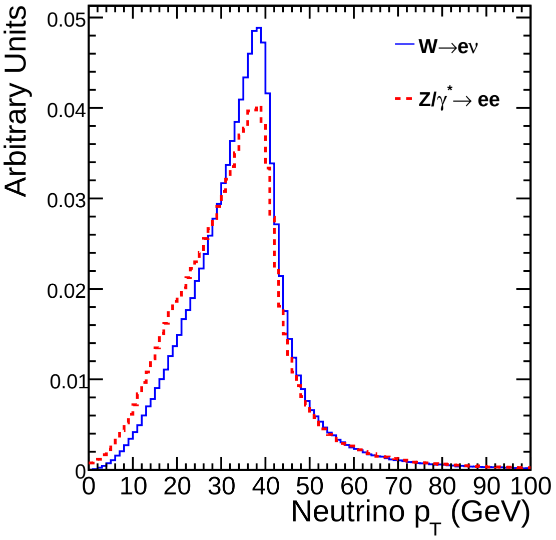

Figure 6.5: Transverse momentum of neutrinos in $\mathrm{W}^{\pm} \to \mathrm{e}^{\pm}\,\nu_{\mathrm{e}}$ and ersatz neutrinos in $\gamma^*/\mathrm{Z} \to \mathrm{e}^+\mathrm{e}^-$. The p_T of ersatz neutrinos from Z has been rescaled to correspond to a boson mass of m_W.

After this rescaling procedure, the distribution of lepton p_T peaks in the correct place, but there is an excess at low p_T. The source of the excess is evident in Figure 6.6, which shows the invariant mass of the rescaled lepton pair from $\gamma^*/\mathrm{Z} \to \mathrm{e}^+\mathrm{e}^-$ and from $\mathrm{W}^{\pm} \to \mathrm{e}^{\pm}\,\nu_{\mathrm{e}}$. The rescaled mass of the γ^*/Z bosons is more likely than the W boson mass to be below m_W. This is due to the off-shell γ^* contribution. Were it not for this additional term, the distribution of m_Z and m_W would be very similar.

The impact of the γ^* can be assessed by reweighting the $\gamma^*/\mathrm{Z} \to \mathrm{e}^+\mathrm{e}^-$ events so that they follow the invariant mass distribution of the $\mathrm{W}^{\pm} \to \mathrm{e}^{\pm}\,\nu_{\mathrm{e}}$ events. The resulting electron transverse momentum distribution (Figure 6.7) replicates that of the electron in $\mathrm{W}^{\pm} \to \mathrm{e}^{\pm}\,\nu_{\mathrm{e}}$ well. The neutrino distribution still shows some discrepancy after this reweighting (Figure 6.8).

A similar mass reweighting can be carried out using only the invariant mass distribution of the $\gamma^*/\mathrm{Z} \to \mathrm{e}^+\mathrm{e}^-$ leptons. The method evaluated here simply 'mirrors' the distribution about the peak. The bin contents in a small region ($\sim\Gamma_Z$) below the peak are preserved, as are the peak and all bins above it. The remaining bins below the peak

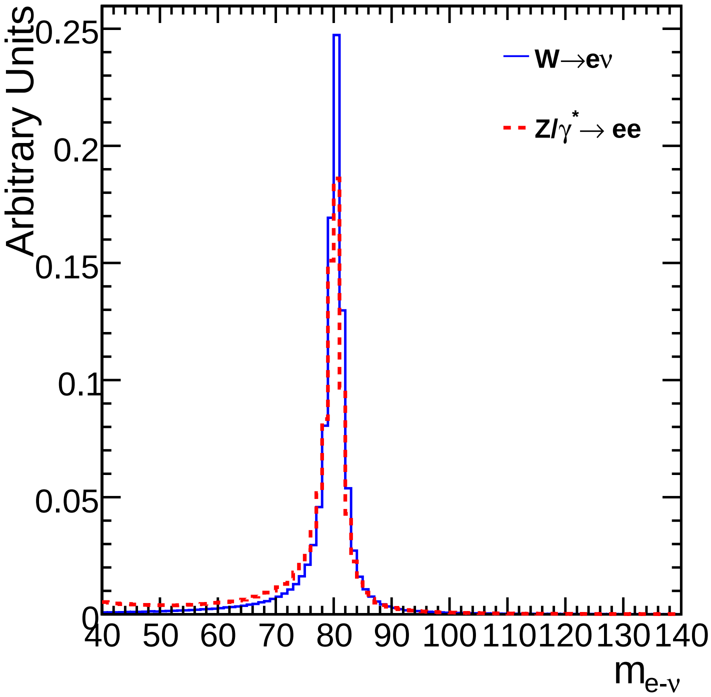

Figure 6.6: Invariant mass of the W and the rescaled electrons in $\gamma^*/\mathrm{Z} \to \mathrm{e}^+\mathrm{e}^-$.

are set to the content of the corresponding bin above it : if x were the peak bin, then the bin $x - i$ would be set to the value of $x + i$. The resulting histogram is then divided by the original invariant mass histogram to calculate a set of event weights. Although improvements to this procedure are possible, it does not introduce any significant difference in the final ersatz missing energy calculation compared to the reweighting using the W distribution.

6.5 The Ersatz Missing Energy Calculation

The ersatz missing energy is calculated by removing the momentum of the ersatz neutrino from the transverse energy sum and substituting the momentum of the remaining electron with its rescaled value. The calculation is carried out using four-vectors with z component set to zero :

$$\not{p}^{\mu}_{ersatz} = \not{p}^{\mu}_{actual} + p^{\mu}_{ersatz-\nu} + p^{\mu}_{e} - (p')^{\mu}_{e} \qquad (6.6)$$

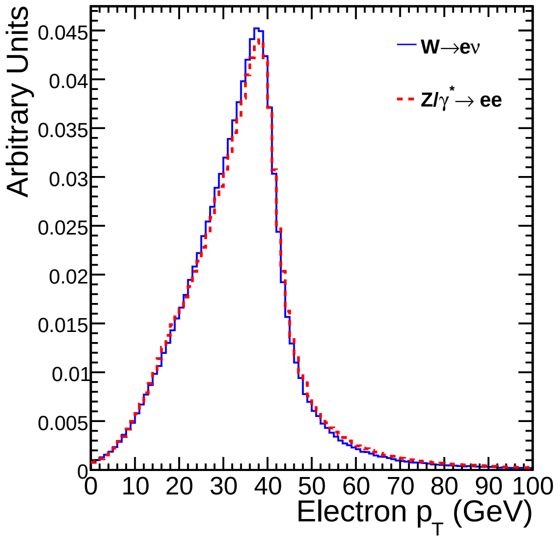

Figure 6.7: Transverse momentum of electrons in $\mathrm{W}^\pm \rightarrow \mathrm{e}^\pm \nu_\mathrm{e}$ and $\gamma^*/\mathrm{Z} \rightarrow \mathrm{e}^+\mathrm{e}^-$. The p_T of electrons from Z has been rescaled to correspond to a boson mass of m_W. The $\gamma^*/\mathrm{Z} \rightarrow \mathrm{e}^+\mathrm{e}^-$ events were reweighted to follow the $\mathrm{W}^\pm \rightarrow \mathrm{e}^\pm \nu_\mathrm{e}$ mass distribution.

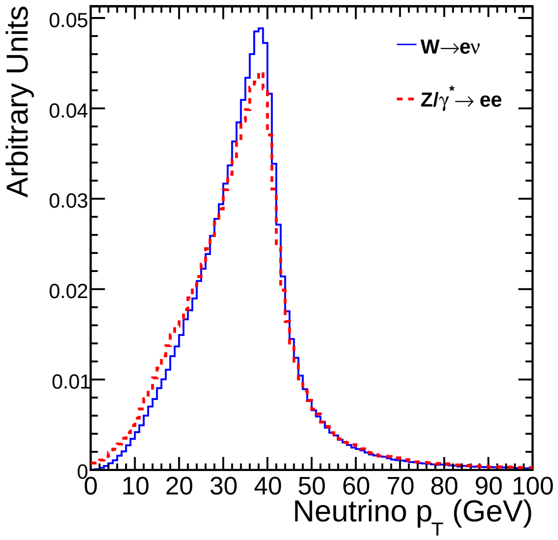

Figure 6.8: Transverse momentum of neutrinos in $\mathrm{W}^\pm \rightarrow \mathrm{e}^\pm \nu_\mathrm{e}$ and ersatz neutrinos in $\gamma^*/\mathrm{Z} \rightarrow \mathrm{e}^+\mathrm{e}^-$. The p_T of ersatz neutrinos from Z has been rescaled to correspond to a boson mass of m_W. The $\gamma^*/\mathrm{Z} \rightarrow \mathrm{e}^+\mathrm{e}^-$ events were reweighted to follow the $\mathrm{W}^\pm \rightarrow \mathrm{e}^\pm \nu_\mathrm{e}$ mass distribution.

$\not{p}^\mu_{ersatz}$ is the ersatz missing momentum. The true missing momentum in the event, $\not{p}^\mu_{actual}$ is calculated as in (6.1) using the properties of the visible simulated particles (i.e. excluding neutrinos). It is shown in Figure 6.9. $p^\mu_{ersatz-\nu}$ is the (unscaled) momentum of the electron chosen to be the ersatz neutrino. The unscaled momentum of the other electron, p^μ_e is replaced with the rescaled $(p')^\mu_e$.

The scalar ersatz missing transverse energy is :

$$\not{E}_T^{\,ersatz} = |\not{p}_{ersatz} \sin\theta| \qquad (6.7)$$

where $\not{p}$ is the spatial momentum component of $\not{p}^\mu$ and $\sin\theta = 1$, since all z-components were set to zero.

The transverse mass of the ersatz W may also be calculated :

$$m_T = \sqrt{2 p_T^{rescaled-e} \not{E}_T^{\;ersatz} (1 - \cos \Delta\phi)} \tag{6.8}$$

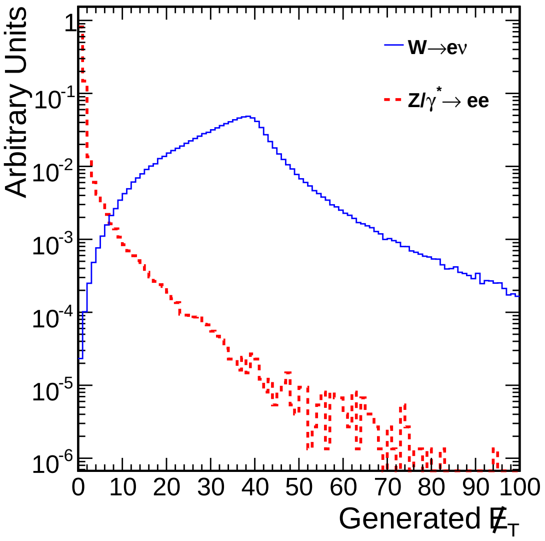

Figure 6.9: True simulated missing transverse energy in $\mathrm{W}^{\pm} \to \mathrm{e}^{\pm}\, \nu_{\mathrm{e}}$ and $\mathrm{Z} \to \mathrm{e}^{+}\, \mathrm{e}^{-}$ events.

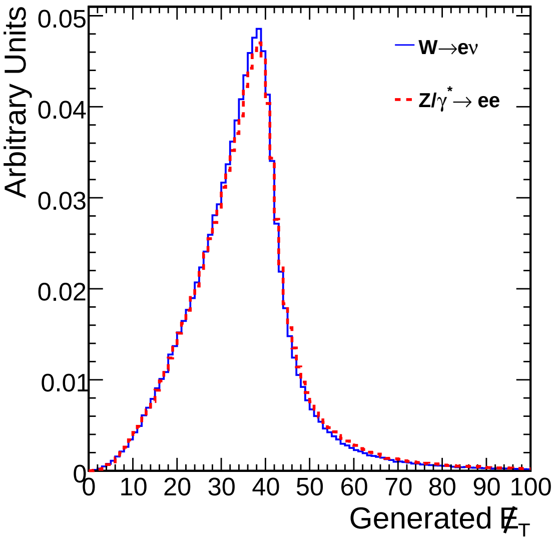

Figure 6.10: Ersatz missing transverse energy in $\mathrm{Z} \to \mathrm{e}^{+}\, \mathrm{e}^{-}$ and true missing transverse energy in $\mathrm{W}^{\pm} \to \mathrm{e}^{\pm}\, \nu_{\mathrm{e}}$.

The resulting distribution of ersatz missing transverse energy, shown in Figure 6.10 bears a close resemblance to the true $\not{E}_T$ in $\mathrm{W}^{\pm} \to \mathrm{e}^{\pm}\, \nu_{\mathrm{e}}$ events, though clear differences remain. A χ^2 test for comparison of the two histograms was performed, following the methodology of [64]. The results were an $X^2/ndf = 871/99$: only a negligible probability that the ersatz $\not{E}_T$ distribution follows the same parent probability density function as the true $\not{E}_T$. The differences likely arise from the differences in boson p_T and angular distribution of the leptons. However, these differences are insignificant in the context of a cross-section measurement with $\int Ldt = 10\,\mathrm{pb}^{-1}$.

The next step in increasing the realism of this study is to demand that the generator level electron has $p_T > 20\,\mathrm{GeV}$. In the $\mathrm{Z} \to \mathrm{e}^{+}\, \mathrm{e}^{-}$ events, this criterion is applied to the rescaled electron p_T. A loose invariant mass cut may be useful in data-taking in order to reduce the number of background events that must be analysed : $m_{ee} > 61\,\mathrm{GeV}$ is demanded in the Z events, with the resulting ersatz $\not{E}_T$ distribution shown in Figure 6.11.

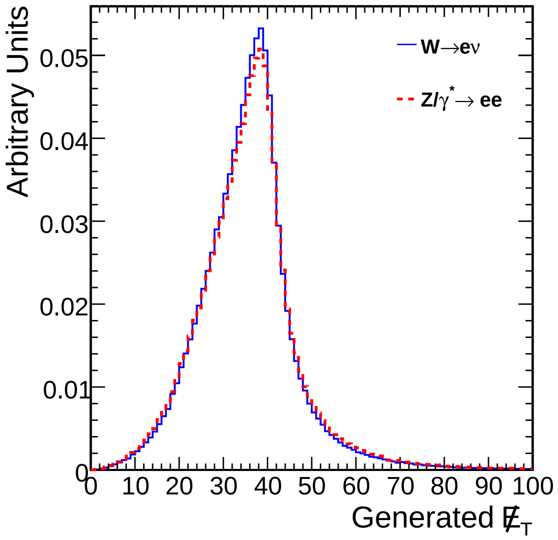

Figure 6.11: Ersatz $\not{E}_T$ and true $\not{E}_T$ in $W^{\pm}\rightarrow e^{\pm}\,\nu_e$. Electron $p_T > 20\,\mathrm{GeV}$ is demanded, as is $m_{ee} > 61\,\mathrm{GeV}$ in $Z\rightarrow e^+e^-$. All available events are used.

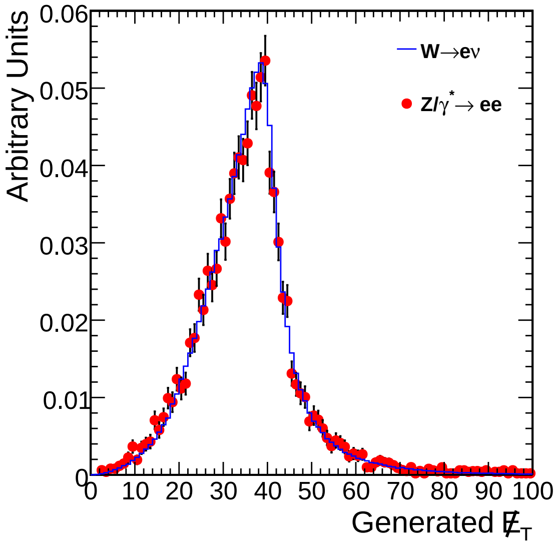

Figure 6.12: Ersatz $\not{E}_T$ and true $\not{E}_T$ in $W^{\pm}\rightarrow e^{\pm}\,\nu_e$. Electron $p_T > 20\,\mathrm{GeV}$ is demanded, as is $m_{ee} > 61\,\mathrm{GeV}$ in $Z\rightarrow e^+e^-$. Number of $Z\rightarrow e^+e^-$ corresponds to $\int L dt = 10\,\mathrm{pb}^{-1}$.

The results for $\int L dt = 10\,\mathrm{pb}^{-1}$ are shown in Figure 6.12. To the limit of the statistical precision, the two histograms are now compatible : $X^2/\mathrm{ndf} = 95.8/99$, corresponding to a probability of 57.2%. The accuracy of the ersatz method is sufficient at the generator-level for the $\mathrm{pp}\rightarrow W\rightarrow e\nu_e$ cross-section measurement with $\int L dt = 10\,\mathrm{pb}^{-1}$.

6.6 Reconstruction Level

In CMS data, the Ersatz Missing Energy method can be applied as follows :

1. Reconstruct and select $Z\rightarrow e^+e^-$ events (from the electron primary dataset).
2. Identify an electron that satisfies the selection used for $W^{\pm}\rightarrow e^{\pm}\,\nu_e$
3. Identify another electron as the ersatz neutrino
4. Remove the energy of the ersatz neutrino from the transverse energy sum
5. Rescale the remaining electron's momentum and recalculate $\not{E}_T$
6. Correct ersatz missing energy for differences in efficiency of electron and neutrino selection with respect to W events

7. Correct ersatz missing energy for limited ersatz neutrino acceptance

In this work, calorimetric missing transverse energy has been used, on the assumption that this $\not\!\!E_T$ measurement will be the most appropriate for early measurements. However, the method could be readily adapted to work with other measurements of missing energy, for example using Particle Flow candidates [65].

6.6.1 Event and Object Selection

To accurately reproduce the $\not\!\!E_T$ properties of the $\mathrm{W}^{\pm} \rightarrow \mathrm{e}^{\pm}\, \nu_{\mathrm{e}}$ events selected for the $\mathrm{W}^{\pm} \rightarrow \mathrm{e}^{\pm}\, \nu_{\mathrm{e}}$ cross-section measurement, the electrons in $\mathrm{Z} \rightarrow \mathrm{e}^{+}\,\mathrm{e}^{-}$ must pass criteria which are as similar as possible to those demanded of the electrons in $\mathrm{W}^{\pm} \rightarrow \mathrm{e}^{\pm}\, \nu_{\mathrm{e}}$. Both $\mathrm{W}^{\pm} \rightarrow \mathrm{e}^{\pm}\, \nu_{\mathrm{e}}$ and $\mathrm{Z} \rightarrow \mathrm{e}^{+}\,\mathrm{e}^{-}$ candidates will be selected from datasets obtained with the single electron trigger, with a minimum p_T threshold foreseen for the early data-taking period of 15 GeV. It is essential that the reconstructed electron satisfying the trigger criteria in $\mathrm{Z} \rightarrow \mathrm{e}^{+}\,\mathrm{e}^{-}$ is the electron which will be taken to correspond to the reconstructed electron in the selected W events. The following results are obtained using the $\mathrm{W}^{\pm} \rightarrow \mathrm{e}^{\pm}\, \nu_{\mathrm{e}}$ electron selection detailed in Chapter 7.

The other electron, which will be considered as the ersatz neutrino, must be identified and selected. In $\mathrm{W}^{\pm} \rightarrow \mathrm{e}^{\pm}\, \nu_{\mathrm{e}}$ events, the neutrino does not have to meet any criteria and so to avoid introducing significant bias, a very loose selection is used. The goal of efficiency also aims to retain as much statistical precision as possible : however it is balanced by the requirement of negligible background passing the combined electron + ersatz neutrino selection. This motivates the use of GSF electrons as the ersatz neutrino, for the requirement of a charged particle track combined with a matching electromagnetic shower rejects many potential background events, while both superclustering and GSF track finding are highly efficient for electrons.

The electron supercluster must be within the ECAL fiducial region in order to avoid forming poor superclusters with unclustered energy that would be removed imprecisely. Demanding low hadronic activity behind the supercluster further reduces background contamination and rejects those electrons which have lost significant energy into the HCAL. The requirement must be loose enough that electrons are not rejected because of noise in the HCAL. Criteria based on shower shape variables reject hadronic background and select clusters that are electron-like and which will be readily removable.

The efficiencies of the ersatz neutrino selections are shown in Tables 6.2 and 6.3, for $\gamma^*/\mathrm{Z} \rightarrow \mathrm{e}^+\mathrm{e}^-$ events which have another reconstructed electron which satisfied the criteria for the $\mathrm{W}^\pm \rightarrow \mathrm{e}^\pm\, \nu_\mathrm{e}$ analysis. Those electron criteria are quite stringent, which allows those on the ersatz neutrino to be loose. However, if a higher level of background contamination is observed in data, these criteria could be tightened and additional ones applied. Figures 6.13 - 6.16 show the distributions of Ersatz $\not\!\!E_T$ calculated in events with and without these additional ersatz neutrino selections, illustrating the level of background contamination, which is $\approx 1\%$.

	$N-1$ Efficiencies (%)			
Requirement	$\gamma^*/\mathrm{Z} \rightarrow \mathrm{e}^+\mathrm{e}^-$	QCD di-jets	$bc \rightarrow e$	$\mathrm{W}^\pm \rightarrow \mathrm{e}^\pm\, \nu_\mathrm{e}$
GSF track matching	97.2 ± 0.0	6.6 ± 3.8	58.6 ± 14.2	10.5 ± 0.6
$E_{2\times 5} > 0.93$ OR $E_{1\times 5} > 0.83$	99.0 ± 0.0	10.8 ± 5.9	53.9 ± 10.9	25.9 ± 1.3
HCAL $E < 3.5\,\mathrm{GeV}$ in $\Delta R < 0.15$	99.4 ± 0.0	41.9 ± 13.0	75.0 ± 5.8	63.1 ± 2.2
Combined Selection	94.9 ± 0.0	0.81 ± 0.25	11.27 ± 4.21	2.78 ± 0.16

Table 6.2: Ersatz neutrino selection criteria for electrons impinging on ECAL barrel, showing N-1 efficiencies. These efficiencies are after the other electron in the event has passed the selection of Chapter 7.

	$N-1$ Efficiencies (%)			
Requirement	$\gamma^*/\mathrm{Z} \rightarrow \mathrm{e}^+\mathrm{e}^-$	QCD di-jets	$bc \rightarrow e$	$\mathrm{W}^\pm \rightarrow \mathrm{e}^\pm\, \nu_\mathrm{e}$
GSF track matching	93.8 ± 0.1	4.86 ± 4.33	$0.0{+}77.1$	3.90 ± 0.31
$\sigma_{i\eta i\eta} < 0.027$	98.0 ± 0.0	16.9 ± 11.4	$0.0{+}100.0$	16.4 ± 1.2
HCAL $E_T < 4.5\,\mathrm{GeV}$ in $\Delta R < 0.15$	99.7 ± 0.0	78.1 ± 25.6	—	78.6 ± 2.9
Combined Selection	86.2 ± 0.1	0.56 ± 0.21	0.00 ± 0.00	0.56 ± 0.04

Table 6.3: Ersatz neutrino selection criteria for electrons impinging on ECAL endcap, showing N-1 efficiencies. These efficiencies are after the other electron in the event has passed the selection of Chapter 7.

Given a reasonable $\mathrm{W}^\pm \rightarrow \mathrm{e}^\pm\, \nu_\mathrm{e}$ selection, it is likely that both electrons in a $\mathrm{Z} \rightarrow \mathrm{e}^+\,\mathrm{e}^-$ event will be capable of passing it. If the selection is such that the selected electrons are a subset of the ersatz neutrinos, then this means that there will be two valid electron–ersatz neutrino combinations in many events. Nevertheless, given inefficiencies in the

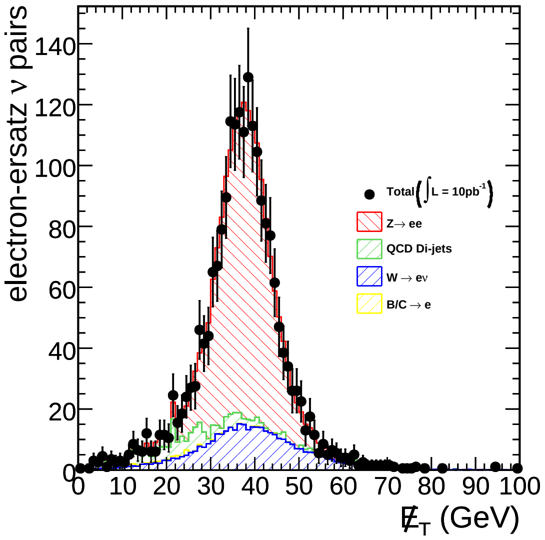

Figure 6.13: Ersatz $\not\!\!E_T$ showing background contamination without ersatz neutrino selection. For events with a 'W electron' in the barrel.

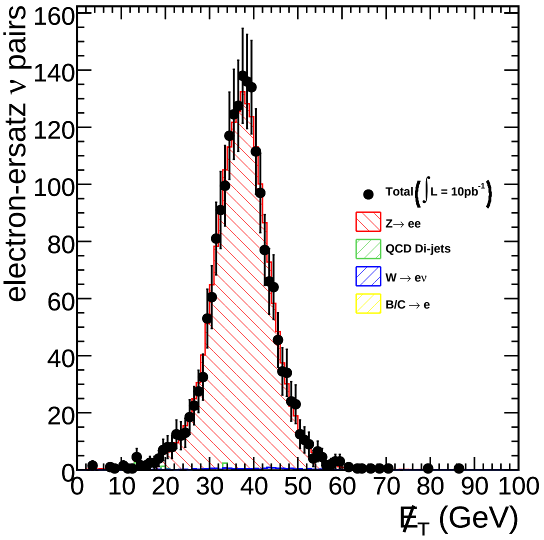

Figure 6.14: Ersatz $\not\!\!E_T$ showing background contamination after ersatz neutrino selection. For events with a 'W electron' in the barrel.

selection, there will be a substantial proportion of events with only one combination. An unbiased selection of electron-ersatz neutrino combinations can be made, recognising that in the ideal case, the inefficiency of electron reconstruction would not be a concern and there is nothing to differentiate between the two combinations. In a realistic scenario, this is equivalent to choosing one electron-ersatz neutrino pair at random in two combination events and using the only electron-ersatz neutrino pair in one combination events, but giving the one-pair events a weighting of 0.5. This 2:1 weight ratio ensures that the one combination events are not overrepresented in the ersatz $\not\!\!E_T$ distribution : without it, incorrect missing energy distributions were obtained. The use of only one combination from the two combination case removes bias due to the overrepresentation of certain kinds of event : for example, events with large boson momentum, or low hadronic activity.

6.6.2 Calorimetric Missing Transverse Energy

Calorimetric missing transverse energy [66, 67] is defined as the two-dimensional vector sum (6.1) over calorimeter towers. Calorimeter towers are combinations of calorimeter

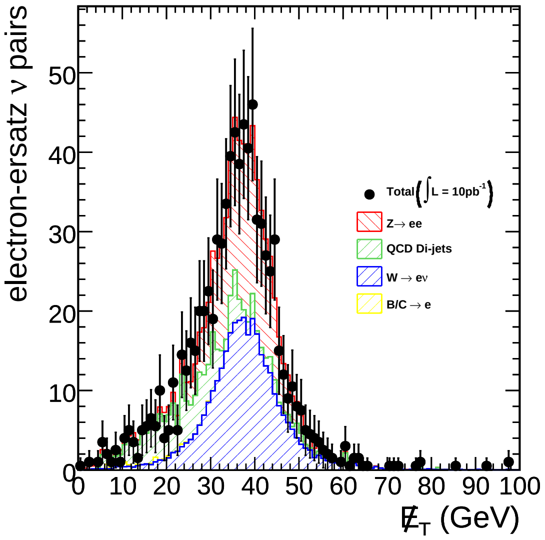

Figure 6.15: Ersatz $\not\!\!E_T$ showing background contamination without ersatz neutrino selection. For events with a 'W electron' in the endcap.

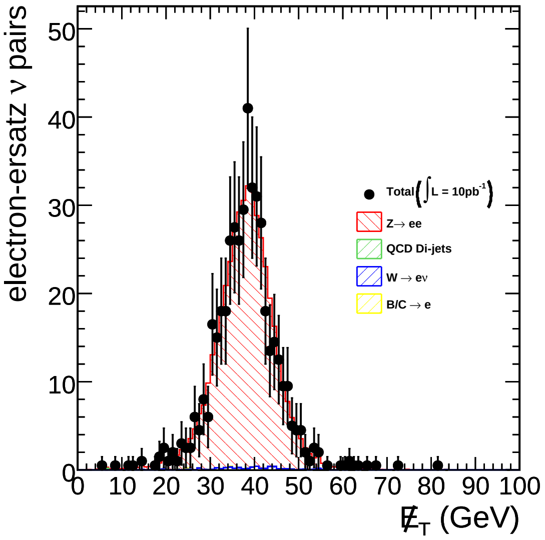

Figure 6.16: Ersatz $\not\!\!E_T$ showing background contamination after ersatz neutrino selection. For events with a 'W electron' in the endcap.

cells used in the reconstruction algorithms for jets and missing energy. In the barrel and endcap calorimeters, they consist of an HCAL tower and the ECAL crystals in front of this tower. In the HF, the short and long fibres are grouped into towers.

The energy of calorimeter towers is reconstructed by summing the energy of the constituent cells. A threshold is imposed on cell energies. These thresholds are applied to suppress noise contributions to the energy measurements. The standard set of thresholds is known as Scheme B [68]. If no cell in a tower passes its threshold, then the tower is not used for jet or missing energy reconstruction.

Not all ECAL crystals are read out in an event. The Selective Readout Processor [69] decides which crystals are read out. The selective readout defines regions of interest based on ECAL trigger tower energies. If a tower is of high interest, the 3×3 array of towers around it is read-out unsuppressed. If a tower is of moderate interest, it alone is read-out unsuppressed. If it is of low interest, it is read-out with zero-suppression (ZS) thresholds applied unless it is a neighbour of a high interest tower. In the zero-suppressed towers, crystals are only read out in EB if $E > 100\,\mathrm{MeV}$ and in EE if $E > 300\,\mathrm{MeV}$[1].

---

[1] In the endcaps, the units read-out unsuppressed or with zero-suppression are 5×5 supercrystals.

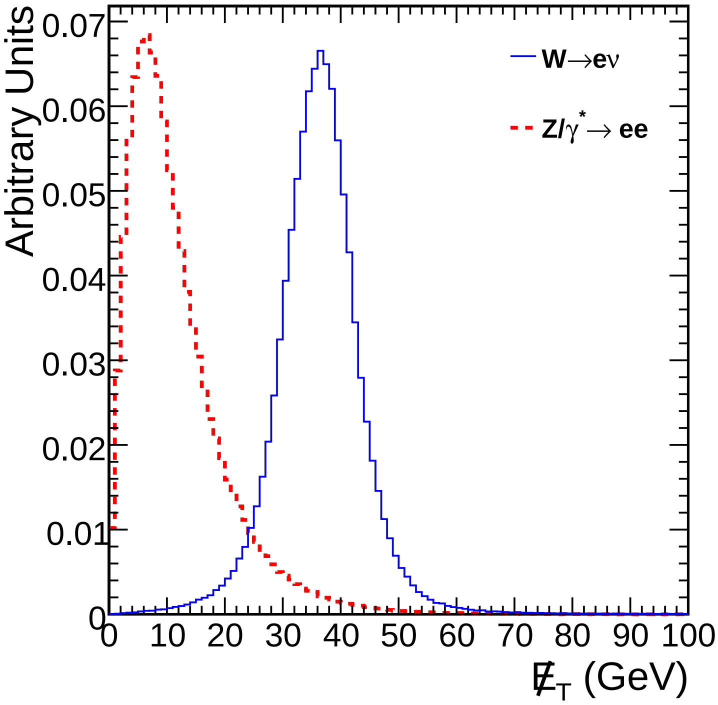

Figure 6.17: Missing transverse energy reconstructed in the calorimeter for $W^\pm \to e^\pm\, \nu_e$ and $\gamma^*/Z \to e^+e^-$ events.

In the datasets analysed here, high interest towers are those with $E_T > 1\,\mathrm{GeV}$ and the moderate interest category is not used.

This zero suppression scheme complicates the formation of ersatz missing energy. Neutrinos deposit no energy in the calorimeter and hence do not promote towers to the high interest category : ersatz neutrinos are electrons, so deposit energy in the calorimeter and do promote towers into the high interest category. This introduces a difference in the treatment of noise. After pedestal subtraction, the noise is symmetric around zero so in the unsuppressed high interest regions, there should be no net noise contribution to the $\not{E}_T$ sum. However, the zero-suppression threshold removes all negative noise contributions, destroying the symmetry and leading to a noise contribution to the $\not{E}_T$ sum.

This introduces a discrepancy between the missing energy reconstructed in $W^\pm \to e^\pm\, \nu_e$ events and the ersatz missing energy. In $W^\pm \to e^\pm\, \nu_e$ events, there will be noise reconstructed as energy around the neutrino – i.e. in the opposite direction to the electron – that will reduce the reconstructed missing energy. In $Z \to e^+\, e^-$ events, there will no such opposing energy reconstructed from noise and so the ersatz $\not{E}_T$ will be larger than in the

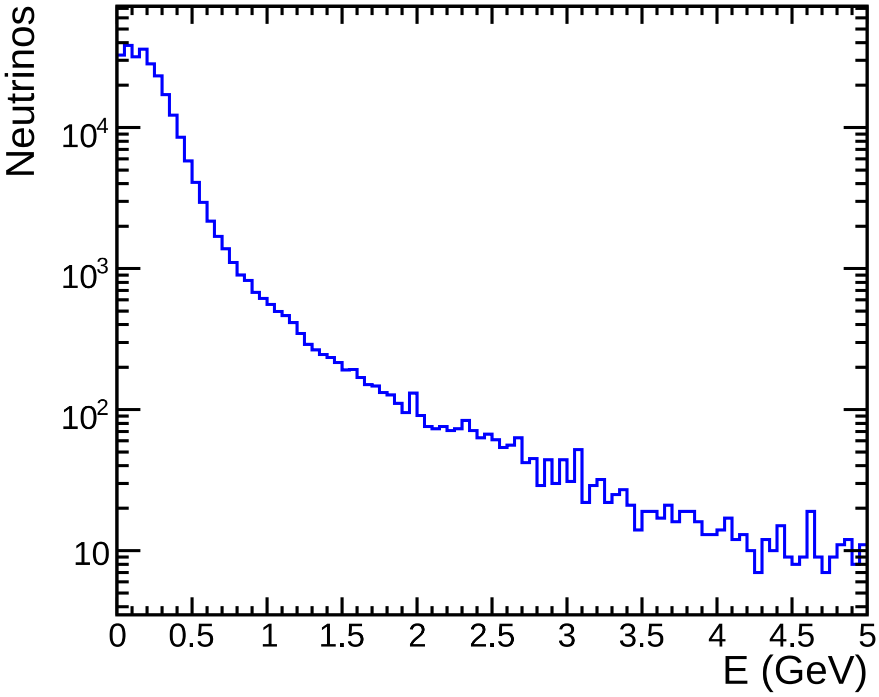

Figure 6.18: Energy reconstructed in 3 × 3 trigger towers around neutrinos ($|\eta^{\nu}| < 1.218$) in $\mathrm{W}^{\pm} \rightarrow \mathrm{e}^{\pm}\, \nu_{\mathrm{e}}$.

$\mathrm{W}^{\pm} \rightarrow \mathrm{e}^{\pm}\, \nu_{\mathrm{e}}$ case. This discrepancy can be remedied by including the small expected noise contribution in the ersatz $\not{E}_T$ sum. It is added in the direction of the neutrino. An example of the noise contribution is shown in Figure 6.18.

6.6.3 Electron Energy Removal

After the ersatz neutrino is selected, its energy must be removed from the missing transverse energy sum. Several different removal methods were assessed. It was found that removing the energy using superclusters provided the best performance in terms of the final ersatz missing energy result; was simple in its implementation; and offered flexibility in that the supercluster could be readily replaced with another object – a Particle Flow electron, for example.

The supercluster properties are used to create fourvectors. The magnitude of these fourvectors was the energy of the supercluster; while the direction was that of the supercluster from the vertex used in the missing energy calculation (always (0, 0, 0) in these data samples).

$$p^{\mu}_{SC} = \left(E_{SC}, \frac{E_{SC}\cos\phi}{\cosh\eta}, \frac{E_{SC}\sin\phi}{\cosh\eta}, E_{SC}\tanh\eta \right) \tag{6.9}$$

The raw energy of these superclusters was used, for the various corrections made to the energy of superclusters are not made to the energies in the calorimetric missing energy sum.

It should be noted that the clustering algorithms do not include all crystals with energy deposits. The missing energy calculation does incorporate all crystals in towers which satisfy the Scheme B thresholds.

6.6.4 Calculation of Ersatz Missing Transverse Energy

The fourvectors of the ersatz neutrino, $p^{\mu}_{ersatz-\nu}$, and the other electron, p^{μ}_{reco-e}, are formed as in (6.9). The rescaling of p^{μ}_{reco-e} into the 'W-like electron' fourvector $(p')^{\mu}_{reco-e}$ is performed following Chapter 6.4. In this case, the properties of the Z boson are calculated from the reconstructed electron objects, rather than just these supercluster fourvectors. Doing this incorporates track information and improves the measurement accuracy of the boost applied.

The apparent momentum imbalance $\not{p}^{\mu}_{ersatz}$ is calculated from these fourvectors and the actual missing energy reconstructed for that event, using (6.6) and (6.7).

6.6.5 Correction for Electron and Ersatz Neutrino Selection Inefficiency

Although the same electron reconstruction algorithms and selection criteria are used in both the $\mathrm{W}^{\pm} \rightarrow \mathrm{e}^{\pm}\, \nu_{\mathrm{e}}$ and $\mathrm{Z} \rightarrow \mathrm{e}^{+}\, \mathrm{e}^{-}$ events, they are a source of discrepancy between the two event types. This is due to the dependence of the efficiency of the reconstruction and selection on the kinematics of the electron : $\epsilon(p_T, \eta)$. In the Ersatz Missing Energy process, the electrons in $\mathrm{Z} \rightarrow \mathrm{e}^{+}\, \mathrm{e}^{-}$ have their kinematics rescaled ($p_T \rightarrow p'_T$, $\eta \rightarrow \eta'$) to represent electrons in $\mathrm{W}^{\pm} \rightarrow \mathrm{e}^{\pm}\, \nu_{\mathrm{e}}$. If $\epsilon(p_T, \eta) \neq \epsilon(p'_T, \eta')$, then the effect is to skew the ersatz $\not{E}_T$ distribution by over- or under-representing events which have electrons with particular properties.

The clearest example is that of a p_T criterion applied to the unrescaled electrons (e.g. a trigger threshold) : suppose electrons with p_T greater than the threshold pass with 100% efficiency and those below the threshold never pass. In this case, passing $\mathrm{Z} \rightarrow \mathrm{e}^+ \mathrm{e}^-$ electrons may have their p_T rescaled below the threshold : leaving a population of $\mathrm{Z} \rightarrow \mathrm{e}^+ \mathrm{e}^-$ electrons in a kinematic region no $\mathrm{W}^\pm \rightarrow \mathrm{e}^\pm \nu_\mathrm{e}$ electrons can populate. This would lead to a bias in the ersatz $\not\!\!E_T$ distribution. Such biases can arise from any kinematically-dependent efficiency.

This bias can be corrected using event weights :

$$w = \frac{\epsilon(p'_T, \eta')}{\epsilon(p_T, \eta)} \tag{6.10}$$

The weights used in this analysis are shown in Figure 6.19. The efficiency terms could in principle be determined using the tag and probe method as described in Chapter 7. As the selection aimed to use criteria with smoothly varying efficiencies, the results obtained with the limited number of $\mathrm{Z} \rightarrow \mathrm{e}^+ \mathrm{e}^-$ events available may be accurate : however the binning used may be too coarse, leading to incorrect weighting. In this analysis, weighting was performed using fine-grained efficiencies determined from simulation. In data-taking, these simulated efficiencies could be verified using the tag and probe results, or the tag and probe results could be used directly.

The inefficiency of the ersatz neutrino selection must be corrected for too, since the true neutrino in $\mathrm{W}^\pm \rightarrow \mathrm{e}^\pm \nu_\mathrm{e}$ does not have to meet any criteria. The efficiency of the ersatz neutrino selection is shown as a function of η in Figure 6.20. The ersatz missing energy distributions were reweighted by the reciprocal of these efficiencies to remove this bias. In data-taking, these efficiencies can be measured using the tag and probe method.

The ersatz $\not\!\!E_T$ distribution after these efficiency reweightings is shown in Figure 6.21, compared with the W $\not\!\!E_T$ for events with the neutrino limited to the detector acceptance.

6.6.6 Correction for Ersatz Neutrino Acceptance

The triggering, reconstruction and selection of $\mathrm{W}^\pm \rightarrow \mathrm{e}^\pm \nu_\mathrm{e}$ events does not involve the direct detection of the neutrino. There is essentially full acceptance for the neutrino. In contrast, the ersatz neutrino is limited by the detector acceptance. This results in a ersatz $\not\!\!E_T$ distribution (Figure 6.22) which is skewed towards higher $\not\!\!E_T$.

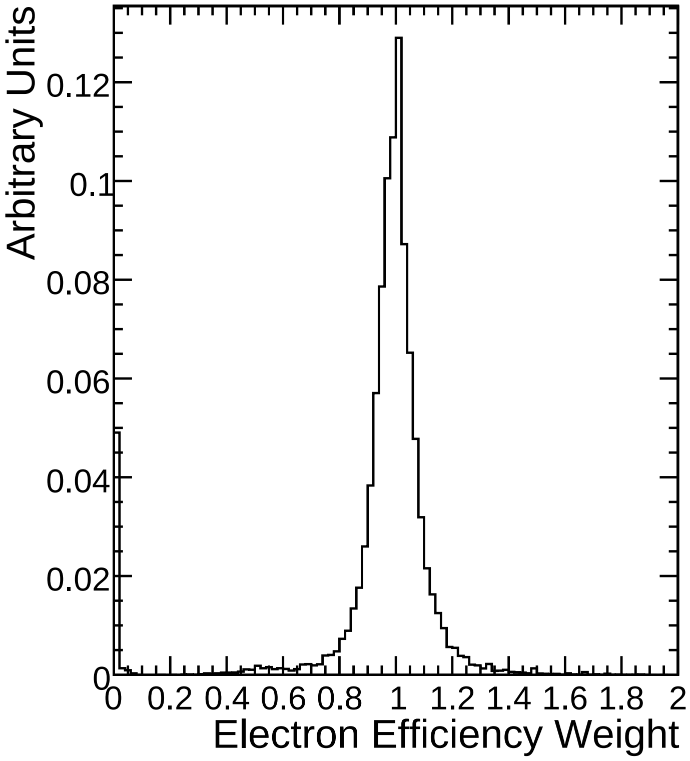

Figure 6.19: Event weights applied for electron $\epsilon(p_T, \eta) \neq \epsilon(p'_T, \eta')$

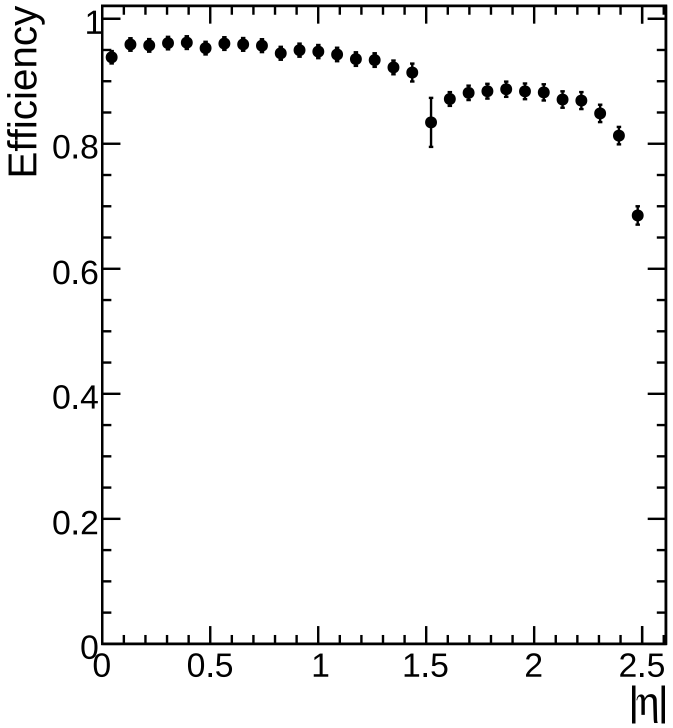

Figure 6.20: Efficiency of ersatz neutrino selection versus $|\eta|$.

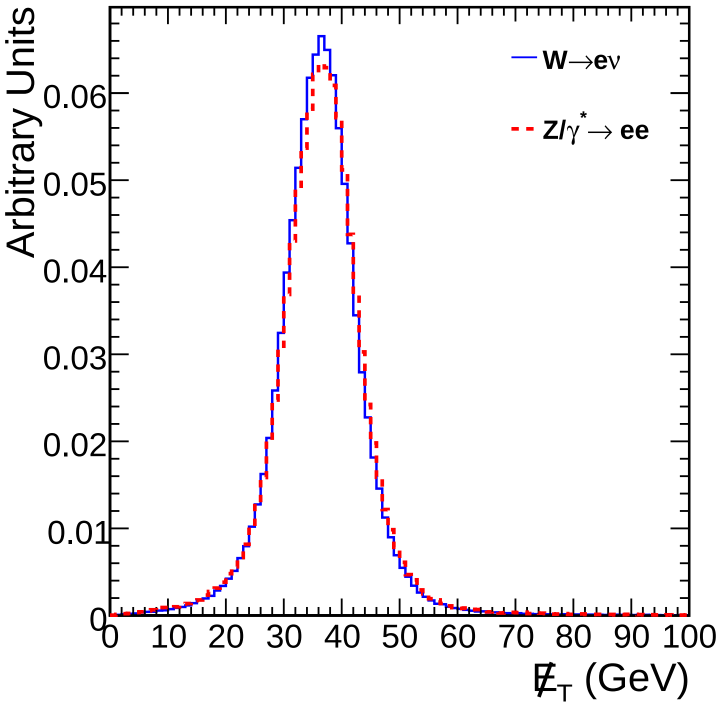

Figure 6.21: Ersatz reconstructed missing transverse energy, compared with $W^\pm \rightarrow e^\pm \nu_e$ events with the neutrino within the detector geometric acceptance.

The correction for this discrepancy must be derived from Monte Carlo simulation. It is calculated by dividing each bin i of the $\not\!\!E_T$ distribution of all $\mathrm{W}^\pm \rightarrow \mathrm{e}^\pm\,\nu_\mathrm{e}$ passing the electron selection, W_i^{tot}, by the $\not\!\!E_T$ distribution of the subset of events that also have the neutrino within the detector acceptance, W_i^{in}. The resulting correction factors (Figure 6.23) then multiply the corresponding bin i of the ersatz distribution.

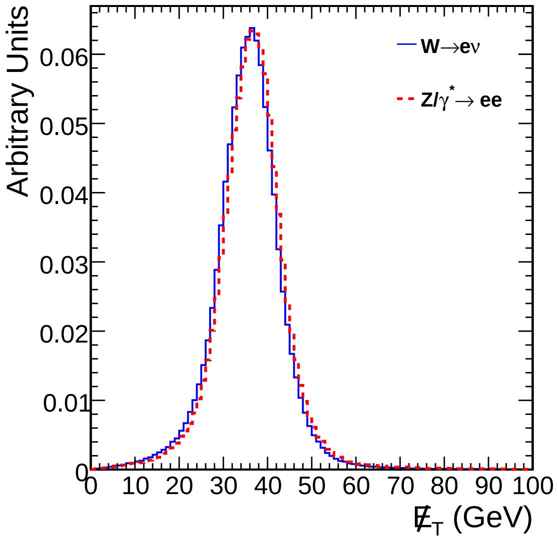

Figure 6.22: Ersatz reconstructed missing transverse energy without neutrino acceptance correction, compared with reconstructed missing transverse energy in $\mathrm{W}^\pm \rightarrow \mathrm{e}^\pm\,\nu_\mathrm{e}$.

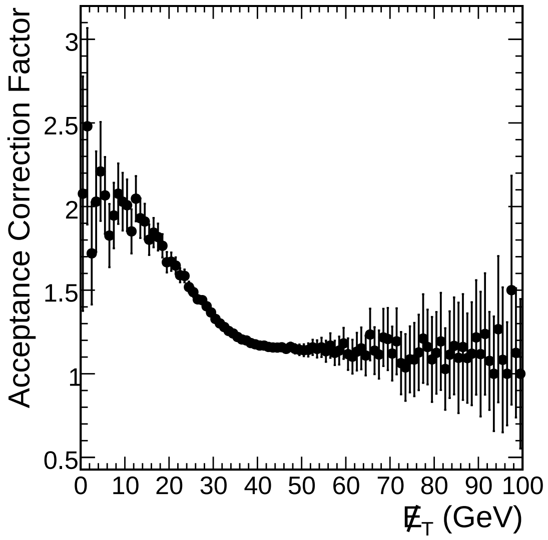

Figure 6.23: Multiplicative factors for each bin of $\not\!\!E_T$, used to correct for limited ersatz neutrino acceptance.

Although this correction is based on Monte Carlo simulation, it is appropriate for use in an early data-driven analysis : the overall effect of the correction is a small one, as illustrated by Figure 6.22; as seen in Chapter 5 the theoretical basis is sound, with accurate predictions; and the detector simulation aspect can be verified by comparing the distribution W_i^{in} with the ersatz $\not\!\!E_T$ distribution before the correction is made.

6.7 Results

The final, fully corrected ersatz $\not\!\!E_T$ distribution is shown in Figure 6.24. A good level of agreement has been obtained at reconstruction level – similar to that achieved using Monte Carlo generator truth objects – although again, differences remain.

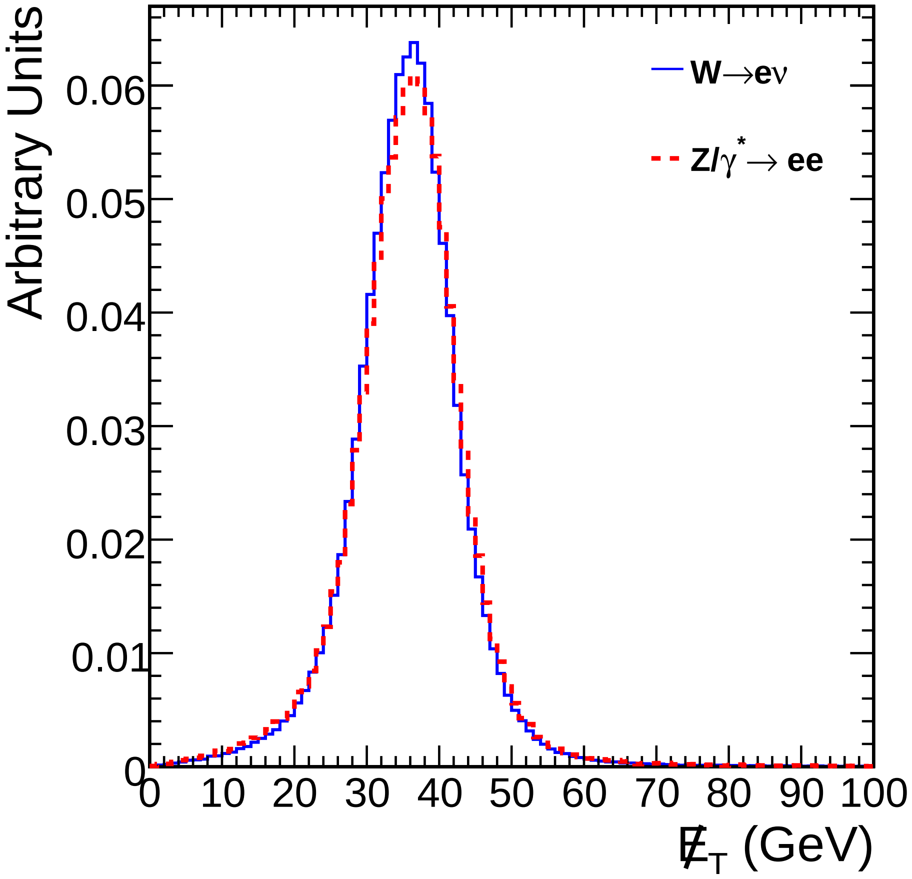

Figure 6.24: Ersatz reconstructed missing energy, with all corrections applied.

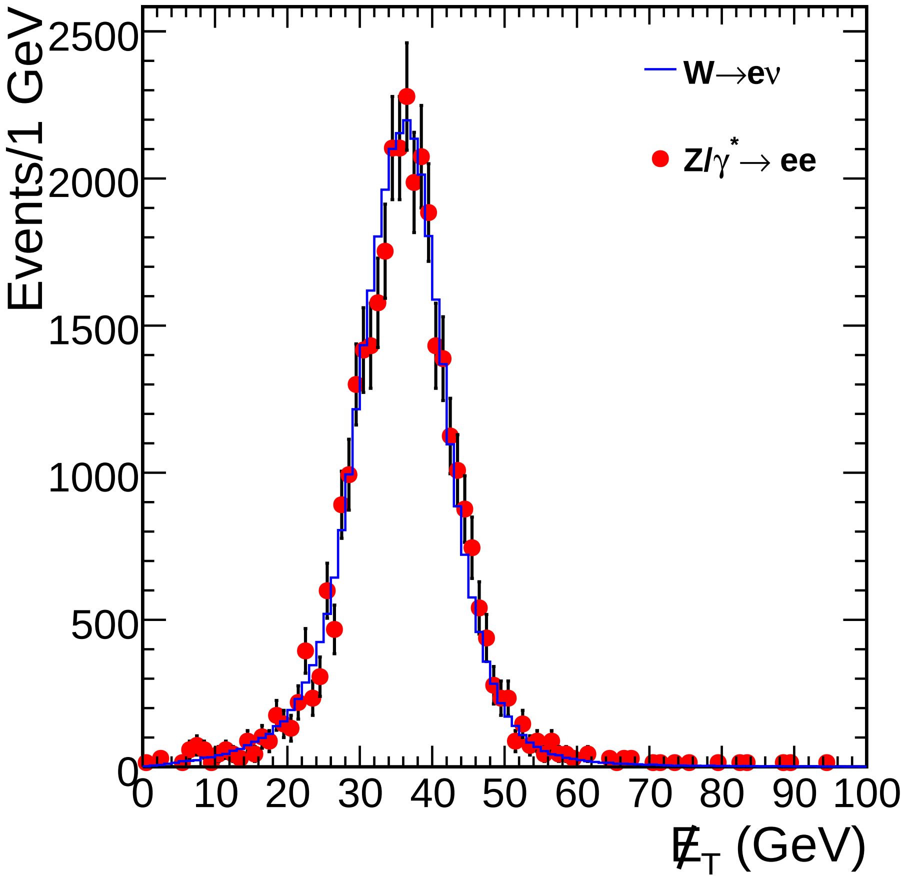

Figure 6.25: Ersatz reconstructed missing energy, with all corrections applied. Normalisation is to the number of $W^{\pm} \to e^{\pm}\,\nu_e$ events expected for $\int Ldt = 10\,\mathrm{pb}^{-1}$. Statistical accuracy corresponds to $\int Ldt = 10\,\mathrm{pb}^{-1}$.

The ersatz $\not\!\!E_T$ distribution obtained with the equivalent of $\int Ldt = 10\,\mathrm{pb}^{-1}$ of data is shown in Figure 6.25. For $\int Ldt = 10\,\mathrm{pb}^{-1}$ statistics, the comparison of the two distributions gives a $X^2/\mathrm{ndf} = 102/99$, corresponding to a p-value of 39.6% [2]. To this statistical precision, the two histograms may be considered compatible.

The significance of the remaining discrepancy in terms of an $\int Ldt = 10\,\mathrm{pb}^{-1}$ cross-section measurement has been evaluated by examining the resultant bias in the measurement of the efficiency of an $\not\!\!E_T > X$ selection criterion. This is shown in Figure 6.26. The bias values were determined by scanning the $\not\!\!E_T$ boundary value across the two distributions : the bias values are therefore correlated with each other. The absolute bias in the efficiency is less than 1.5% over the whole range of $\not\!\!E_T$ thresholds.

---

[2] The exact values of this χ^2 test should be treated with caution as some bins in the ersatz $\not\!\!E_T$ distribution were unpopulated.

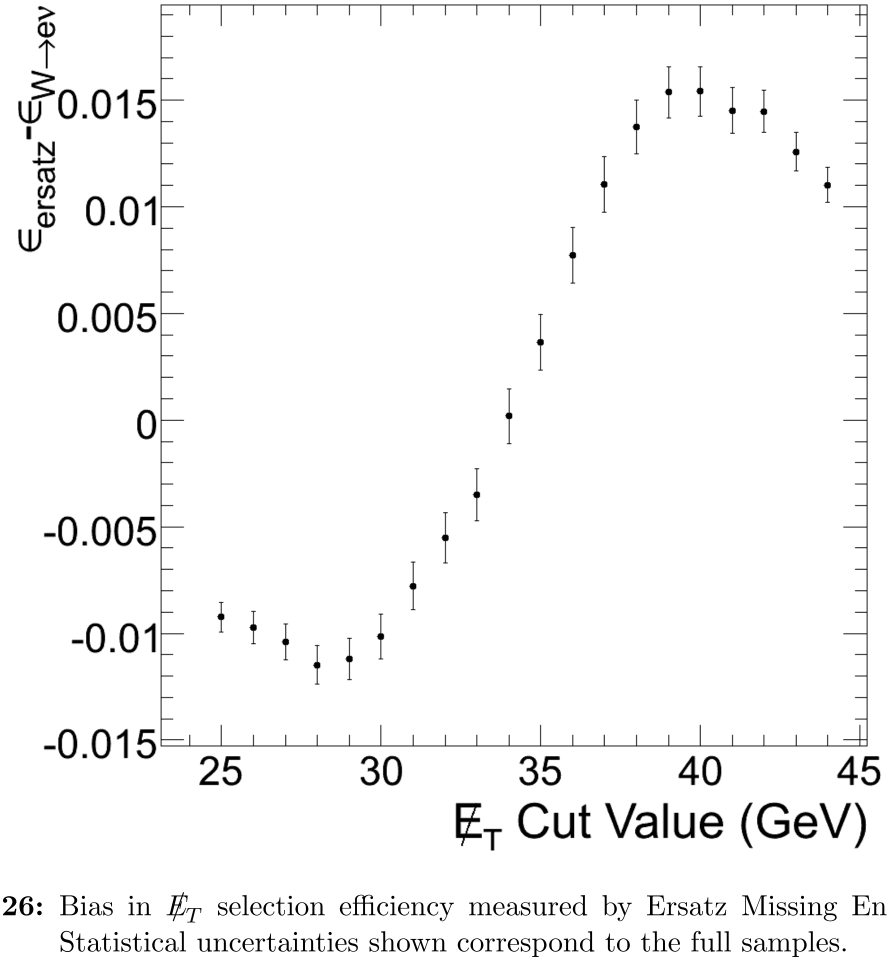

Figure 6.26: Bias in $\not\!\!E_T$ selection efficiency measured by Ersatz Missing Energy method. Statistical uncertainties shown correspond to the full samples.

The effect of the various corrections applied to the ersatz $\not\!\!E_T$ can be seen in Table 6.4, which shows the increases in the efficiency determination bias when the corrections are not applied. Applying all the corrections gives the best $\not\!\!E_T$ description, although the improvement gained by reweighting according to electron efficiency is small. This correction could be neglected for the $\int Ldt = 10\,\mathrm{pb}^{-1}$ cross-section measurement (unless the kinematic dependence of the electron efficiencies increased dramatically).

Correction Not Applied	Maximum Efficiency Bias Found
None	1.5%
Electron efficiency weighting	1.7%
Ersatz neutrino efficiency weighting	2.0%
Ersatz neutrino noise correction	3.8%
Ersatz neutrino acceptance correction	4.7%

Table 6.4: Maximum biases in $\not\!\!E_T > X$ ($25\,\mathrm{GeV} < X < 45\,\mathrm{GeV}$) efficiency determination when the specified correction is not applied.

Potential sources for the remaining bias in the fully corrected ersatz $\not\!\!E_T$ are the fundamental physical differences between $\mathrm{W}^{\pm} \rightarrow \mathrm{e}^{\pm}\,\nu_{\mathrm{e}}$ and $\mathrm{Z} \rightarrow \mathrm{e}^{+}\,\mathrm{e}^{-}$; the measurement of the Z boson properties using reconstructed electrons; the energy measurements of the electron and the ersatz neutrino, in particular for energy removal; and the mass reweighting.

All of these sources of the discrepancy and the correlations between them are included in the simulation and this analysis. Thus, the bias values shown in Figure 6.26 provide an estimate for the systematic uncertainties associated with these sources. However, there are other potential sources of systematic uncertainty in the real measurement which have not been incorporated : the statistical uncertainties associated with the Tag and Probe method; and mis-modelling of the calorimeter $\not\!\!E_T$ simulation used in the ersatz neutrino acceptance calculation.

The uncertainties on the tag and probe method arising from the limited statistics have been evaluated by performing 10000 pseudo-experiments, in which the neutrino efficiency weights were varied. The weights were calculated using efficiencies sampled at the beginning of each experiment from distributions representing each efficiency and its statistical uncertainty for $\int Ldt = 10\,\mathrm{pb}^{-1}$. The uncertainty in the $\not\!\!E_T > X$ efficiency was found to be negligible.

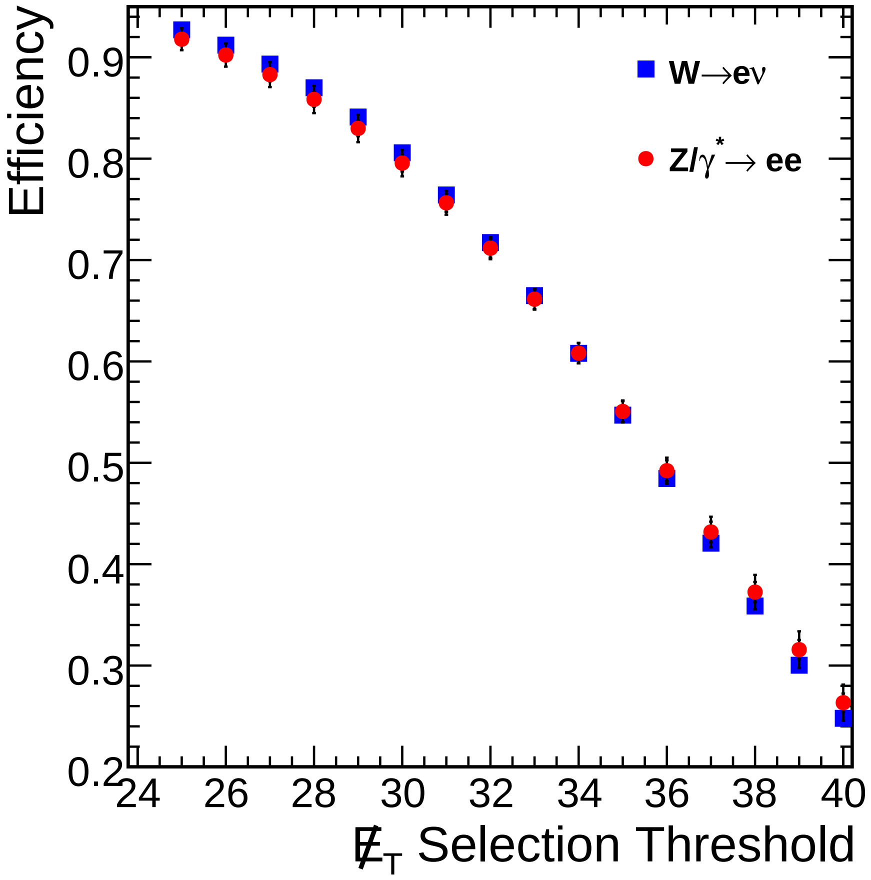

Figure 6.27: $\not{E}_T$ selection efficiency measured by Ersatz Missing Energy method, compared with the actual efficiencies. The inner error bar represents the statistical uncertainty; the outer the combined statistical and systematic uncertainties.

The systematic uncertainty arising from the neutrino acceptance calculation will be reducible in the data-taking, as the simulation of the calorimetric missing energy will be tuned to match the observed data. Indeed, the Ersatz Missing Energy method may be useful in this process as described earlier. With these considerations, the systematic uncertainty has been evaluated by performing 10000 pseudo-experiments in each of which the simulated $\mathrm{W}^{\pm} \rightarrow \mathrm{e}^{\pm}\, \nu_{\mathrm{e}}$ calorimetric $\not{E}_T$ has been shifted by some random factor sampled from a Gaussian, $\mu = 1$ and $\sigma = 0.05$. The maximum induced uncertainty in the efficiency is for $\not{E}_T > 37\,\mathrm{GeV}$, with $\sigma = \pm 0.4\%$. For $\not{E}_T > 30\,\mathrm{GeV}$, the uncertainty $\sigma = \pm 0.2\%$.

Figure 6.27 shows $\not{E}_T$ selection efficiencies measured using the Ersatz Method and their actual values. Shown are both the statistical and the systematic uncertainties. For the particular $\not{E}_T > 30\,\mathrm{GeV}$ value used in the following Chapter, the ersatz measured efficiency is :

$$\epsilon(\not\!\!E_T > 30\,\mathrm{GeV}) = 79.6 \pm 0.6(\mathrm{stat}) \pm 1.0(\mathrm{syst})\% \tag{6.11}$$

The results of Chapter 7 show that the uncertainty introduced into the final cross-section measurement by the Ersatz Method is of a comparable magnitude to that of the other data-driven techniques used. Furthermore, it is much smaller than the 10% uncertainty associated with the integrated luminosity measurement. On this basis, the Ersatz Method is an appropriate tool for an early, data-driven cross-section measurement.

7 Measurement of the W and Z Cross-Sections

"There are two possible outcomes: if the result confirms the hypothesis, then you've made a measurement. If the result is contrary to the hypothesis, then you've made a discovery."

— Enrico Fermi

This chapter describes the current strategy for the measurement of the electroweak vector boson production cross-sections in early data using the CMS detector, following from the discussion and analysis of the previous chapters. The author was heavily involved in the first iteration of the cross-section analysis [70], both in formulating the strategy and implementing it in a technical sense. The results shown are from a more recent iteration [60]. While this update benefits from improvements in the reconstruction and selection algorithms, little has changed in terms of philosophy, technique or final results.

7.1 Introduction

A cross-section measurement made with $10\,\mathrm{pb}^{-1}$ will be one of the first results from CMS and the LHC. For this early data, the ultimate calibration and alignment of the detector will not be available and Monte Carlo simulations may not yet accurately describe the detector and the LHC environment. Thus the strategy for making the measurements place emphasis on mitigating any effects consequent to this : simple and robust selections are employed and data-driven methods are used to measure efficiencies and estimate signal and background yields.

7.2 Cross-section Measurement

The $\mathrm{W}^{\pm} \rightarrow \mathrm{e}^{\pm}\, \nu_{\mathrm{e}}$ cross section is calculated using the following formula :

$$\sigma_W \cdot BR(\mathrm{W}^{\pm} \rightarrow \mathrm{e}^{\pm}\, \nu_{\mathrm{e}}) = \frac{N_W^{sig} - N_W^{bkgd}}{A_W \epsilon_W \int Ldt} \tag{7.1}$$

N_W^{sig} and N_W^{bkgd} are the number of signal and background events selected in the data. ϵ_W is the efficiency of triggering, reconstructing and selecting the $\mathrm{W}^{\pm} \rightarrow \mathrm{e}^{\pm}\, \nu_{\mathrm{e}}$ events. A_W is the geometric and kinematic acceptance, which is determined from simulation. The integrated luminosity, $\int Ldt$, will be measured in an independent analysis.

The same equation gives the $\gamma^*/\mathrm{Z} \rightarrow \mathrm{e}^+\mathrm{e}^-$ cross-section :

$$\sigma_Z \;\cdot\; BR(\gamma^*/\mathrm{Z} \rightarrow \mathrm{e}^+\mathrm{e}^-) \;=\; \frac{N_Z^{sig} - N_Z^{bkgd}}{A_Z \;\times\; \epsilon_Z \;\times\; \int Ldt} \tag{7.2}$$

7.3 Data Analysed

This analysis was performed in CMSSW 2.2.8 on the Summer 08 datasets listed in Table 7.1. Details of the production of the samples are given in Section 6.2. The cross-section predictions for the electroweak processes were scaled from the PYTHIA 6.416 values to those of MC@NLO [71]. The $\mathrm{t\bar{t}}$ sample used TAUOLA [72] to decay the $\mathrm{t\bar{t}}$ pair generated by PYTHIA. The γ + jet samples were filtered at generator level to demand the photon had $E_T > 15\,\mathrm{GeV}$ and $|\eta| < 2.4$.

7.4 Event Selection

7.4.1 Trigger

All events selected for use in both the $\mathrm{W}^{\pm} \rightarrow \mathrm{e}^{\pm}\, \nu_{\mathrm{e}}$ and $\gamma^*/\mathrm{Z} \rightarrow \mathrm{e}^+\mathrm{e}^-$ cross-section measurements must have been accepted by the single electron trigger HLT_Ele15_LW_L1R. L1R indicates that at Level-1 both isolated and non-isolated electromagnetic candidates are accepted, providing their $E_T > 10\,\mathrm{GeV}$. The HLT demands the electron supercluster

Process	σ (pb)	ϵ	Equivalent $\int Ldt$ (pb^{-1})
$\mathrm{W}^\pm \to \mathrm{e}^\pm \nu_\mathrm{e}$	13865 (NLO)	0.738	109
$\gamma^*/\mathrm{Z} \to \mathrm{e}^+\mathrm{e}^-$ ($m_{ee} > 20\,\mathrm{GeV}$)	2276 (NLO)	1	200
$\gamma/\mathrm{Z} \to \tau\tau$ ($m_{\tau\tau} > 40\,\mathrm{GeV}$)	1271 (NLO)	1	980
$\mathrm{W} \to \tau\nu_\tau$	13853 (NLO)	1	79.3
$\mathrm{t}\,\bar{\mathrm{t}}$	353 (NLO)	1	293
Light flavour di-jets :			
$20\,\mathrm{GeV} < \hat{p}_T < 30\,\mathrm{GeV}$	4×10^8	8×10^{-3}	6.36
$30\,\mathrm{GeV} < \hat{p}_T < 80\,\mathrm{GeV}$	1×10^8	4.7×10^{-2}	8.15
$80\,\mathrm{GeV} < \hat{p}_T < 170\,\mathrm{GeV}$	1.9×10^6	0.15	20.9
Heavy flavour di-jets :			
$20\,\mathrm{GeV} < \hat{p}_T < 30\,\mathrm{GeV}$	4×10^8	4.8×10^{-4}	10.4
$30\,\mathrm{GeV} < \hat{p}_T < 80\,\mathrm{GeV}$	1×10^8	2.4×10^{-3}	8.40
$80\,\mathrm{GeV} < \hat{p}_T < 170\,\mathrm{GeV}$	1.9×10^6	1.2×10^{-2}	47.2
γ + jet :			
$15\,\mathrm{GeV} < \hat{p}_T < 20\,\mathrm{GeV}$	1.8×10^5	0.49	1.07
$20\,\mathrm{GeV} < \hat{p}_T < 25\,\mathrm{GeV}$	62000	0.55	3.38
$25\,\mathrm{GeV} < \hat{p}_T < 30\,\mathrm{GeV}$	27000	0.57	8.95
$30\,\mathrm{GeV} < \hat{p}_T < 35\,\mathrm{GeV}$	13000	0.59	21.9
$35\,\mathrm{GeV} < \hat{p}_T$	19000	0.64	27.2

Table 7.1: Datasets analysed in $\mathrm{W}^\pm \to \mathrm{e}^\pm \nu_\mathrm{e}$ and $\gamma^*/\mathrm{Z} \to \mathrm{e}^+\mathrm{e}^-$ cross-section measurement analysis. ϵ is the efficiency of the generator level filtering (e.g. to account for geometrical acceptance) and is included in the equivalent $\int Ldt$. All samples were generated using PYTHIA 6.416 at $\sqrt{s} = 10\,\mathrm{TeV}$. The (NLO) cross-sections are scaled to the MC@NLO values.

has $E_T > 15\,\mathrm{GeV}$ (Ele15) and the pixel-matching is performed using the large windows (LW) defined in Table 4.2.

The criteria demanded by this trigger are very loose to ensure that very few $\mathrm{W}^\pm \to \mathrm{e}^\pm \nu_\mathrm{e}$ and $\gamma^*/\mathrm{Z} \to \mathrm{e}^+\mathrm{e}^-$ events are lost. No isolation or electron identification criteria beyond those in Section 4.5 are demanded and the large windows for the pixel hit search are used to maintain efficiency even with a displaced beamspot and a misaligned tracker.

7.4.2 Electron Selection

The event selection for both $\mathrm{W}^{\pm} \rightarrow \mathrm{e}^{\pm}\, \nu_{\mathrm{e}}$ and $\gamma^{*}/\mathrm{Z} \rightarrow \mathrm{e}^{+}\mathrm{e}^{-}$ uses the electron identification and isolation variables defined in Sections 4.3 and 4.4. The selection criteria are applied as a series of discrete cuts, with the thresholds applied shown in Tables 7.2 and 7.5.

These thresholds were selected using an algorithm described in detail in [73]. This algorithm takes a set of selection criteria and sets the thresholds which will achieve a certain target S/B (number of signal events/number of background events) ratio while maintaining the highest possible signal efficiency. The algorithm is an iterative procedure, which uses two event samples – one signal and the other background. Starting from a very loose selection, it varies each selection threshold in turn until a small, predefined improvement in S/B is achieved. The variable which achieves this improvement with the smallest efficiency loss has its threshold updated and the process reiterates. This continues until the target S/B is achieved.

It has been shown [73] that the algorithm can be used on samples defined in data, despite their impurities. One suitable definition for the background sample is electron candidates in events that have $\not{E}_T < 20\,\mathrm{GeV}$ and no second electron candidate. A high purity signal sample can be defined using the Tag and Probe method (Section 7.5), although this will limit the statistical accuracy of the method. An alternative definition, with lower purity but giving access to many more events, is electron candidates in events that have $\not{E}_T > 30\,\mathrm{GeV}$.

7.4.3 Selection of $\mathrm{W}^{\pm} \rightarrow \mathrm{e}^{\pm}\, \nu_{\mathrm{e}}$ Events

From the events passing HLT_Ele15_LW_L1R, $\mathrm{W}^{\pm} \rightarrow \mathrm{e}^{\pm}\, \nu_{\mathrm{e}}$ events were selected by demanding an electron that satisfies the criteria in Table 7.2; has $E_T > 30\,\mathrm{GeV}$; and is within the ECAL fiducial region. Events with a second reconstructed electron $E_T > 20\,\mathrm{GeV}$ were rejected. Tables 7.3 and 7.4 show the efficiencies for this selection. The distribution of $\not{E}_T$ for events passing this complete selection is shown in Figure 7.1.

Criterion	EB Threshold	EE Threshold
$\sigma_{i\eta i\eta}$ <	0.0099	0.028
$\Delta\phi_{\text{in}}$ <	0.025	0.020
$\Delta\eta_{\text{in}}$ <	0.004	0.0066
Track $\sum p_T$ <	2.2 GeV	1.1 GeV
ECAL $\sum E_T$ <	4.2 GeV	3.4 GeV
HCAL $\sum E_T$ <	2.0 GeV	1.3 GeV

Table 7.2: Electron selection criteria used for the $W^\pm \rightarrow e^\pm \nu_e$ cross-section analysis.

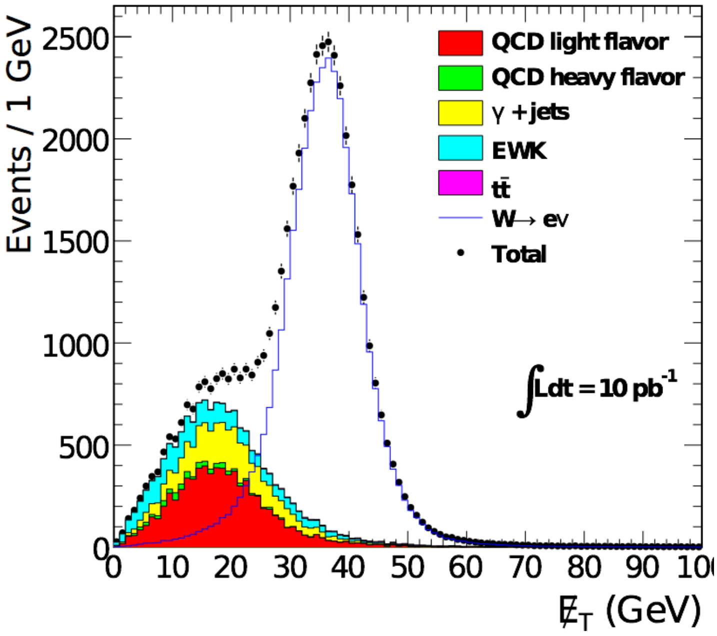

Figure 7.1: $\not{E}_T$ distribution of events after $W^\pm \rightarrow e^\pm \nu_e$ selection, showing signal and background.

	Number of Events (Relative Efficiency)			
		Light Flavour	Heavy Flavour	
Requirement	$W^{\pm} \to e^{\pm}\,\nu_e$	di-jets	di-jets	γ + jet
Electron, $E_T > 30\,\mathrm{GeV}$	47158	1.20×10^6	1.24×10^5	11850
Electron Isolation	40369 (85.6%)	31515 (2.62%)	862 (0.70%)	6953 (58.7%)
Electron Identification	37524 (93.0%)	7661 (24.3%)	454 (52.7%)	3906 (56.2%)
No second electron	37221 (99.2%)	7468 (97.5%)	441 (97.1%)	3848 (98.5%)
Combined Selection	$78.9 \pm 0.0\%$	$0.62 \pm 0.01\%$	$0.36 \pm 0.02\%$	$32.4 \pm 0.4\%$

Table 7.3: $W^{\pm} \to e^{\pm}\,\nu_e$ event selection efficiencies for signal and QCD background, as determined using MC truth. The uncertainties are statistical and correspond to full datasets.

	Number of Events (Relative Efficiency)			
Requirement	$\gamma^*/Z \to e^+e^-$	$W \to \tau\nu_\tau$	$\gamma/Z \to \tau\tau$	$t\,\bar{t}$
Electron, $E_T > 30\,\mathrm{GeV}$	7851	1394	374	852
Electron Isolation	6658 (84.8%)	652 (46.8%)	195 (52.1%)	322(37.8%)
Electron ID	6241 (93.7%)	543 (83.3%)	161 (82.3%)	303(94.1%)
No second electron	2344 (37.6%)	530 (97.6%)	150 (93.2%)	224(73.9%)
Combined Selection	$29.9 \pm 0.1\%$	$38.0 \pm 0.5\%$	$40.1 \pm 0.3\%$	$26.3 \pm 0.3\%$

Table 7.4: $W^{\pm} \to e^{\pm}\,\nu_e$ event selection efficiencies for electroweak backgrounds, as determined using MC truth. The uncertainties are statistical and correspond to full datasets.

7.4.4 Selection of $\gamma^*/Z \to e^+e^-$ Events

From the events passing HLT_Ele15_LW_L1R, those selected as $\gamma^*/Z \to e^+e^-$ contained two superclusters that each satisfied the criteria in Table 7.5; had $E_T > 20\,\mathrm{GeV}$; and were within the ECAL fiducial region. In order to select $Z \to e^+\,e^-$ events, a cut was placed on the di-electron invariant mass : $70\,\mathrm{GeV} < m_{ee} < 110\,\mathrm{GeV}$. Tables 7.6 and 7.7 show the efficiencies for this selection. The distribution of di-electron invariant mass for events passing this complete selection is shown in Figure 7.2.

Criterion	EB Threshold	EE Threshold
$\sigma_{i\eta i\eta} <$	0.01	0.028
$\Delta\eta_{\mathrm{in}} <$	0.0071	0.0066
Track $\sum p_T <$	7.2 GeV	5.1 GeV
ECAL $\sum E_T <$	5.7 GeV	5.0 GeV
HCAL $\sum E_T <$	8.1 GeV	3.4 GeV

Table 7.5: Electron selection criteria applied for the $\gamma^*/\mathrm{Z} \to \mathrm{e}^+\mathrm{e}^-$ cross-section analysis.

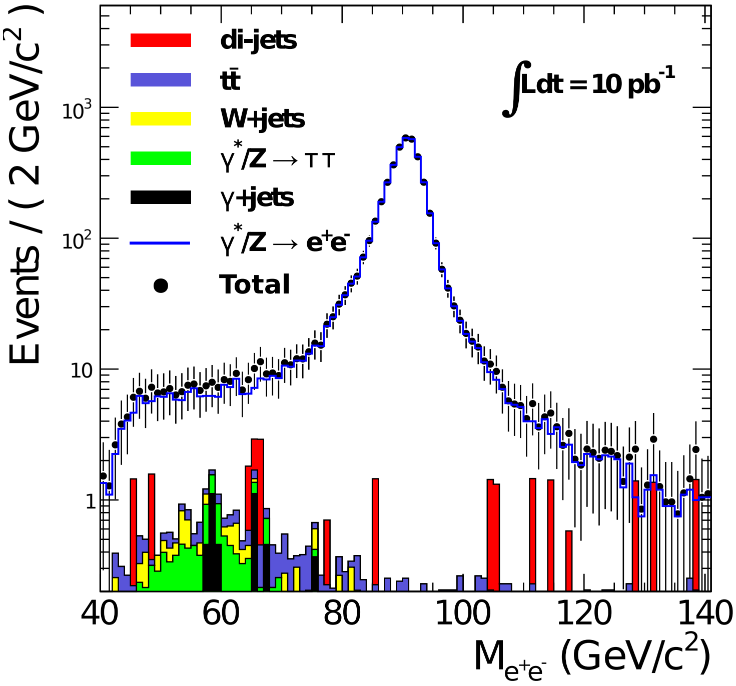

Figure 7.2: m_{ee} distribution of events after $\gamma^*/\mathrm{Z} \to \mathrm{e}^+\mathrm{e}^-$ selection, showing signal and background. The $70\,\mathrm{GeV} < m_{ee} < 110\,\mathrm{GeV}$ selection has not yet been applied.

Requirement	Number of Events (Relative Efficiency) $\gamma^*/Z \to e^+e^-$	Light Flavour di-jets	Heavy Flavour di-jets	γ + jet
2 Electrons, $E_T > 20\,\text{GeV}$	5208	90367	17823	240
Electron Isolation	4753 (91.3%)	343 (0.38%)	43 (0.24%)	16 (6.7%)
Electron Identification	4541 (95.5%)	23 (6.71%)	11 (20.0%)	4 (25%)
$70\,\text{GeV} < m_{ee} < 110\,\text{GeV}$	4258 (93.8%)	3 (13.0%)	2 (18.3%)	0 (0%)
Combined Selection	$81.8 \pm 0.01\%$	$0.00 \pm 0.00\%)$	$0.00 \pm 0.01\%$	$0 \pm 0\%$

Table 7.6: $\gamma^*/Z \to e^+e^-$ event selection efficiencies for signal and QCD background, as determined using MC truth. The uncertainties are statistical and correspond to full datasets.

Requirement	Number of Events (Relative Efficiency) $\gamma^*/Z \to e^+e^-$	$W^\pm \to e^\pm \nu_e$	$t\,\bar{t}$	$\gamma/Z \to \tau\tau$
2 Electrons, $E_T > 20\,\text{GeV}$	5208	555	296	52
Electron Isolation	4753 (91.3%)	26 (4.68%)	21 (7.09%)	18 (34.6%)
Electron Identification	4541 (95.5%)	8 (30.8%)	18 (85.7%)	10 (55.6%)
$70\,\text{GeV} < m_{ee} < 110\,\text{GeV}$	4258 (93.8%)	3 (37.5%)	5 (27.8%)	1 (10.0%)
Combined Selection	$81.8 \pm 0.01\%$	$0.55 \pm 0.09\%$	$1.69 \pm 0.14\%$	$1.92 \pm 0.19\%$

Table 7.7: $\gamma^*/Z \to e^+e^-$ event selection efficiencies for signal and electroweak backgrounds, as determined using MC truth. The uncertainties are statistical and correspond to full datasets.

7.5 Tag and Probe Efficiency Measurements

The efficiencies of the electron trigger, reconstruction and selection can be measured from data using the “Tag and Probe” method [74]. An unbiased and pure sample of leptons is obtained from $Z \to e^+ e^-$ for measuring the efficiency of a particular selection or reconstruction step. One electron, the ‘tag’, must meet stringent identification criteria to ensure it is an electron. It must also satisfy the requirements of the single electron trigger used to select the event. The other, ‘probe’ electron need satisfy only loose criteria and so is left unbiased. The purity of the probe sample is ensured by restricting the invariant mass of the electron pair to be about the Z mass.

This unbiased and pure probe sample can be used to measure the efficiency of a given electron reconstruction or selection step by simply dividing the number which pass this step, N_{pass} by the total number of probes, N_{tot}

$$\epsilon = \frac{N_{pass}}{N_{tot}} \tag{7.3}$$

7.5.1 Tag and Probe Selection

It is possible that the two electrons in a $\gamma^*/\mathrm{Z} \rightarrow \mathrm{e}^+\mathrm{e}^-$ event will each satisfy both the tag and the probe criteria. In this case both probes would be included in the efficiency determination. For this analysis, the tag was defined as a reconstructed electron that :

- is a geometric match to the object which passed the HLT_Ele15_LW_L1R single electron trigger path.
- passes the $\mathrm{W}^{\pm} \rightarrow \mathrm{e}^{\pm}\,\nu_{\mathrm{e}}$ electron identification criteria
- satisfies loose isolation criteria (track $\sum p_T < 5\,GeV$; ECAL and HCAL isolation $\sum E_T < 5\,GeV$ each).

The probe definition depended on the efficiency under study.

7.5.2 Factorisation of Efficiency

The efficiency for the complete offline electron reconstruction and selection, $\epsilon_{offline}$, could be calculated in one step : however it is beneficial to factorise the efficiency. Doing so provides data about the performance of each individual step that will be particularly useful in the early CMS running. The chosen factorisation sequence is :

$$\epsilon_{offline} = \epsilon_{GSFelec} \cdot \epsilon_{isolation} \cdot \epsilon_{ID} \tag{7.4}$$

where $\epsilon_{GSFelec}$ is the efficiency to reconstruct an electron object, given a supercluster; $\epsilon_{isolation}$, the efficiency of the GSF electron isolation conditions; and ϵ_{ID}, the efficiency of the electron ID, given an isolated electron. This factorisation scheme matches the sequence of reconstruction and selections steps used, although different factorisations can be used.

To account for correlations between the factorised efficiencies, the probes used to determine a particular efficiency must have passed all the preceding steps : e.g. the probes for $\epsilon_{isolation}$ are the electrons reconstructed from the passing supercluster probes of $\epsilon_{GSFelec}$. $\epsilon_{offline}$ is independent of the order of factorisation.

It should be noted that $\epsilon_{offline}$ does not include the efficiency of superclustering. This efficiency is dominated by the threshold turn-on curve, which will be determined using tuned simulation. Currently, the superclustering efficiency is included in the acceptance term. This entangles and confuses the meanings of acceptance and efficiency somewhat.

Despite the high background rejection power of the tag selection and the tag-probe invariant mass criteria, there will be significant background contamination of the probe sample for the determination of $\epsilon_{GSFelec}$. Subsequent probe samples will be effectively free of background due to the additional rejection inherent in demanding a GSF track matched to the supercluster. Although various background subtraction methods have been studied [74], unfortunately none could be applied in this analysis. Therefore no background is included in these efficiency measurements.

The efficiency for an electron to pass the trigger, ϵ_{online}, is defined relative to the offline efficiency, i.e. probes are fully reconstructed and selected electrons which must match the electron reconstructed by the trigger in order to pass. Defining the efficiencies in this way preserves the generality of the offline efficiency, allowing it to be applied to events with a different trigger scheme.

7.5.3 Kinematically Dependent Efficiencies

The definition of efficiencies in terms of electrons rather than events allows them to be applied to different event types. However, the electron efficiencies are functions of the electron kinematics, which differ between event types. In particular, it was shown in Chapter 5 that the kinematics of the electrons in $\gamma^*/\mathrm{Z} \rightarrow \mathrm{e}^+\mathrm{e}^-$ and $\mathrm{W}^\pm \rightarrow \mathrm{e}^\pm\, \nu_\mathrm{e}$ events are different.

In order to apply efficiencies measured in $\gamma^*/\mathrm{Z} \rightarrow \mathrm{e}^+\mathrm{e}^-$ events to $\mathrm{W}^\pm \rightarrow \mathrm{e}^\pm\, \nu_\mathrm{e}$ electrons, it is therefore necessary to bin them against the differing kinematic variables simultaneously : $\epsilon = \epsilon(E_T, \eta)$. To estimate the integrated electron efficiency for $\mathrm{W}^\pm \rightarrow \mathrm{e}^\pm\, \nu_\mathrm{e}$ events, the binned efficiencies, ϵ_{ij}, can be weighted with the relative abundance of electrons in the bins, a_{ij} and summed in order to estimate the integrated efficiency :

$$\epsilon = \sum_i \sum_j a_{ij}\epsilon_{ij} \tag{7.5}$$

The relative abundance of electrons is the fraction of electron acceptance in that bin and must be determined from simulation :

$$a_{ij} = \frac{\mathcal{A}_i}{\mathcal{A}} \tag{7.6}$$

The efficiencies of the full chain of electron reconstruction, selection and triggering are shown in Figures 7.3 to 7.6. In these figures, each bin i contains the efficiency ϵ_i, which has been summed over the other kinematic variable :

$$\epsilon_i = \sum_j a_j \epsilon_{ij} \tag{7.7}$$

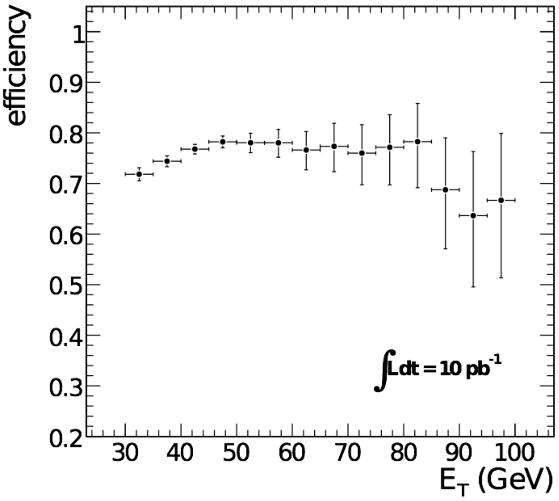

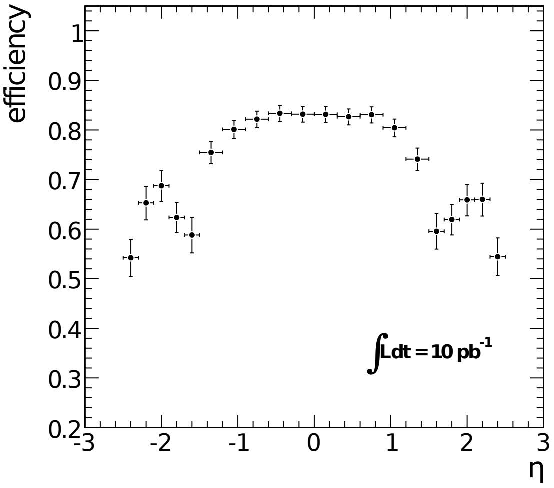

Figure 7.3: ϵ_W *vs* E_T. Each bin in E_T shows the efficiency $\epsilon_W(E_T, \eta)$ integrated over η.

Figure 7.4: ϵ_W *vs* η. Each bin in η shows the efficiency $\epsilon_W(E_T, \eta)$ integrated over E_T.

7.5.4 Event Efficiencies

These integrated electron efficiencies can then be used to calculate the complete event efficiencies. For $\mathrm{W}^\pm \rightarrow \mathrm{e}^\pm \nu_\mathrm{e}$, the final efficiency is :

$$\epsilon_W = \epsilon_{offline} \cdot \epsilon_{online} = \epsilon_{GSFele} \cdot \epsilon_{isolation} \cdot \epsilon_{ID} \cdot \epsilon_{online} \tag{7.8}$$

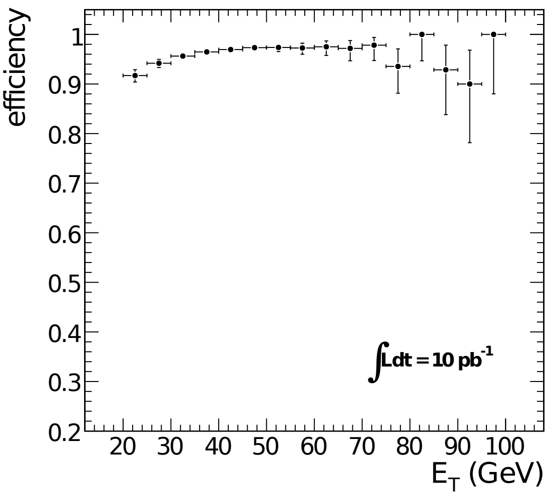

Figure 7.5: ϵ_Z *vs* E_T. Each bin in E_T shows the efficiency $\epsilon_Z(E_T, \eta)$ integrated over η.

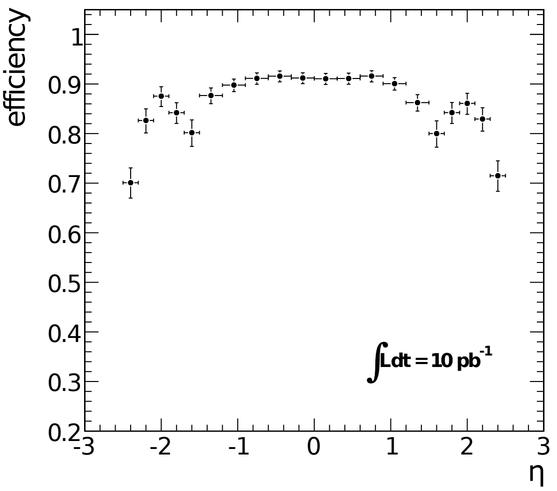

Figure 7.6: ϵ_Z *vs* η. Each bin in η shows the efficiency $\epsilon_Z(E_T, \eta)$ integrated over E_T.

The efficiency, ϵ_W, must also be corrected for the small inefficiency (0.9%) of the requirement that no second electron with $E_T > 20\,\mathrm{GeV}$ is present in the event. This is currently estimated from simulation and so is not included in Table 7.8.

In $\gamma^*/\mathrm{Z} \rightarrow \mathrm{e}^+\mathrm{e}^-$, both electrons must satisfy the electron selection, leading to an efficiency term of $\epsilon^2_{offline}$. However, only one electron need satisfy the trigger requirement, so :

$$\epsilon_{trigger} = 1 - (1 - \epsilon_{online})^2 = \epsilon^2_{online} - 2\epsilon_{online} \tag{7.9}$$

leading to an event efficiency :

$$\epsilon_Z = \epsilon^2_{offline} \cdot \epsilon_{trigger} = \epsilon^2_{offline}\left(\epsilon^2_{online} - 2\epsilon_{online}\right) \tag{7.10}$$

7.5.5 Tag and Probe Efficiency Results

The Tag and Probe measured efficiency is compatible with the true efficiencies. For an $\int Ldt = 10\,\mathrm{pb}^{-1}$ measurement, the dominant uncertainty in the Tag and Probe efficiency is assumed to be statistical.

Efficiency Type	$W^\pm \rightarrow e^\pm \nu_e$ Efficiency (%)	$\gamma^*/Z \rightarrow e^+e^-$ Efficiency (%)
$\epsilon_{offline}$	74.4 ± 0.6	90.4 ± 0.3
ϵ_{online}	97.2 ± 0.3	96.8 ± 0.2
ϵ_{event} (T&P)	72.3 ± 0.6	81.6 ± 0.5
ϵ_{event} (True)	73.0	82.1

Table 7.8: Tag and Probe efficiency results for $W^\pm \rightarrow e^\pm \nu_e$ and $\gamma^*/Z \rightarrow e^+e^-$.

7.6 Signal Yield and Background Estimation

7.6.1 Signal Yield Estimation for $Z \rightarrow e^+ e^-$

The presence of two electrons to identify in $\gamma^*/Z \rightarrow e^+e^-$ events, combined with the invariant mass constraint, means that the sample of selected $Z \rightarrow e^+ e^-$ events is effectively background free (Figure 7.2). Consequently no background subtraction is performed and the signal yield estimate is simply the total number of events in the $Z \rightarrow e^+ e^-$ sample. Therefore, $N_Z^{sig} = 4723 \pm 65$ and $N_Z^{background}$ is assumed to be zero. In fact, the signal sample contains 11 background events.

In data-taking, the level of background contamination in $Z \rightarrow e^+ e^-$ events will be estimated using a number of techniques as described in [60].

7.6.2 Background Subtraction and Signal Yield for $W^\pm \rightarrow e^\pm \nu_e$

With only one electron to be identified in $W^\pm \rightarrow e^\pm \nu_e$ events, significant background contamination remains in the sample after the full selection (Figure 7.1). This contamination can be separated into two categories : electroweak backgrounds and hadronic backgrounds.

The electroweak backgrounds can be estimated reliably from Monte Carlo simulation, since the physics is well understood and the level of contamination is relatively small. The normalisations of these background sources can be set relative to the number of observed $Z \rightarrow e^+ e^-$ events in order to remove uncertainties from the integrated luminosity measurement.

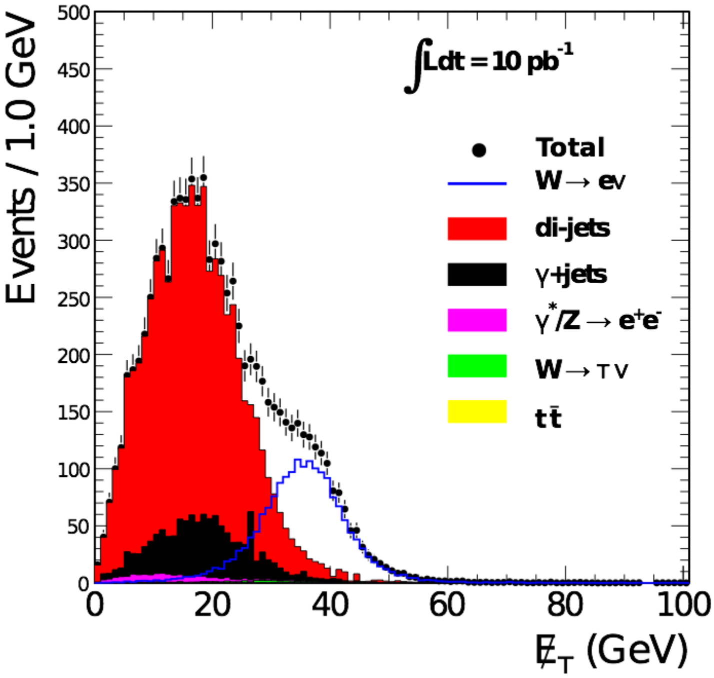

Figure 7.7: $\not{E}_T$ distribution, showing the composition of the sample which passes the $W^{\pm} \rightarrow e^{\pm}\, \nu_e$ selection apart from the track isolation criterion, which it fails.

Hadronic backgrounds, on the other hand, must be estimated from data. This cross-section analysis uses the "Matrix" [75] or "ABCD" [76] method, which creates discrete subsets of the available data in order to estimate the background-subtracted signal yield. A relatively pure hadronic sample is obtained by performing the full $W^{\pm} \rightarrow e^{\pm}\, \nu_e$ selection, but inverting one of the criteria. The track isolation criterion is used because it is highly efficient for signal and QCD di-jets are inherently non-isolated. The $\not{E}_T$ distribution of the sample which meets all but the track isolation requirements is shown in Figure 7.7.

Both the signal sample and the background sample are further subdivided by a $\not{E}_T$ threshold. The resulting four regions (Figure 7.8), their populations and the relationships between these populations are used to estimate the number of signal events in the signal sample. The four regions used are :

A : electron candidate passes full $W^{\pm} \rightarrow e^{\pm}\, \nu_e$ selection and event $\not{E}_T > 30\,\text{GeV}$

B : electron candidate passes full $W^{\pm} \rightarrow e^{\pm}\, \nu_e$ selection and event $\not{E}_T < 30\,\text{GeV}$

C : electron candidate fails the track isolation condition and event $\not{E}_T < 30\,\text{GeV}$

D : electron candidate fails the track isolation condition and event $\not{E}_T > 30\,\text{GeV}$

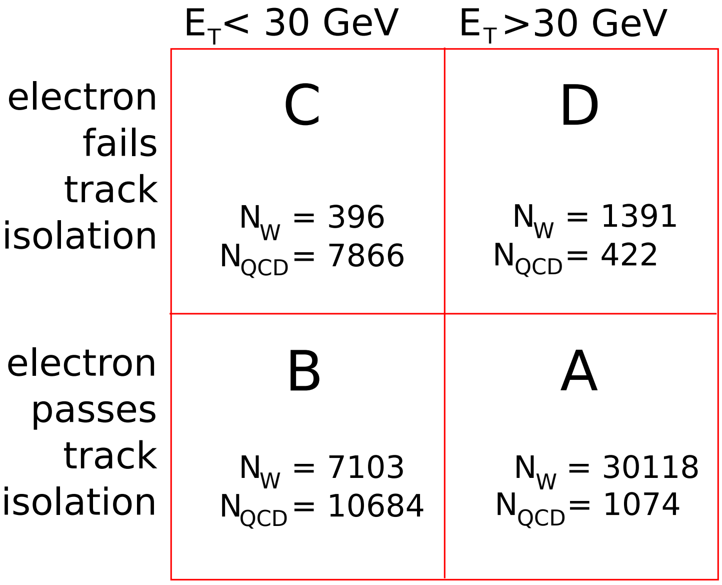
E_T< 30 GeV
E_T>30 GeV
electron fails track isolation
electron passes track isolation
C
N_W = 396
N_{QCD}= 7866
D
N_W = 1391
N_{QCD}= 422
B
N_W = 7103
N_{QCD}= 10684
A
N_W = 30118
N_{QCD}= 1074

Figure 7.8: Division of the data into four separate regions for signal yield estimation.

The signal sample is the conjoined region AB. The majority of signal events will be in region A. Regions B, C and D will be background dominated.

In the method, the following relationship between the amount of hadronic background in each region is asserted :

$$\frac{N_A^{QCD}}{N_B^{QCD}} = \frac{N_D^{QCD}}{N_C^{QCD}} \tag{7.11}$$

where N_X^{QCD} is the number of hadronic events in region X. The assertion of (7.11) is only valid if the $\not\!\!E_T$ distribution of the hadronic events is uncorrelated with the track isolation of electrons in those events. Figure 7.9 shows the $\not\!\!E_T$ distribution for regions BA and CD. It is clear that the two variables are in fact correlated.

In limit that A is the sole region which is populated by signal, then the total amount of hadronic background in this signal region can be estimated (after electroweak background subtraction) by :

$$N_A^{QCD} = \frac{N_B N_D}{N_C} \tag{7.12}$$

The applicability of (7.12) can be extended if signal in regions other than A is accounted for. It is evident from Figure 7.1 that a significant fraction of $\mathrm{W}^{\pm} \rightarrow \mathrm{e}^{\pm}\,\nu_{\mathrm{e}}$ events have $\not\!\!E_T < 30\,\mathrm{GeV}$. This fraction can be estimated using the Ersatz Missing

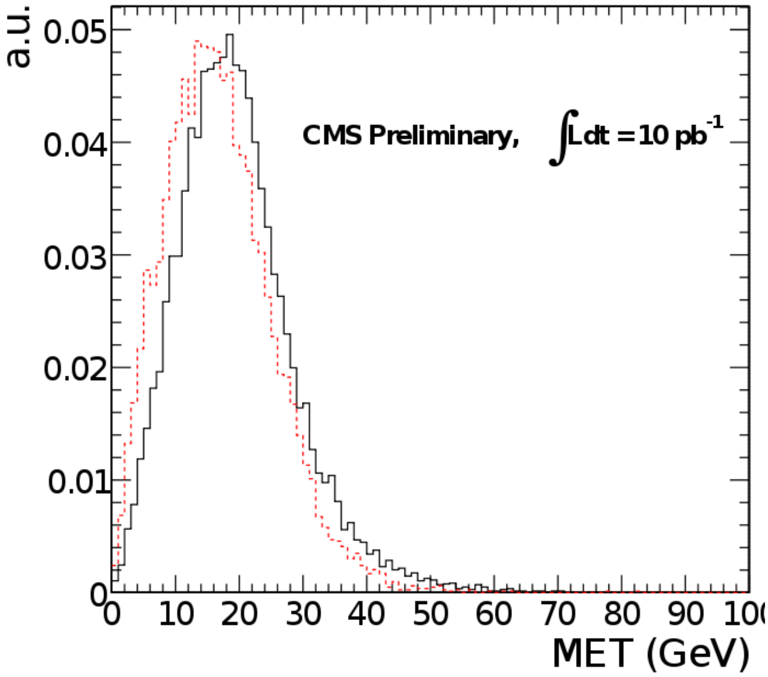

Figure 7.9: Comparison of $\not\!\!E_T$ distribution of the hadronic background in region BA (solid line) to the $\not\!\!E_T$ distribution of the hadronic background in region CD (dashed line).

Energy method, as discussed in Chapter 6. This relationship can be expressed as :

$$F_Z = \frac{N_A^{\mathrm{W}^\pm \rightarrow \mathrm{e}^\pm \nu_\mathrm{e}}}{N_B^{\mathrm{W}^\pm \rightarrow \mathrm{e}^\pm \nu_\mathrm{e}}} = \frac{\epsilon_{MET}}{1 - \epsilon_{MET}} \tag{7.13}$$

The fraction of signal which leaks into region CD is the inefficiency of the track isolation criteria, which is measured by Tag and Probe :

$$1 - \epsilon_{trackiso} = \frac{N_C^{\mathrm{W}^\pm \rightarrow \mathrm{e}^\pm \nu_\mathrm{e}} + N_D^{\mathrm{W}^\pm \rightarrow \mathrm{e}^\pm \nu_\mathrm{e}}}{N_{tot}^{\mathrm{W}^\pm \rightarrow \mathrm{e}^\pm \nu_\mathrm{e}}} \tag{7.14}$$

The distribution of signal between C and D, F'_Z, can again be determined by the Ersatz method.

These relations account for the leakage of signal into the other regions, allowing a more accurate determination of the final signal yield. If $F_Z = F'_Z$, then the number of signal events in the signal sample is given by :

$$N_A^{\mathrm{W}^\pm \rightarrow \mathrm{e}^\pm \nu_\mathrm{e}} + N_B^{\mathrm{W}^\pm \rightarrow \mathrm{e}^\pm \nu_\mathrm{e}} = \frac{\epsilon_{trackiso}(F_Z + 1)(N_D N_B - N_A N_C)}{\epsilon_{trackiso}(F_Z N_C - N_D) + (\epsilon_{trackiso} - 1)N_A - F_Z N_B} \tag{7.15}$$

If $F_Z \neq F'_Z$, (7.15) becomes more algebraically complicated : the exact solution is given in [60].

7.6.3 Uncertainties in $\mathrm{W}^\pm \rightarrow \mathrm{e}^\pm \nu_\mathrm{e}$ Signal Yield Estimation

The major source of bias in the signal yield estimation is the assumption that there is no correlation in the hadronic background between electron track isolation and event $\not{E}_T$. This systematic is kept in check by insisting on an efficient selection with high background rejection power. With the current selection, the bias is 1.8%.

The effect of the uncertainties of the Ersatz $\not{E}_T$ method can be evaluated. In the previous chapter, it was determined by the Ersatz method that for the $\not{E}_T > 30\,\mathrm{GeV}$ threshold used in this analysis, the efficiency was :

$$\epsilon(\not{E}_T > 30\,\mathrm{GeV}) = 79.6 \pm 0.6(\mathrm{stat}) \pm 1.0(\mathrm{syst})\%$$

The −1.0% systematic bias observed is equivalent to a −6.0% bias in F_Z. From Figure 7.10, this corresponds to a ± 1.6% systematic uncertainty in the signal yield estimation.

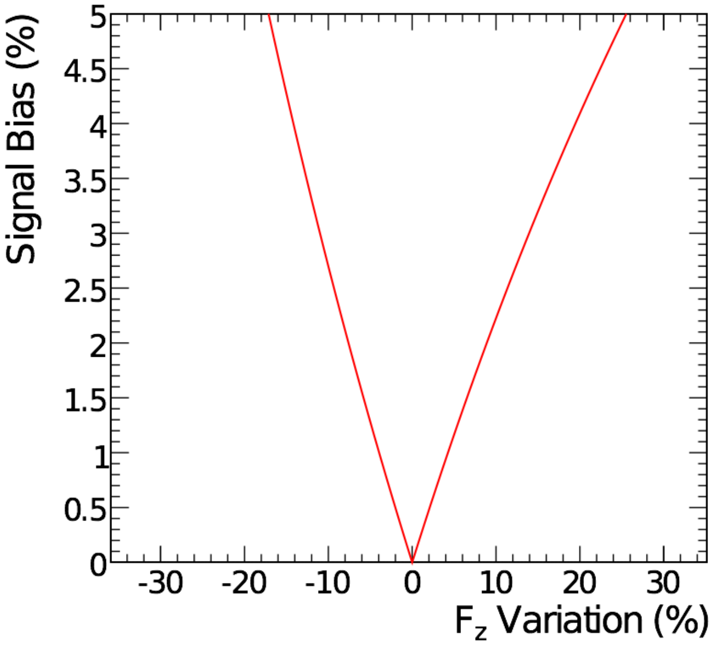

Figure 7.10: $W^{\pm} \rightarrow e^{\pm}\,\nu_e$ signal yield uncertainty versus F_z bias.

The determination of F'_Z is statistically limited and has a higher background contamination ($\sim 5\%$). The efficiency result obtained is :

$$\epsilon(\not\!\!E_T > 30\,\mathrm{GeV}) = 78.1 \pm 3.1(\mathrm{stat}) \pm 1.0(\mathrm{syst})\%$$

The bias of +1% is equivalent to an F'_Z bias of 6.8%, which corresponds to an uncertainty of $\pm 0.24\%$ in the signal yield estimation. The small size of the final uncertainty is a result of the low signal population of regions C and D.

The statistical uncertainty of the W yield includes the statistical uncertainties in the F_Z, F'_Z and $\epsilon_{trackiso}$ determinations which are governed by the number of $\gamma^*/Z \rightarrow e^+e^-$ events.

The systematic uncertainty introduced by using the tag and probe method to measure the efficiency of the track isolation criterion is negligible. The uncertainty associated with the electroweak background estimation is also negligible.

These systematic uncertainties were added in quadrature, to reach a total uncertainty on the signal yield of 2.4%.

7.6.4 Signal Yield Estimate for $W^{\pm} \rightarrow e^{\pm}\,\nu_e$

The final background subtracted signal yield was found to be :

$$N_W^{sig} - N_W^{bkgd} = 37500 \pm 450(\text{stat}) \pm 900(\text{sys}).$$

The true value was 37221 events.

7.7 Integrated Luminosity Measurement

There are a number of different methods of determining the LHC luminosity, but the one most likely to be used for early cross-section measurements derives the luminosity from measurements of LHC beam parameters. The instantaneous luminosity of the machine for bunches of particles colliding in an interaction region is given as :

$$L = \frac{N_b^2 n_b f_{rev}}{A_{eff}} \tag{7.16}$$

where N is the number of particles in each bunch; n_b, the number of bunches; f_{rev}, the revolution frequency of the beams; and A_{eff}, the effective transverse area in which collisions take place.

The revolution frequency and the number of bunches are accurately known. The number of particles in each bunch is known to $\sim 1\%$ precision from measurements of the beam current. The uncertainty in the knowledge of A_{eff} is the limiting uncertainty in this luminosity measurement. A_{eff} can be predicted *ab initio* with an accuracy of $20-30\%$ from the detailed studies of the LHC performance undertaken to enable machine operation.

This uncertainty can be reduced by measuring A_{eff}. For beams with Gaussian transverse profiles, $A_{eff} = 4\pi\sigma_x\sigma_y$. The transverse widths, σ_x and σ_y, can be measured following [77]. This technique measures the relative rate of beam-beam interactions as one beam is laterally displaced relative to the other. The measurements can be made quickly, for the necessary beam conditions correspond to the conditions expected in the first physics runs.

For an early cross-section measurement, the expected integrated luminosity uncertainty from such a determination is estimated to be $\pm 10\%$.

7.8 Acceptance Calculation

The acceptance for the $\mathrm{W}^\pm \rightarrow \mathrm{e}^\pm\, \nu_\mathrm{e}$ cross-section measurement has been defined as the fraction of events which have an electron that is within the geometric constraints of the detector fiducial volume and has been reconstructed as a supercluster with $E_T >$ 30 GeV. This is necessarily estimated from Monte Carlo simulation. The supercluster is geometrically matched to the simulated electron with a cone $\Delta R < 0.2$. The estimated acceptance, $\mathcal{A}$, for $\mathrm{W}^\pm \rightarrow \mathrm{e}^\pm\, \nu_\mathrm{e}$ events is $\mathcal{A} = 0.366 \pm 0.001(\mathrm{stat})$.

The acceptance for the $\gamma^*/\mathrm{Z} \rightarrow \mathrm{e}^+\mathrm{e}^-$ cross-section measurement has been defined similarly to the $\mathrm{W}^\pm \rightarrow \mathrm{e}^\pm\, \nu_\mathrm{e}$ case, but requiring that both electrons are within the fiducial volume of the detector and are each reconstructed as a supercluster with $E_T > 20\,\mathrm{GeV}$. The invariant mass of the two superclusters is required to be : $70\,\mathrm{GeV} < m_{SC-SC} < 110\,\mathrm{GeV}$. The estimated acceptance for $\gamma^*/\mathrm{Z} \rightarrow \mathrm{e}^+\mathrm{e}^-$ events is $\mathcal{A} = 0.404 \pm 0.002(\mathrm{stat})$.

There are several sources of uncertainty in these calculated acceptances. Incorporating the superclustering efficiency into the acceptance leads to a small uncertainty, from the effect of ECAL energy scale uncertainty. As this is expected to be well controlled, even at start-up, the resulting uncertainty is estimated as $\pm 0.16\%$ in the $\gamma^*/\mathrm{Z} \rightarrow \mathrm{e}^+\mathrm{e}^-$ acceptance and $\pm 0.8\%$ in $\mathrm{W}^\pm \rightarrow \mathrm{e}^\pm\, \nu_\mathrm{e}$.

The uncertainties on the acceptance arising from missing higher order QCD and electroweak corrections are shown in Table 7.9. These are calculated by generating events at the next highest order and taking the difference between the resulting and original estimates. The QCD uncertainty also includes factorisation and renormalisation scale dependence uncertainties estimated by repeating the calculations with the scales multiplied by 0.5 or 2.

The uncertainties from the parton distribution functions are also shown in Table 7.9. These are estimated using the N_P eigenvector PDF sets provided (for the acceptance uncertainties, MSTW2008 sets [53]). The eigenvectors describe the behaviour of the PDF global fit χ^2 around the global minimum and act to quantify the uncertainties in the PDF parameterisations [54]. The resulting uncertainty in an observable X defined as :

$$\Delta X = \frac{1}{2}\left(\sum_{i=1}^{N_p} \left(X(S_i^+) - X(S_i^-)\right)^2\right)^{\frac{1}{2}} \tag{7.17}$$

where $X\left(S_i^{\pm}\right)$ is the predicted X value when the PDF set used has eigenvector S_i varied in the positive or negative direction (all other eigenvectors are held fixed).

	Acceptance Uncertainties (%)		
Source of Uncertainty	$\gamma^*/\mathrm{Z} \rightarrow \mathrm{e}^+\mathrm{e}^-$	$\mathrm{W}^+ \rightarrow \mathrm{e}^+\nu_\mathrm{e}$	$\mathrm{W}^- \rightarrow \mathrm{e}^-\overline{\nu}_\mathrm{e}$
QCD	0.35 ± 0.38	0.58 ± 0.38	1.11 ± 0.36
Electroweak	2.11 ± 1.51	1.82 ± 1.44	2.03 ± 1.57
PDF	1.03 ± 0.00	1.41 ± 0.00	1.31 ± 0.00

Table 7.9: Theoretical uncertainties in the calculated acceptances for $\gamma^*/\mathrm{Z} \rightarrow \mathrm{e}^+\mathrm{e}^-$, $\mathrm{W}^+ \rightarrow \mathrm{e}^+\nu_\mathrm{e}$ and $\mathrm{W}^- \rightarrow \mathrm{e}^-\overline{\nu}_\mathrm{e}$.

7.9 Results

The $\mathrm{W}^{\pm} \rightarrow \mathrm{e}^{\pm}\,\nu_\mathrm{e}$ and $\gamma^*/\mathrm{Z} \rightarrow \mathrm{e}^+\mathrm{e}^-$ cross-section calculations are summarised in Tables 7.10 and 7.11. Only the statistical uncertainties are shown in this table. The systematic uncertainties are listed in Tables 7.12 and 7.13 The dominant systematic uncertainty in both cross-section measurements is the 10% uncertainty arising from the integrated luminosity measurement. In both measurements, the introduction of background into the Tag and Probe method will lead to an uncertainty, but this cannot yet be quantified.

Variable	Result
$N_W^{sig} - N_W^{bkgd}$	37500 ± 450
ϵ_W	0.714 ± 0.006
$\mathcal{A}$	0.366 ± 0.001
$\int Ldt$	$10\,\mathrm{pb}^{-1}$
$\sigma_W \cdot BR(\mathrm{W}^{\pm} \rightarrow \mathrm{e}^{\pm}\,\nu_\mathrm{e})$	$14350 \pm 200\,\mathrm{pb}$
$\sigma_W \cdot BR(\mathrm{W}^{\pm} \rightarrow \mathrm{e}^{\pm}\,\nu_\mathrm{e})$ (True)	$13865\,\mathrm{pb}$

Table 7.10: $\mathrm{W}^{\pm} \rightarrow \mathrm{e}^{\pm}\,\nu_\mathrm{e}$ cross-section results. Only statistical uncertainties are shown.

Variable	Result
$N_Z^{sig} - N_Z^{bkgd}$	4270 ± 70
ϵ_Z	0.816 ± 0.005
$\mathcal{A}$	0.404 ± 0.002
$\int Ldt$	$10\,\mathrm{pb}^{-1}$
$\sigma_Z \cdot BR(\gamma^*/\mathrm{Z} \rightarrow \mathrm{e}^+\mathrm{e}^-)$	$1296 \pm 20\,\mathrm{pb}$
$\sigma_Z \cdot BR(\gamma^*/\mathrm{Z} \rightarrow \mathrm{e}^+\mathrm{e}^-)$ (True)	$1296\,\mathrm{pb}$

Table 7.11: $\gamma^*/\mathrm{Z} \rightarrow \mathrm{e}^+\mathrm{e}^-$ cross-section results. Only statistical uncertainties are shown.

Source of Uncertainty	Uncertainty on Cross-Section (pb)
Tag and probe ϵ_W ($\gamma^*/\mathrm{Z} \rightarrow \mathrm{e}^+\mathrm{e}^-$ statistical)	± 120
Signal yield $N_W^{sig} - N_W^{bkgd}$	± 340
Ersatz $\not{E}_T$	± 230
Background $\not{E}_T$-isolation correlation	± 260
Acceptance	± 360
Electroweak	± 120
QCD	± 280
PDF	± 200
$\int Ldt$	± 1500

Table 7.12: Sources of systematic uncertainty in $\mathrm{W}^{\pm} \rightarrow \mathrm{e}^{\pm}\,\nu_{\mathrm{e}}$ cross-section measurement and their components. Potential correlations between the uncertainties have not yet been properly assessed.

Using the electron branching ratios from [78] gives $\sigma_W = 132 \pm 2\,\mathrm{nb}$ and $\sigma_Z = 38.5 \pm 0.6\,\mathrm{nb}$.

7.10 Conclusions

Analysis strategies for measuring the inclusive production cross-sections of the W and Z bosons have been formulated and tested for the early data-taking period of CMS.

Source of Uncertainty	Uncertainty on Cross-Section (pb)
Acceptance	± 32
Electroweak	± 29
QCD	± 3
PDF	± 13
$\int Ldt$	± 130

Table 7.13: Sources of systematic uncertainty in $\gamma^*/\mathrm{Z} \rightarrow \mathrm{e}^+\mathrm{e}^-$ cross-section measurement and their components. Potential correlations between the uncertainties have not yet been properly assessed.

These strategies use robust selections and data-driven methods to extract efficiencies and background-corrected signal yields. This mitigates the effects of imprecise knowledge of the alignment and calibration of the detector and the impact of possibly inaccurate detector simulations.

Significant results can be obtained with only $10\,\mathrm{pb}^{-1}$ of data.

8 Summary and Conclusions

“Data! Data! Data!” he cried impatiently. ”I can’t make bricks without clay.”

— Sir Arthur Conan Doyle

8.1 Summary

The main results reported in this thesis are summarised below.

Amplitude Reconstruction in the Electromagnetic Calorimeter

The electromagnetic calorimeter has been extensively studied in test beams in preparation for LHC data-taking. In contrast to particles resulting from LHC collisions, electrons from the test beam do not interact with the ECAL at fixed phase to the 40 MHz clock used in the electronics. As a result, amplitude reconstruction in the test beam could not achieve the accuracy expected in LHC running unless special, crystal specific weights were used in the amplitude reconstruction algorithm.

A novel technique for deriving such weights was developed. This method could be used for every crystal exposed to beam, improving on the previous method which was limited to those channels exposed to extremely large number of electrons.

The energy resolution of the calorimeter was measured using these optimised weights and found to be :

$$\left(\frac{\sigma}{E}\right)^2 = \left(\frac{3.37\%}{\sqrt{E}}\right)^2 + \left(\frac{0.108}{E}\right)^2 + 0.25\%$$

Electron Reconstruction

The electron charge measurement is complicated by the radiation of bremsstrahlung photons that convert into electron-positron pairs. The additional tracker hits that result lead to mistakes in track finding and fitting and hence to an incorrect charge determination.

A complementary measurement of the electron's charge using the azimuthal angle between the electron pixel seed and the supercluster was studied. It was found to give a competitive level of accuracy to the track-based measurement, with only a minority of the mis-measured electrons overlapping between the two methods. The implementation of this new method of charge measurement in the latest CMS reconstruction was described. A 50% reduction in charge mis-identification rate has been achieved with no loss of efficiency.

Missing Transverse Energy

Missing energy is a powerful discriminating variable in events – such as $\mathrm{W}^\pm \rightarrow \mathrm{e}^\pm \nu_\mathrm{e}$– that feature a neutrino in the final state. However, the accuracy of the missing energy can be reduced by instrumental problems such as noise or dead channels; by miscalibration; and by pile-up. These problems are expected to be significant in the early data and are difficult to incorporate into the detector simulations.

The Ersatz Missing Energy method creates an apparent missing energy in data from readily reconstructible $\gamma^*/\mathrm{Z} \rightarrow \mathrm{e}^+\mathrm{e}^-$ events. The energy of one electron – the "ersatz neutrino" – is removed from the missing energy sum. The resulting missing energy is corrected to remove discrepancies between the different event types. For example, corrections are made for the differing boson masses and the limited acceptance for the ersatz neutrino.

After these corrections are made, the ersatz missing energy is an accurate representation of the missing energy in $\mathrm{W}^\pm \rightarrow \mathrm{e}^\pm \nu_\mathrm{e}$ events, suitable for use in the $\mathrm{W}^\pm \rightarrow \mathrm{e}^\pm \nu_\mathrm{e}$ cross-section measurement. The efficiency of a $\not\!\!E_T > 30\,\mathrm{GeV}$ selection was found using the Ersatz method to be :

$$\epsilon(\not\!\!E_T > 30\,\mathrm{GeV}) = 79.6 \pm 0.6(\mathrm{stat}) \pm 1.0(\mathrm{syst})\%$$

compared to the real efficiency, $\epsilon(\not\!\!E_T > 30\,\mathrm{GeV}) = 80.6\%$.

The ersatz method was used in the final $\mathrm{W}^{\pm} \rightarrow \mathrm{e}^{\pm}\, \nu_{\mathrm{e}}$ cross-section measurement to estimate the background-subtracted signal yield. The systematic error it introduced to the estimate was less than 50% of the largest uncertainty.

Measurement of the W and Z Cross-Sections

The measurement of the inclusive W and Z cross-sections using the electron decay modes will be one of the first LHC physics results. The analysis methodology uses a robust trigger, reconstruction and selection in order to mitigate the effects of inprecise calibration and alignment knowledge. Methods to measure efficiencies and background-subtracted signal yields with a minimal reliance on simulation were developed and evaluated.

The analysis was carried out on simulated data and the measured cross-section results were in good agreement with the true input value. It was found that a statistically significant result could be obtained with the equivalent of $\int Ldt = 10\,\mathrm{pb}^{-1}$ data. The systematic uncertainties introduced by the data-driven methods were all a factor of five smaller than the anticipated uncertainty on the integrated luminosity.

8.2 Epilogue

The Large Hadron Collider will restart operation at the end of 2009. The results obtained by the Compact Muon Solenoid and the other experiments will reveal the mechanism of electroweak symmetry breaking and perhaps new phenomena not incorporated into the Standard Model. For any discovery to be credible, it must first be demonstrated that the CMS detector and the LHC environment are understood. This thesis presented work towards making that demonstration.

Bibliography

[1] The UA1 Collaboration, "Experimental Observation of Isolated Large Transverse Energy Electrons with Associated Missing Energy at $\sqrt{s} = 540\,GeV$," *Physics Letters B*, vol. 122, no. 1, pp. 103 – 116, 1983.

[2] The UA1 Collaboration, "Experimental Observation of Lepton Pairs of Invariant Mass Around 95 GeV/c^2 at the CERN SPS Collider," *Physics Letters B*, vol. 126, no. 5, pp. 398 – 410, 1983.

[3] The UA2 Collaboration, "Evidence for $\mathrm{Z}^0 \rightarrow \mathrm{e}^+\mathrm{e}^-$ at the CERN $\bar{\mathrm{p}}\mathrm{p}$ collider," *Physics Letters B*, vol. 129, no. 1-2, pp. 130 – 140, 1983.

[4] The UA2 Collaboration, "Observation of Single Isolated Electrons of High Transverse Momentum in Events with Missing Transverse Energy at the CERN $\bar{\mathrm{p}}\mathrm{p}$ collider," *Physics Letters B*, vol. 122, no. 5-6, pp. 476 – 485, 1983.

[5] I. Aitchison and A. Hey, *Gauge Theories in Particle Physics: a Practical Introduction.* Taylor & Francis, 2003.

[6] R. Ellis, W. Stirling, and B. Webber, *QCD and Collider Physics.* Cambridge University Press, 1996.

[7] T. GREENSHAW, ed., *Proceedings of the School for Experimental High Energy Physics Students.* RAL, 2006.

[8] E. Leader and E. Predazzi, *An Introduction to Gauge Theories and Modern Particle Physics*, vol. 1. Electroweak Interactions, the "New Particles" and the Parton Model. Cambridge University Press, 1996.

[9] S. Coleman and D. J. Gross, "Price of Asymptotic Freedom," *Phys. Rev. Lett.*, vol. 31, pp. 851–854, Sep 1973.

[10] The LEP Working Group for Higgs Boson Searches, "Search for the Standard Model Higgs boson at LEP," *Physics Letters B*, vol. 565, pp. 61 – 75, 2003.

[11] The TEVNPH Working Group, "Combined CDF and DZero Upper Limits on Standard Model Higgs-Boson Production with up to 4.2 fb^{-1} of Data," 2009, arXiv:0903.4001[hep-ex].

[12] P. Dirac, “The Quantum Theory of the Electron,” *Proceedings of the Royal Society of London. Series A, Containing Papers of a Mathematical and Physical Character*, pp. 610–624, 1928.

[13] Noether, Emmy, “Invariante Variationsprobleme (Invariant Variation Problems),” *Nachr. d. König. Gesellsch. d. Wiss. zu Göttingen, Math-phys. Klasse*, no. arXiv:physics/0503066v1, pp. 235–257, 1918.

[14] S. L. Glashow, “Partial-Symmetries of Weak Interactions,” *Nuclear Physics*, vol. 22, no. 4, pp. 579 – 588, 1961.

[15] A. Salam and J. Ward, “Electromagnetic and Weak Interactions,” *Physics Letters*, vol. 13, no. 2, pp. 168 – 171, 1964.

[16] S. Weinberg, “A Model of Leptons,” *Phys. Rev. Lett.*, vol. 19, pp. 1264–1266, Nov 1967.

[17] R. Plačakytė, “High Q^2 Cross Sections, Electroweak Measurements and Physics Beyond the Standard Model at HERA,” *arxiv:0906.4490[hep-ex]*, 2009.

[18] N. Cabibbo, “Unitary Symmetry and Leptonic Decays,” *Phys. Rev. Lett.*, vol. 10, pp. 531–533, Jun 1963.

[19] M. Kobayashi and T. Maskawa, “CP violation in the renormalizable theory of weak interaction,” *Theor. Phys*, vol. 49, pp. 652–657, 1973.

[20] M. Goldhaber, L. Grodzins, and A. W. Sunyar, “Helicity of Neutrinos,” *Phys. Rev.*, vol. 109, pp. 1015–1017, Feb 1958.

[21] J. Goldstone, “Field Theories with ≪Superconductor≫ Solutions,” *Il Nuovo Cimento*, vol. 19, no. 1, pp. 154–164, 1961.

[22] P. W. Higgs, “Broken Symmetries and the Masses of Gauge Bosons,” *Phys. Rev. Lett.*, vol. 13, pp. 508–509, Oct 1964.

[23] The ALEPH, DELPHI, L3, OPAL, SLD Collaborations, the LEP Electroweak Working Group, the SLD Electroweak and Heavy Flavour Groups, “Precision Electroweak Measurements on the Z Resonance,” *Physics Reports*, vol. 427, no. 5-6, pp. 257 – 454, 2006.

[24] The ALEPH, CDF, DELPHI, D0, L3, OPAL, SLD Collaborations, the LEP Electroweak Working Group, the Tevatron Electroweak Working Group, the SLD Electroweak and Heavy Flavour Groups, “Precision Electroweak Measurements and Constraints on the Standard Model,” Tech. Rep. CERN-PH-EP/2008-020, CERN, November 2008.

[25] The CMS Collaboration, “The 2008 CMS Computing Software and Analysis Challenge,” IN 2008/044, CERN, 2008.

[26] The CMS Collaboration, “Determination of Jet Energy Scale Using Z$\rightarrow e^+e^-$ + Jet p_T Balance and Procedure for Combining Data Driven Corrections,” PAS JME-09-005, CERN, 2009.

[27] P. Meridiani and R. Paramatti, “Use of $Z \rightarrow e^+e^-$ Events for ECAL Calibration,” CMS Note 2006/039, CERN, 2006.

[28] The CMS Collaboration, “The CMS experiment at the CERN LHC,” *Journal of Instrumentation*, vol. 3, no. 08, p. S08004, 2008.

[29] L. Evans and P. B. (editors), “LHC Machine,” *Journal of Instrumentation*, vol. 3, no. 08, p. S08001, 2008.

[30] The ATLAS Collaboration, “The ATLAS Experiment at the CERN Large Hadron Collider,” *Journal of Instrumentation*, vol. 3, no. 08, p. S08003, 2008.

[31] The LHCb Collaboration, “The LHCb Detector at the LHC,” *Journal of Instrumentation*, vol. 3, no. 08, p. S08005, 2008.

[32] The ALICE Collaboration, “The ALICE Experiment at the CERN LHC,” *Journal of Instrumentation*, vol. 3, no. 08, p. S08002, 2008.

[33] P. Schleper, G. Steinbrueck, and M. Stoye, “Software Alignment of the CMS Tracker using MILLEPEDE II,” CMS Note 2006/011, 2006.

[34] E. Widl, R. Frühwirth, and W. Adam, “A Kalman Filter for Track-based Alignment,” CMS Note 2006/022, 2006.

[35] The CMS Electromagnetic Calorimeter Group, “Intercalibration of the Barrel Electromagnetic Calorimeter of the CMS Experiment at Start-up,” *Journal of Instrumentation*, vol. 3, no. 10, p. P10007, 2008.

[36] The CMS Collaboration, “Commissioning of the CMS Experiment and the Cosmic Run at Four Tesla,” CMS Paper 009/008, CERN, 2009.

[37] G. Daskalakis and I. van Vulpen, “Position Resolution in the CMS ECAL using 2003 Testbeam Data,” CMS Internal Note 2004/024, May 2004.

[38] The CMS Electromagnetic Calorimeter Group, “Reconstruction of the Signal Amplitude of the CMS Electromagnetic Calorimeter,” *Eur. Phys. J. C*, vol. S1, no. 46, pp. 23–35, 2006.

[39] The CMS Electromagnetic Calorimeter Group, “Energy Resolution of the Barrel of the CMS Electromagnetic Calorimeter,” *Journal of Instrumentation*, vol. 2, p. P04004, 2007.

[40] J. Gaiser, *Charmonium Spectroscopy from Radiative Decays of the* J/ψ *and* ψ'*, ch. Appendix F. SLAC, 1982.

[41] S. Baffioni *et al.*, "Electron Reconstruction in CMS," Note 2006/040, CERN, 2006.

[42] E. Meschi, T. Monteiro, C. Seez, and P. Vikas, "Electron Reconstruction in the CMS Electromagnetic Calorimeter," CMS Note 2001/034, CERN, 2001.

[43] D. L. Evans, "A Review of Clustering," CMS AN [in preparation], CERN, 2009.

[44] C. Charlot, "Tracking in Electron Reconstruction," CMS Talk `http://indico.cern.ch/getFile.py/access?contribId=1&resId=1&materialId=slides&confId=44569`, CERN, November 2008.

[45] W. Adam and R. Früwirth, "Reconstruction of Electrons with the Gaussian-Sum Filter in the CMS Tracker at the LHC," CMS Note 2005/001, CERN, 2005.

[46] P. Billoir and S. Qian, "Simultaneous Pattern Recognition and Track Fitting by the Kalman Filtering Method," *Nuclear Instruments and Methods in Physics Research Section A: Accelerators, Spectrometers, Detectors and Associated Equipment*, vol. 294, no. 1-2, pp. 219 – 228, 1990.

[47] H. Bethe and W. Heitler, "On the Stopping of Fast Particles and on the Creation of Positive Electrons," *Proceedings of the Royal Society of London. Series A, Containing Papers of a Mathematical and Physical Character*, vol. 146, no. 856, pp. 83–112, 1934.

[48] O. Gutsche *et al.*, "Electron Charge Misidentification Rate," CMS Talk `http://indico.cern.ch/getFile.py/access?contribId=3&resId=1&materialId=slides&confId=64436`, CERN, July 2009.

[49] C. Broutin, "Improvements in Electron Charge ID," CMS Talk `http://indico.cern.ch/getFile.py/access?contribId=1&resId=0&materialId=slides&confId=67008`, CERN, August 2009.

[50] J. Branson, M. Gallinaro, P. Ribeiro, R. Salerno, and M. Sani, "A Cut Based Method for Electron Identification in CMS," CMS AN 2008/082, CERN, 2008.

[51] The CMS Collaboration, *CMS Physics Technical Design Report*, vol. 1. CERN/LHCC, 2006.

[52] H. D. Politzer, "Reliable perturbative results for strong interactions?," *Phys. Rev. Lett.*, vol. 30, pp. 1346–1349, Jun 1973.

[53] A. D. Martin, W. J. Stirling, R. S. Thorne, and G. Watt, "Parton Distributions for the LHC," 2009, 0901.0002.

[54] J. Pumplin *et al.*, "New Generation of Parton Distributions with Uncertainties from Global QCD Analysis," *JHEP*, vol. 07, p. 012, 2002, hep-ph/0201195.

[55] G. Altarelli and G. Parisi, "Asymptotic Freedom in Parton Language," *Nuclear Physics B*, vol. 126, no. 2, pp. 298 – 318, 1977.

[56] A. Martin, R. Roberts, W. Stirling, and R. Thorne, “Parton Distributions and the LHC: W and Z production,” *The European Physical Journal C-Particles and Fields*, vol. 14, no. 1, pp. 133–145, 2000.

[57] T. Gleisberg *et al.*, “Predictions for Multi-Particle Final States with SHERPA,” *arxiv:*, no. hep-ph/0409122v1, 2004.

[58] C. Anastasiou *et al.*, “High-precision QCD at Hadron Colliders : Electroweak Gauge Boson Rapidity Distribution at NNLO,” no. hep-ph/0312266, 2003.

[59] H. Jung and A. D. Roeck, eds., *HERA and the LHC*, no. DESY-PROC-2009-02, 2009.

[60] N. Adam *et al.*, “Towards a Measurement of the Inclusive Wev and Zee Cross Sections in pp Collisions at sqrt(s) = 10 TeV,” CMS AN 2009/098, CERN, 2009.

[61] T. Sjöstrand, S. Mrenna, and P. Skands, *PYTHIA 6.4 Physics and Manual*, March 2006.

[62] S. Agostinelli *et al.*, “GEANT4–a Simulation Toolkit,” *Nuclear Instruments and Methods in Physics Research Section A: Accelerators, Spectrometers, Detectors and Associated Equipment*, vol. 506, no. 3, pp. 250 – 303, 2003.

[63] T. Sjöstrand et. al, “Z Physics at LEP1,” Tech. Rep. CERN 89-08, CERN, 1989.

[64] N. D. Gagunashvili, “Comparison of weighted and unweighted histograms,” *arxiv*, no. physics/0605123v1, 2006.

[65] CMS Particle Flow Object Group, “Particle Flow Reconstruction of Jets, Taus and MET,” CMS AN 2009/039, CERN, 2009.

[66] S. Esen *et al.*, “$\not{E}_T$ Performance in CMS,” CMS AN 2007/041, CERN, 2007.

[67] J. Alexander *et al.*, “$\not{E}_T$ Reconstruction, Performance and Validation,” CMS AN 2008/089, CERN, 2008.

[68] R. Demina *et al.*, “Calorimeter Cell Energy Thresholds for Jet Reconstruction in CMS,” CMS Note 2006/020, CERN, 2006.

[69] N. Almeida *et al.*, “The Selective Read-Out Processor for the CMS Electromagnetic Calorimeter,” *IEEE Trans. On Nuclear Science*, vol. 52, no. 3, pp. 772–777, 2005.

[70] N. Adam *et al.*, “Towards a Measurement of the Inclusive W → eν and Z → ee Cross Sections in p p Collisions at $\sqrt{s} = 14\,\mathrm{TeV}$,” CMS AN 2007/026, CERN, 2007.

[71] S. Frixione and B. R. Webber, “Matching nlo qcd computations and parton shower simulations,” *Journal of High Energy Physics*, vol. 2002, no. 06, pp. 029–029, 2002.

[72] Z. Was, “TAUOLA, the Library for τ Lepton Decay, and KKMC/KORALB/KORALZ/... Status Report,” *Nuclear Physics B - Proceedings Supplements*, vol. 98, no. 1-3, pp. 96 – 102, 2001.

[73] G. Daskalakis, N. Rompotis, and C. Seez, “Data Driven Selection Cut Tuning for Electrons,” CMS AN 2009/108, CERN, 2009.

[74] G. Daskalakis, D. Evans, C. Hill, J. Jackson, P. Vanlaer, J. Berryhill, J. Haupt, D. Futyan, C. Seez, C. Timlin, and D. Wardrope, “Measuring Electron Efficiencies at CMS with Early Data,” CMS AN 2007/019, CERN, November 2007.

[75] The D0 Collaboration, “Measurement of $\gamma^*/\mathrm{Z} \rightarrow \mathrm{e}^+\mathrm{e}^-$ and $\mathrm{W}^\pm \rightarrow \mathrm{e}^\pm \nu_\mathrm{e}$ Production Cross Sections Using One Tight Central Electron,” D0 Note 4897, FNAL, 2004.

[76] The CDF Collaboration, “Measurements of Inclusive W and Z Cross Sections in p $\overline{\mathrm{p}}$ Collisions at $\sqrt{s} = 1.96$TeV,” *arxiv:hep-ex/0508029v1*, August 2005.

[77] S. van der Meer, “Calibration of the Effective Beam Height in the ISR,” tech. rep., CERN, 1968.

[78] C. Amsler, M. Doser, M. Antonelli, D. Asner, K. Babu, H. Baer, H. Band, R. Barnett, E. Bergren, J. Beringer, *et al.*, “Review of particle physics,” *Physics Letters B*, vol. 667, no. 1-5, pp. 1–6, 2008.